



Thèse

2022

Open Access

This version of the publication is provided by the author(s) and made available in accordance with the copyright holder(s).

Influenza A Virus: From Infection to Prevention. Long-term Effects of an Early Life IAV Infection in vivo and Optimization of the Live Attenuated Influenza A Vaccine Backbone Using Mouse Models

Pereira Bonifacio Lopes, Joao Pedro

How to cite

PEREIRA BONIFACIO LOPES, Joao Pedro. Influenza A Virus: From Infection to Prevention. Long-term Effects of an Early Life IAV Infection in vivo and Optimization of the Live Attenuated Influenza A Vaccine Backbone Using Mouse Models. 2022. doi: 10.13097/archive-ouverte/unige:166495

This publication URL: <https://archive-ouverte.unige.ch//unige:166495>

Publication DOI: [10.13097/archive-ouverte/unige:166495](https://doi.org/10.13097/archive-ouverte/unige:166495)

UNIVERSITÉ DE GENÈVE

FACULTÉ DES MÉDECINE

Section de médecine fondamentale

Département de microbiologie et médecine moléculaire

Professeur M. Schmolke

Influenza A Virus: From Infection to Prevention. Long-term Effects of an Early Life IAV Infection *in vivo* and Optimization of the Live Attenuated Influenza A Vaccine Backbone Using Mouse Models

THÈSE

présentée aux Facultés de médecine et des sciences de l'Université de Genève
pour obtenir le grade de Docteur ès sciences en sciences de la vie,
mention Sciences biomédicales

par

João Pedro PEREIRA BONIFÁCIO LOPES

de

Setúbal (Portugal)

Thèse N°

GENÈVE

Nom de l'Atelier d'Impression

2022

UNIVERSITÉ DE GENÈVE

FACULTÉ DES MÉDECINE

Section de médecine fondamentale

Département de microbiologie et médecine moléculaire

Professeur M. Schmolke

Influenza A Virus: From Infection to Prevention. Long-term Effects of an Early Life IAV Infection *in vivo* and Optimization of the Live Attenuated Influenza A Vaccine Backbone Using Mouse Models

THÈSE

présentée aux Facultés de médecine et des sciences de l'Université de Genève
pour obtenir le grade de Docteur ès sciences en sciences de la vie,
mention Sciences biomédicales

par

João Pedro PEREIRA BONIFÁCIO LOPES

de

Setúbal (Portugal)

Thèse N°

GENÈVE

Nom de l'Atelier d'Impression

2022

Abstract

Influenza A virus (IAV) is one of the major causative agents of acute respiratory infections in humans. Influenza disease causes up to 650,000 deaths every year with its burden highest among high-risk populations. A major complication during IAV infections is the increased susceptibility to bacterial secondary infections, however the impact on the commensal bacterial community is still poorly understood. This is particularly important during childhood, when IAV infections are frequent and the microbiota community is still developing. Vaccination is the best way to prevent influenza disease. The live attenuated influenza vaccine (LAIV) provides good protection and induces mucosal responses important in blocking transmission. However, due to safety concerns, key target populations that could benefit from the advantages of this vaccine, are left out. The aim of this thesis was two-fold. To optimize the current LAIV backbone and increase its safety profile and to explore the effects of a childhood IAV infection on the development of the host microbiota and their impact in adult life using a mouse model. To address the first aim, we performed targeted mutagenesis on the backbone of the LAIV and rescued an optimized LAIV (optiLAIV) with a higher attenuation degree. We characterized optiLAIV in two mouse models representing infants under 2-years old and highly susceptible populations to viral infections. In neonatal mice, we showed that optiLAIV is cleared faster from the upper respiratory tract (URT) while still maintaining its protective ability against two challenge models. Additionally, we showed that in adult mice lacking a key player of the interferon signaling response, optiLAIV presented reduced replication in the lower respiratory tract (LRT) and caused no signs of morbidity compared to a 50% mortality rate observed in animals vaccinated with LAIV. OptiLAIV induced UPR-related genes in a human nasal epithelial tissue model suggesting this pathway as a potential mechanism of attenuation. Our results present an optimized LAIV candidate that could be explored as a safer alternative to the licensed LAIV in high-risk patient groups. To address the second aim, we used a neonatal mouse model, in which we report that a single subclinical IAV infection leads to a significant decrease in the bacterial abundance of the small intestine in adulthood. This observation was accompanied by an enrichment of Enterobacteriales and a reduction of Clostridiales. Furthermore, IAV-imprinted male animals had an increased body weight and lower energy expenditure compared to mock imprinted animals. Cohousing experiments abrogated the body weight differences observed while a high-fat-high-sucrose diet enhanced the phenotype, suggesting a microbiota-dependent effect. Our results show that an acute respiratory infection during childhood induces long-term dysbiosis with possible consequences on host metabolic processes. Together, our findings highlight the

importance of preventing IAV infections during childhood and propose an alternative strategy to do so.

Résumé

Le virus de l'influenza A (IAV) est l'un des principaux agents responsables des infections respiratoires aiguës chez l'homme. La grippe cause jusqu'à 650 000 décès chaque année, avec un taux de mortalité plus élevé chez les populations à haut risque. L'augmentation de la susceptibilité aux surinfections bactériennes constitue l'une des principales complications des infections au virus de la grippe. Cependant, son impact sur la communauté bactérienne commensale est encore peu compris. Ceci est particulièrement important pendant l'enfance, lorsque les infections à IAV sont fréquentes mais la communauté microbienne est encore en cours de développement. La vaccination reste le meilleur moyen de prévenir la maladie de la grippe. Le vaccin vivant atténué contre la grippe (LAIV) offre une protection efficace et induit des réponses muqueuses importantes pour bloquer la transmission. Cependant, en raison de problèmes de sécurité, des populations cibles clés, qui pourraient en bénéficier, sont laissées de côté. Ce travail de thèse avait deux objectifs différents concernant le virus de la grippe: (1) d'une part, l'optimisation du LAIV actuel et l'amélioration de son profil de sécurité; et (2) d'autre part, l'exploration, en utilisant un modèle de souris, des effets d'une infection infantile par le IAV sur le développement du microbiote de l'hôte et de leur impact à l'âge adulte. Pour atteindre le premier objectif, nous avons préparé, par mutagenèse dirigée à partir de l'actuel LAIV, une version optimisée (optiLAIV) avec un degré d'atténuation plus élevé. Nous avons caractérisé l'optiLAIV dans deux modèles de souris représentant des nourrissons de moins de 2 ans et des populations très sensibles aux infections virales. Chez les souris néonatales, nous avons montré que l'optiLAIV est éliminé plus rapidement des voies respiratoires supérieures (VRS) tout en conservant sa capacité de protection contre deux modèles de provocation. De plus, nous avons montré que chez les souris adultes dépourvues d'élément clé de la réponse de signalisation de l'interféron, le virus optiLAIV présentait une réplication réduite dans les voies respiratoires inférieures (VRI) et ne provoquait aucun signe de morbidité, contrairement aux souris vaccinées avec le LAIV où le taux de mortalité était de 50%. OptiLAIV a induit des gènes liés au stress du réticulum endoplasmique (la voie du UPR) dans un modèle de tissu épithélial nasal humain, suggérant que cette voie constituerait un mécanisme potentiel d'atténuation. Nos résultats suggèrent un candidat vaccin LAIV optimisé qui pourrait être étudié comme une alternative plus sûre au LAIV autorisé dans les groupes de patients à haut risque. Concernant le deuxième objectif, nous avons utilisé un modèle de souris néonatale, dans lequel nous rapportons qu'une seule infection subclinique par le IAV entraîne une diminution significative de l'abondance bactérienne de l'intestin grêle à l'âge adulte. Cette observation s'accompagne d'un enrichissement des Enterobacterales et d'une réduction des

Clostridiales. De plus, les animaux mâles ayant reçu une empreinte IAV avaient un poids corporel plus élevé et une dépense énergétique plus faible que les animaux utilisés comme contrôle. Les expériences de cohabitation ont aboli les différences de poids corporel observées, tandis qu'un régime riche en graisses et en saccharose a renforcé le phénotype, ce qui suggère un effet dépendant du microbiote. Nos résultats montrent qu'une infection respiratoire aiguë pendant l'enfance induit une dysbiose à long terme avec des conséquences possibles sur les processus métaboliques de l'hôte. Ensemble, nos résultats soulignent l'importance de la prévention des infections au virus de la grippe A pendant l'enfance et proposent une stratégie alternative pour y parvenir.

Acknowledgements

Before anything, I would like to acknowledge and thank my PhD supervisor Prof. Mirco Schmolke. Almost four years of engaging scientific discussions, support, guidance, and a lot of patience. Thank you for teaching me how to think and ask questions with a clear goal and always providing the means to achieve any crazy ideas I had.

I would like to thank my thesis committee: Prof. Simone Becattini, Prof. Arnaud Didierlaurent, and Prof. Ronald Dijkman for accepting to read and comment this work. Our scientific exchanges have been very enlightening so far and I am sure that future discussions will be extremely fruitful and widen my knowledge beyond the focus of this project.

I would like to thank all my scientific collaborators and the exceptional people that taught me how to perform the experiments that fell outside of my comfort zone. Laure, Paola and Ingrid, your contributions were key to finish this project.

I want to express my utmost gratitude to a special person that followed my journey from the beginning: Filomena Silva. Minha protetora, meu anjo, e salvadora! I can think of a million reasons to thank you including your support, your good will, your invaluable expertise, but nothing was more important than your emotional and personal support. Thank you! Thank you! Thank you! You made this step of my career possible and I will take with me everything I learned from you.

I would like to thank the present and past lab members: Dr. Beryl Mazel-Sanchez, Dr. Ines Boal-Carvalho, Dr. Soner Yildiz, Nathalia Williams, Alicia Besomi, Chengyue Niu and Marion Lagune for their help and companionship.

I wish to express my gratitude for all the staff and members of the microbiology department. Dylan for always being helpful and efficient in solving any kind of problems. Genevieve for her good humor and always lifting my spirit with funny French words and jokes.

Also, I thank my friends in the PhD school and outside of the University. Inês Filipe, Callum, Albert and Josh, Safa and Rouaa, Nathalia, thank you for always providing me with

an escape from work, encouraging my love for boardgames and never saying no to a drink after negative results! This thesis would not be possible without your support

I would like to thank my parents, my sisters and my grandparents, for always answering my facetime calls, for supporting me emotionally throughout my thesis even at a distance, and for helping to shape the person I am today. This would not be possible without you!

And lastly, but most importantly, I would like to thank my partner Chris Baker for his unconditional support, love and care. Thank you for understanding my crazy meltdowns, encouraging my career ambitions, and always believing in me!

Table of Contents

1. Introduction	11
1.1. Chapter 1: Influenza A Virus	11
1.1.1. Influenza A Virus Classification	11
1.1.2. Influenza A Virus Tropism	12
1.1.3. Influenza A Virus Structure and Morphology	13
1.1.4. Influenza A Virus Replication Cycle	14
1.1.5. Influenza A Virus Glycoproteins	16
1.1.5.1. Hemagglutinin	16
1.1.5.2. Neuraminidase	17
1.1.6. Influenza A Virus Nonstructural Proteins	18
1.1.6.1. NS1	18
1.1.7. Influenza A Virus in the Human Population	19
1.1.8. Influenza A Pandemics History	20
1.1.9. The Influenza Disease	22
1.1.9.1. High-risk patient groups	23
1.1.9.1.1. Children under 5 years old	23
1.1.9.1.2. Individuals with chronic medical conditions	24
1.1.9.1.3. The elderly	24
1.1.9.1.4. Pregnant Women:	25
1.1.10. Host responses to Influenza Virus	26
1.1.10.1. Innate immune responses	26
1.1.10.2. Innate immune cells	27
1.1.10.2.1. Neutrophils	27
1.1.10.2.2. Natural Killer Cells	27
1.1.10.2.3. Macrophages and Dendritic Cells	27
1.1.10.3. Adaptive Immune responses	29
1.1.11. Influenza Virus Vaccine Targets	30
1.1.11.1. Surface proteins as vaccine targets	31
1.1.11.2. Internal proteins as vaccine targets	32
1.1.12. Influenza Prevention	32
1.1.12.1. Influenza Vaccines	33
1.1.12.1.1. Production models	33
1.1.12.1.2. Inactivated vaccines (IIV)	33
1.1.12.1.3. Recombinant vaccines	34
1.1.12.1.4. Live attenuated influenza vaccines (LAIV)	34
1.1.12.2. Universal Influenza Vaccine	36
1.1.12.3. Influenza vaccines in high-risk groups	36
1.2. Chapter 2: The human microbiota	37
1.2.1. General introduction	37
1.2.2. Microbiome nomenclature	38
1.2.3. Characterization of the Human Microbiome	38
1.2.3.1. Compositional Characterization	39
1.2.3.2. Functional Characterization	39
1.2.3.3. Anatomic Location	40
1.2.3.3.1. The gut microbiota	40
1.2.3.3.2. The respiratory tract microbiota	41
1.2.3.4. Animal models in the characterization of the Human microbiome	42
1.2.3.5. Human microbiome in health and disease	43
1.2.3.5.1. Colonization Resistance	43

1.2.3.5.2.	Secondary Metabolites	45
1.2.3.5.3.	Imprinting and Immunoregulation	45
1.2.3.6.	Influenza infections and dysbiosis	46
2.	Aims	48
2.1.	Aim 1	48
2.2.	Aim 2	49
3.	Results	50
3.1.	Optimizing the live attenuated influenza A vaccine (LAIV) backbone for high-risk patient groups	50
3.1.1.	Published Results	50
3.1.2.	Complementary Unpublished Results	78
3.1.2.1.	Results	78
<input type="checkbox"/>	Humoral response to LAIV and optiLAIV	78
3.1.2.2.	Materials and Methods	78
<input type="checkbox"/>	ELISA	78
<input type="checkbox"/>	Microneutralization assay	79
3.2.	A single respiratory tract infection early in life reroutes healthy microbiome development and affects adult metabolism in a preclinical animal model	80
3.2.1.	Published Results	80
3.2.2.	Complementary Unpublished Results	95
3.2.2.1.	Results	95
<input type="checkbox"/>	IAV causes long term dysbiosis in GPR41/43 knockout mice	95
<input type="checkbox"/>	IAV imprinting does not affect humoral responses after vaccination	98
<input type="checkbox"/>	IAV imprinting causes long-term dysbiosis in lung microbiota	98
3.2.2.2.	Materials and Methods	100
<input type="checkbox"/>	Animals	100
<input type="checkbox"/>	RT-qPCR	100
<input type="checkbox"/>	Immunization and antibody response	101
<input type="checkbox"/>	ELISA assay	101
3.3.	Visualization of respiratory commensal bacteria in context of their natural host environment	102
3.3.1.	Published Results	102
4.	Discussion	111
4.1.	Optimizing the live attenuated influenza A vaccine (LAIV) backbone for high-risk patient groups	111
4.2.	A single respiratory tract infection early in life reroutes healthy microbiome development and affects adult metabolism in a preclinical animal model	115
4.3.	General Discussion	118
5.	List of Abbreviations	120
6.	List of Figures and Tables	124
7.	References	125
8.	Appendix - Contributions to Other Publications	162
8.1.	Respiratory tissue-associated commensal bacteria offer therapeutic potential against pneumococcal colonization	162
8.2.	Influenza A viruses balance ER stress with host protein synthesis shutoff	195

1. Introduction

1.1. Chapter 1: Influenza A Virus



















Viral pathogens with a pandemic potential rank among the top threats to global health. While SARS-CoV-2 is the most recent example, influenza viruses stand as one of the oldest and best described pathogens with a history of at least five human pandemics and a devastating burden on human lives¹. Influenza viruses are zoonotic viruses from the Orthomyxoviridae family divided into four types, i.e. A, B, C and D. Influenza A virus (IAV) has a natural reservoir in wild waterfowl and infects multiple animal species including swine, bats, domestic poultry, horses, birds, and humans. Influenza B virus (IBV) and influenza C virus (ICV) are restricted to human circulation with a few reported cases in pigs, dogs, and seals. Influenza D virus (IDV) mainly circulates in cattle. Regarding human disease, only types A, B and C cause acute infections presenting mild to severe respiratory symptoms, with types A and B accounting for more than 90% of reported cases². Of these two, IAV is of utmost medical importance, being responsible for up to 75% influenza infections in humans and the causative agent of devastating influenza pandemics³⁻⁵. For these reasons, the focus of this thesis will be on influenza A virus.

1.1.1. Influenza A Virus Classification

Influenza A viruses are classified according to the antigenicity and phylogenetic diversity of their surface glycoproteins hemagglutinin (HA) and neuraminidase (NA). HA antigenicity is based on antibody recognition determined by a double immunoprecipitation assay. According to a World Health Organization (WHO) memorandum, a consensus in the antigen classification was established based on the diffusion of antibody-antigen complexes⁶. Upon mixture of different HA (or NA) with rabbit hyperimmune sera, these complexes will present characteristic diffusion patterns which classify the glycoprotein into distinct subtypes⁷⁻⁹. So far, 18 HA (H1-H18) subtypes and 11 NA subtypes (N1-N11) have been described. Moreover, to account for minor variations within the same IAV subtype, a hemagglutination inhibition (HI) assay further classifies HA-like subtypes. The HI assay measures the titration of serum from an infected animal required to bind viral HA and prevent red blood cell hemagglutination. Based on the Center for Disease Control and Prevention (CDC) guidelines, a difference smaller than a 4-fold dilution in HI titers defines two HAs from the same subtype as “like” each other¹⁰. HA phylogenetic diversity is based on gene sequence similarities and separates IAVs into two main groups. Group 1 comprises H1, H2, H5, H6, H8, H9, H11, H12,

H13, H17 and H18 and group 2 comprises H3, H4, H7, H10, H14 and H15¹¹, which can be further attributed to different clades and subclades^{12,13}.

Both categorizations are helpful to define the evolution of influenza viruses and the ecology of outbreaks. This allows a better design of effective public health countermeasures such as the establishment of surveillance networks, targeted vaccination campaigns, and zoonotic control programs. In fact, several subtypes have been found to circulate in multiple animal species (Table 1), a phenomenon known to drive the emergence of antigenically unique strains with pandemic propensity¹⁴.

Subtype	People	Poultry	Swine	Bats
H1, H2, H3				
H4				
H5				
H6, H7				
H8				
H9				
H10				
H11-H16				
H17, H18				









Subtype	People	Poultry	Swine	Bats
N1, N2				
N3, N4, N5				
N6-N9				
N10, N11				

Table 1: Hemagglutinin and neuraminidase subtypes and the species in which they have been detected. Adapted from the Center for Disease Control and Prevention¹⁵

1.1.2. Influenza A Virus Tropism

In addition to its role in IAV classification, HA is also an important player in determining viral tropism¹⁶. Viral tropism indicates the ability of an IAV strain to productively infect a particular cell, tissue or host species and represents a key element in the dynamics of IAV transmission. One critical factor defining viral tropism is the specificity of the receptor binding protein of IAV to its host receptor. Although no single protein has been described as the main receptor for influenza viruses, the ability of HA to bind sialic acids is a central dogma of IAV biology. Sialic acids are small sugars present at the outmost end of long carbohydrate chains that decorate proteins and lipids¹⁷. Sialic acids are linked to the subterminal galactose residue of glycans in two main configurations, alpha 2,3 or alpha 2,6¹⁸, which govern HAs preference to the host cell. For example, the human upper respiratory tract (URT) is predominantly decorated with an alpha-2,6-linked sialic acids and human IAV strains express HA subtypes that bind this configuration¹⁹. On the other hand, avian respiratory and intestinal epithelial cells are predominantly decorated with alpha-2,3-linked sialic acids, explaining why

most avian IAV strains express HAs that preferentially bind alpha-2,3-linked sialic acids and cause a gastro-intestinal disease in birds²⁰. Curiously, pigs contain both sialylation patterns and are susceptible to co-infections with swine, avian and human IAVs^{21,22}. Thus, pigs have been proposed as an optimal mixing vessel for the generation of pandemic strains, although the evidence for this is only circumstantial^{23–26}. Another aspect governing IAV tropism is temperature²⁷. By infecting a multitude of hosts, IAVs adapt their optimal replication temperature accordingly. In birds and bats, core body temperatures reach 41°C, while in humans and pigs they vary between 33°C in the upper airways, to 37°C in the lower airways^{28–30}. The repercussions of temperature and receptor specific adaptations as drivers of viral tropism are observed during spillover events. Avian IAVs causing severe disease in humans were shown to replicate best in the lower respiratory tract (LRT) of humans, where there is a higher density of alpha 2-3-linked sialic acids and temperatures are closer to the avian intestinal tract. Alongside sialic acid preference and temperature, other factors driving viral tropism have been reported, such as glycan topology, sialic acid density, other non-described receptors and species-specific restriction factors^{31,32}.

1.1.3. Influenza A Virus Structure and Morphology

Influenza A virus is a negative, single stranded, segmented enveloped RNA virus. Infectious viral particles span from 80-120 nm in diameter and their spatial organization ranges from spherical to filamentous shapes, with the latter reaching up to 20 µm in length^{33,34}. Each particle contains 8 different RNA segments encoding for at least 15 proteins from which 8 are essential for the structural composition of IAV particles (Figure 1).

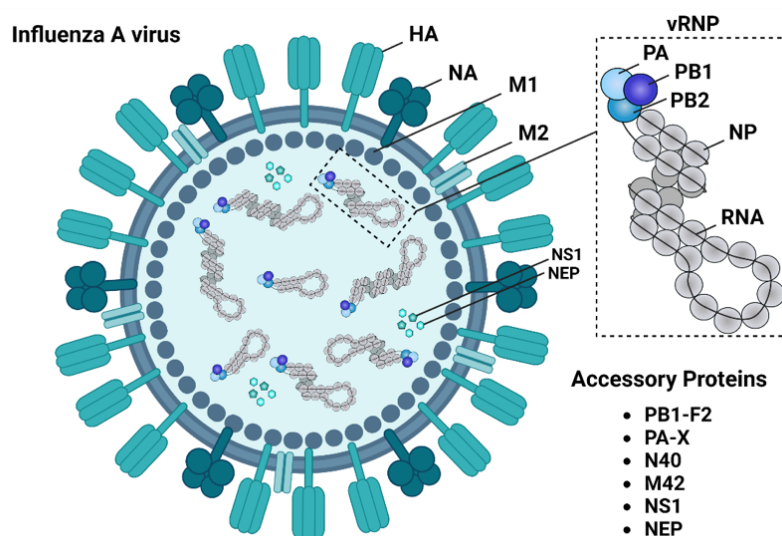


Figure 1: Structure and morphology of IAV genome. Adapted from *Journal of Infectious Diseases* 2021³⁵.

The nucleoprotein (NP) forms long multimers with each RNA segment wrapped around them in a coiled conformation. The 3' and 5' ends fold back and protrude from the same side to form a double-strand structure which is bound by the influenza viral polymerase (FluPol). FluPol, an RNA-dependent RNA polymerase, is composed of three subunits: polymerase basic protein 1 (PB1), polymerase basic protein 2 (PB2) and acidic polymerase (PA). Altogether, these four viral proteins associate to a single genomic RNA segment of IAV and constitute the viral ribonucleoprotein (vRNP)³⁶. Each vRNP is anchored to the viral envelope through interactions with a fifth structural protein, the matrix protein 1 (M1). On the surface of each IAV particle, HA, NA and the matrix protein 2 (M2) represent the last three structural proteins of influenza particles. The glycoproteins HA and NA govern viral entry and release from the host cell^{37,38} while the less abundant M2 protein is an ion channel involved in fusion with the host cell. Non-structural proteins encoded by IAV act during viral replication and focus on avoiding the host response or promoting viral replication. The most well characterized example is the non-structural protein 1 (NS1). Other examples – PB1-F2, PA-X, N40, M42, NEP - derive from alternative splicing or open reading frames and are expressed in a strain dependent manner.

1.1.4. Influenza A Virus Replication Cycle

The replication cycle of IAV starts with the viral attachment to its host cell (Figure 2). This interaction starts with receptor-binding HA binding to sialic acids present in the cell surface. After endocytosis, endosomal acidification and the presence of the ion channel M2 enable the influx of H⁺ protons into the viral particle. The lower pH provokes an extensive conformational rearrangement in HA exposing the fusion peptide (FP). Each individual FP is inserted in the endosomal membrane bringing the viral envelope to close proximity. Subsequently, both membranes fuse and expel the vRNPs into the cytoplasm of the infected cell. Nuclear localization signals present in the NP allow translocation of vRNPs into the nucleus where FluPol initiates mRNA transcription and vRNA replication. During transcription, two interesting strategies adopted by FluPol allow viral transcripts to exploit the translational machinery of the host cell without being detected. First, FluPol sequesters 5'-caps from nascent host RNAs and uses them as the starting template for viral messenger RNA (mRNA) generation, a phenomenon known as cap-snatching³⁹. Second, a repetition of uracil nucleotides at the 3' end of each vRNA leads to a transcription stutter generating long poly-A tails⁴⁰. Capped and polyadenylated viral mRNAs are then indistinguishable from host mRNAs and exported into the cytoplasm where translation will start. In parallel, accumulation of viral NP is believed to switch polymerase function from transcription to replication and intermediate

positive strands of the vRNA segments are generated by FluPol, which serve as template for the production of new vRNAs.

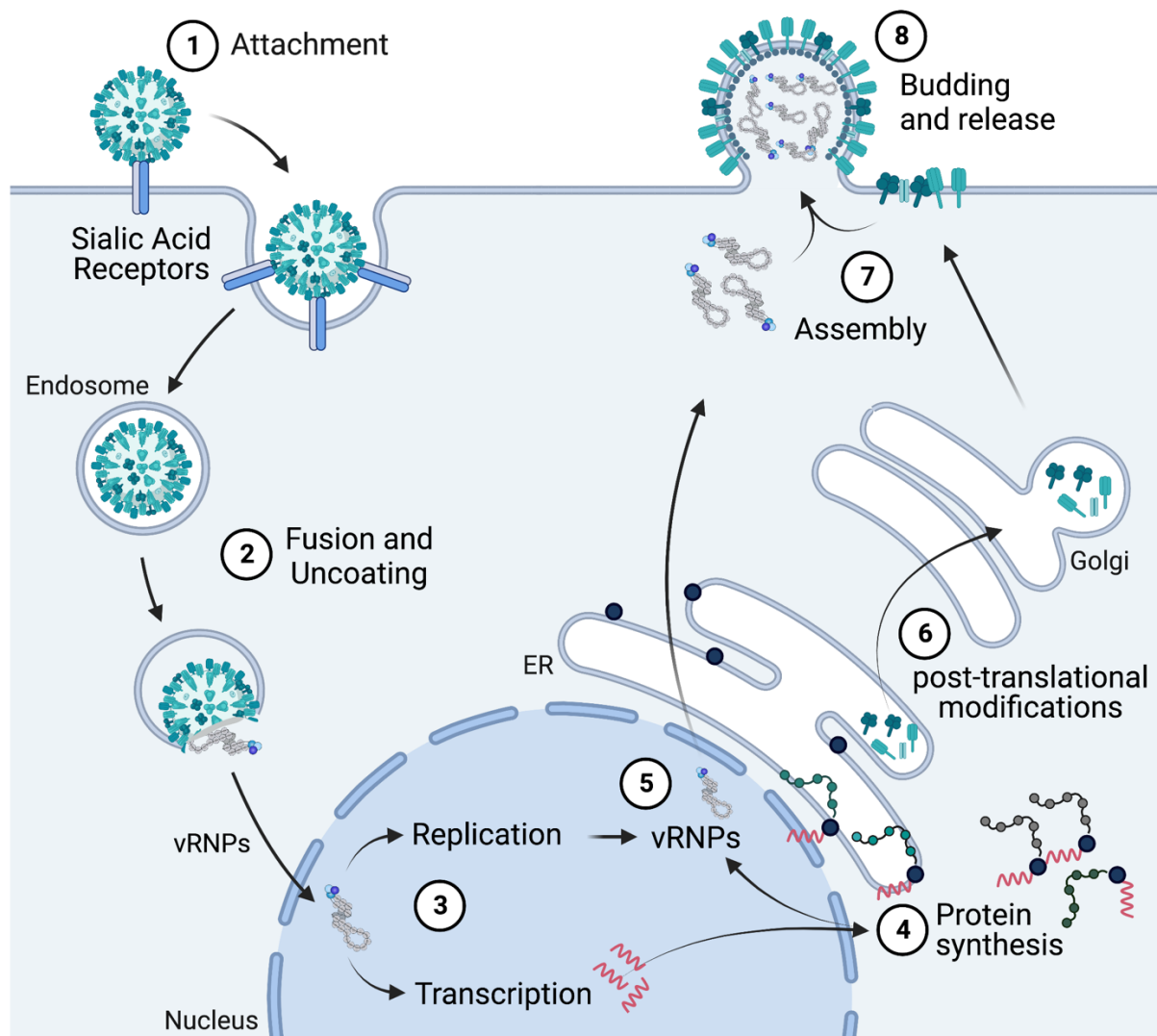


Figure 2: Influenza A virus replication cycle. (1) Virus attachment to sialic acid receptors via HA; (2) fusion of virus particle with the endosome and uncoating; (3) vRNPs entry into the nucleus followed by transcription of mRNA and replication of the viral RNA genome; (4) viral protein translation in cytoplasmic ribosomes and ER-associated ribosomes; (5) import of NP, M1 and FluPol into the nucleus and assembly with newly synthesized genomic RNA into vRNPs and export to the cell surface; (6) trafficking of HA, NA and M2 through endoplasmic reticulum (ER) and Golgi apparatus where post-translational modifications take place; (7) assembly of viral components; (8) budding at the host cell membrane and release of new viral particles from the host cell. *Adapted from vaccines 2021*⁴¹

Viral protein synthesis is exclusively dependent on the host cell machinery and occurs either in ER-associated ribosomes (for viral envelope proteins) or in cytosolic ribosomes (for the remaining proteins). Upon translation, viral envelope proteins HA and NA are translocated into the ER lumen and the Golgi apparatus where folding and glycosylation take place,

respectively. Fully mature HA trimers and NA tetramers are trafficked in vesicles to the cell membrane where they accumulate in cholesterol-rich lipid rafts. On the other hand, structural viral proteins from cytosolic ribosomes re-enter the nucleus via a nuclear import sequence or co-shuttling with host proteins and form new vRNPs with the recently copied genomes. With the help of NEP and M1, fully assembled vRNPs are then exported to the plasma membrane interface where they localize in close proximity to viral glycoproteins^{36,42,43}. Ultimately, an infectious IAV particle assembles the eight different vRNPs and buds out from the host cell through a M1-dependent process⁴⁴. As a final step, viral release from infected cells occurs upon sialic acid cleavage by NA present in the membrane of newly formed virions.

1.1.5. Influenza A Virus Glycoproteins

A successful IAV replication cycle is orchestrated by a balance between the binding strength of HA and the enzymatic activity of NA. These two glycoproteins are essential for the structure and infectivity of IAV and represent the main targets of host immune responses. In the next paragraphs I will introduce the structural and functional characteristics of HA and NA.

1.1.5.1. Hemagglutinin

Hemagglutinin is distributed along the viral envelop as trimeric spikes and represents ~80% of viral surface proteins^{38,45}. During viral replication, HA is expressed as a single polypeptide (HA0) and a cleavage event by host proteases is necessary to achieve its final active conformation as HA1 and HA2 linked by a disulfide bond (Figure 3A). The cleavage site of HA is an important dictator of viral pathogenicity by modulating the sensitivity of HA to different proteases. For example, human IAV strains usually encode HAs with a monobasic cleavage site susceptible to extracellular or membrane bound serine-proteases restrictively expressed in the respiratory tract. In turn, highly pathogenic avian influenza (HPAI) viruses encode a multibasic cleavage site susceptible to ubiquitously expressed proteases, corroborating the high dissemination and pathogenicity associated with these viruses when they infect humans⁴⁶. HA cleavage is part of the post-translational modifications during trans-Golgi transit but can also be achieved after viral release by extracellular proteases^{47,48}. After proper folding and glycosylation, HA monomers associate into trimer spikes which are trafficked in Golgi-generated vesicles to the cell membrane. Structurally, HA is divided in a globular head domain and a stalk domain. The head domain (shaped by the central portion of the HA1 polypeptide) contains the receptor-binding site and therefore directly impacts host tropism⁴⁹. HA head domain constitutes the antigenically immunodominant region of HA and is the primary target of antibodies. As a result of such high selective pressure, most of the variability between each HA subtype is located in the globular head domain⁵⁰. The stalk

domain (shaped mostly by the HA2 polypeptide) bridges the globular head domain and the transmembrane region of HA. Because of its spatial conformation, this region is shielded from the immune system rendering it antigenically immunosubdominant^{51–53}. It is therefore, the most conserved region amongst different HAs and the target of broadly neutralizing antibodies. In humans, this is evidenced by the ability of patient serum containing anti-stem antibodies to neutralize IAVs from different antigenic groups^{54–56}.

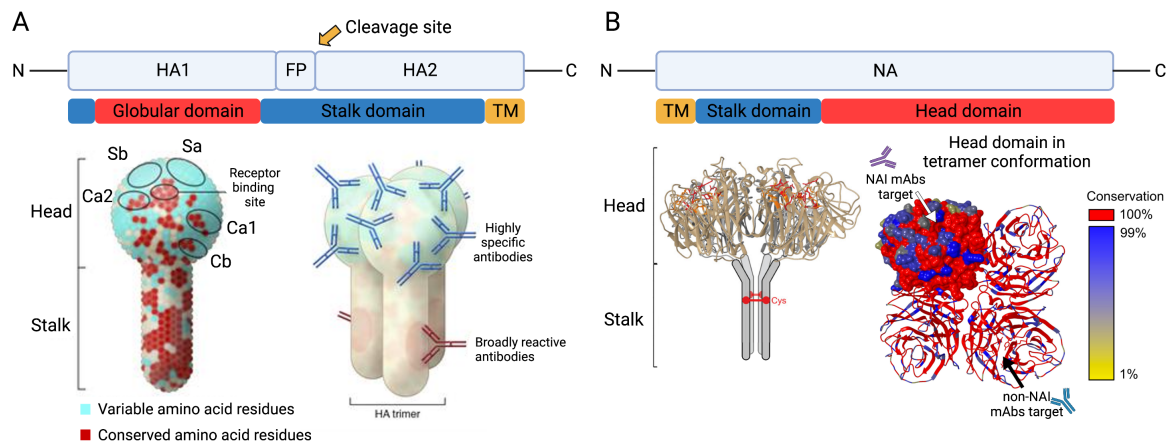


Figure 3: Linear and 3D structure of influenza HA and NA. (A) *upper panel* Schematic representation of IAV HA linear structure. The fusion peptide (FP) is flanked by the HA1 and HA2 polypeptides. The globular head domain is represented in red, stalk domain in blue and transmembrane (TM) in yellow. *Lower panel* Schematic representation of immunodominant antigenic sites and the conserved amino acids along HA monomeric structure. Sa and Sb sites are the main target of strain-specific antibodies, while Ca1, Ca2 and Cb are the main target of cross-reactive antibodies. *Adapted from JCI 2018*⁵⁰. (B) *upper panel* Schematic representation of IAV NA linear structure. The head domain is represented in red, stalk domain in blue and transmembrane (TM) in yellow. *Lower panel* Schematic representation of the 3D structure of N1 and the sequence conservation among N1 subtypes. White and black arrow represent the target of anti-NA inhibiting antibodies and anti-NA non-inhibiting antibodies, respectively. *Adapted from Frontiers 2021*⁵⁷

1.1.5.2. Neuraminidase

Neuraminidase is a sialidase which removes sialic acid from glycoconjugates in host cell proteins. It is the second most abundant influenza surface glycoprotein (~17%) and decorates the viral envelope as tetramer spikes. Like HA, NA is divided in a stalk domain and a globular head domain docking the enzymatic activity of the protein (Figure 3B). By cleaving sialic acids, NA exerts three main functions in IAV transmission and infectivity^{58,59}. The first is during the passage through the respiratory tract, where NA strips sialic acid from mucous proteins and thus, prevents entrapment of viral particles within the mucous layer of respiratory tract. The second is during the lateral rolling of the virus particle on the host cell surface after attachment, where sialic acid cleavage by NA increases virus motility and internalization⁶⁰. The third is during viral release from the host cell membrane, where it strips sialic acid at regions from which new viral particles bud out, preventing reattachment to the recently infected

cell. Additionally, NA also cleaves sialic acids from the viral glycoproteins preventing unproductive virus-virus interactions and facilitating viral segregation and spread⁶¹. Being exposed on the viral envelope surface, NA is accessible to the immune system and is also a target of antibodies. Indeed, NA-binding antibodies are detected in naturally infected patients and can protect against both N2 and N1 subtypes during a lethal challenge in animal models⁶².

1.1.6. Influenza A Virus Nonstructural Proteins

As an obligatory intracellular pathogen, influenza virus replication is heavily dependent on the host cell machinery. While the structural proteins of influenza virus are essential for proper viral assembly and replication, several accessory viral proteins have evolved to counteract host signaling pathways and facilitate viral replication. For the purpose of my thesis, I will solely focus on NS1.

1.1.6.1. NS1

NS1 is encoded by the smallest vRNA segment and represents the best described virulence factor of IAV. NS1 has an RNA-binding domain (RBD) and an effector domain (ED) separated by a linker sequence. Upon expression, NS1 dimerizes and acts both in the cytosol and the nucleus. NS1 best-described function is to counteract the antiviral response. In the cytosol, the RBD domain binds to RNA sensor retinoic acid-inducible gene I (RIG-I) which recognizes double stranded RNAs (dsRNA). The amino acid residues at position 38 and 41 mediate this interaction which impairs interferon expression⁶³. Furthermore, the same motif also binds tripartite motif containing 25 (TRIM25) and inhibits downstream regulatory checkpoints of the RIG-I pathway⁶⁴. Besides modulating the antiviral response, NS1 is also capable of inhibiting inflammatory responses by blocking nuclear factor kappa-light-chain-enhancer of activated B cells (NF- κ B) signaling⁶⁵, sustaining cell survival by binding phosphatidylinositol-3-kinase (PI3K) and promoting viral replication⁶⁶. The RNA-binding protein kinase (PKR), another cellular protein recognizing viral byproducts and triggering antiviral effector mechanisms, is also inhibited by direct binding with NS1⁶⁷, highlighting the breadth of NS1 effector mechanisms⁶⁸. An important feature of NS1 is the tight regulation happening at the post-translational level during its expression. NS1 can be phosphorylated, acetylated, ISGylated and SUMOylated⁶⁹. These processes are mediated by the host cell machinery and modulate NS1 functions. For example, phosphorylation at the threonine residue 49 reduced binding to RIG-I and TRIM25 complex⁷⁰.

NS1 also interferes with cellular transcription. This is mainly achieved in the nucleus, where NS1 ED binds to a protein complex involved in the processing of host transcripts. NS1 binding to the cleavage and polyadenylation specificity factor 30 (CPSF30) blocks the cleavage

and polyadenylation of cellular mRNAs and induces a host transcription shutoff defined by a drastic reduction of antiviral genes expression^{71,72}. Since it is FluPol that mediates the polyadenylation of viral transcripts, inhibition of CPSF30 outlines a precise mechanism to interfere with the infected cell machinery without affecting viral replication. Generally, NS1 effector strategies converge into promoting viral replication by limiting the antiviral response and delaying the onset of an immune response capable of clearing the virus. Consequently, IAV strains with NS1 deletions are attenuated *in vivo*⁷³. Furthermore, knocking out central players of the antiviral response, i.e. signal transducer and activator of transcription 1 (STAT-1) and interferon receptors (IFNRs), in mice, reverts the attenuated phenotype of NS1-deleted viruses⁷⁴. These observations indicate the interferon signaling as a main target of NS1 mediated strategies to counteract the host response. Interestingly, a recent report showed that NS1 is capable of modulating another signaling pathway called the unfolded protein response (UPR), independently of the canonical interferon response. This mechanism was dependent on the ability of NS1 to bind CPSF30, which reduced the expression of key mRNAs involved during UPR. Furthermore, mice infected with IAV NS1 mutants with gradual CPSF30-binding phenotypes presented increased body weight loss and higher viral loads in their respiratory tract⁷⁵. The ability to limit the UPR in addition to the IFN response represents a complementary strategy of IAV to control host signaling pathways in favor of viral replication.

1.1.7. Influenza A Virus in the Human Population

The broad antigenic diversity together with a wide host-species range and the abundance of strategies to evade host defenses makes IAV a constant threat to humans. Records of influenza-like illness in humans date back to 412 BC, suggesting a long history of IAV in the human population. Over the years, IAV has established itself as an endemic pathogen in humans causing seasonal outbreaks every year. The evolutionary success of influenza viruses can be mainly attributed to two particular features. One comes from the RNA nature of IAVs, which encode a polymerase with a high error rate. An accumulation of point mutations, particularly in the receptor-binding interface of HA, results in the emergence of new variants capable of avoiding antibody recognition, changing host tropism and efficiently spreading throughout the population. The best example are the HA mutations E190D/G225E observed in the pandemic strain of 1918 which conferred specificity to α -2,6 linked sialic acids and increased transmissibility in a ferret model, possibly contributing to its emergence in humans^{76,77}. Known as antigenic drift, this phenomenon is the reason why influenza outbreaks happen every year. The second feature stems from the segmented nature of IAVs, which enables gene reassortment. Under the circumstance of co-infections, i.e. in permissive animal

reservoirs, IAV strains of different origins can interchange whole segments and produce variants with distinctive antigenic and replicative properties⁷⁸. Also known as antigenic shift, when this process happens between zoonotic and human IAVs, it can generate highly infectious strains with enhanced transmissibility causing worldwide pandemics.

1.1.8. Influenza A Pandemics History

So far, IAV has been responsible for at least five pandemics, namely the Spanish Flu (1918), Asian Flu (1957), Hong Kong Flu (1968), Russian Flu (1977) and the Swine Flu (2009) (Figure 4).

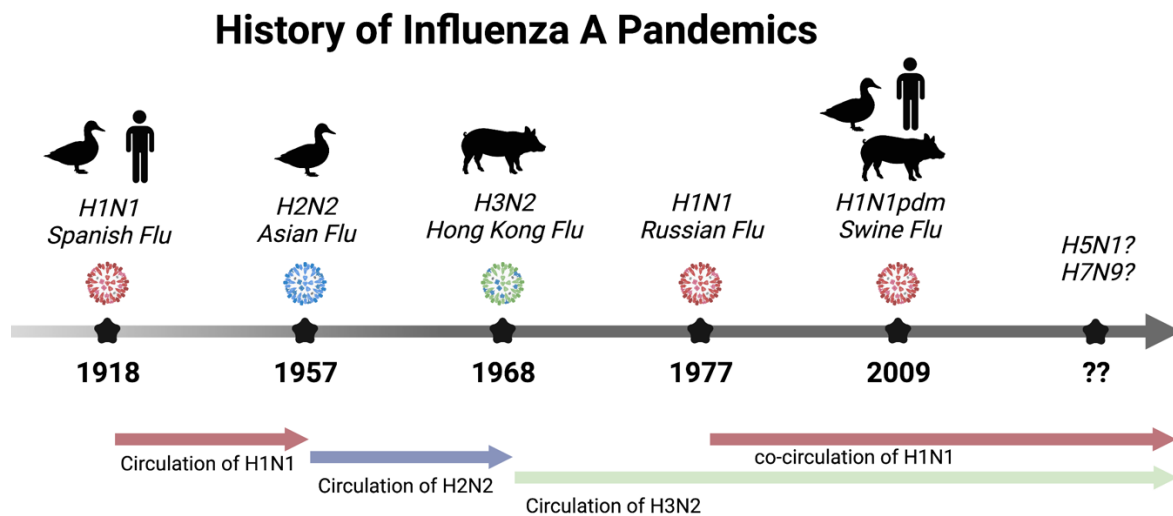


Figure 4: Influenza pandemics timeline. Adapted from Francis et al 2019⁷⁹

The Spanish Flu had the worst unfolding, with death tolls reaching up to 50 million and affecting healthy young population groups. The reason behind this is still not well understood⁸⁰, although the absence of available vaccines and antibiotic treatments during this period are likely main contributors to the aggravated outcomes⁸¹. Indeed, the majority of deaths were due to secondary bacterial infections⁸². The strain responsible for this pandemic was an avian H1N1 influenza A virus that accumulated enough adaptations conferring high infectivity in humans. It is still debated if the 1918 IAV strain acquired its adaptations in a mammalian host preceding the pandemic outbreak or if it jumped directly from an avian host into humans^{83,84}. Nevertheless, after emerging in the human population, it established itself as the dominant seasonal circulating strain causing outbreaks every year⁸⁵. Almost forty years later, a reassortment with a H2N2 avian virus caused the Asian Flu in 1957. This virus replaced H1N1 strains and circulated for about 11 years until it reassorted again with another avian virus, this time a H3N2 subtype, causing the Hong Kong Flu pandemic in 1968. Although less severe than the Spanish Flu, the mortality rates during these pandemics were still high, with two million deaths reported during the Asian Flu and one million deaths during the Hong Kong

Flu⁷⁹. Curiously, a H1N1 subtype re-emerged in the human population around 1977 and caused a pandemic in Russia. This strain showed high genetic identity with the H1N1 subtype dated from the pre-Asian Flu era. It is still debated whether its re-emergence after 20 years occurred naturally or through human misconduct⁸⁶. Since then, H1N1 and H3N2 subtypes have started co-circulating in the human population and account for over 90% of seasonal IAV outbreaks. In 2009, a novel pandemic IAV strain emerged. It was the result of a reassortment between a swine IAV and a triple reassorted swine IAV containing gene segments from swine, human and avian viruses⁸⁷⁻⁸⁹. This H1N1 pandemic strain caused the Swine Flu of 2009 and replaced circulating human H1N1 subtypes at the time. The death toll of the 2009 Swine Flu was lower compared to other pandemics with total number of deaths ranging between 155'700 and 575'400. Despite the inherent advances in medicine throughout the years with better access to healthcare and wide-spread vaccination programs, the 2009 pandemic had an unprecedented burden in younger populations⁹⁰. This is partially explained by the presence of pre-existing cross-reactive antibodies in older adults against pre-1957 H1N1 strains, which are antigenically similar to the 2009 pandemic H1N1⁹¹⁻⁹³. Seasonal influenza A virus H1N1 strains circulating up until this day are derived from the 2009 pandemic H1N1 strain and cause millions of severe flu cases every year⁹⁴.

Given the history of recurrent IAV pandemics and their devastating impact on global health, it is essential to monitor the evolution of animal-origin influenza strains. Thus, in 1952, the WHO created the global influenza surveillance and response system (GISRS), a systematic network responsible for monitoring and characterizing zoonotic IAVs. Notably, the GISRS detected two avian subtypes as high-level threats for causing the next pandemic. Responsible for small and contained outbreaks, avian H5N1 viruses cause infections mainly in humans directly working in poultry farms and present more than 50% mortality rates⁹⁵. Likewise, a H7N9 avian strain in China has caused 1'568 human infections since 2013 with a case-fatality rate of 39%⁹⁶. Although limited human-to-human transmission has been reported, these HPAI viruses could have catastrophic consequences if they acquire human-to-human transmissibility⁹⁷. Moreover, the measures in place to contain avian outbreaks, particularly in poultry farms, involve the culling of an astonishing number of domestic birds with severe economic and environmental consequences. From October 2021 to May 2022, for instance, more than 77 million birds worldwide have been culled to curb the spread of an H5N1 virus⁹⁸⁻

100.

1.1.9. The Influenza Disease

Influenza virus is the main causative agent of acute respiratory infections in humans commonly referred to as “the flu”. The WHO estimates that 1 billion cases, 3-5 million severe cases and over 500’000 deaths occur due to influenza virus infections every year⁹⁴. Influenza is an airborne virus that thrives on rapid and efficient transmission between each host. Transmission occurs via fomites, aerosols, and droplet nuclei, which carry infectious particles upon coughing and sneezing. The physical properties and size of air droplets allow the transport of viable viral particles throughout relatively long distances and even maintain them suspended in the air for hours^{101,102}, reflecting the highly transmissible profile of influenza viruses. According to human challenge studies, transmission is higher during symptomatic disease and correlates with viral shedding, which peaks at an average of 4.8 days post infection. However, several reports also point to active shedding during incubation periods, which contributes to undetected viral spread¹⁰³. Flu has an incubation period of two days after which symptoms may appear. Based on paired seroconversion data, it is known that, in healthy adults, ~75% of influenza virus infections are asymptomatic or present mild symptoms¹⁰⁴. Common mild symptoms include dry cough, headaches, fever and myalgia, and resolve within 10 days. Severe disease is infrequent and characterized by acute respiratory distress syndrome, otitis, pneumonia, and sinusitis. In addition, secondary bacterial and viral co-infections can exacerbate influenza pathology leading to multiorgan failure, sepsis, and death¹⁰⁵. In animal models, influenza pathogenesis is characterized by disseminated replication in the LRT and an exacerbated inflammatory response associated with tissue damage. Ultimately, acute infection interferes with primary physiological functions of the lung by inducing loss of alveolar structure, airways obstruction and degradation of the lung epithelial layer, leading to respiratory failure and death^{106,107}.

The precise mechanisms driving disease severity are still poorly understood, however a mixture of host and viral characteristics seem to be involved¹⁰⁸. From the virus side, expression of virulence factors, replication fitness and host-adaption mutations have all been described to enhance pathology in animal models and in humans^{109,110}. For example, a single mutation in the virulence factor PB1-F2 of the H5N1 HPAI strain was attributed to its severe phenotype in mice¹¹¹. In line with this observation, HPAI preference to replicate in the LRT together with a stronger host response led to high mortality rates among healthy young adults^{112–114}. Moreover, lungs of avian H5N1 infected patients present elevated levels of pro-inflammatory cytokines (known as “cytokine storm”) followed by development of severe pneumonia, arguing in favor of intrinsic characteristics of the virus being able to dictate disease

severity and pathogenicity^{115,116}. From the host side, a range of individual characteristics has been associated with disease severity¹¹⁷. Some examples include: vaccination status, pre-existing immunity, genetics, sex, ethnicity, pregnancy, age, and underlying medical conditions¹¹⁸.

Pregnancy, age and underlying medical conditions denote three relevant clinical risk factors for flu severity since they define key populations severely affected by influenza complications¹¹⁹. Understanding how flu affects these populations is helpful to design targeted preventive measures and mitigate the socio-economic impact of the higher hospitalization and mortality rates observed. For example, when vaccination campaigns prioritized care homes, pre-schools and solid organ transplant recipients, flu incidence, all-cause pneumonia and mortality risks were reduced^{120–124}. According to CDC, high-risk patient groups can be divided into four main categories: children under 5 years old, individuals with chronic medical conditions, pregnant women and adults over 65 years old^{125,126}. In the following sections, I will summarize the risks and burden associated with flu in these patient groups.

1.1.9.1. High-risk patient groups

1.1.9.1.1. Children under 5 years old

The impact of flu in children is highlighted by a recent systematic review estimating the burden of flu across the world. It was estimated that 109.5 million influenza virus episodes occurred in children under 5 years old with 870 000 hospital admissions and 34 800 deaths in 2018 alone¹²⁷. Compared to older children, children under 5 are more likely to be hospitalized and develop complications after flu infection^{128–130}. A recent study performed in Norway further confirmed this observation after evaluating hospitalization rates among 1000 children with laboratory confirmed influenza in the period of 2017-2019. Their findings report a decline in hospitalization rates as the age of the patients increased¹³¹. Moreover, when stratified by age, influenza burden is even higher in children under 1 year old. In this demographic, higher mortality rates are more frequent among hospitalized children with severe illness¹³². Amid the factors contributing to this higher susceptibility, the lack of previous exposure to influenza virus and the immature state of their immune system are thought to play a major role^{133,134}. Besides higher hospitalizations and flu-related complications, young children also have longer and intensified shedding of influenza virus^{135,136}. In combination with an environment of close contact with peers, e.g. in pre-schools and childcare centers, children represent an important target-population for flu outbreak control¹³⁷. In fact, preschools have been pointed out as an important element in the chain of transmission during flu outbreaks in different countries^{138–141}. Notably, young children are also the most likely index case in household transmissions¹⁴².

Altogether, these observations have led WHO, CDC and the European CDC to include this age group as a high-risk population galvanizing the development of new strategies to prevent and mitigate the burden of influenza disease in this demographic.

1.1.9.1.2. Individuals with chronic medical conditions

Several underlying medical conditions are associated with higher rates of severe complications from influenza infections. A systematic review evaluated different chronic conditions affecting the risk of hospitalizations, intensive care unit (ICU) admission and all-cause mortality in patients with laboratory-confirmed influenza or influenza-like illness. Obesity, chronic lung disease, asthma, diabetes, neuromuscular disease, cardiovascular disease, metabolic disorders, and liver disease were all accounted for as risk factors for higher rates of at least one of the assessed outcomes^{118,143}. In addition, patients receiving immunosuppressive treatment or with impaired immune functions are also more susceptible to flu complications. The immunosuppressed status can derive from inherited genetic disorders (primary immunodeficiencies) or environmental factors (secondary immunodeficiencies). Among immunosuppressed patients, those most affected by flu are individuals with primary immunodeficiencies (PID), patients who have received solid organ transplant (SoT) or hematopoietic stem cell transplant (HSCT), HIV-infected patients, individuals receiving corticosteroid therapy and cancer patients undergoing chemotherapy treatment. These patients have higher viral replication, prolonged shedding and are at higher risk of developing pneumonia, reflecting an increased mortality rate after influenza infections^{144–147}. In the case of SoT and HSCT, pulmonary chronic dysfunction might still develop even after acute infection has been resolved¹⁴⁸. Importantly, the higher viral replication and longer shedding observed in these patients offer a suitable environment for the emergence of drug resistant IAV strains¹⁴⁹.

1.1.9.1.3. The elderly

Populations over 65 years old represent the most affected high-risk group by influenza. According to a study published by CDC, 70 to 85% of flu-related deaths are among this population in the US¹⁵⁰. Older populations are more prone to live with other medical conditions, such as diabetes, renal dysfunctions and cardiovascular complications which are all risk factors for influenza-related complications¹⁵¹. In addition, three important phenomena define this population's higher susceptibility to flu. The first is named the original antigenic sin (OAS) or immune imprinting and is described by a skewed immune response to influenza subtypes encountered during childhood¹⁵². The second phenomenon named “inflammaging” is characterized by a chronic inflammatory status associated with defective immune

responses^{153,154}. The third is defined as a status of immune senescence and corresponds to a general unresponsiveness of the immune system to extrinsic stimulus impairing immune responses to infections¹⁵⁵. This was associated with the inability of monocytes from elder patients to control viral replication due to a lack of antiviral responses^{156,157}. Another explanation for the higher susceptibility of older patients is their propensity to develop pneumonia due to suboptimal lung function. Lung elastic recoil and mucous development are two important mechanisms determining pathogen clearance which are both affected by age¹⁵⁸.

1.1.9.1.4. Pregnant Women:

During pregnancy, the body goes through physiological and immunological changes to accommodate the growth of the fetus. Pregnant women have a transient immunosuppressive status, decreased lung capacity and increased oxygen consumption, which challenge their ability to fight infections. Although clinical symptoms in pregnant women are comparable to healthy adults, pregnant women infected with flu have higher rates of morbidity and mortality, and these increase with each trimester^{159–161}. Flu infections during pregnancy also affect birth outcomes. A large cohort study recently reported higher rates of miscarriage and reduced birthweights if the mother contracted flu during gestation¹⁶². Moreover, a systematic review found an increased risk of stillbirth for pregnant women with laboratory confirmed flu¹⁶³. Collectively, the available evidence places pregnancy as a risk factor on its own, regardless of comorbidities or underlying medical conditions, characterizing pregnant women as a high-risk patient group¹⁶⁴.

Given the severe consequences of flu in the aforementioned groups, it is remarkable that ~75% of infections are asymptomatic or present mild symptoms. In addition, IAV infections are usually resolved without the need of medical assistance. This is mainly due to a functional immune system that can control the virus and clear infection without complications. An efficient response to influenza viruses involves the rapid and coordinated interaction between the innate immune system and the infected cells to contain viral replication until the arrival of the adaptive immune response which fully clears reminiscent viral particles. Concomitantly, a precise regulation of the immune response is crucial to avoid harmful reactions to the infected tissue.

1.1.10. Host responses to Influenza Virus

1.1.10.1. Innate immune responses

The recurrent host-pathogen interactions happening over millions of years resulted in the evolution of complex defense mechanisms from the host side, capable of recognizing and fighting infections at multiple stages. As a respiratory virus, influenza's first obstacle is a thick layer of mucus lining the upper respiratory tract. The mucus matrix is composed of heavily glycosylated proteins called mucins, which serve as decoy receptors entrapping viral particles. Mucins also provide a viscous consistency to the mucus slowing down dissemination of virions along the respiratory tract. Moreover, ciliated cells line the surface of the respiratory epithelium, which constantly renew the mucous layer through a paced, beating movement resulting in viral particles clearance. Defensins and surfactant proteins provide an extra layer of defense by directly binding to HA and aggregating viral particles, blocking viral entry into permissive host cells¹⁶⁵⁻¹⁶⁷.

Only by surpassing these obstacles can the influenza virus bind to epithelial cells where it establishes a productive infection and complete its viral cycle. Once inside the cell, it has to evade several subsets of proteins responsible for detecting pathogen associated molecular patterns (PAMPs) named pattern recognition receptors (PRRs). PRRs can be divided into five families: *Toll*-like Receptors (TLRs), NOD-like Receptors (NLRs), RIG-like receptors (RLRs), C-type lectin receptors (CLRs) and AIM2-like receptors (ALRs)¹⁶⁸. The molecular mechanisms through which PRRs recognize viral components are reviewed elsewhere and are thus, not discussed in this thesis^{169,170}. Importantly, some PRRs activation converge into a rapid and direct antiviral response characterized by the induction of interferons (IFNs) and interferon-stimulated genes (ISGs). IFNs are small protein molecules with multiple effector functions dependent on their type, receptor, and target cell. For example, type I and III IFNs act on epithelial cells and induce the expression of ISGs which encode proteins that can directly inhibit viral replication at multiple steps.

Another alarm system triggered during active viral replication is the UPR^{171,172}. The massive demand to produce glycosylated viral proteins amidst the intrinsic host cell's protein production, overloads the folding capacity of the endoplasmic reticulum (ER), leading to an accumulation of misfolded proteins. Consequently, quality control chaperones such as the binding immunoglobulin protein (BiP), signal ER receptors to activate the transcription machinery of the UPR and increase protein production capacity, ER volume, and expression of additional chaperones, ultimately restoring proteostasis. Concomitantly, UPR cross talks with immune signaling pathways and induces expression of cytokines and chemokines.

Ultimately, if not resolved, ER stress culminates in cell death via apoptosis and aborts viral replication. Different strains of influenza have been shown to activate this pathway during HA and NA production^{75,173,174}, however it is still debated if IAV exploits this pathway to enhance their own protein production or if its activation is detrimental to viral replication by alerting the innate immune system.

Collectively, PRR- and UPR-mediated induction of inflammatory cytokines and chemokines results in the recruitment of different subsets of immune cells aiming to control viral replication at the tissue level. Neutrophils, natural killer (NK) cells, macrophages and dendritic cells (DCs) deploy incremental effector functions which are responsible for controlling early viral replication and dissemination until the adaptive response initiates.

1.1.10.2. Innate immune cells

1.1.10.2.1. Neutrophils

Neutrophils are the most abundant immune cells infiltrating infected tissue and are important mediators of viral elimination by phagocytosing viral particles, promoting antibody-dependent cellular cytotoxicity (ADCC), discharging cytotoxic granules and releasing DNA extracellular traps¹⁷⁵. In mice, depletion of neutrophils prior to IAV infection aggravates disease severity by increasing lung inflammation and reducing respiratory function¹⁷⁶. In humans, on the other hand, exacerbated infiltration of neutrophils combined with their bursting artillery often leads to collateral tissue damage and is associated with poorer prognosis of severe IAV infections, highlighting the importance of fine-tuning the immune response to avoid tissue damage¹⁷⁷⁻¹⁷⁹.

1.1.10.2.2. Natural Killer Cells

NK cells represent an important cell population during viral infections. They contribute to IAV clearance by producing inflammatory cytokines, mediating ADCC and eliminating infected cells^{180,181}. In mice, NK cells accumulate in the lungs upon infection¹⁸², however their role in viral clearance is still elusive. While some studies show that depletion of NK cells aggravates mortality after IAV infection¹⁸³, other reports show that the presence of NK cells promote immunopathology and enhanced disease severity in mice¹⁸⁴. Once again, these observations likely reflect the balance between viral clearance and tissue damage required for an ideal infection resolution. In agreement with the role of neutrophils, it seems that optimal NK activity promotes viral clearance while exacerbated activation enhances disease.

1.1.10.2.3. Macrophages and Dendritic Cells

Macrophages and DCs are professional phagocytes able to control viral spread by engulfing infected cells and viral aggregates. In the lung, macrophages take on multiple roles

during infection depending on their phenotype. Alveolar macrophages can uptake viral byproducts triggering internal PRRs which culminate in IFN secretion. Moreover, alveolar macrophages also respond to IFNs by secreting potent inflammatory cytokines such as tumor necrosis factor alpha (TNF- α) and interleukin 6 (IL-6) which provoke and sustain a killing phenotype in phagocytes at the site of infection. On the other hand, interstitial lung macrophages undertake a regulatory role acting on the resolution phase of the infection, clearing cell debris, promoting tissue repair and dampening inflammation^{185,186}. Most functions of macrophages overlap with DCs during IAV infection and, *in vivo*, experimental evidence struggles to correctly attribute the observed outcomes to either cell type. This is partly due to the vast use of clodronate-mediated depletion techniques, which target phagocytes in general^{186,187}. Nevertheless, depletion of both cell populations shows increased viral loads, higher morbidity, tissue damage and mortality after IAV infection underscoring their crucial role in resolving infection¹⁸⁷⁻¹⁸⁹. Another defense mechanism of macrophages and DCs is that influenza replication is abortive, depicting a strategy to limit viral spread¹⁹⁰. Moreover, when infected, these cells function as signal amplifiers since they have a higher basal expression of PRRs and the ability to secrete high levels of cytokines and chemokines. In particular, the NLRP3 pathway induces a burst of interleukin 1 β (IL-1 β) and interleukin 18 (IL-18), which is essential to elicit cytotoxic IAV-specific T CD8⁺ cells, an important cell population for viral clearance and protection against disease^{191,192}.

Altogether, this general recognition of pathogens characterizes the innate immune response. By fine-tuning cytokine production and immune cells' recruitment and activation, the innate immune response orchestrates the balance between the desired ability to control the virus (antiviral resistance) and the undesired consequences of the inflammatory response (disease tolerance). Meanwhile, during this phase, antigen presenting cells (APCs) migrate to secondary lymphoid tissues, bridging the communication between the unspecific innate response and the precise adaptive immune response. The adaptive immune response is the ultimate defense barrier of the host, and its effector mechanisms peak around one week after infection. Activation of this branch of the immune response depends on tightly coordinated steps described elsewhere¹⁹³ and culminates in infection resolution and establishment of a memory surveillance network.

1.1.10.3. Adaptive Immune responses

The late onset of the adaptive immune response is balanced by the specificity of its effector mechanisms. They are divided into two key categories: humoral immunity (mainly mediated by antibodies) and cellular immunity (mainly mediated by T lymphocytes). The antibody response is characterized by different classes of immunoglobulins (Ig). In a naïve subject, Immunoglobulins M (IgMs) are the predominant effector Igs that bind IAV, block viral entry and activate the complement system^{194,195}. Upon the first encounter with IAV, B lymphocytes go through antibody maturation and class-switching processes and differentiate into antibody producing cells named plasma cells (PCs). PCs secrete highly specific and protective anti-IAV antibodies such as Immunoglobulin G (IgG) and Immunoglobulin A (IgA). IgGs circulate in the bloodstream and correlate with a better disease prognosis by limiting viral spread into the LRT, while IgAs are most abundant in the mucosal cavity and prevent transmission^{196,197}. Mechanistically, these immunoglobulins mainly recognize viral surface proteins and promote viral neutralization, viral particle aggregation, phagocytosis of infected cells and ADCC. The presence of antibodies during early stages of viral infection makes this branch of the adaptive response a crucial player in providing sterilizing immunity, particularly if antibodies are readily available at the viral entry site¹⁹⁸. For this reason, eliciting neutralizing mucosal antibodies is the desired goal of novel vaccine strategies^{199–201}. On the other hand, the humoral response can only act on IAV during its extracellular phases, e.g., just before infection and during particle release and spread. Thus, activating the cellular immunity branch of the adaptive response is still key to achieve broader levels of protection.

Cellular immunity is mostly mediated by CD8⁺ cytotoxic T lymphocytes (CTLs) and CD4⁺ T-helper lymphocytes (Th)²⁰². CTLs directly recognize infected cells by interacting with MHC I molecules complexed to antigens deriving from internal viral proteins. This cell subtype adds an extra layer of protection by acting synergistically with the humoral response. In mice lacking antibody responses, adoptive transfer of IAV-specific T CD8⁺ cells partially recovered protection against a lethal IAV challenge²⁰³. Mechanistically, CTLs secrete granules containing granzymes and perforins, and engage with Fas receptors to promote cell apoptosis²⁰⁴. Moreover, CTLs also secrete effector cytokines such as interleukin 2 (IL-2), IFN- γ and TNF- α which sustain immune activation and promote viral clearance^{205–207}. The essential role of mediator cytokines is highlighted by CD4⁺ Th lymphocytes. By secreting defined cocktails of cytokines, CD4⁺ Th lymphocytes amplify the cytotoxic phenotype of other immune cells, mediate antibody maturation and immunoglobulin class switch and stimulate memory responses^{208,209}.

In summary, beyond the intrinsic physical and chemical barriers, the main goal of the innate immune response is to buy time until a potent adaptive response arrives and vanquishes active infectious agents. When fully synchronized, both responses coordinate efficient viral control, neutralization and clearance whilst promoting a non-detrimental resolution of the active infection from the respiratory tract. Yet, the fundamental aspect of the adaptive immune response relies on the generation of long-lived, pathogen-specific memory cells. During activation and differentiation of B and T lymphocytes, a fraction of each effector cell population acquires a memory phenotype responsible for continuous surveillance of the host organism. Upon re-encounter with an antigenically similar pathogen, memory cells are promptly activated, and control pathogen spread, drastically reducing the probability of the host to develop disease. In the case of IAV, memory responses prevent re-infection with matching strains but are particularly important to grant cross protection against different IAV subtypes²¹⁰⁻²¹³. This memory response is an extraordinary feature of the immune system and the mechanistic basis of vaccination.

1.1.11. Influenza Virus Vaccine Targets

Vaccination works by priming the immune system with components from a pathogen to induce a robust memory response. Thus, after a natural encounter with that pathogen, a fast and effective recall response is triggered, preventing disease onset. An optimal vaccine contains antigens that are important for the entry process, are capable of activating multiple facets of the adaptive response and are accessible to the immune system during infection. In the case of IAV, most vaccines target the major surface glycoprotein HA, although the design of alternative antigenic peptides capable of eliciting a broader, cross-protective response is an active field of research²¹⁴⁻²¹⁶. This is partly due to immune-escape mutants arising from antigenic drift in seasonal strains. Indeed, single mutations in the exposed globular head domain of HA were shown to evade antibody recognition in humans²¹⁷⁻²¹⁹. Effectively, the

ability to design an optimal vaccine against flu benefits from a thorough understanding of the targets of the immune response during influenza infections (Figure 5).

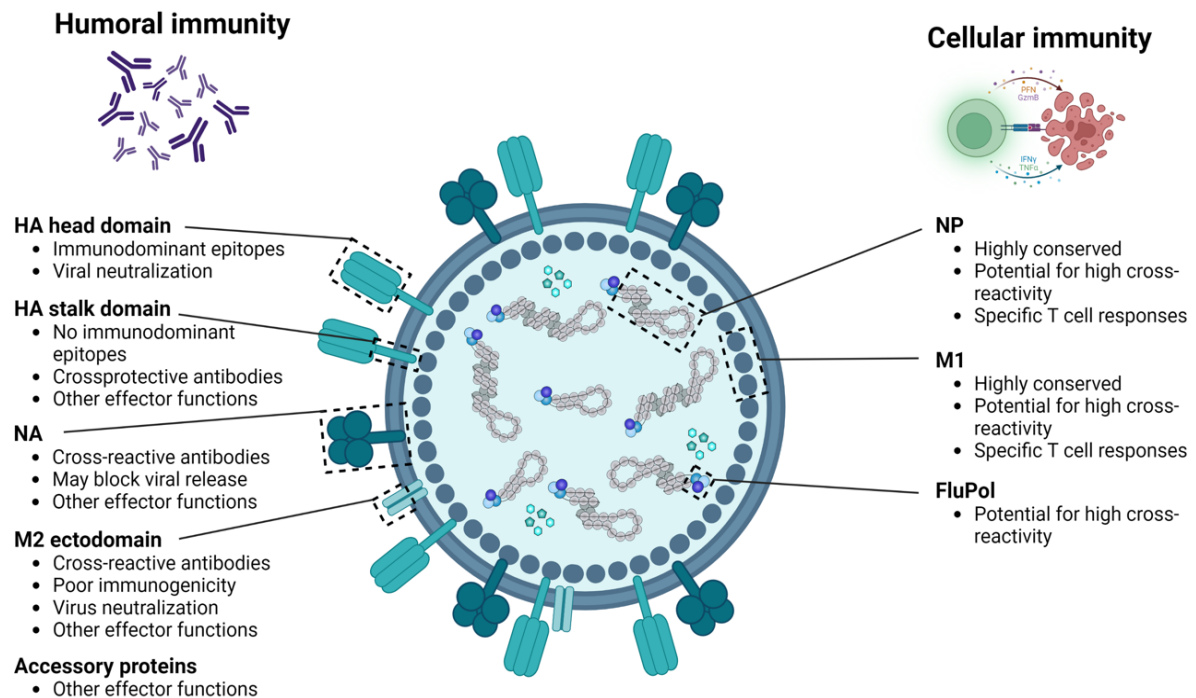


Figure 5: Antigenicity of IAV. Adapted from *Vaccines 2021*²²⁰

1.1.11.1. Surface proteins as vaccine targets

HA and NA are the main target of the immune response to influenza virus and can elicit protective neutralizing antibodies. In fact, sera with a titer of HA binding antibodies higher than 1:40 for adults, or 1:320 for children, are considered the gold standard correlate of protection against influenza illness^{221–223}. Still, most available vaccines achieve only partial protection, particularly against heterologous subtypes. Hence, novel vaccines focus on formulations capable of inducing broadly neutralizing antibodies against conserved regions of HA and NA. A promising strategy proposes the use of hyper-glycosylation patterns and cysteine bonds to stabilize HA trimers and redirect the immunodominance of HA towards desired epitopes²²⁴. The M2 protein is also a strong vaccine candidate^{225,226}. Antibodies against M2 ectodomain (M2e) have been identified after natural infection in humans and protected mice in heterosubtypic challenges^{227,228}. Thus, vaccine candidates targeting M2e conserved epitopes are a common strategy in vaccine development. Other examples include headless-HA proteins, chimeric HA constructs and NA-based vaccines, which are undergoing clinical trials trying to achieve a broadly protective influenza vaccine^{229–231}. For example, a recent phase I trial testing a chimeric hemagglutinin-based vaccine showed a strong induction of broad and long-lasting anti-stalk antibodies²³².

1.1.11.2. Internal proteins as vaccine targets

Flupol, NP and M1 constitute key structural components of the viral particle performing essential roles during replication. These viral proteins are enclosed by the virus membrane avoiding direct exposure to antibodies. Consequently, they are less prone to the selective pressure enforced by the immune system. Moreover, their multifunctional role during the different steps of viral replication renders them less tolerant to mutations. These features reflect on the sequence conservation of internal proteins along different strains²³³ making them promising vaccine targets, important to elicit cross-protective T cell responses. In a proof-of-concept study, mice vaccinated with a NP peptide fused to a penetrating peptide to promote antigen delivery induced high levels of NP-specific CD8⁺ T cells. Moreover, vaccinated mice were protected against three different lethal challenges using H1N1, H3N2 and H9N2 subtypes of IAV²³⁴. Likewise, human phase II clinical trials with a vaccine candidate containing NP and M1 also induce higher T cell responses²³⁵. No currently licensed vaccine targets any of these proteins directly, however several clinical trials show robust cross protection of vaccine formulations containing diverse combinations of these antigens²³⁶.

1.1.12. Influenza Prevention

Seasonal flu imposes a large economic and medical burden to the healthcare system of every country. In the US alone, the CDC estimates between 9 and 41 million flu cases every year with an associated cost of 11.2 billion US dollars to the healthcare system, highlighting the utmost need of prophylactic interventions^{237,238}. The best way to prevent influenza was verified during the covid-19 pandemic and consists of a combination of different public health measures. Self-isolation, hygienic practices, mask wearing and avoiding contact reduced flu cases by 99% characterizing an unprecedented flu season with only 1675 reported cases in the US²³⁹. Nevertheless, these measures are not sustainable since they impose severe socio-economic consequences. Thus, vaccination remains the most cost-effective method of preventing flu. Dating back from 1930s, influenza vaccines protect millions of individuals against flu illness every year. During the 2019/2020 flu season, mathematical models estimated that 7.52 million illnesses and 3.69 million medical visits were averted by influenza vaccination²⁴⁰. To date, there are 26 licensed inactivated influenza vaccines, 2 live attenuated influenza vaccines and 1 recombinant influenza vaccine across Europe and the US with the majority being produced in embryonated chicken eggs. The next section will introduce the production models and the different types of vaccines available, highlighting their advantages and disadvantages.

1.1.12.1. Influenza Vaccines

1.1.12.1.1. Production models

Every year vaccine formulation needs to be updated according to a GISRS report predicting the circulating influenza variants for the upcoming flu season. The choice of vaccine formulation initiates large-scale production of influenza vaccines in embryonated chicken eggs. The lack of the interferon response in this model allows the vaccine virus to replicate unencumbered and yield high stock titers. However, three main disadvantages arise from this production method. First, vaccine strains require an adaptation period to achieve optimal growth in eggs. Second, the presence of egg-derived contaminants in the final vaccine formulation which poses a risk for individuals with egg allergies²⁴¹. Third, and more importantly, the possible egg-adaptation mutations that can occur during viral propagation which have been shown to interfere with protective antibody responses^{242,243}. Altogether, these constraints reduce vaccine efficacy and curb pandemic preparedness initiatives that rely on a quick and accessible vaccine production. Consequently, alternative manufacturing processes are extensively explored to tackle these problems. For example, the use of canine kidney immortalized cell line (MDCKs) to produce influenza vaccine stocks which has been licensed since 2007²⁴⁴. Another alternative production model, characteristic of recombinant vaccines, is the expression of HA proteins in insect cells which was granted approval in 2013²⁴⁵.

1.1.12.1.2. Inactivated vaccines (IIV)

Inactivated vaccines are the most commonly available licensed vaccines for flu. Most IIVs are licensed for human use from 6 months old, when maternal antibody titers start to wane^{246,247}. After propagation of the chosen vaccine variants in chicken eggs, the harvested allantoic fluid is submitted to high temperatures or chemical treatment such as formaldehyde and β -propiolactone. High temperatures cause protein denaturation while chemical agents form protein crosslinks, both leading to viral particle inactivation. Inactivated vaccines can be further divided into whole particle vaccines (WPVs), split virion (SV) vaccines and subunit (SU) vaccines.

WPVs are cheaper and require a less laborious process. After concentration and removal of non-viral contaminants, the harvested allantoic fluid containing viral particles is formulated into a vaccine. WPVs were first approved for military use but rapidly replaced by SV and SU vaccines due to pronounced reactogenicity and unwanted side effects. Nowadays, WPVs are mostly used to prevent avian influenza outbreaks in poultry farms²⁴⁸.

SV vaccines go through an additional treatment with detergents to disrupt the viral envelope and expose internal viral proteins. The presence and accessibility of internal viral

proteins in split vaccines triggers the cellular branch of the immune response²⁴⁹, important to promote viral clearance and protect against disease. Indeed, in elderly populations, which often present suboptimal antibody responses, SV vaccines seem to offer the best protection among all IIVs²⁵⁰, however the overall clinical evidence is still weak²⁵¹.

The last type of inactivated influenza vaccine differs from split vaccines by an additional enrichment step. SU vaccines lack the viral ribonucleoproteins and matrix proteins²⁵², containing mainly HA and NA. Thus, the antibody response to SV and SU vaccines is similar denoted by several studies showing equivalent seroconversion rates^{253–256}.

1.1.12.1.3. Recombinant vaccines

Recombinant influenza vaccines are licensed for adults ranging from 18 to 54 years old and administered intramuscularly. Recombinant vaccines are generated by expression of HA in insect cells and overcome several disadvantages related to the egg reliance of other vaccines. Recombinant vaccines are devoid of egg contaminants, require no pre-adaptation of vaccine strains to optimal growth in eggs or cells and bypass the appearance of unwanted mutations that could compromise immunogenicity^{54,257}. Additionally, recombinant vaccines are formulated with an antigen amount three times higher (45ug/dose) than SV and SU vaccines²⁵⁸ which augments antibody responses. The recombinant HA is also trimerized in its pre-fusion state (HA0) from the lack of furin-like proteases in the insect production system. This structural characteristic, which is absent in other inactivated vaccines, exposes unique epitopes capable of eliciting broadly neutralizing antibodies²⁵⁹.

1.1.12.1.4. Live attenuated influenza vaccines (LAIV)

The third type of influenza vaccines is based on a replication-competent virus that was attenuated after several passages in chicken eggs at low temperatures²⁶⁰. The currently licensed LAIV strains are generated via recombinant mutagenesis using the 6 gene segments of a master donor virus (MDV) cold-adapted strain (*caA/AnnArbor/6/1960(H2N2)*) and HA and NA segments encoding the surface glycoproteins of the virus strains recommended by the GISRS. The MDV possesses three main attributes conferring its suitability as a vaccine backbone, i.e. temperature-sensitive (ts), cold adapted (ca) and attenuated (att). The mutations conferring each of these phenotypes are well described in the literature and mapped to five different substitutions in the segments encoding PB1, PB2 and NP²⁶¹. The combination of ca, ts and att phenotypes limits viral replication to the URT of humans and prevent LAIV from causing disease. LAIV ability to replicate in the URT offers advantages compared to inactivated and recombinant vaccines. It mimics a natural infection exposing a plethora of internal and surface antigens, it is delivered through a needle-free intranasal spray increasing the likelihood of

vaccine uptake, and it triggers an immune response at the site of infection inducing mucosal immunity with potent IgA and memory T CD8⁺ cell responses. Such features of LAIV have been associated to the potential of limiting transmission and reflect the good efficacy profile reported for this vaccine, particularly in children^{262,263}. The replicative nature of LAIV also provides an extra source of immunogenicity by self-amplifying the antigen content of the vaccine and continuously exposing it to the immune system, dispensing the use of additional adjuvants. On the other hand, LAIV's ability to replicate is also a major concern over its safety profile, especially in high-risk target populations. Live attenuated vaccines designed for other diseases have shown complications after administration in immunocompromised patients due to uncontrolled replication, transmission of vaccine strains to vulnerable populations and reversion to virulence causing disease²⁶⁴⁻²⁶⁷. In the case of LAIV, so far, no incidents of reversion to virulence have been reported in humans and only one example of vaccine virus transmission was described^{268,269}. This relatively safe profile of LAIV is most likely due to the three attenuation phenotypes of the vaccine strain spread out amongst three different segments. However, higher prevalence of wheezing, coughing and rhinorrea in children under 2 years old has been observed after LAIV administration^{270,271}. Thus, the fear of uncontrolled replication and reversion to virulence and the higher rates of adverse events prevent LAIV from being applied to high-risk populations. Even though IIVs can be safely administered in vulnerable populations with relatively good levels of protection, the added effect of a safe mucosal vaccine, capable of inducing robust cellular and humoral immunity would certainly benefit high-risk population groups.

The high mutagenic profile of IAV retains vaccine effectiveness at suboptimal levels ranging between 30-60%²⁷²⁻²⁷⁴. In fact, up to 10% of healthy individuals do not produce adequate levels of antibodies after IAV vaccination²⁷⁵. Apart from the general aspects of vaccination failure, i.e. low vaccine uptake, differences in the immune responses and discrepancies in methodology assessing effectiveness, other factors such as age, genetic diversity, immune status and previous exposure to other viruses also contribute to vaccine failure²⁷⁶⁻²⁷⁹. The distinctive antigenic drift and shift events also contribute to low vaccine effectiveness. In fact, vaccine strain mismatch is a main concern during influenza vaccine design and can be responsible for decreased vaccine effectiveness²⁸⁰⁻²⁸⁴. Nevertheless, even when the match is good, vaccine effectiveness is still low, encouraging the pursuit of a universal vaccine able to surpass the aforementioned obstacles and achieve broad protection against multiple IAV subtypes, including zoonotic emergent strains³⁵.

1.1.12.2. Universal Influenza Vaccine

According to the National Institute of Allergy and Infectious Disease (NIAID), a universal influenza vaccine (UIV) must achieve at least 75% efficacy against symptomatic disease, provide durable protection for at least 1 year, cross-protect against group 1 and 2 IAVs, and be approved for all age groups. In the last decade, 27 UIV candidates were tested in human clinical trials spanning different immunization routes, administration regimens, adjuvants and target antigens²⁸⁵. One of them, a trivalent adjuvanted virus-like particle vaccine, underwent a phase III clinical trial showing seroconversion rates of 99, 99 and 92.2% towards H1N1, H3N2 and influenza B, respectively^{286,287}. In addition, UIVs' ability to induce broad protection is often explored by using antigens that are conserved among different strains and can elicit strong cellular responses²⁸⁸. Thus, formulations with internal proteins such as NP and M1 are common amongst UIV candidates^{289,290}.

1.1.12.3. Influenza vaccines in high-risk groups

As mentioned above, children, pregnant women, immunocompromised and patients with comorbidities and individuals over 65 years old categorize populations at higher risk of developing flu-related complications. They represent a subset of the population which benefits the most from vaccination and thus, are the core target of vaccine recommendation guidelines. In fact, an extensive body of literature reviews the benefits of IIVs in pregnant women²⁹¹, immunocompromised patients²⁹², elderly^{293,294} and very young children²⁹⁵⁻²⁹⁸.

Although IIVs provide satisfactory protection in most of these population groups and present a good safety profile, they are the only vaccine type accessible to them. Thus, alternative strategies are adopted to offer extra layers of protection to these vulnerable populations. One example is to target other population groups in close contact with susceptible patients. Indeed, influenza vaccination campaigns aiming at school children and healthcare workers provide herd immunity and block chains of transmission towards the elderly and the immunocompromised community^{122,299}. Additionally, this strategy also proved to be highly cost-effective by protecting a wider community. In a controlled study, childhood vaccination reduced general practitioner visits, absenteeism from employment, ICU admissions and antibiotic prescriptions³⁰⁰⁻³⁰².

1.2. Chapter 2: The human microbiota

1.2.1. General introduction

For centuries, microorganisms have been associated with harm when it comes to human health. Mostly associated to a pathogenic behavior and being the causative agent of many deadly diseases, microbes have been actively kept away from our organisms through the use of disinfectants, antiseptics and medicinal substances with antimicrobial properties. This mentality started to change at the beginning of the 20th century, when Pasteur observed that bacteria in fermented milk could have beneficial effects for the human gut. However, it was only several years later that a commensal microbial community was described in relation to relevant physiological processes³⁰³. These microbial communities constitute the host microbiome which includes bacteriophages, archaea, bacteria, eukaryotic virus, and fungi. The host microbiome plays an essential role in the maintenance and development of a healthy functional organism³⁰⁴. It does this by participating in the metabolism of complex carbohydrates and drugs, producing important metabolites, priming the immune system and offering protection against other pathogens.³⁰⁴

The first moment of interaction between humans and their commensals is still debated, with inconsistent evidence for in utero exposure³⁰⁵. Regardless, upon birth, newborns are subjected to a robust influx of microbes that colonize various surfaces. The warm, humid and nutrient-rich environment of the human mucosa allows the establishment of microbial communities at different body sites, i.e. gut, airways, skin. Several factors affect this process such as delivery mode, antibiotic usage, host genetics, feeding type and environmental exposure^{306,307}. The acquisition of certain species during this period is key to establish a healthy mature microbiota³⁰⁸. During infancy, the commensal community is characterized by a low diversity and biomass, with major changes in composition happening over a time of 2 to 3 years³⁰⁹. Due to this immature state of the microbiome, emerging evidence defines childhood as a critical period, susceptible to external cues that shape the host microbiota with consequences to health in adult life (Figure 6). Accordingly, several pathologies in adulthood, including cardiovascular, metabolic, neurological and allergic diseases, are associated with perturbances in early life microbiome composition such as excessive antibiotic treatment and malnutrition³¹⁰⁻³¹². The adult microbiota is characterized by a generally stable and resilient community with the ability of restoring its equilibrium after a perturbation^{313,314}. Geographical location, diet and lifestyle contribute to the structure of the adult microbiota across different human populations. However, even in adult life, external challenges can still cause temporary or permanent fluctuations in the composition of the host microbiota, potentially leading to or

supporting diseases. Thus, understanding the underlying mechanisms governing host-microbiota interactions represent an important field of research with great impact for human health.

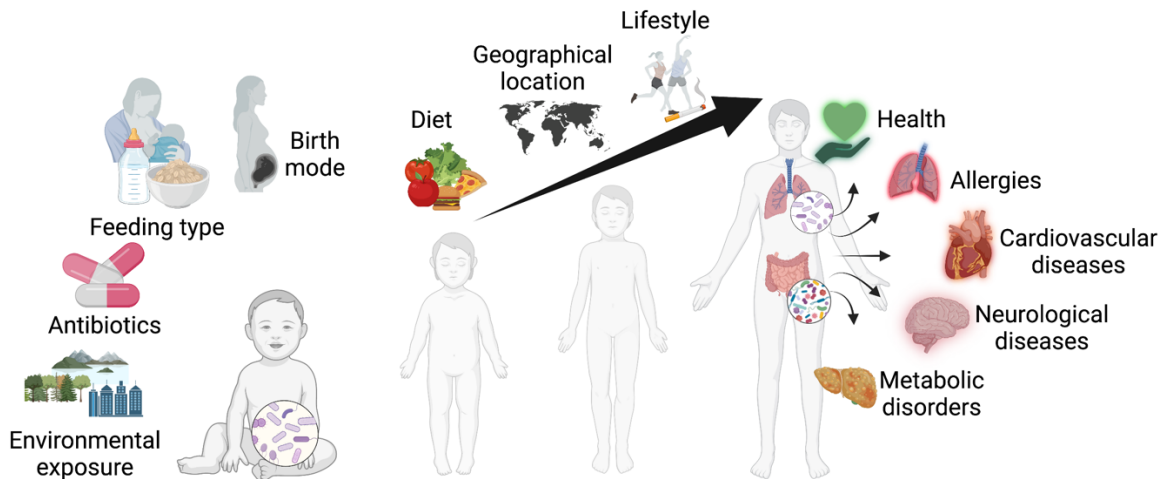


Figure 6: Human microbiota development. Upon birth a variety of microorganisms colonize the newborn body surface. This process is influenced by environmental exposure, antibiotics use, birth mode and feeding type. During childhood, the microbiota is characterized by a low biomass and is shaped by external cues along human development. Diet, geographical location and lifestyle modulate the composition of the host microbiota, particularly during the first 2 to 3 years of life. By that time, human microbiota matures into a stable, steady-state community which remains until adulthood. In adults, the host microbiota has a direct impact on human health with different compositions being associated to several diseases. *Adapted from Journal of Laboratory Medicine 2021 and eBioMedicine 2021*^{315,316}

1.2.2. Microbiome nomenclature

Two main terms are used to describe our microbial communities. While the term microbiota solely refers to the compositional aspect of a particular community, i.e. taxonomic classification, the term microbiome describes the individual microorganisms alongside their genomes, metabolomes and dynamic interactions³¹⁷. Another important aspect is the diverse composition of the human microbiota. An organized terminology exists that divides it into “omes” according to the nature of the microorganism. For instance, the human virome describes the viral component of the microbiome³¹⁸ while the human mycobiome describes the fungal component³¹⁹. Since the second part of this thesis refers to the bacterial component, namely the human microbiome, the next subchapters will refer specifically to it.

1.2.3. Characterization of the Human Microbiome

The human microbiome is a dynamic network of microorganisms constantly changing and adapting to external and internal stimuli. Since the discovery of its role in human health, a huge effort has been put into describing a steady-state core universal community shared across different populations. The Human Microbiome Project (HMP) represents the largest consortium trying to achieve that with a database consisting of 11’000 sampled specimens over

18 body sites from 300 individuals across the globe³²⁰. Although a universal core microbiota was never found, these studies contributed to the characterization of different microbiota communities according to their composition, function, and anatomical location.

1.2.3.1. Compositional Characterization

The appearance of culture-independent techniques revolutionized the field of microbiology. Nowadays, most of the studies employ high-throughput sequencing as a way to classify the host microbiota according to specific marker genes³²¹. The most common is the 16S ribosomal RNA gene (16S rRNA) which contains nine variable regions (V1-9) each flanked by conserved sequences throughout the bacteria kingdom. By sequencing the variable regions and matching them to a reference database, it is possible to map the different phylotypes present in a sample and structurally characterize the microbiota. It is estimated that hundreds of species have been identified within the human microbiota using this technology that were previously not cultivable *in vitro*. Moreover, the large volumes of data generated using this platform allowed the systematic assessment of the human microbiota across different populations, as evidenced in branch studies from the HMP. In doing so, it became clear that changes in diversity correlate with a wide spectrum of human conditions³²². Indeed, disease-associated microbiota communities are commonly associated with a loss in biodiversity by overrepresentation and/or depletion of specific phylotypes compared to healthy controls^{323–326}. For example, in patients with obesity and metabolic disorders, an overrepresentation of Proteobacteria is often observed in their gut microbiota³²⁷.

Two important parameters are used to measure microbiota diversity, namely alpha and beta diversity. Alpha-diversity quantifies the total number of different species present within a community (richness) and their abundance (evenness). Beta-diversity describes the variation observed between communities. Both parameters represent key tools to describe the degree of diversity between and within samples and establish reliable correlations regarding pathological phenotypes across different human populations^{328,329}.

1.2.3.2. Functional Characterization

Besides compositional analysis, another important aspect of microbiome characterization includes metagenomic, proteomic and metabolomic analysis. These approaches identify and characterize collective genomes, proteins and metabolites present in a defined environment or ecosystem, hence giving insight into the functions of non-cultivable bacteria. Highly diverse communities with similar functional roles better predict a core microbiome profile shared within different human populations. A complementary study to the HMP highlighted this by using metagenomic approaches to characterize over 3 million

bacterial genes from fecal specimens of 124 European individuals. When these genes were pooled and used to predict functional outcomes of each microbiota community, they revealed specific signatures shared amongst all sampled individuals³³⁰. This also applies for disease states. Five Crohn's disease patients with very different microbial communities in compositional terms presented equivalent behaviors in functional terms, yielding similar metabolic profiles³³¹. A good example attesting the added value of the functional characterization of the microbiota is the case of the *Bifidobacterium spp.* In children, the lack of this genera correlates with higher systemic inflammation³³². Through the combination of 16S sequencing with metagenomic data and metabolic profiling, it was found that these bacteria possess a gene signature capable of metabolizing human milk oligosaccharides (HMOs)³³³. In turn, the ability to metabolize HMOs promotes a subset of regulatory T cells capable of attenuating inflammation³³⁴. Another relevant application of these analyses is shown through the use of metabolomic profiling to fish for potential biomarkers able to predict disease progression and treatment outcome³³⁵. For instance, a recent study reported a set of microbiome-derived metabolites that were detected exclusively in colon rectal cancer patients³³⁶.

1.2.3.3. Anatomic Location

Anatomic location is also an important criterion during microbiome characterization. In humans, several niches have been described with a characteristic microbiota, namely the skin, the ear, the oral cavity, the genitourinary tract, the vaginal zone, the respiratory tract and the gastro-intestinal tract. For the purpose of this thesis, I will focus on the methods used to characterize the last two body sites.

1.2.3.3.1. The gut microbiota

The gut microbiota is represented by microorganisms lining the epithelial surface of the gastro-intestinal (GI) tract and is the larger community in the human body, with an estimated bacterial load of 10^{11} microbial cells per gram in the colon³³⁷ (Figure 7A). The GI tract spans from the oral cavity to the rectum, passing through the oesophagus, stomach, small intestine and large intestine. Serving as a passageway for food digestion, the GI tract is characterized by different nutritional and chemical gradients, and extreme physiological conditions, favoring different niches of microbial communities along its length. For instance, the acidic environment of the stomach promotes a microbiota enriched in acid-resistant species³³⁸, while the lack of oxygen in the distal part of the large intestine nurtures a predominantly anaerobic community³³⁹. The predominant phyla of the GI tract microbiota are Actinobacteria, Bacteroidetes, Firmicutes, Proteobacteria and Tenericutes, with the first three phyla

representing up to 90% of all the known members³⁴⁰. However, most studies rely on stools and rectal swabs as the standard sampling procedure, using stool-derived microbiota as a proxy for the GI tract composition. Although this approach is a non-invasive procedure, requires fewer resources, and allows longitudinal follow-up, it does not fully reflect the gut microbiota community. This is shown in two studies comparing microbiota composition in feces and biopsy samples from the same individuals which have reported significant differences between the two communities^{341,342}. Alternative sampling techniques include biopsy collection via luminal brush, surgery, catheter aspiration and laser capture microdissection, however they all employ invasive procedures with inevitable cross-contamination.

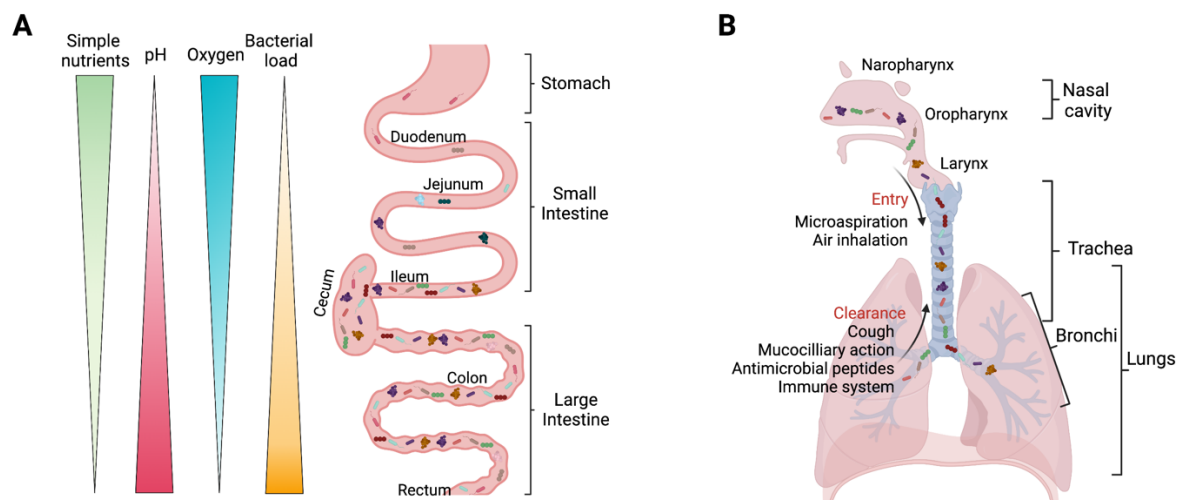


Figure 7: Microbiota distribution along the gut and lungs. (A) Gradients of pH and oxygen along the longitudinal axis define the bacterial community in the small intestine with low bacterial load in the proximal areas and abundant bacterial loads in the distal regions. Simple nutrients overflow in the small intestine and sustain the growth of taxa able to effectively consume these compounds. In contrast, the large intestine is populated by taxa that can break down more complex compounds such as dietary fibers. (B) The lung microbiome is defined by a balance between immigration from the URT by microaspiration and air inhalation and elimination via immune and mechanical processes. *Adapted from Environmental microbiology 2017*³⁴³ & *Journal of Clinical Investigation 2021*³⁴⁴

1.2.3.3.2. The respiratory tract microbiota

The human airways are a dynamic environment with high influx and efflux of material. They are divided into URT and LRT. The URT comprises the nasal cavity, naropharynx, oropharynx and larynx and a detailed description of their microbiota composition has been reviewed elsewhere^{345–347}. Being on the interface between the external environment and the LRT, the URT contains a highly dynamic microbiota that heavily influences the composition of the LRT microbiota through a bidirectional flow of bacteria due to micro aspiration and air inhalation³⁴⁸. In fact, the oropharynx cavity is the main source of the LRT microbiota and can be a major driving force of pathological colonization of the LRT^{349,350}. *Streptococcus pneumoniae* and *Staphylococcus aureus*, two major pathobionts that can cause severe

pneumonia, are frequently part of the URT commensal microbiota³⁵¹. Sampling of the URT includes swabs, nasal rinses and dry filter papers.

The LRT comprises the trachea, bronchi and the lungs. For a long time, the LRT was believed to be sterile, with microbial content only observed during pathological conditions³⁵². With the advance of sequencing techniques, it is now accepted that the LRT is also colonized by a healthy microflora. As opposed to the GI tract, the intricate architecture of the LRT, combined with a dynamic retrograde flux of material and active immunosurveillance, makes the presence of commensal microbes transient at this body site (Figure 7B). Nonetheless, the biological relevance of the lung microbiome is supported by observational studies in humans where alterations of the LRT microbiota diversity have been associated with a plethora of diseases such as asthma, chronic obstruction of pulmonary disease (COPD) and cancer^{353–357}. In humans, it is technically challenging to sample the LRT microbiota. Not only due to its low bacterial load, which is three orders of magnitude lower than the GI tract microbiota, but also because most sampling techniques are invasive and require qualified trained staff^{358,359}. Nevertheless, common sample specimens of the LRT are sputum and the bronco-alveolar lavage (BAL)^{360–362} which are used to describe a healthy human lung microbiota containing Firmicutes and Bacteroidetes as the predominant phyla. However, this composition has been challenged by recent studies directly analyzing biopsies of lung tissue, where Proteobacteria were the prevailing taxa³⁶³. The cross contamination from the URT and the oral cavity during BAL and sputum collection have been pointed to as the sources of the discrepancies observed in the literature³⁶⁴. The clear contrast between lung microbiome composition studies highlights the importance of properly defining sampling methods and carefully controlling for contaminants from the oral cavity during sampling procedures. Alternative techniques such as protected brushing and surgical resection of lung tissue have been employed to study lung microbiota, however both represent extremely invasive procedures.

1.2.3.4. Animal models in the characterization of the Human microbiome

Defining the composition and function of the human microbiota is important to understand the physiological roles of the microbiome and its impact on human health. However, the biological relevance of the microbiome field is undermined by a lack of causality studies, mostly from scarce evidence defining the changes in the microbiota as a cause or a consequence of the disease state^{365,366}. So far, only two human diseases, i.e. *Helicobacter pylori*-associated peptic ulceration and *Clostridium difficile* infection-associated diarrhea, have been described with an established causal relationship between microbiota and pathology^{367,368}. In addition, the inherent heterogeneity of the human microbiome, along with the immeasurable

number of confounding factors and the technical and ethical constraints associated with human experimental designs represent other obstacles when defining causal relationships between the human microbiome and disease. Thus, a common approach is to use animal models. Animal models resolve some of the issues associated with human studies by controlling for environmental, behavioral and genetic confounders. Also, the possibility to maintain germ-free (GF) animals is a useful tool to assess the contribution of human microbiota to pathologies and establish causality^{369,370}. A good example is the use of human microbiota-associated rodents in which human fecal microbiota from diseased patients is transplanted into the intestine of GF animals to monitor disease phenotypes compared to fecal microbiota from healthy patients³⁷¹. For instance, transplanting fecal microbiota from obese human donors, but not lean, into mice, resulted in increased total body and fat mass, as well as obesity-associated metabolic phenotypes³⁷². Moreover, the use of gnotobiotic animals colonized with selected bacterial species enables reductionist approaches to evaluate the pathological and physiological relevance of particular microbiota constituents³⁷³. On the other hand, the use of different animal vendors, housing facilities, and diet regimens creates huge reproducibility problems and generates conflicting results. Nevertheless, *in vivo* mechanistic studies coupled with functional and compositional characterization of the microbiota serve as a good basis to formulate hypotheses regarding the biological relevance of the microbiome in human health. In fact, several mechanisms have been proposed to mediate important functions in metabolic processes, immune homeostasis, and protection against pathogens. The next section will introduce key examples of these mechanisms which have a direct impact in health and disease outcomes.

1.2.3.5. Human microbiome in health and disease

The human microbiota exerts its effects on human health through different mechanisms. First, it can outcompete pathogenic strains offering a layer of protection towards other pathogens (colonization resistance). Second, it can produce secondary metabolites with the ability to modulate different physiological processes. These include short-chain fatty acids (SCFAs), neurotransmitters, microbe-associated molecular patterns, secondary bile acids and enterosynes. Third, through its active role during immune maturation, it can imprint the immune system compartment into a less reactive phenotype.

1.2.3.5.1. Colonization Resistance

Colonization resistance represents a major benefit of the commensal microbiota which protects against other pathogens^{374,375}. This can happen via direct interactions between microbial communities such as nutrient competition, niche exclusion and secretion of bacteriocins³⁷⁶ or indirectly via mucous stimulation, promotion of epithelial integrity and

modulation of the immune system by inducing IgA production and Th17 lymphocytes^{377,378}. The pathobiont *Clostridium difficile* illustrates a good example of the many mechanisms characterizing colonization resistance^{379–381} (Figure 8A). Under homeostatic conditions, production of bacteriocins by *Bacillus thuringiensis* has been shown to control *C. difficile* expansion³⁸². Moreover, the consumption of sialic acids and monomeric glucose by the cecal microflora also depletes nutrients essential for the growth of *C. difficile*³⁸³. Overall, the medical relevance of these interactions between host health and microbiota is evidenced by a rise in opportunistic infections in hospitalized patients after antibiotic treatment^{384,385}.

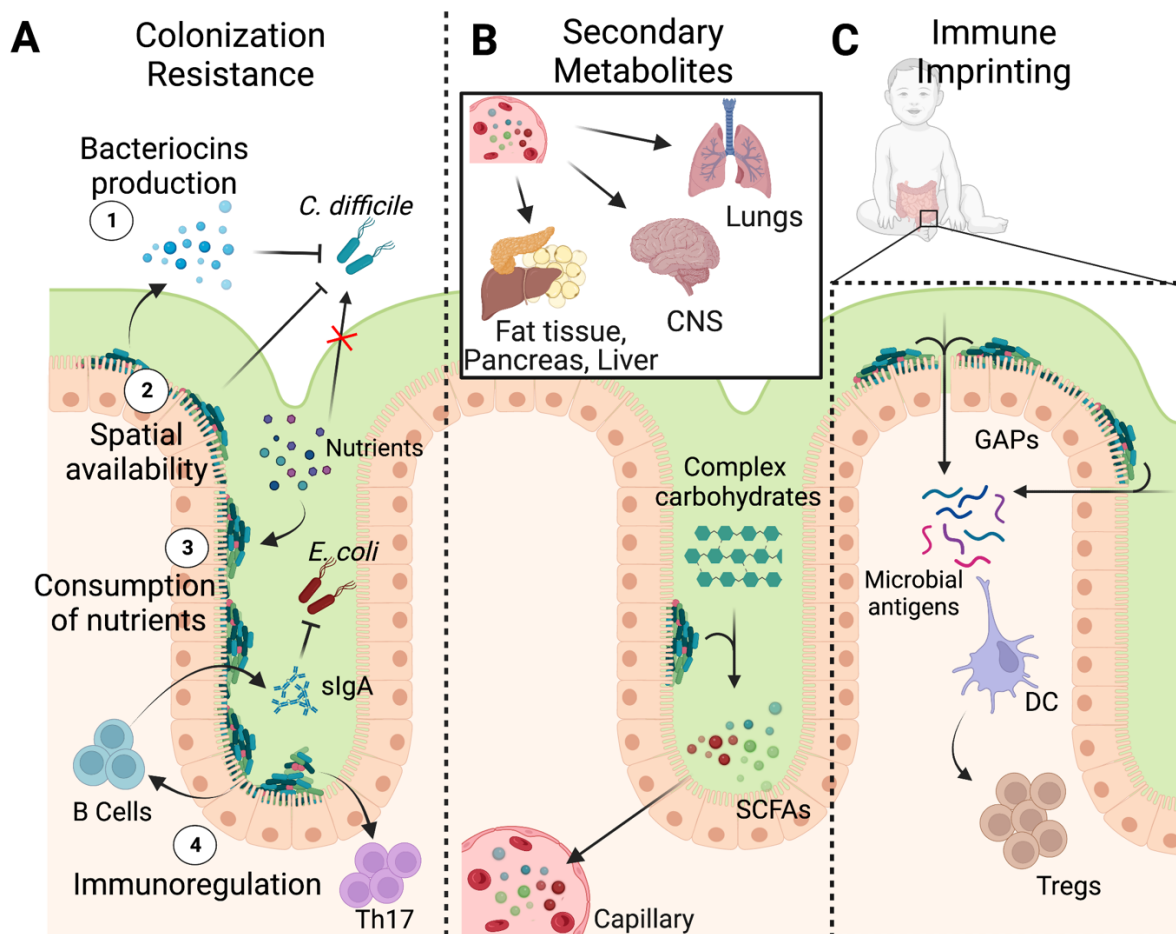


Figure 8: Host microbiota effector mechanisms implicated in health and disease. (A) The intestinal microbiota promotes colonization resistance to intestinal opportunistic pathogens by both direct and indirect mechanisms of action: (1) Production of microbial products (bacteriocins) protecting against infection by directly killing pathogenic bacterial species. (2) Spatial occupation of the intestinal epithelial surface by commensal species preventing attachment of pathogenic strains. (3) Competing for nutrients preventing overgrowth of opportunistic species. (4) Increased production of IgA by B cells and differentiation of T helper 17 (Th17) cells strengthening the immune and epithelial barrier against invading pathogens. (B) Anaerobic fermentation of indigestible polysaccharides such as dietary fiber and resistant starch into short chain fatty acids (SCFAs). Colon-derived SCFAs reaches the systemic circulation and other tissues, leading to fat tissue activation, regulation of liver mitochondrial function, increased insulin secretion by β -pancreatic cells, modulation of neuroinflammation in the central nervous system (CNS), and maintenance of lung metabolic tone. (C) The presence of a microbial community in the infant’s gut leads to the passage microbial antigens through a process named goblet cell-associated antigen passage (GAP). DCs take up these antigens and in the absence of an infection

or an inflammatory environment, a population of T regulatory cells (Tregs) expands which correlates to less immunoreactive phenotypes in adult life. *Adapted from Nature Reviews Immunology 2013*³⁸⁶; *Frontiers in Endocrinology 2020*³⁸⁷; *Journal of allergy and clinical immunology 2020*³⁸⁸

1.2.3.5.2. Secondary Metabolites

SCFAs are the most abundant secondary metabolites produced from dietary fibers by the gut microbiota. The main SCFAs are acetate, propionate and butyrate. Concentrations of SCFA can reach the millimolar range in the intestinal lumen, where they act locally by strengthening the epithelial barrier, inducing the production of antimicrobial peptides and serving as the primary energy source for epithelial colon cells³⁸⁹. Upon absorption, these molecules enter the bloodstream and exert tissue-specific effects at distal organs (Figure 8B). SCFAs have been implicated in cardiovascular health³⁹⁰, skeletal muscle function³⁹¹, glucose and lipid metabolism^{392,393} and immune regulation³⁹⁴. The discovery of the pleiotropic effects of SCFA boosted specific fields of research dedicated to understanding the crosstalk between the gut microbiota and specific organs, namely gut-lung axis, brain-gut axis and liver-gut axis³⁹⁵⁻³⁹⁷. Mechanistically, SCFAs signal through the G-protein coupled receptors GPR41, GPR43 and GPR109A, expressed in immune, epithelial and adipose cells^{398,399}. The physiological relevance of SCFAs is highlighted in studies using GPR41 and GPR43 deficient mice which present decreased heart rate⁴⁰⁰, reduced weight gain⁴⁰¹, increased steatosis⁴⁰², exacerbated inflammation⁴⁰³ and increased colon cancer progression⁴⁰⁴. Alternatively, SCFAs can also directly inhibit the activity of histone deacetylases (HDAC) and regulate gene expression. The ability of the gut microbiota to produce SCFAs together with the pervasive tissue-specific activity of these molecules makes the gut microbiota a key player in maintaining systemic homeostasis.

1.2.3.5.3. Imprinting and Immunoregulation

Being in direct contact with the mucosal surface since birth, the human microbiota provides a constant source of bacterial antigens under a nonpathogenic context which contributes to the development and education of the host immune system. In line with this imprinting phenomenon, GF mice present aberrant gut-associated lymphoid tissue (GALT) with deficient maturation of IgA producing B cells, colonic T cell development and aberrant levels of IgE and pro-allergic cells⁴⁰⁵⁻⁴⁰⁸. Interestingly, GF mice colonized before weaning but not after, reversed their susceptibility to inflammatory colitis, pointing towards a specific period where the immune system is susceptible to microbiota-induced modulations⁴⁰⁹⁻⁴¹¹. The time restriction of this microbiota imprinting seems to coincide with the transition from liquid to solid food in mammals. Mechanistically, a very exciting ongoing theory proposes that during infancy, the formation of transient goblet cells-associated passages, triggered by the cessation

of milk, allows bacterial components to be transported into GALTs, where they induce tolerogenic cell populations⁴¹² (Figure 8C). In mice, this window of opportunity is transient and characterized by the expression of the inflammatory markers TNF- α and IFN- γ in the distal portion of the small intestine, a site enriched in GALTs. Termed ‘the weaning response’, this phenomenon expands a population of T regulatory cells which will imprint the immune system towards a tolerogenic state in adult life⁴¹⁰.

Another consequence of this imprinting phenomenon is observed in the immune response to vaccines⁴¹³. Mice treated with antibiotics in early life but not in adulthood, had impaired antibody responses to 13 different vaccines⁴¹⁴. In humans, this is evidenced by large cohort studies comparing vaccine efficacy in high and lower-middle income countries. In the latter, gut dysbiosis in infants caused by short-term breast-feeding, malnutrition and higher rates of diarrhea accounted for the decreased antibody titers post vaccination⁴¹⁵. Moreover, the presence of *Bifidobacterium* genus in infants from 6 to 15 weeks of age positively correlated with better T CD4⁺ responses and memory responses after Bacillus Calmette-Guérin (BCG) and stool IgAs after oral polio vaccination^{416,417}. Thus, several interventional approaches focus on using probiotics and commensal bacteria as adjuvant alternatives during vaccine administration to boost efficacy. In fact, a systematic review evaluating 26 randomized controlled trials (RCTs) using probiotics as an intervention to ameliorate vaccine responses in infants showed a beneficial role of this strategy⁴¹⁸.

1.2.3.6. Influenza infections and dysbiosis

An abundance of external factors can perturb the steady state microbiota and can unbalance the mutualistic relationship with its host organism, an outcome termed ‘dysbiosis’. Although dysbiosis is not defined by a specific microbiota composition, it is commonly described in the literature as the absence of eubiosis. Dysbiosis has been reported in a multitude of non-communicable diseases including ulcerative colitis⁴¹⁹, asthma⁴²⁰, diabetes⁴²¹ and obesity⁴²², but also infectious diseases^{423,424}. While antibiotic administration and diet are two obvious drivers of dysbiosis, only recently infectious diseases, in particular influenza infections, have been implicated in dysbiosis with significant impacts on human health^{425,426}.

The consequences of an active viral infection on the host microbiota have only been recently described⁴²⁷. In the case of IAV infections, both mice and human studies indicate a direct impact of influenza on the gut microbiota which is transiently destabilized during acute infection⁴²⁸⁻⁴³⁰. A recent study addressed the mechanism of IAV-associated dysbiosis using a mouse model. During IAV pathogenesis, the loss of appetite induced a shift in food intake which altered the composition of gut microbiota. A decrease in fermenting bacteria led to lower

SCFA production which in turn reduced the killing activity of alveolar macrophages. To prove their idea, naïve mice were transplanted with microbiota from IAV-infected animals which rendered them more susceptible to bacterial superinfection⁴³¹. In another study, transplanting gut microbiota of mice that survived a H7N9 infection into naïve mice improved their survival following a lethal challenge with the same virus. This effect was lost when the transplanted gut microbiota came from animals that succumbed to infection⁴³². These studies support the idea that gut microbiota dysbiosis after IAV infections is capable of modulating susceptibility to subsequent infections and disease.

Although most studies focus on alterations in the microbial community of the gut after IAV infections, few have explored their impact on the dynamics of the lung microbiota^{429,433,434}. Since lung microbiota dysbiosis has already been shown to affect an array of physiological functions of the lung and inflammation^{435,436}, this is an important topic of research that could uncover novel mechanisms steering IAV pathogenesis and susceptibility to respiratory infections. More importantly, studies exploring the effect of IAV infections in gut and lung microbiota during the maturation phase of the immune system are scarce in the literature. This is partly due to the novelty of this field, but also to the rarity of clinical evidence in humans from the lack of appropriate controls, since most IAV infections can be asymptomatic and/or pass undetected. Nevertheless, we believe that using mouse models to address the impact of respiratory infections during microbiota maturation could shed light onto important, overlooked mechanisms of host dysbiosis with long term consequences in health outcomes.

2. Aims

2.1. Aim 1

The search for novel influenza vaccines is overwhelmingly saturated by candidates with a universal protective profile⁴³⁷, particularly in young and adult populations. On the other hand, strategies to improve current vaccines targeting high-risk patient groups, the most affected during flu seasons, are scarce. The breadth of potential applications and advantages offered by LAIVs make it a promising candidate for further optimization. In fact, a body of literature reports several attempts to improve the safety and immunogenic profile of LAIVs⁴³⁸. However, the lengthy and costly process of transitioning a preclinical vaccine candidate into humans, confines most of these vaccine candidates to preclinical models. In addition, these candidates are mostly tested in adult healthy animals which do not account for an impaired immune response often observed in high-risk groups.

With that in mind, the aim of the first block of this PhD thesis was to modify the already licensed LAIV backbone and increase its safety profile envisioning its application in high-risk patient groups. In order to achieve that I aimed to:

- Perform targeted mutagenesis in the NS1 gene of the LAIV backbone and increase the attenuated phenotype of the vaccine virus
- Evaluate the production efficiency of the optimized vaccine (optiLAIV) using two different manufacturing models
- Confirm vaccine efficacy in healthy adult animals
- Characterize the replication and efficacy of the optimized LAIV in two *in vivo* models mimicking high-risk patients
- Describe the immune response to optiLAIV and compare it to the parental LAIV
- Characterize distinct molecular pathways induced by the optimized LAIV *in vitro* and the mechanisms of attenuation.

2.2.Aim 2

IAV infections are a known source of dysbiosis in the intestinal microbiota⁴²⁹. Animal studies propose biological plausible mechanisms for this phenomenon which culminates in susceptibility to secondary bacterial infections, both in the intestine and in the respiratory airways^{431,439,440}. However, little is known about the impact of a subclinical viral infection during infancy on the composition and maturation of the host microbiota at different body sites. As described above, this period represents a window of opportunity to prime the host immune system by exposure to distinct microbial species and metabolites. Moreover, the establishment of a steady-state microbiota takes place during infancy which can imprint future physiological processes. Thus, in the second block of this thesis, I aimed to evaluate the impact of a subclinical IAV infection during infancy on the microbiota composition and its consequences in adult life using a neonatal mouse model. In order to achieve that, the main questions this thesis aimed to answer were:

- Does a subclinical IAV infection during infancy causes dysbiosis in the lungs or the intestine of infected mice?
- Does this dysbiosis last until adulthood?
- What are the consequences of this dysbiosis in the host metabolism?
- What are the consequences of this dysbiosis in the responses to vaccination?
- Are these effects dependent on microbiota compositional changes?
- What are the molecular mechanisms leading to the consequences of the dysbiosis process?

3. Results

3.1. Optimizing the live attenuated influenza A vaccine (LAIV) backbone for high-risk patient groups

3.1.1. Published Results

João P. P. L. Bonifacio¹, Nathalia Williams¹, Laure Garnier¹, Stephanie Hugues^{1,2}, Mirco Schmolke^{1,2}, Beryl Mazel-Sanchez¹

¹*Department of Microbiology and Molecular Medicine, University of Geneva, Geneva, Switzerland*

²*Geneva Center for inflammation research (GCIR), University of Geneva, Geneva, Switzerland*

Status:

Manuscript published in Journal of Virology – PMID: 36190240

Summary:

The first part of my thesis aimed to improve LAIV efficacy by reducing the ability of LAIV NS1 to bind CPSF30. This would prevent the host shutoff and abolish its interference on the establishment of the UPR. We hypothesised that, a LAIV candidate that no longer inhibits the host response would have an enhanced attenuated profile combined with increased immunostimulatory properties. Using target mutagenesis, we introduced five point mutations in the NS1 segment of *caAnnArbor* and rescued our optimised live attenuated influenza vaccine (optiLAIV) virus expressing an NS1 with reduced binding to CPSF30. In adult mice, we observed lower replication of optiLAIV compared to LAIV and similar protection after challenge. The attenuated phenotype of optiLAIV led us to evaluate the safety profile of this vaccine in a neonatal mouse model, representing a high-risk patient group. In neonatal mice, we observed lower replication of optiLAIV in the upper respiratory tract with earlier clearance compared to LAIV. Despite lower replication, optiLAIV equally protected mice against a long-term heterologous challenge and a heterosubtypic challenge. We further confirmed the safety profile of optiLAIV in STAT1^{-/-} mice, which are highly susceptible to viral infections. optiLAIV-administered mice showed no signs of morbidity or mortality, compared to a 50% mortality rate observed in animals vaccinated with *wt* LAIV. Corroborating to previous results published by our group, optiLAIV induced UPR-related genes in a human nasal epithelial tissue model suggesting this pathway as a potential mechanism of attenuation. Interestingly, we show that UPR is induced in an IFN signalling-independent manner. We propose that optiLAIV allows the establishment of the UPR triggered by ER stress, which contributes to the attenuated phenotype of optiLAIV. Based on our results, optiLAIV could be explored as a safer alternative candidate to the licensed LAIV.

Personal Contribution:

For this project, I conceptualized, designed and performed all the experiments, analysed and interpreted all the results and wrote the manuscript with contributions from my thesis supervisor Mirco Schmolke and co-supervisor Beryl Mazel Sanchez. In addition, Laure Garnier and Stephanie Hugues provided the expertise and reagents necessary to conceive figure S2 and perform the analysis of flow cytometry data. Nathalia Williams assisted with the animal work.



Optimizing the Live Attenuated Influenza A Vaccine Backbone for High-Risk Patient Groups

João P. P. L. Bonifacio,^a Nathalia Williams,^a Laure Garnier,^a Stephanie Hugues,^{a,b} Mirco Schmolke,^{a,b} Beryl Mazel-Sanchez^a

^aDepartment of Microbiology and Molecular Medicine, University of Geneva, Geneva, Switzerland

^bGeneva Center for inflammation research (GCIR), University of Geneva, Geneva, Switzerland

ABSTRACT Together with inactivated influenza vaccines (IIV), live attenuated influenza vaccines (LAIV) are an important tool to prevent influenza A virus (IAV) illnesses in patients. LAIVs present the advantages to have a needle-free administration and to trigger a mucosal immune response. LAIV is approved for healthy 2- to 49-year old individuals. However, due to its replicative nature and higher rate of adverse events at-risk populations are excluded from the benefits of this vaccine. Using targeted mutagenesis, we modified the nonstructural protein 1 of the currently licensed LAIV in order to impair its ability to bind the host cellular protein CPSF30 and thus its ability to inhibit host mRNA poly-adenylation. We characterized our optimized LAIV (optiLAIV) in three different mouse models mimicking healthy and high-risk patients. Using a neonatal mouse model, we show faster clearance of our optimized vaccine compared to the licensed LAIV. Despite lower replication, optiLAIV equally protected mice against homosubtypic and heterosubtypic influenza strain challenges. We confirmed the safer profile of optiLAIV in Stat1^{-/-} mice (highly susceptible to viral infections) by showing no signs of morbidity compared to a 50% mortality rate observed following LAIV inoculation. Using a human nasal 3D tissue model, we showed an increased induction of ER stress-related genes following immunization with optiLAIV. Induction of ER stress was previously shown to improve antigen-specific immune responses and is proposed as the mechanism of action of the licensed adjuvant AS03. This study characterizes a safer LAIV candidate in two mouse models mimicking infants and severely immunocompromised patients and proposes a simple attenuation strategy that could broaden LAIV application and reduce influenza burden in high-risk populations.

IMPORTANCE Live attenuated influenza vaccine (LAIV) is a needle-free, mucosal vaccine approved for healthy 2- to 49-year old individuals. Its replicative nature and higher rate of adverse events excludes at-risk populations. We propose a strategy to improve LAIV safety and explore the possibility to expand its applications in children under 2-year old and immunocompromised patients. Using a neonatal mouse model, we show faster clearance of our optimized vaccine (optiLAIV) compared to the licensed LAIV. Despite lower replication, optiLAIV equally protected mice against influenza virus challenges. We confirmed the safer profile of optiLAIV in Stat1^{-/-} mice (highly susceptible to viral infections) by showing no signs of morbidity compared to a 50% mortality rate from LAIV. OptiLAIV could expand the applications of the current LAIV and help mitigate the burden of IAV in susceptible populations.

KEYWORDS influenza, high-risk patient, live attenuated vaccine, optimization, vaccine

Influenza A viruses (IAV) are the etiological agents of one of the most significant respiratory tract infections, accounting for approximately 2% of all annual respiratory deaths (1). Hospitalizations and deaths occur mainly among high-risk groups, which include children, elderly, pregnant women and immunocompromised patients (2–4). One of the most

Editor Mark T. Heise, University of North Carolina at Chapel Hill

Copyright © 2022 Bonifacio et al. This is an open-access article distributed under the terms of the [Creative Commons Attribution 4.0 International license](https://creativecommons.org/licenses/by/4.0/).

Address correspondence to Beryl Mazel-Sanchez, Beryl.Mazel-Sanchez@unige.ch. The authors declare no conflict of interest.

Received 6 June 2022

Accepted 5 September 2022

effective ways to prevent influenza illnesses is vaccination. Three types of vaccines are available against IAV: recombinant influenza vaccines (RIV) and split-virus inactivated influenza vaccine (IIV), both injected intramuscularly, and a live-attenuated influenza vaccine (LAIV), in the form of a nasal spray. LAIV uses the genetic backbone of a temperature sensitive (ts), cold-adapted (ca), attenuated (att) influenza strain derived from A/Ann Arbor/6/1960. These features restrict vaccine virus replication to the upper respiratory tract at 33°C, thus preventing disease onset (5, 6). LAIV mimics a natural infection, which brings the advantage of triggering mucosal (7), cellular and cross-protective (8, 9) immune responses. Hence, LAIV vaccine effectiveness (VE) ranges from 40 to 69%, which is equivalent to the VE observed for IIVs (10–14). The nature of this vaccine, however, excludes key-populations from LAIV recommendation guidelines. The major concern being higher rates of fever, rhinorrhea and wheezing observed following LAIV administration in children younger than 2 years old. Uncontrolled replication of the vaccine virus and reversion to virulence in immunocompromised patients has been reported for other attenuated vaccines (15–18). Therefore, different strategies have been explored to improve the safety of the LAIV with a particular focus on the modulation of IAV nonstructural protein 1 (NS1) (19–21).

NS1 is a virulence factor that modulates the cellular antiviral response (22). In part this was attributed to its interference with host mRNA maturation by interacting with the 30 kDa subunit of the cleavage and polyadenylation specificity factor (CPSF30). CPSF30 is a key factor in the polyadenylation complex. In its absence, cellular pre-mRNAs are not polyadenylated and thus rapidly degraded leading to a reduced host cell protein production. The interaction between NS1 and CPSF30 is well described in the literature (23) with a crystal structure showing the amino acids responsible for it (24). While positions 103 and 106 are important to stabilize the interaction, positions 108, 125 and 189 were shown to antagonize the innate immune response by reducing antiviral genes expression (25, 26). We recently demonstrated that during IAV infection, NS1 binding to CPSF30 is also essential to limit the unfolded protein response (UPR) induced by excessive neuraminidase production in the endoplasmic reticulum (ER) (27). UPR is an intrinsic mechanism cells use to adjust the folding capacity of the ER in times of elevated glycoprotein production. Viruses often exploit the UPR to enhance their replication (28, 29). Recent findings describe a cross talk between UPR and innate immune responses with implications on viral clearance and induction of an antiviral state (30, 31). Moreover, UPR contributes to the adjuvant effect of AS03, a licensed adjuvant present in the formulation of the inactivated influenza vaccine Prepandrix (32).

In this study, we applied a targeted approach to mutate the NS1 protein of the LAIV backbone rendering it unable to bind the host factor CPSF30. The goal is to improve the safety profile of the existing LAIV and present a suitable vaccine candidate for a broader target population. We confirm that our approach would not reduce vaccine manufacture efficiency or production using standard models. We demonstrate a safer replication profile of our optimized vaccine (optiLAIV) in three relevant *in vivo* models representative of adult, infant and highly susceptible populations. OptiLAIV provided similar protection compared to the current LAIV. As a mechanism of action, we propose a self-adjuvanted effect through activation of the UPR, independent of the cellular interferon response.

RESULTS

Limiting NS1-CPSF30 binding ability does not impact vaccine virus growth. We generated a LAIV parental strain encoding the genetic backbone (segments 1, 2, 3, 5, 7 and 8) of the cold-adapted influenza A/Ann Arbor/6/1960 (H2N2) and segments 4 and 6 (hemagglutinin and neuraminidase) from A/Puerto Rico/8/1934 (H1N1) as described previously (33). We refer to this 6 + 2 virus as LAIV. In a targeted approach, we abolished exclusively the ability of NS1 to interact with the cellular host factor CPSF30. We used targeted mutagenesis to introduce the following amino acid changes in the LAIV backbone: F103S, M106I, K124E, D144R and D189G. We then rescued the mutant virus by reverse genetics and refer to this vaccine candidate as optiLAIV.

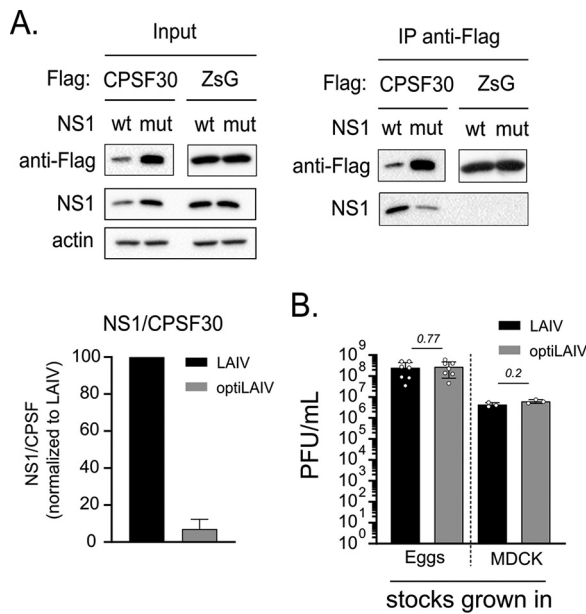


FIG 1 OptiLAIV NS1 binds to CPSF30 without compromising vaccine virus growth in eggs or MDCK cells. (A) 293T cells were transfected with pCAGGS.Flag-CPSF30 or pCAGGS.Flag-ZsGreen for 24 h prior to infection with either LAIV or optiLAIV at a multiplicity of infection (MOI) of 5. Cells were incubated for 16 h at 33°C and then lysed. Anti-Flag M2 affinity beads were used to immunoprecipitate (IP) the flag-tagged protein and its interactors. Precipitates were separated by SDS-PAGE and detected by Western blotting (WB) using the anti-flag antibody and the anti-NS1 antibody. The amount of NS1 protein that was bound to Flag-CPSF30 was quantified via a densitometric analysis ($n = 2$). (B) 10-day-old embryonated chicken eggs were infected with 100 PFU, and MDCK B cells were infected at a MOI of 0.1. After 46 h at 33°C, allantoic fluid and supernatant were collected. Viral titers were determined via plaque assay in MDCK cells at 33°C. Graphs represent the mean \pm standard deviation (SD) of $n = 3$ to 7 repeats. Statistical significance was determined using a Mann-Whitney test.

To confirm that the five amino acids mutations introduced abrogate NS1-CPSF30 binding in context of infection, we overexpressed a flag-tagged CPSF30 protein in HEK 293T cells and superinfected those cells with either vaccine virus. Following immunoprecipitation of CPSF30, we successfully retrieved LAIV NS1. Compared to LAIV, optiLAIV NS1 coprecipitation was reduced by 80%, indicating reduced CPSF30-NS1 interaction (Fig. 1A). Enhanced attenuation of LAIV could result in deleterious replication defects, with unwanted consequences for large scale vaccine production (19, 21). We thus compared the replication of LAIV and optiLAIV in embryonated chicken eggs and MDCK cells, two relevant vaccine production models. Titers of LAIV and optiLAIV were similar in both production systems (Fig. 1B).

These results indicate that the targeted mutagenesis used to produce optiLAIV significantly impaired its NS1 protein ability to bind CPSF30 without compromising its potential for large-scale vaccine production.

OptiLAIV is attenuated without compromising protection in adult mice. In order to demonstrate that our targeted NS1 mutagenesis strategy results in an attenuated phenotype *in vivo*, adult mice were vaccinated with a weight-adjusted dose of LAIV or optiLAIV according to recommendations for human adults (34) (Fig. 2A and Fig. S1). Then we monitored body weight as a general indication of well-being and viral titers in the upper and lower respiratory tract as an indication of viral fitness. In comparison to mock-vaccinated animals, neither vaccine virus caused alterations in body weight of adult mice (Fig. 2B), reflecting the already attenuated phenotype of the parental vaccine virus in immunocompetent hosts. However, we observed a clear difference in viral replication both in the upper and lower respiratory tract. Indeed, at 4 days postvaccination, we detected LAIV in both upper and lower respiratory tracts of vaccinated mice, while optiLAIV was absent in all snout samples and was present in only 2 out of 7 (28%) lung samples at viral loads close to the limit of detection (Fig. 2C).

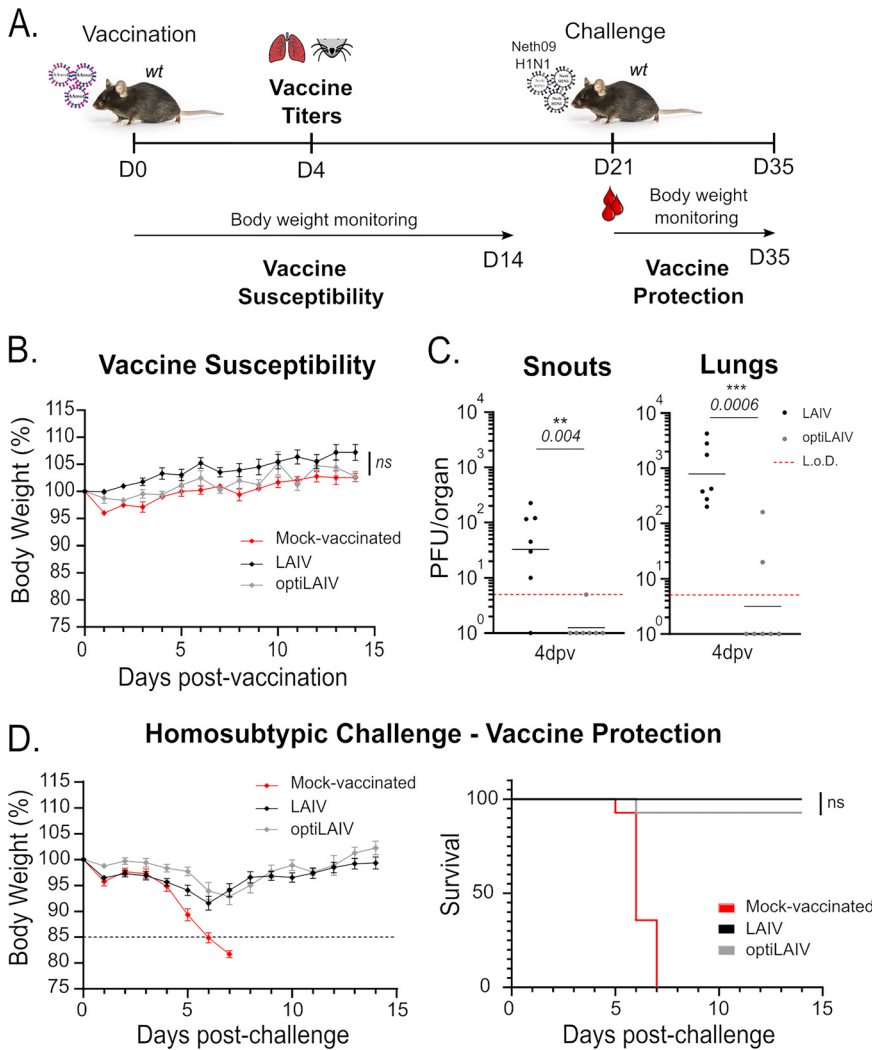


FIG 2 OptiLAIV is attenuated and protects adult mice against a homosubtypic/heterologous challenge. (A) Scheme of mouse immunization and challenge. (B) Female 8-week-old mice were vaccinated intranasally under anesthesia with 10^4 PFU LAIV or optiLAIV in $25 \mu\text{L}$ PBS and body weight was monitored for 14 days postvaccination. (C) Female 8-week-old mice were vaccinated intranasally under anesthesia with 10^5 PFU LAIV or optiLAIV in $25 \mu\text{L}$ and at 4 days postvaccination snouts (left panel) and lungs (right panel) were collected and vaccine viral titers were determined by plaque assay ($n = 7$ per group). (D) Female 8-week-old mice vaccinated with 10^4 PFU of LAIV or optiLAIV were challenged at day 21 postvaccination with 20 PFU ($10 \times \text{LD}_{50}$) of mouse adapted A/Netherlands/602/2009 (H1N1) in $20 \mu\text{L}$ PBS under light anesthesia ($n = 14$ per group). Body weight (left panel) and survival (right panel) were monitored for 14 days postchallenge. The statistical significances between LAIV group and optiLAIV group were determined using Mann-Whitney test in panel B; two-way ANOVA with the Geisser-Greenhouse correction and *post hoc* Dunn's multiple-comparison test in panels B and D and Mantel-Cox test for survival curve. *P*-values are indicated in the figure. L.o.D. = limit of detection (5 PFU). Graphs are representative of 3 independent experiments and indicate geometric mean for panel C or mean \pm SEM for panels B and D. Symbols represent data from individual mice for panels a and b. In D, black dotted line represents 15% body weight loss cutoff.

The mutation introduced in the NS1 of the optiLAIV renders it less efficient in limiting host transcription (35, 36), which might result in undesired detrimental inflammatory responses. A hallmark of lung inflammation is the infiltration of immune cells into the lung tissue. Thus, we characterized the immuno-population of the respiratory tract of vaccinated mice at 4 days postvaccination. When comparing lungs and snouts of mice administered with PBS, we observed that, optiLAIV does not significantly change the total of cell infiltrates or population composition compared to the LAIV (Fig. S2). When considering the optiLAIV as an alternative candidate for LAIV, the absence of

viral load and comparable cellular infiltration in the respiratory tract argue in favor of a generally increased safety profile.

Since, previous studies associated lower replication fitness of different LAIV strains to lower immunogenicity and decreased vaccine effectiveness (37, 38), we evaluated if the protection elicited by optiLAIV was compromised compared to LAIV. 8 weeks-old mice were vaccinated intranasally with increasing doses of LAIV or optiLAIV. At 21 days postvaccination, the animals were challenged with influenza A/Netherlands/602/2009 (H1N1) strain, simulating a severely drifted virus based on HA sequences (homosubtypic/heterologous challenge). We monitored body weight (Fig. 2D – left panel) and survival (Fig. 2D – right panel) for 14 days after challenge. All animals were protected after a weight-adjusted dose for either vaccine (Fig. 2D). While we found a trend toward a longer recovery of the initial body weight (Fig. S1A) and a reduced protection with lower vaccine doses of optiLAIV (Fig. S1B), there was overall no statistically significant difference observed for the protective dose 50 (PD₅₀) of both vaccines (Fig. S1C). In conclusion, compared to LAIV, our vaccine candidate presented impaired replication in the respiratory tract of adult mice, while still conferring similar protection against infection with a virus harboring a severely drifted HA.

OptiLAIV is attenuated without compromising protection in neonatal mice. An important target population outside the recommendation guidelines for LAIV administration are children under 2 years of age (39, 40). Indeed, clinical trials have reported higher incidence of adverse events, such as wheezing and coughing following vaccination (41, 42). To demonstrate an improved safety profile of optiLAIV in an animal model closer to this target population, we vaccinated neonatal mice (7 days old) with an adult dose of LAIV and optiLAIV. We then monitored body weight daily for 14 days and vaccine virus replication in the respiratory tract every other day up to 9 days after vaccination (Fig. 3A). Neither vaccine caused any significant alteration in body weight gain of neonatal mice (Fig. 3B), once again reflecting the already attenuated phenotype of LAIV. In line with the results obtained in adult mice, at 2 days postvaccination we observed lower viral titers in optiLAIV-vaccinated animals compared to LAIV in the upper respiratory tract (Fig. 3C). While at day 4 viral loads of both vaccines were reduced compared to day 2, we observed that at day 8 postvaccination, LAIV was still present in 7 out of 13 (53%) vaccinated animals. This was not the case for the optiLAIV group, where only 2 out of 12 (16%) vaccinated animals had detectable virus. After 9 days, both vaccine viruses were cleared from the upper respiratory tract. In lungs, we did not consistently detect virus after infection with either vaccine (data not shown), which is most likely a consequence of vaccine administration in the absence of anesthesia. We conclude from these data that optiLAIV reaches lower peak titers and is cleared faster from the airways of neonatal mice compared to LAIV.

The immune system of young children is in an immature state with compromised immune responses to vaccines (43). Thus, we asked if LAIV administered in our neonatal mouse model could elicit protection and if the attenuated phenotype of optiLAIV would impair this effect. To answer this question, we evaluated protection after a heterosubtypic challenge with A/Vietnam/2004 (H5N1) (Fig. 3D) or a homosubtypic/heterologous challenge with influenza A/Netherlands/09 (H1N1) (Fig. 3E). In both challenge models, significant protection was observed for both vaccines in a similar fashion (Fig. 3D and E – right panels). Unexpectedly, after heterosubtypic challenge, mock-vaccinated mice showed 50% survival after challenge with 20 adult LD₅₀, nevertheless significant protection was still observed in vaccinated animals even with lower doses of both vaccines (Fig. S3A, B). After the homosubtypic/heterologous challenge, only the adult-dose of optiLAIV was protective compared to LAIV (Fig. 3E and Fig. S3C, D). However, there was no overall statistically significant difference observed for the protective dose 50 (PD₅₀) of each vaccine (Fig. S3E). In conclusion, similar to LAIV, our vaccine candidate optiLAIV protects neonatal mice against both a homosubtypic and a heterosubtypic challenge.

Higher adverse reactions observed in young children might be explained by an

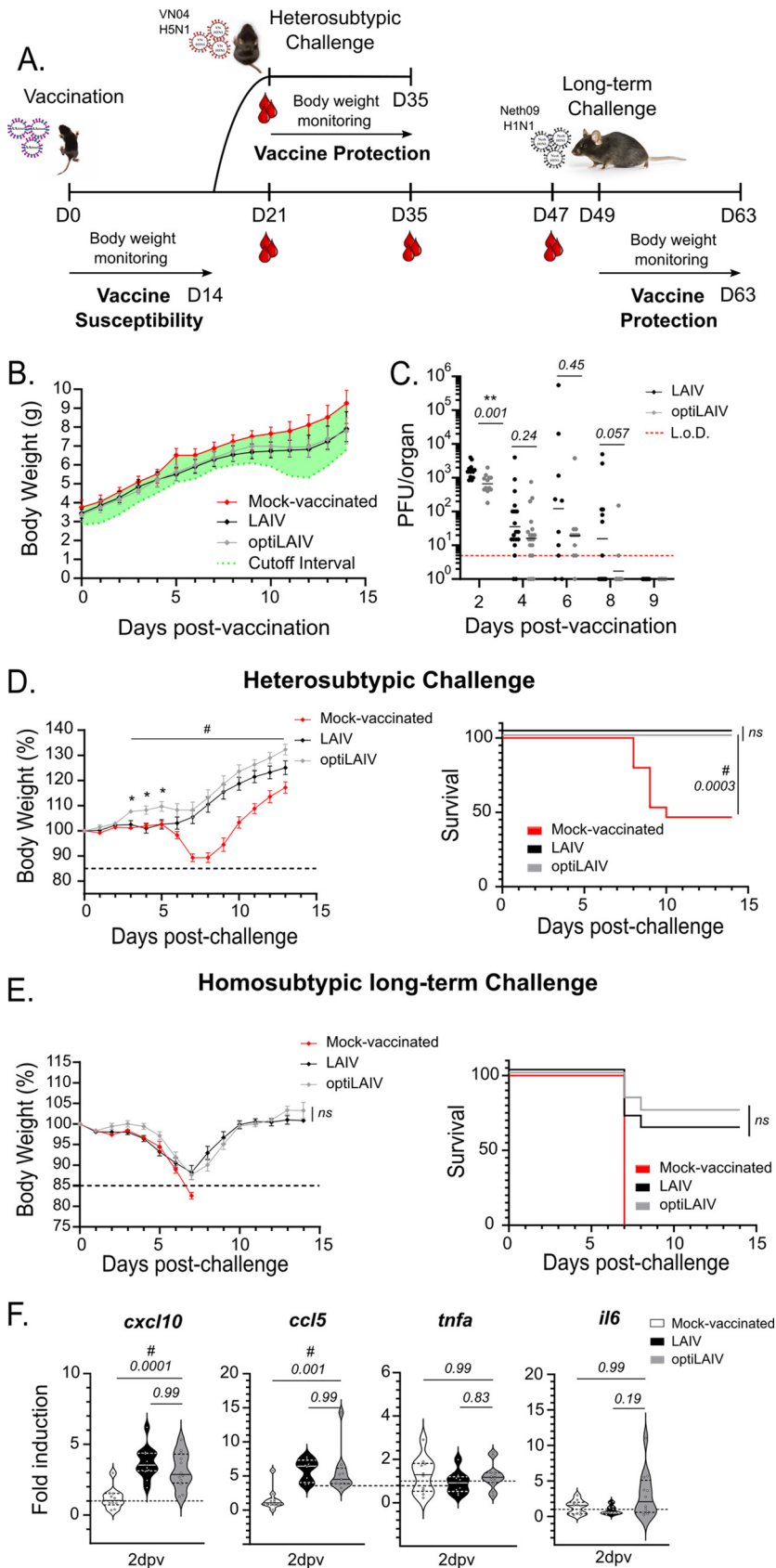


FIG 3 OptiLAIV is attenuated and protects neonatal mice against homosubtypic/heterologous challenge and heterosubtypic challenge. (A) Scheme of mouse immunization and challenge. (B) Seven-day-old mice (Continued on next page)

exacerbated host response to a replicating virus (41, 44, 45). By unblocking host transcription and protein translation, optiLAIV could induce a damaging host response in young patients and worsen potential adverse reactions in this target population. Hence, we assessed the expression of two inflammatory genes implicated in a deleterious response in neonatal mice respiratory tract at 2 days postvaccination, when vaccine titers peaked (Fig. 3C). No significant expression of *Tnfa* and *Il6* was observed compared to mock-vaccinated animals (Fig. 3F). Furthermore, both vaccines induced expression of antiviral cytokines *Cxcl10* and *Ccl5* at similar levels. Overall, our data do not support a differential induction of innate immune or inflammatory genes by optiLAIV that could exacerbate any unwanted reactions compared to LAIV.

OptiLAIV is attenuated and safer in Stat1^{-/-} adult mice. Due to its replicative nature, LAIV is not recommended for immunocompromised patients (39, 40) who might struggle to clear the vaccine virus. Further attenuation of this vaccine could be beneficial to this target population. To simulate a patient highly susceptible to viral infections, we used Stat1-deficient (Stat1^{-/-}) adult mice, which are largely devoid of type I, II and III interferon responses and consequently lack key defense mechanisms to combat pathogen challenges. Stat1^{-/-} adult mice were vaccinated with an adult dose of LAIV or optiLAIV and we monitored body weight after vaccination as a general indication of well-being (Fig. 4A). OptiLAIV vaccinated mice showed no weight loss and no mortality while vaccination with LAIV resulted in weight loss 5 days postvaccination and 50% mortality (Fig. 4B).

This pronounced difference led us to explore the dose-range equivalence between LAIV and optiLAIV for the induction of adverse effects (Fig. S5A). We found that a LAIV dose of 10³ PFU caused equivalent body weight loss as a 10⁵ PFU dose of optiLAIV (Fig. S5B). Notably, one out of five animals vaccinated with 10³ PFU of LAIV lost more than 15% body weight and had to be sacrificed, while all optiLAIV vaccinated mice stayed above this threshold. In order to evaluate if the two vaccines might protect Stat1^{-/-} mice, the remaining animals were challenged with a lethal dose of A/Netherlands/602/2009 (H1N1) (Fig. S5C). We observed that all optiLAIV vaccinated mice survived with an overall mild weight loss, while LAIV vaccinated mice had a more pronounced weight loss, with one animal crossing the experimental threshold. Considering both vaccination and challenge, our results point toward a safety window of 100-fold between LAIV and optiLAIV doses.

In order to understand the differences in morbidity and mortality observed in Stat1^{-/-} mice, we quantified vaccine virus replication in both upper and lower respiratory tract. Compared to *wild-type* animals, Stat1^{-/-} animals have approximately 100-fold higher viral titers in both upper and lower respiratory tracts at 4 days postvaccination.

FIG 3 Legend (Continued)

were vaccinated intranasally with 10⁴ PFU LAIV or optiLAIV in 5 μ L PBS and body weight was monitored for 14 days postvaccination. Cutoff was defined as twice the difference between the average weight of the nonvaccinated group and the lightest mouse of that group, calculated daily. (C) Seven-day-old mice were vaccinated intranasally with 10⁵ PFU of LAIV or optiLAIV in 5 μ L PBS. At 2, 4, 6, 8 and 9 days postvaccination vaccine viral titers in the snouts were determined by plaque assay ($n = 11$ to 19 per group). (D) Seven-day-old mice vaccinated with 10⁴ PFU of LAIV or optiLAIV were challenged at day 21 postvaccination with 10³ PFU (20 \times LD₅₀) of A/Vietnam/1203/2004 (H5N1) in 20 μ L PBS under anesthesia ($n = 11$ per group). Body weight (left panel) and survival (right panel) were monitored for 14 days postchallenge. (E) Seven-day-old mice vaccinated with 10⁴ PFU of LAIV or optiLAIV were challenged at day 49 postvaccination with 20 PFU (10 \times LD₅₀) of A/Netherlands/602/2009 (H1N1) in 20 μ L PBS under anesthesia ($n = 11$ to 17 per group). Body weight (left panel) and survival (right panel) were monitored for 14 days postchallenge. (F) Seven-day-old mice ($n = 11$ to 12) were vaccinated intranasally with 10⁵ PFU of LAIV or optiLAIV in 5 μ L PBS. At 2 days postvaccination snouts were harvested and RT-qPCR was performed from isolated RNA. The statistical significances between LAIV group and optiLAIV group were determined using multiple Mann-Whitney tests in panel C; two-way ANOVA with the Geisser-Greenhouse correction and *post hoc* Dunn's multiple-comparison test in panels B, D and E and Mantel-Cox test for survival curves; Kruskal-Wallis test and *post hoc* Dunn's multiple-comparison test in panel F. *P-values* are indicated in the figure. *, comparison between LAIV and optiLAIV; #, comparison between mock and optiLAIV. L.o.D. = limit of detection (5 PFU). Graphs are representative of 2 independent experiments and indicate geometric mean for panel C; mean \pm SEM for panels B, D and E; mean \pm SD for panel F. Symbols represent data from individual mice for panel C. In D and E, black dotted line represents 15% body weight loss cutoff.

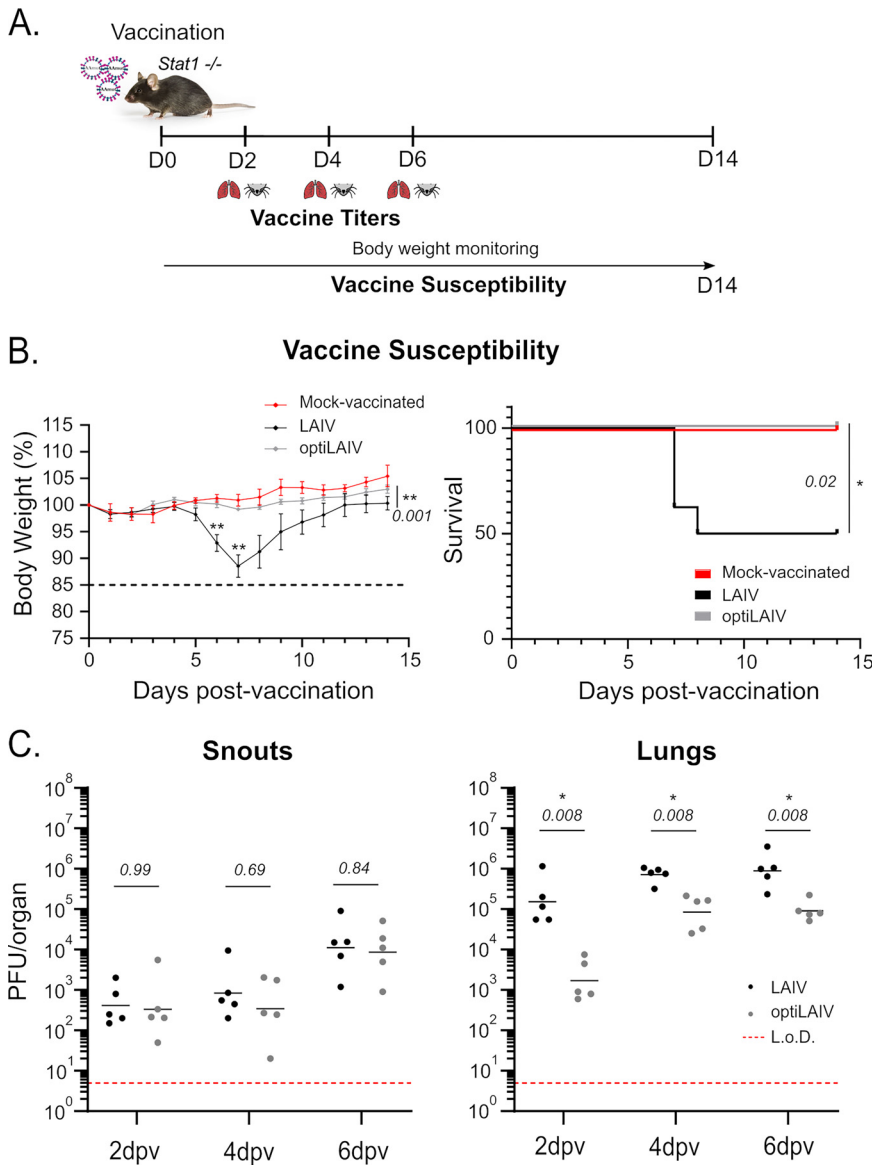


FIG 4 OptiLAIV is attenuated and safe in Stat1^{-/-} mice. (A) Scheme of mouse immunization. (B) 8-week-old Stat1^{-/-} mice were vaccinated intranasally under anesthesia with 10⁴ PFU LAIV or optiLAIV in 25 μ L and body weight (left panel) and survival (right panel) were monitored for 14 days postvaccination ($n = 4$ mock-vaccinated group; $n = 8$ per vaccinated group). (C) 8-week-old Stat1^{-/-} mice were vaccinated intranasally under anesthesia with 10⁵ PFU LAIV or optiLAIV in 25 μ L PBS. At 2, 4 and 6 days postvaccination snouts (left panel) and lungs (right panel) were collected and viral titers were determined by plaque assay ($n = 5$ per group). The statistical significances between LAIV group and optiLAIV group were determined using two-way ANOVA with the Geisser-Greenhouse correction and *post hoc* Dunn's multiple-comparison test in panel B and Mantel-Cox test for survival curve; multiple Mann-Whitney tests in panel C; *P*-values are indicated in the figure. *, comparison between LAIV and optiLAIV. L.o.D. = limit of detection (5 PFU/mL). Graphs are representative of 2 independent experiments and indicate mean \pm SEM for panel B and geometric mean for panel C. Symbols represent data from individual mice for panel B. In C, black dotted line represents 15% body weight loss cutoff.

Importantly, optiLAIV titers remained lower than LAIV titers in the lower respiratory tract, confirming its enhanced attenuated phenotype (Fig. 4C).

In conclusion, in the absence of a functional type I, II and III interferon response, optiLAIV vaccine virus safety profile was improved compared to LAIV.

OptiLAIV induces the unfolded protein response *in vitro*. The ability of NS1 to bind CPSF30 was thought to only antagonize the innate antiviral host response (46, 47). However, mutations of the CPSF30-binding domain of NS1 were recently described to modulate ER stress activation and the UPR through the XBP1 pathway (27). We introduced

the same mutations in the NS1 of optiLAIV and hypothesized that the establishment of a host response, mediated by UPR, could explain the attenuated phenotype of optiLAIV. Indeed, the reduced viral replication of optiLAIV was STAT1-independent, pointing to a mechanism independent of the canonical interferon-mediated antiviral response.

Proving an involvement of ER stress *in vivo* is technically challenging. While knock-out of the main UPR component, XBP1, is lethal during embryonic development, the fast turnover of this response largely narrows the window of detectable signal *in vivo*. In addition, there is high background signal from unspliced XBP1 mRNA present in uninfected cells. This technical hurdle was confirmed by analysis of two UPR-induced genes at vaccine virus peaks in neonatal mice respiratory tract (Fig. S4A). Thus, we turned to *in vitro* models to address our hypothesis.

First, we asked if the lower CPSF30 binding ability of optiLAIV NS1 allowed the establishment of the UPR upon infection. We infected A549 human lung epithelial cells and evaluated the splicing of XBP1 mRNA by semiquantitative RT-PCR and the expression of the spliced form of XBP1 protein (sXBP1) by Western blot. sXBP1 mRNA levels in optiLAIV-infected A549 increased compared to LAIV (Fig. 5A). Accordingly, we observed that sXBP1 protein expression increased in a time-dependent manner after infection, an increase that was more pronounced in cells infected with optiLAIV (Fig. 5B). We also analyzed by RT-qPCR the induction of genes downstream of the transcription factor sXBP1, namely, *DDIT3* and *DNAJB9*. Compared to LAIV, expression of these two genes increased in cells infected with optiLAIV (Fig. 5C, upper panel), in line with previous published results (27). Of note, induction of UPR genes by optiLAIV was independent of Stat1 signaling (Fig. 5C, lower panel). This increase was also observed when we used a murine lung epithelial cell line (Fig. S4B) indicating that this phenomenon is species independent and could occur in our murine *in vivo* models. Additionally, viral replication was similar in all three cell models ruling out possible differences in replication kinetic as an explanation for the phenotype observed (Fig. 5D and Fig. S4C).

Next, we used a relevant 3D cell model of stratified primary human nasal epithelial cells grown in air-liquid interface. In line with the results obtained with immortalized epithelial cell lines, we observed an increased induction of UPR-induced genes in optiLAIV infected tissues compared to LAIV, and no differences in the induction of antiviral response genes or inflammatory cytokine genes (Fig. 5E). These cells would be the first in contact with LAIV virus in case of vaccination of human patients and the upregulation of *DNAJB9* and *DDIT3* in this model, corroborates our hypothesis of UPR as a potential optiLAIV attenuation mechanism.

DISCUSSION

From a medical and immunological point of view the LAIV platform provides advantages over the inactivated vaccine, including easier, needle-free application, a broader immune response against IAV and a reduction of viral transmission due to mucosal immunity as demonstrated in animal models (48, 49). Regrettably, safety concerns exclude highly susceptible populations to IAV from benefiting from this vaccine platform.

In the present work, we modify LAIV protein NS1 in a targeted manner and characterize optiLAIV, a vaccine candidate with an increased attenuated profile without affecting its efficacy. Other groups described that an IAV with full NS1 deletion used as a single intranasal dose was well tolerated, safe, and able to induce neutralizing antibodies in three different clinical trials (20, 50, 51). Similarly, IAV vaccines expressing truncated NS1 were safe and protected both adult ferrets and aged mice (52, 53). These approaches, however, rely on blunt removal of the effector domain of NS1 affecting multiple host-pathogen interaction pathways. Additionally, efficacy and safety were not assessed against the current standard of care (LAIV). Our strategy to attenuate LAIV exploits a more targeted approach by performing five single amino acid substitutions in the currently licensed LAIV backbone and we characterized its safety profile in two relevant animal models that are representative of high-risk patient groups. Moreover, we compare efficacy and safety to the parental LAIV. Interestingly, a similar targeted approach mutated two key amino acids for CPSF30 binding (F103S/M106I)

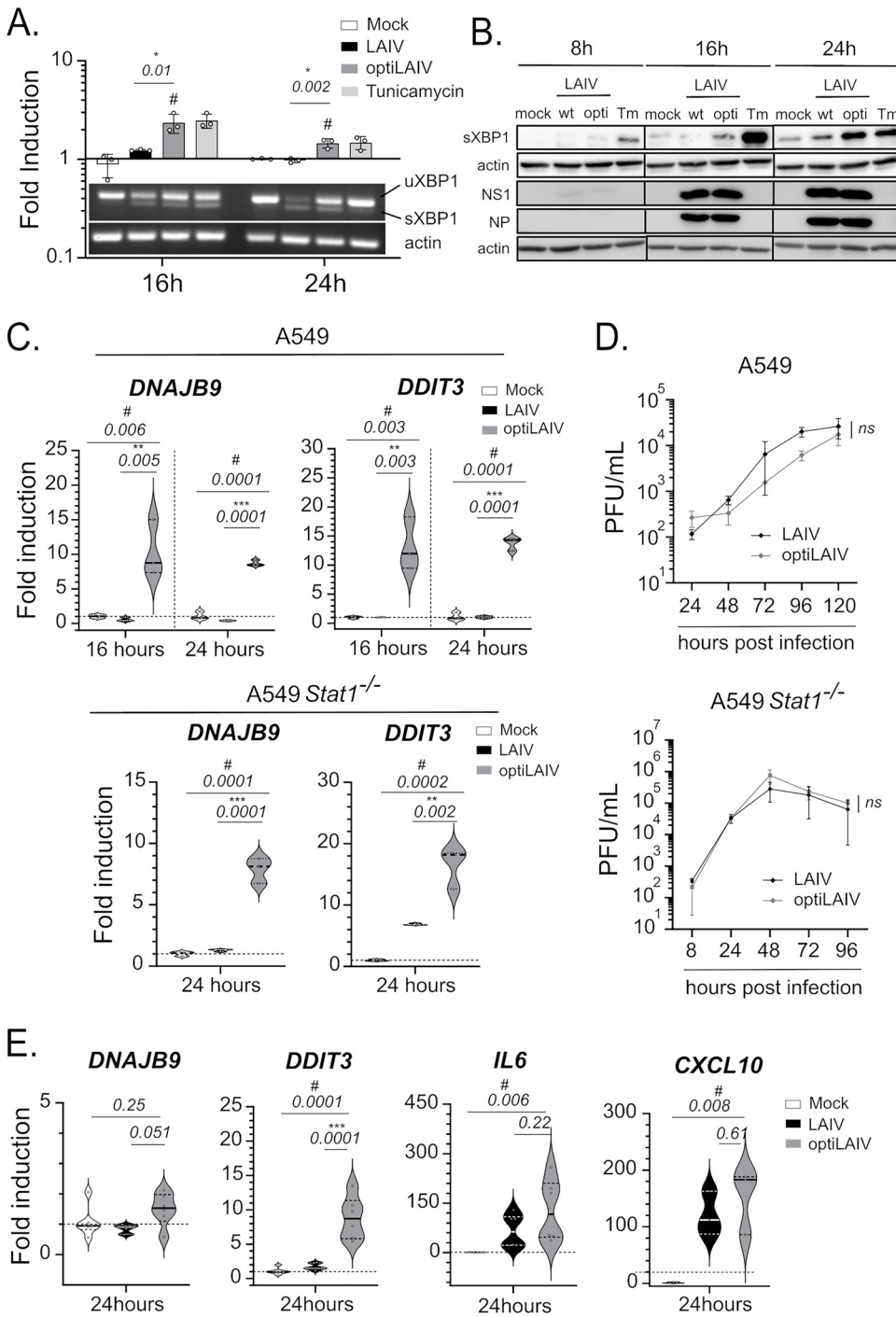


FIG 5 OptiLAIV NS1 allows unfolded protein response activation in human cell models. (A–B) A549 cells were infected at an MOI of 5 with LAIV or optiLAIV or treated with tunicamycin at 5 μ g/mL. At 16 h and 24 h postinfection RT-PCR was performed from isolated RNA for the spliced form of XBP1 mRNA (A). In parallel at 8 h, 16 h and 24 h postinfection, lysates were analyzed by Western blot for expression of sXBP1, actin, NP and NS1 proteins (B). (C) A549wt cells (upper panel) or A549Stat1^{-/-} cells (lower panel) were infected at an MOI of 5 with LAIV or optiLAIV and RT-qPCR for UPR-induced genes DNAJB9 and DDIT3 was performed in RNA lysates at 16 h and 24 h postinfection. (D) A549wt cells (upper panel) or A549Stat1^{-/-} cells (lower panel) were infected at an MOI of 0.01 with either LAIV or optiLAIV. Supernatants were collected at indicated time postinfection and viral titers determined by plaque assay. (E) Primary human nasal epithelial cells (Mucilair) were infected at an MOI of 5 with LAIV or optiLAIV. Cells were lysed at 24 h postinfection and RT-qPCR for each respective gene was performed. The statistical significances between LAIV group and optiLAIV group were determined using one-way ANOVA with *post hoc* Tukey’s multiple-comparison test for panels A, C and E; two-way ANOVA with the Geisser-Greenhouse correction and *post hoc* Dunn’s multiple-comparison test for panel D. *, comparison between LAIV and optiLAIV; #: comparison between mock and optiLAIV; ns = nonsignificant. Graphs are representative of 3 independent experiments and indicate mean \pm SD.

in the LAIV A/Ann Arbor/6/60 backbone; however, this strategy failed to revert the shutoff of the host response and did not increase LAIV safety in adult mice (54). Our data suggest that the additional three mutations in NS1 (K108R/D125E/D189G) are responsible for the accelerated clearance of optiLAIV from adult and neonatal mice.

Abrogation of NS1 binding to CPSF30 is largely associated with an increased expression of IFN-mediated genes (23–25, 35), however, optiLAIV's attenuated phenotype was Stat1-independent, pointing to an alternative mechanism of attenuation. A thorough RNA-seq analysis performed in cells infected with weak NS1-CPSF30 binding influenza strains showed upregulation of UPR-induced genes (55). This observation led us to postulate that UPR activation during optiLAIV replication induces a self-adjuvanting mechanism contributing to its faster clearance without affecting its protective efficacy. In accordance, UPR activation was described in mice as the mechanism of action of AS03, a licensed adjuvant used in IIV formulation (32). Furthermore, upregulation of UPR-induced XBP1 after IIV administration in human patients was suggested as a molecular marker for seroconversion against the three vaccine strains present in the vaccine's formulation (56).

One limitation of the present study is the lack of *in vivo* data linking UPR to the attenuated profile of optiLAIV. The transient nature of this pathway, together with the background noise from uninfected cells makes detection of ER stress *in vivo* challenging. On top, mice deficient for central elements of the ER stress sensing pathway are unviable (57). Still, our data encourages future studies to explore how UPR impacts the immune response to live replicating viral vaccines (58).

LAIV is approved for 2 to 49 years old immunocompetent patients. Our data provides the first attempt to characterize and improve it in a neonatal mouse model. We provide unprecedented evidence of LAIV cross-protection in a neonatal mouse model. Furthermore, the observed optiLAIV attenuation in this model could be used in combination with strategies to develop a universal vaccine against influenza. For example, matching internal influenza segments to circulating strains (59) and inducing immunity against conserved epitopes in the stem region of HA (60) could be strategies incorporated into the optiLAIV backbone. Generating an immunogenic yet safer vaccine could broaden LAIV application to high-risk patients. This is particularly interesting in children under 2 years old. In France alone, more than 28'000 children below the age of 2 were admitted to a hospital with an IAV infection for the period of 2011 to 2020 (61). While IIV is available for this target population, a needle-free applicable LAIV, which does not cause severe side effects, could increase the willingness of parents to vaccinate their children. Additionally, mathematical models predict better efficacy for live attenuated vaccines if vaccinees are children without previous exposure to circulating strains (62), which encourages LAIV implementation in this population in which protection from maternal antibodies start to wane (63, 64). This is specifically interesting since the first exposure to IAV is believed to imprint later immune responses (65). This bias could potentially be overcome by an early targeted exposure to H1 and H3 antigens in context of LAIV administration.

We also characterize for the first time LAIV in a severely immunocompromised Stat1-deficient mouse model. While Stat1-deficient mice do not reproduce the full spectrum of phenotypes from a chemically induced immunosuppression, the absence of clinical signs after vaccination of optiLAIV in this model suggests that it could be safely used in target populations with milder immunosuppression such as organ transplant recipients or patients with other comorbidities. In fact, LAIV has already been shown safe without causing any adverse reactions in ferrets under a regimen of immunosuppressors (66). We hypothesize that the use of optiLAIV in immunocompromised patients would represent an additional safety measure to ensure the absence of side effects. Also, we showed in a preliminary proof-of-concept experiment that a higher dose of optiLAIV could be safely administered and achieved full protection. It would be of interest to further investigate the relation between optiLAIV vaccine dose and protection in clinically relevant animal models.

In summary, we propose here an optimized LAIV backbone, with an improved

TABLE 1 Antibodies and dyes for flow cytometry staining

Antibodies	Source	Clone	Cat. number
eBioscience Fixable Viability eFluor 780	Thermo Fischer	NA	65-0865-14
CD45 BUV395	BD biosciences	30-F11	564279
CD11b BV605	biolegend	M1/70	101237
CD11c Pcy7	Thermofischer	N418	25-0114-82
F4/80 PE e610	Thermofischer	BM8	61-4801-82
MHCII A700	Biolegend	M5/114.15.2	107622
Ly6G APC	Thermofischer	1A8-Ly6g	17-9668-82
Ly6C BV510	Biolegend	HK1.4	128033
CD68 BV421	Biolegend	FA-11	137017
NK1.1 PercPcy5.5	Thermofischer	PK136	45-5941-82
Siglec F PE	Thermofischer	1RNM44N	12-1702-82

safety profile in adult, neonatal and immunocompromised hosts, while still protecting against lethal infection. Deriving from an already licensed vaccine, optiLAIV possesses the scalability to be produced at similar titers as the current LAIV, without major challenges. It would be interesting to study in more detail the immune responses triggered by this vaccine and its safety in higher mammal models before proceeding to clinical studies. In addition, the mechanism of attenuation remains to be fully characterized, although our data suggest a potential role of the UPR. Our approach opens the possibility to expand the applications of the current LAIV with the possibility of targeting high-risk populations in which IAV burden is still a serious problem.

MATERIALS AND METHODS

Materials availability. All unique/stable reagents generated in this study are available from the Lead Contact with a completed Materials Transfer Agreement.

Reagents. Antibodies for immunoblotting include: mouse anti-actin HRP (Abcam number ab49900), mouse anti-Flag HRP (Sigma number A8592), rabbit anti-XBP1 (ThermoFisher number PA5-27650), rabbit anti-influenza NP (ThermoFisher number PA5-32242), rabbit anti-influenza NS1 (1-93) (kind gift from A. Garcia-Sastre) and goat anti-rabbit IgG HRP (Sigma-Aldrich number A8275).

Antibodies and dyes for flow cytometry staining are detailed in Table 1.

All oligonucleotides (Table 2) were purchased from Microsynth (France).

Plasmids. pCAGGS.Flag-CPSF30 and pCAGGS.Flag-ZsGreen. The plasmids of the LAIV strain A/AA/1960 ca (AA) were kindly provided by Peter Palese and Adolfo Garcia-Sastre (Icahn School of Medicine at Mount Sinai, New York, NY, USA). pDZ plasmids contain a bidirectional expression cassette for a given influenza A gene segment and have been described previously (67). The AA NS viral segment was

TABLE 2 Oligonucleotides

Application	Name	Forward (5' to 3')	Reverse (5' to 3')
Mutation of CPSF30 binding site in	flank	TCGCTCTTCTGGGAGCAAAGCAGGGTG	TCGCTCTTCTATTAGTAGAAACAAGGGTGTIT
IAV NS1	mut1	CAAGGGACTGGAGCATGCTAATCCCCAGACAGA AAGTGGC	GCCACTTCTGCTGGGGATTAGCATGCTCCAG TCCCTTG
	mut2	GACCAGGCAATCATGGAGAAGAACATCATATTG	CAATATGATGTTCTTCCATGATTGCCTGGTC
	mut3	GGACTTGAATGGAATGGTAACACAGTTCGAGTC	GACTCGAACTGTGTTACCATTCCATTCAAGTCC
PCR	hXBP1	TTACGAGAGAAAACATCATGGCC	GGGTCCAAGTTGTCCAGAATGC
	β actin	GGGTCTCAGAAAGGATTCTATG	GGTCTCAAACATGATCTGGG
qPCR	hCXCL10	GGAACCTCCAGTCTCAGACCA	AGACATCTCTTCTACCCTTC
	hIL29	GCCCCAAAAAGGAGTCCG	AGGTTCCCATCGGCCACATA
	hDDIT3	AGAACCAGGAAACGGAAACAGA	TCTCCTTCATGCGCTGCTTT
	hDNAJB9	TCTTAGGTGTGCCAAAATCGG	TGTCAGGGTGTACTTCATGG
	mcxcl10	TTCACCATGTGCCATGCC	GAACTGACGAGCTGAGCTAGG
	mddit3	GGAGTCTGTCTCAGATGAA	GCTCCTCTGTCAGCCAAGCTAG
	mdnajb9	CTCCACAGTCAGTTTTCTGCTT	GGCCTTTTTGATTGTGCTGC
	mcc15	TGCCCCAGTCAAGGAGTATTC	TCCTAGCTCATTCCAATAGTTGATG
	mtnfa-fwd	AGAAACACAAGATGCTGGGACAGT	CCTTTGCAGAACTCAGGAATGG
	mil6	TGAGATCTACTCGGCAAACCTAGTG	CTTCGTAGAGAACAACATAAGTCAGATACC

subcloned into a pDZ plasmid (68) to introduce the following mutations using site-directed mutagenesis: T333A, T334G (F103S), G344C (M106I), A349G, G350A (K108R), T401G (D125E) and A592G (D189G).

Cell lines. A549 and A549 STAT1^{-/-} (adenocarcinomic human alveolar basal epithelial cells, ATCC) were grown in DMEM/F12 (Dulbecco's Modified Eagle Medium: Nutrient Mixture F-12, Gibco) supplemented with 10% (vol/vol) heat-inactivated fetal bovine serum (Gibco) and 100 U/mL Pen/Strep. HEK 293T (human embryonic kidney, ATCC) and MDCK (Madin-Darby canine kidney, ATCC) cells were grown in DMEM (Dulbecco's Modified Eagle Medium, Gibco) supplemented with 10% (vol/vol) heat-inactivated fetal bovine serum (Gibco) and 100 U/mL Pen/Strep. LA4 (lung adenoma) cells were grown in DMEM/F12 (Dulbecco's Modified Eagle Medium: Nutrient Mixture F-12, Gibco) supplemented with 15% (vol/vol) heat-inactivated fetal bovine serum (Gibco) and 100 U/mL Pen/Strep. Human airway epithelia (MucilAir, Epithelix Sàrl, Switzerland) were maintained in Mucilair medium (Epithelix Sàrl, Switzerland) that was changed every 2 days. The total number of differentiated cells was estimated to be 200,000 cells per well. All cells were maintained at 37°C with 5% CO₂ and 90% humidity.

Animals. All animal procedures were in accordance with federal regulations of the Bundesamt für Lebensmittelsicherheit und Veterenärwesen (BLV) Switzerland (Tierschutzgesetz) and approved by an institutional review board and the cantonal authorities (license number GE/105/19 and GE96). C57BL/6J mice and C57BL/6J Stat1^{-/-} (7 to 8 weeks of age) were purchased from Charles River Laboratories (France) and housed under SPF/BSL2 conditions. All animals were housed for 7 days to adjust to housing conditions under a strict 12 h light/dark cycle and fed *ad libitum* before entering an experiment or the breeding process. Breeding cages were checked three times a day during labor period and time of birth was recorded for each dam. Litters born in the same day were divided into equal groups and left with the lactating parent until weaning at 21 days of age. After weaning, males and females were separated in groups of 4 to 5 animals/cage.

Viruses. A/Netherlands/602/09 (H1N1) (mouse adapted after two passages in mice) (Neth602) was kindly provided by Krammer (Icahn School of Medicine at Mount Sinai, New York, NY, USA). A/Viet Nam/1203/2004 HALo (low pathogenic version) (H5N1) (VN1203) was rescued by reverse genetic as described previously (27).

Recombinant LAIV virus was produced using the eight-plasmid rescue system (68). The A/AA/1960 ca PB2, PB1, PA, NP, M and NSwt (GenBank: [M23968.1](#)) or NSmut pDZ plasmids and PR8 HA and NA pDZ plasmids were used to rescue the vaccine virus LAIV and optiLAIV. Briefly, HEK293T (6-well plate format, 1 × 10⁶ cells/well) were cotransfected in suspension, using Lipofectamine 2000 and Opti-MEM medium with 500 ng of each plasmid and incubated at 37°C. At 24 h posttransfection, supernatants were collected and used to infect fresh monolayers of MDCK cells (6-well plate format, 1 × 10⁶ cells/well) and incubated at 33°C with 5% CO₂. After 48 h, unique viral clones were isolated after plaque assay on MDCK and grown either in embryonated eggs or in MDCK cells, as described before (69). Virus stocks were quantified by plaque assay in MDCK cells at 33°C and sequenced.

Immunoprecipitation assay. 293T were transfected with 1 μg of pCAGGS.Flag-CPSF30 or with 0.5 μg of pCAGGS.Flag-ZsGreen using 2 μL/μg DNA of TransIT-LT1 (Mirus number Mir2304). 24 h posttransfection, cells were infected at an MOI of 5 with either LAIV or optiLAIV. Cells were lysed on ice after 16h in 300 μL IP lysis buffer (50 mM Tris HCl pH 7.5, 150 mM NaCl, 0.5% vol/vol NP-40, 5 mM EDTA with protease inhibitors [Pierce number 88266]). 50 μL of the cleared lysate were mixed 1:1 with protein lysis buffer (50 mM Tris HCl pH 6.8, 10% glycerol, 2% SDS, 0.1 M DTT and 0.1% bromophenol blue in H₂O) to serve as whole-cell lysate control, while the remaining 200 μL was processed for immunoprecipitation over night at 4°C using anti-Flag M2 affinity gel (Sigma number A2220). Samples were then used in a Western blot.

Viral growth kinetic. Multicycle growth kinetics were carried out by infecting A549 cells (12-well plate format, 2 × 10⁵ cells/well, triplicates) with indicated viruses at a multiplicity of infection (MOI) of 0.01. After 45 min of viral adsorption at 33°C, supernatants were replaced by fresh infection medium supplemented with 0.1 μg/mL of N-tosyl-L-phenylalanine chloromethyl ketone (TPCK)-treated trypsin (Sigma number T1426) and plates were incubated at 33°C with 5% CO₂. Supernatants were collected at the indicated times postinfection and viral titers were determined by plaque assay in MDCK cells.

Infections. For A549 and LA4, infections were carried out in a 12-well plate format (2 × 10⁵ cells/well) with indicated viruses at a multiplicity of infection (MOI) of 5. After 45 min of viral adsorption at 33°C, supernatants were replaced by fresh infection medium and incubated at 33°C with 5% CO₂. Tunicamycin (Merck number T7765) was added to the culture medium at 5 μg/mL. At the indicated time point, cells were washed with PBS and either TRK lysis buffer (E.Z.N.A) or protein lysis buffer (TrisHCl 50 mM pH 6.8, glycerol 10%, SDS 2% and DTT 100 mM) was added to the wells and stored at -70°C until further analysis.

For human airway epithelia, cells were incubated with PBS supplemented with Ca²⁺ and Mg²⁺ (100 mg/L of CaCl₂ and 100 mg/L of MgCl₂-6H₂O) for 45 min at 37°C, 5% CO₂ and subsequently washed three times with PBS with Ca²⁺ and Mg²⁺. Cells were then inoculated in triplicates with LAIV or optiLAIV at MOI 5 for 3 h at 33°C, 5% CO₂. Cells were then washed three times with PBS with Ca²⁺ and Mg²⁺ and then left at the air-liquid interface at 33°C with 5% CO₂ and 90% humidity. At the indicated time point, cells were washed with PBS and TKR lysis buffer (E.Z.N.A) was added to the apical side. Lysates were collected and stored at -70°C until further analysis.

RT-PCR and RT-qPCR. Following infection, total cellular RNA was isolated using E.Z.N.A Total RNA kit 1 (Omega Bio-Tek number R6834-01) according to manufacturer's instructions. cDNA was synthesized using M-MLV Reverse transcriptase (Promega number M170A) according to manufacturer's instructions using 500 ng of RNA as starting material and 500 ng of oligo dT as primers.

To perform PCR, GoTaq G2 DNA polymerase (Promega number M784B) was used with 5 × Green GoTaq reaction buffer (Promega number M791A). The primers were designed to flank the splicing site of XBP1 mRNA in order to amplify both the unspliced and spliced form. A PCR for β-actin was used as a control. PCR

products were separated on a 3% agarose gel containing EtBr for visualization. Images were acquired using GelDoc XR+ System (Bio-Rad) and analyzed with Image Lab software (v4.1 from Bio-Rad).

To perform qPCR, 1 μ L of cDNA was mixed with 10 μ L of 2 \times KAPA SYBR FAST qPCR Master Mix-universal (KAPA Biosystems, USA), 1 μ L of each respective forward (0.5 μ M) and reverse (0.5 μ M) primers in a final volume of 20 μ L with RNase, DNase Free Molecular Biology Grade Water (Amimed, BioConcept, Switzerland). Quantitative PCR was performed following a thermal cycling protocol of an initial denaturation step at 95°C for 5 min, followed by 40 cycles of denaturation at 95°C for 30 s and annealing/extension at 60°C for 60s. After each reaction melting curves were determined for each primer set to confirm the correct amplification of the target gene.

Western blots. Cell lysates were sonicated and boiled for 5 min at 95°C. The same volume of lysates was loaded on a denaturing SDS-polyacrylamide gels, transferred to Polyvinylidene fluoride (PVDF) membranes (GE Healthcare), blocked with 5% skimmed milk in TBS containing 0,1% Tween 20 (Applichem) and incubated with the respective primary antibodies overnight at 4°C. Secondary anti-mouse or anti-rabbit conjugated to HRP were incubated for 1 h and developed using the WesternBright ECL-spray (Advanta).

Plaque assays. Monolayers of MDCK cells (6-well plate format, 1,5 \times 10⁶ cells/well) were infected with 10-fold serial dilutions in PBS + 0,2% BSA of the correspondent virus for 45 min at 33°C. Supernatants were replaced by fresh overlay medium supplemented with 1 μ g/mL of N-tosyl-L-phenylalanine chloromethyl ketone (TPCK)-treated trypsin (Sigma) and 0,6% purified agar (Oxoid) and plates were incubated at 33°C 5% CO₂ (70). After 48 h, cells were fixed for 1 h at RT with 4% paraformaldehyde (PFA) and the overlays were removed. Cells were stained using a solution of 16% Metanol and crystal violet and plaques were counted visually.

Flow cytometry. Lungs and snouts were cut into small pieces and digested in RPMI containing 1 mg/mL collagenase IV (cat. number LS004189, Worthington Biochemical Corporation), 40 mg/mL DNase I, and 2% FCS for 30 min at 37°C. Any tissue remaining after 30 min was further digested with 1 mg/mL collagenase D (cat. number 1108882001, Roche), and 40 mg/mL DNase I and 1% of FCS for 20 min at 37°C. The reaction was stopped by addition of 5 mmol/L EDTA and 10% BSA. Samples were further disaggregated through a 70-mm cell strainer and blocked with anti-CD16/32 (cat. number 14-0161-86, Invitrogen). Single-cell suspensions were counted and stained with antibodies as previously described (71). Intracellular staining with anti-CD68 was done using the Intracellular Fixation and Permeabilization buffer set (Thermo Fisher): Fixation/permeabilization concentrate (cat. number 00-5123-43) and Diluent (cat. number 00-5223-56), Permeabilization Buffer 10 \times (cat. number 00-8333-56). Cells were acquired on a Fortessa and analyzed using FlowJo software using the gating strategy depicted in Fig. S2A.

Animal vaccination. For neonatal mice, at 7 days postbirth, pups were weighed and marked. All animals over 3 g in weight were inoculated with 5 μ L of the indicated dose of vaccine diluted in cold-PBS via the intranasal route.

For adult mice, 8 weeks-old females were weighed, marked and injected intraperitoneally with 10 μ L/g of ketamin/xylazine (100 mg/kg and 5 mg/kg, respectively) diluted in sterile PBS. Upon reaching deep anesthesia, mice were inoculated with the respective doses of each vaccine in 20 μ L PBS via the intranasal route.

To assess vaccine susceptibility, body weight was monitored for 14 days after vaccination. For neonatal mice, the cutoff threshold was determined as the interval from the difference between the average weight of the mock-vaccinated group and the lightest mouse of that group (biological variation of the pups' weight), times two, calculated for each day postvaccination. For adults, a 15% body weight loss from the initial weight was used.

To assess virus replication, 7 days-old mice or 8 weeks-old females were vaccinated with 1 \times 10⁵ PFU of either vaccine and at the indicated day postvaccination animals were euthanized by decapitation (pups) or controlled CO₂ exposure (adults). Snouts and lungs were harvested immediately after euthanasia using sterile tools in 1 mL cold-PBS and homogenized twice with ¼" ceramic grinding balls (MPBio, USA) using a Bead Blaster 24 (Benchmark Scientific, USA) with a speed setting of 6 m/s for 30 s with a 30 s break on ice between each cycle. Samples were centrifuged at 10,000 \times g for 10 min at 4°C. Supernatants were collected and frozen at -70°C to be used in plaque assays. Pellets were resuspended in 1 mL TRIzol (Invitrogen) and frozen at -70°C for further RNA extraction.

To assess antibodies response, blood samples were harvested on the respective days by lateral tail-vein bleeding. Briefly, mice were placed under a plastic restrainer and an orthogonal incision was made on the left vein of the tail. Blood was collected in 1,5 mL polystyrene tubes and incubated at room temperature for 30 min to 1 h to allow coagulation. Samples were centrifuged at 10,000 \times g for 5 min at room temperature and supernatants collected into fresh tubes and stored at -20°C to be used in micro-neutralization assays.

Animal challenge. At the indicated day, vaccinated mice were injected intraperitoneally with 10 μ L/g of ketamin/xylazine (100 mg/kg and 5 mg/kg, respectively) diluted in sterile PBS. Upon reaching deep anesthesia, mice were challenged with 20 μ L of 10 \times LD₅₀ of A/Netherlands/2009 (H1N1) or 20 \times LD₅₀ of A/VietNam/1203/2004 (H5N1) HALo (low pathogenic version) in cold-PBS via the intranasal route. Body weight was monitored for 14 days postchallenge and upon reaching experimental or humane endpoints (85% of initial body weight) animals were euthanized using controlled CO₂ exposure.

Statistics. Statistical analysis was performed using GraphPad Prism 8 and statistical tests applied are indicated in each respective figure legend.

Data availability. The data generated and analyzed during this study are available from the corresponding author upon reasonable request.

SUPPLEMENTAL MATERIAL

Supplemental material is available online only.

SUPPLEMENTAL FILE 1, PDF file, 1.8 MB.

ACKNOWLEDGMENTS

We specially thank the Service Zootechnie of the CMU for their continuous technical support with animal experiments.

Mouse icons were printed with permission from The Jackson Laboratory.

We declare no competing interests.

J.P.P.L.B., L.G., S.H., M.S., and B.M.-S. contributed to the conception and design of the work. J.P.P.L.B., N.W., L.G., and B.M.-S. contributed to the acquisition of the data. J.P.P.L.B., L.G., M.S., and B.M.-S. contributed to the analysis and interpretation of the data. J.P.P.L.B., M.S., and B.M.-S. wrote the manuscript.

REFERENCES

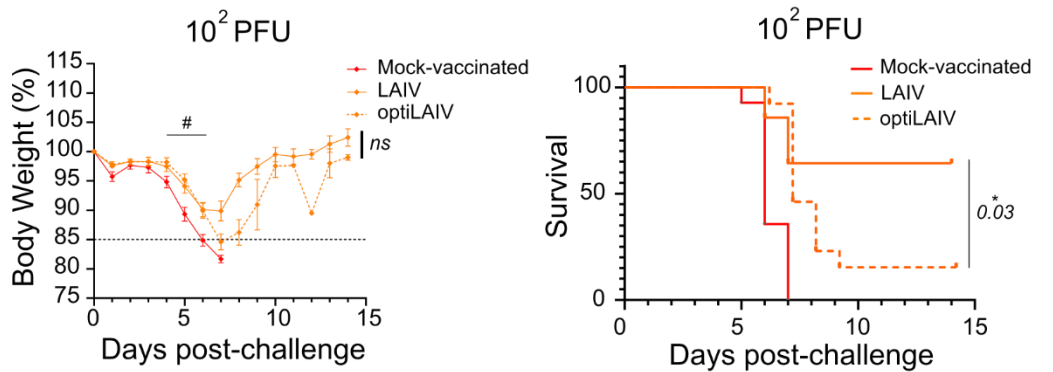
1. Paget J, Spreuwenberg P, Charu V, Taylor RJ, Luliano AD, Bresee J, Simonsen L, Viboud C. 2019. Global mortality associated with seasonal influenza epidemics: new burden estimates and predictors from the GLaMOR Project. *J Glob Health* 9. <https://doi.org/10.7189/JOGH.09.020421>.
2. Collins JP, Campbell AP, Openo K, Farley MM, Cummings CN, Hill M, Schaffner W, Lou Lindegren M, Thomas A, Billing L, Bennett N, Spina N, Bargsten M, Lynfield R, Eckel S, Ryan P, Yousey-Hindes K, Herlihy R, Kirley PD, Garg S, Anderson EJ. 2020. Outcomes of immunocompromised adults hospitalized with laboratory-confirmed influenza in the United States, 2011–2015. *Clin Infect Dis An Off Publ Infect Dis Soc Am* 70:2121–2130. <https://doi.org/10.1093/cid/ciz638>.
3. Wang X, Li Y, O'Brien KL, Madhi SA, Widdowson M-A, Byass P, Omer SB, Abbas Q, Ali A, Amu A, Azziz-Baumgartner E, Bassat Q, Abdullah Brooks W, Chaves SS, Chung A, Cohen C, Echavarría M, Fasce RA, Gentile A, Gordon A, Groome M, Heikkinen T, Hirve S, Jara JH, Katz MA, Khuri-Bulos N, Krishnan A, de Leon O, Lucero MG, McCracken JP, Mira-Iglesias A, Moisi JC, Munywoki PK, Ouhouiré M, Polack FP, Rahi M, Rasmussen ZA, Rath BA, Saha SK, Simões EA, Sotomayor V, Thamthitwat S, Treurnicht FK, Wamukoya M, Yoshida L-M, Zar HJ, Campbell H, Nair H, Nair H, Campbell H, et al. 2020. Respiratory Virus Global Epidemiology Network, global burden of respiratory infections associated with seasonal influenza in children under 5 years in 2018: a systematic review and modelling study. *Lancet Glob Heal* 8:e497–e510. [https://doi.org/10.1016/S2214-109X\(19\)30545-5](https://doi.org/10.1016/S2214-109X(19)30545-5).
4. Lafond KE, Porter RM, Whaley MJ, Suizan Z, Ran Z, Aleem MA, Thapa B, Sar B, Proschle VS, Peng Z, Feng L, Coulibaly D, Nkwembe E, Olmedo A, Ampofo W, Saha S, Chadha M, Mangiri A, Setiawaty V, Ali SS, Chaves SS, Otorbaeva D, Keosavanh O, Saleh M, Ho A, Alexander B, Oumzil H, Baral KP, Sue Huang Q, Adebayo AA, Al-Abaidani I, von Horoch M, Cohen C, Tempia S, Mmbaga V, Chittaganpitch M, Casal M, Dang DA, Couto P, Nair H, Bresee JS, Olsen SJ, Azziz-Baumgartner E, Pekka Nuorti J, Widdowson MA, Flora MS, Wangchuk S, Fasce RA, Olivares MF, Qin Y, Global Respiratory Hospitalizations–Influenza Proportion Positive (GRIPP) Working Group., et al. 2021. Global burden of influenza-associated lower respiratory tract infections and hospitalizations among adults: a systematic review and meta-analysis. *PLoS Med* 18:e1003550–17. <https://doi.org/10.1371/journal.pmed.1003550>.
5. Cox A, Baker SF, Nogaes A, Martínez-Sobrido L, Dewhurst S. 2015. Development of a mouse-adapted live attenuated influenza virus that permits in vivo analysis of enhancements to the safety of live attenuated influenza virus vaccine. *J Virol* 89:3421–3426. <https://doi.org/10.1128/JVI.02636-14>.
6. Blanco-Lobo P, Nogaes A, Rodríguez L, Martínez-Sobrido L. 2019. Novel approaches for the development of live attenuated influenza vaccines. *Viruses* 11:190. <https://doi.org/10.3390/v11020190>.
7. Hoft DF, Lottenbach KR, Blazevic A, Turan A, Blevins TP, Pacatte TP, Yu Y, Mitchell MC, Hoft SG, Belshe RB. 2017. Comparisons of the humoral and cellular immune responses induced by live attenuated influenza vaccine and inactivated influenza vaccine in adults. *Clin Vaccine Immunol* 24. <https://doi.org/10.1128/CI.00414-16>.
8. Jang YH, Seong BL. 2021. Immune responses elicited by live attenuated influenza vaccines as correlates of universal protection against influenza viruses. *Vaccines* 9:353. <https://doi.org/10.3390/vaccines9040353>.
9. Mohn KGI, Brokstad KA, Islam S, Oftung F, Tøndel C, Aarstad HJ, Cox RJ. 2020. Early induction of cross-reactive CD8+ T-cell responses in tonsils after live-attenuated influenza vaccination in children. *J Infect Dis* 221:1528–1537. <https://doi.org/10.1093/infdis/jiz583>.
10. Pebody R, Sile B, Warburton F, Sinnathamby M, Tsang C, Zhao H, Ellis J, Andrews N. 2017. Live attenuated influenza vaccine effectiveness against hospitalisation due to laboratory-confirmed influenza in children two to six years of age in England in the 2015/16 season. *Eurosurveillance* 22:30450. <https://doi.org/10.2807/1560-7917.ES.2017.22.4.30450>.
11. Mohn KGI, Smith I, Sjursen H, Cox RJ. 2018. Immune responses after live attenuated influenza vaccination. *Hum Vaccin Immunother* 14:571–578. <https://doi.org/10.1080/21645515.2017.1377376>.
12. Buchan SA, Booth S, Scott AN, Simmonds KA, Svenson LW, Drews SJ, Russell ML, Crowcroft NS, Loeb M, Warshawsky BF, Kwong JC. 2018. Effectiveness of live attenuated vs inactivated influenza vaccines in children during the 2012–2013 through 2015–2016 influenza seasons in Alberta, Canada: a Canadian Immunization Research Network (CIRN) study. *JAMA Pediatr* 172:e181514. <https://doi.org/10.1001/jamapediatrics.2018.1514>.
13. Krishnan A, Dar L, Saha S, Narayan VV, Kumar R, Kumar R, Amarchand R, Dhakad S, Chokker R, Choudekar A, Gopal G, Choudhary A, Potdar V, Chadha M, Lafond KE, Lindstrom S, Widdowson MA, Jain S. 2021. Efficacy of live attenuated and inactivated influenza vaccines among children in rural India: a 2-year, randomized, triple-blind, placebo-controlled trial. *PLoS Med* 18:e1003609. <https://doi.org/10.1371/journal.pmed.1003609>.
14. Pebody R, McMenamin J, Nohynek H. 2018. Live attenuated influenza vaccine (LAIV): recent effectiveness results from the USA and implications for LAIV programmes elsewhere. *Arch Dis Child* 103:101–105. <https://doi.org/10.1136/archdischild-2016-312165>.
15. Banovic T, Yanilla M, Simmons R, Robertson I, Schroder WA, Raffelt NC, Wilson YA, Hill GR, Hogan P, Nourse CB. 2011. Disseminated varicella infection caused by varicella vaccine strain in a child with low invariant natural killer T cells and diminished CD1d expression. *J Infect Dis* 204:1893–1901. <https://doi.org/10.1093/infdis/jir660>.
16. Jean-Philippe P, Freedman A, Chang MW, Steinberg SP, Gershon AA, LaRussa PS, Borkowsky W. 2007. Severe varicella caused by varicella-vaccine strain in a child with significant T-cell dysfunction. *Pediatrics* 120:e1345–e1349. <https://doi.org/10.1542/peds.2004-1681>.
17. Kamboj M, Sepkowitz KA. 2007. Risk of transmission associated with live attenuated vaccines given to healthy persons caring for or residing with an immunocompromised patient. *Infect Control Hosp Epidemiol* 28:702–707. <https://doi.org/10.1086/517952>.
18. Poliomyelitis: vaccine derived polio (available at <https://www.who.int/news-room/questions-and-answers/item/poliomyelitis-vaccine-derived-polio>).
19. Richt JA, García-Sastre A. 2009. Attenuated influenza virus vaccines with modified NS1 proteins. *Curr Top Microbiol Immunol* 333:177–195.
20. Wacheck V, Egorov A, Groiss F, Pfeiffer A, Fuereder T, Hoeflmayer D, Kundi M, Popow-Kraupp T, Redlberger-Fritz M, Mueller CA, Cinatl J, Michaelis M, Geiler J, Bergmann M, Romanova J, Roethl E, Morokutti A, Wolschek M, Ferko B, Seipelt J, Dick-Gudenus R, Muster T. 2010. A novel type of influenza vaccine: safety and immunogenicity of replication-deficient influenza virus created by deletion of the interferon antagonist NS1. *J Infect Dis* 201:354–362. <https://doi.org/10.1086/649428>.
21. Wang P, Zheng M, Lau S-Y, Chen P, Mok B-W, Liu S, Liu H, Huang X, Cremin CJ, Song W, Chen Y, Wong Y-C, Huang H, To KK-W, Chen Z, Xia N, Yuen K-Y, Chen H. 2019. Generation of DeLNS1 influenza viruses: a strategy

- for optimizing live attenuated influenza vaccines. *mBio* 10. <https://doi.org/10.1128/mBio.02180-19>.
22. Hale BG, Randall RE, Ortin J, Jackson D. 2008. The multifunctional NS1 protein of influenza A viruses. *J Gen Virol* 89:2359–2376. <https://doi.org/10.1099/vir.0.2008/004606-0>.
 23. Twu KY, Noah DL, Rao P, Kuo R-L, Krug RM. 2006. The CPSF30 binding site on the NS1A protein of influenza A virus is a potential antiviral target. *J Virol* 80:3957–3965. <https://doi.org/10.1128/JVI.80.8.3957-3965.2006>.
 24. Das K, Ma LC, Xiao R, Radvansky B, Aramini J, Zhao L, Marklund J, Kuo RL, Twu KY, Arnold E, Krug RM, Montelione GT. 2008. Structural basis for suppression of a host antiviral response by influenza A virus. *Proc Natl Acad Sci U S A* 105:13093–13098. <https://doi.org/10.1073/pnas.0805213105>.
 25. Hale BG, Steel J, Medina RA, Manicassamy B, Ye J, Hickman D, Hai R, Schmolke M, Lowen AC, Perez DR, García-Sastre A. 2010. Inefficient control of host gene expression by the 2009 pandemic H1N1 influenza A virus NS1. *J Virol* 84:6909–6922. <https://doi.org/10.1128/JVI.00081-10>.
 26. Wang BX, Brown EG, Fish EN. 2017. Residues F103 and M106 within the influenza A virus NS1 CPSF4-binding region regulate interferon-stimulated gene translation initiation. *Virology* 508:170–179. <https://doi.org/10.1016/j.virol.2017.05.009>.
 27. Mazel-Sanchez B, Iwaszkiewicz J, Bonifacio JPP, Silva F, Niu C, Strohmeier S, Eletto D, Krammer F, Tan G, Zoete V, Hale BG, Schmolke M. 2021. Influenza A viruses balance ER stress with host protein synthesis shutoff. *Proc Natl Acad Sci U S A* 118. <https://doi.org/10.1073/pnas.2024681118>.
 28. Prasad V, Greber UF. 2021. The endoplasmic reticulum unfolded protein response – homeostasis, cell death and evolution in virus infections. *FEMS Microbiol Rev* 45:1–19.
 29. Khanna M, Agrawal N, Chandra R, Dhawan G. 2021. Targeting unfolded protein response: a new horizon for disease control. *Expert Rev Mol Med* 23. <https://doi.org/10.1017/erm.2021.2>.
 30. Goulding LV, Yang J, Jiang Z, Zhang H, Lea D, Emes RD, Dottorini T, Pu J, Liu J, Chang KC. 2020. Thapsigargin at non-cytotoxic levels induces a potent host antiviral response that blocks influenza A virus replication. *Viruses* 12:1093. <https://doi.org/10.3390/v12101093>.
 31. Slaine PD, Kleer M, Duguay BA, Pringle ES, Kadijk E, Ying S, Balgi A, Roberge M, McCormick C, Khapersky DA. 2021. Thiopurines activate an antiviral unfolded protein response that blocks influenza A virus glycoprotein accumulation. *J Virol* 95. <https://doi.org/10.1128/JVI.00453-21>.
 32. Givord C, Welsby I, Detienne S, Thomas S, Assabban A, Lima Silva V, Molle C, Gineste R, Vermeersch M, Perez-Morga D, Leo O, Collignon C, Didierlaurent AM, Goriely S. 2018. Activation of the endoplasmic reticulum stress sensor IRE1 α by the vaccine adjuvant AS03 contributes to its immunostimulatory properties. *NPJ Vaccines* 3:20. <https://doi.org/10.1038/s41541-018-0058-4>.
 33. Rodriguez L, Blanco-Lobo P, Reilly EC, Maehigashi T, Nogales A, Smith A, Topham DJ, Dewhurst S, Kim B, Martínez-Sobrido L. 2019. Comparative study of the temperature sensitive, cold adapted and attenuated mutations present in the master donor viruses of the two commercial human live attenuated influenza vaccines. *Viruses* 11:928. <https://doi.org/10.3390/v11100928>.
 34. Fluenz Tetra nasal spray suspension influenza vaccine (live attenuated, nasal) - summary of product characteristics (SmPC) - (emc) (available at <https://www.medicines.org.uk/emc/medicine/29112#grf>).
 35. Nogales A, Rodriguez L, DeDiego ML, Topham DJ, Martínez-Sobrido L. 2017. Interplay of PA-X and NS1 proteins in replication and pathogenesis of a temperature-sensitive 2009 pandemic H1N1 influenza A virus. *J Virol* 91. <https://doi.org/10.1128/JVI.00720-17>.
 36. Hilimire TA, Nogales A, Chiem K, Ortego J, Martínez-sobrido L. 2020. Increasing the safety profile of the master donor live attenuated influenza vaccine. *Pathog (Basel, Switzerland)* 9. <https://doi.org/10.3390/PATHOGENS9020086>.
 37. Lau Y-F, Santos C, Torres-Velez FJ, Subbarao K. 2011. The magnitude of local immunity in the lungs of mice induced by live attenuated influenza vaccines is determined by local viral replication and induction of cytokines. *J Virol* 85:76–85. <https://doi.org/10.1128/JVI.01564-10>.
 38. Hawksworth A, Lockhart R, Crowe J, Maeso R, Ritter L, Dibben O, Bright H. 2020. Replication of live attenuated influenza vaccine viruses in human nasal epithelial cells is associated with H1N1 vaccine effectiveness. *Vaccine* 38:4209–4218. <https://doi.org/10.1016/j.vaccine.2020.04.004>.
 39. Live Attenuated Influenza Vaccine [LAIV] (the nasal spray flu vaccine). CDC (available at <https://www.cdc.gov/flu/prevent/nasalspray.htm>).
 40. Fluenz Tetra nasal spray suspension influenza vaccine (live attenuated, nasal) - Patient Information Leaflet (PIL) - (emc) (available at <https://www.medicines.org.uk/emc/product/3296/pil#grf>).
 41. Belshe RB, Edwards KM, Vesikari T, Black SV, Walker RE, Hultquist M, Kemble G, Connor EM. 2007. Live attenuated versus inactivated influenza vaccine in infants and young children. *N Engl J Med* 356:685–696. <https://doi.org/10.1056/NEJMoa065368>.
 42. Prutsky GJ, Domecq JP, Elraiyah T, Prokop LJ, Murad MH. 2014. Assessing the evidence: live attenuated influenza vaccine in children younger than 2 years. A systematic review. *Pediatr Infect Dis J* 33:106–115.
 43. Siegrist CA. 2001. Neonatal and early life vaccinology. *Vaccine* 19:3331–3346. [https://doi.org/10.1016/S0264-410X\(01\)00028-7](https://doi.org/10.1016/S0264-410X(01)00028-7).
 44. Kaiser L, Fritz RS, Straus SE, Gubareva L, Hayden FG. 2001. Symptom pathogenesis during acute influenza: interleukin-6 and other cytokine responses. *J Med Virol* 64:262–268. <https://doi.org/10.1002/jmv.1045>.
 45. Mallory RM, Yi T, Ambrose CS. 2011. Shedding of Ann Arbor strain live attenuated influenza vaccine virus in children 6–59 months of age. *Vaccine* 29:4322–4327. <https://doi.org/10.1016/j.vaccine.2011.04.022>.
 46. Noah DL, Twu KY, Krug RM. 2003. Cellular antiviral responses against influenza A virus are countered at the posttranscriptional level by the viral NS1A protein via its binding to a cellular protein required for the 3' end processing of cellular pre-mRNAs. *Virology* 307:386–395. [https://doi.org/10.1016/S0042-6822\(02\)00127-7](https://doi.org/10.1016/S0042-6822(02)00127-7).
 47. Kochs G, García-Sastre A, Martínez-Sobrido L. 2007. Multiple anti-interferon actions of the influenza A virus NS1 protein. *J Virol* 81:7011–7021. <https://doi.org/10.1128/JVI.02581-06>.
 48. Loving CL, Lager KM, Vincent AL, Brockmeier SL, Gauger PC, Anderson TK, Kitikoon P, Perez DR, Kehrl ME. 2013. Efficacy in pigs of inactivated and live attenuated influenza virus vaccines against infection and transmission of an emerging H3N2 similar to the 2011–2012 H3N2v. *J Virol* 87:9895–9903. <https://doi.org/10.1128/JVI.01038-13>.
 49. Lowen AC, Steel J, Mubareka S, Carnero E, García-Sastre A, Palese P. 2009. Blocking interhost transmission of influenza virus by vaccination in the guinea pig model. *J Virol* 83:2803–2818. <https://doi.org/10.1128/JVI.02424-08>.
 50. Mössler C, Groiss F, Wolzt M, Wolschek M, Seipelt J, Muster T. 2013. Phase I/II trial of a replication-deficient trivalent influenza virus vaccine lacking NS1. *Vaccine* 31:6194–6200. <https://doi.org/10.1016/j.vaccine.2013.10.061>.
 51. Nicolodi C, Groiss F, Kiselev O, Wolschek M, Seipelt J, Muster T. 2019. Safety and immunogenicity of a replication-deficient H5N1 influenza virus vaccine lacking NS1. *Vaccine* 37:3722–3729. <https://doi.org/10.1016/j.vaccine.2019.05.013>.
 52. Zhou B, Li Y, Belsler JA, Pearce MB, Schmolke M, Subba AX, Shi Z, Zaki SR, Blau DM, García-Sastre A, Tumpey TM, Wentworth DE. 2010. NS-based live attenuated H1N1 pandemic vaccines protect mice and ferrets. *Vaccine* 28:8015–8025. <https://doi.org/10.1016/j.vaccine.2010.08.106>.
 53. Pica N, Langlois RA, Krammer F, Margine I, Palese P. 2012. NS1-truncated live attenuated virus vaccine provides robust protection to aged mice from viral challenge. *J Virol* 86:10293–10301. <https://doi.org/10.1128/JVI.01131-12>.
 54. Hilimire TA, Nogales A, Chiem K, Ortego J, Martínez-sobrido L. 2020. Increasing the safety profile of the master donor live attenuated influenza vaccine. *Pathogens* 9:86. <https://doi.org/10.3390/pathogens9020086>.
 55. Chaimayo C, Dunagan M, Hayashi T, Santoso N, Takimoto T. 2018. Specificity and functional interplay between influenza virus PA-X and NS1 shutoff activity. *PLoS Pathog* 14:e1007465. <https://doi.org/10.1371/journal.ppat.1007465>.
 56. Carre C, Wong G, Narang V, Tan C, Chong J, Chin HX, Xu W, Lu Y, Chua M, Poidinger M, Tambyah P, Nyunt M, Ng TP, Larocque D, Hessler C, Bosco N, Quemeneur L, Larbi A. 2021. Endoplasmic reticulum stress response and bile acid signatures associate with multi-strain seroresponsiveness during elderly influenza vaccination. *iScience* 24:102970. <https://doi.org/10.1016/j.isci.2021.102970>.
 57. Reimold AM, Etkin A, Clauss I, Perkins A, Friend DS, Zhang J, Horton HF, Scott A, Orkin SH, Byrne MC, Grusby MJ, Glimcher LH. 2000. An essential role in liver development for transcription factor XBP-1. *Genes Dev* 14:152–157. <https://doi.org/10.1101/gad.14.2.152>.
 58. Janssens S, Pulendran B, Lambrecht BN. 2014. Emerging functions of the unfolded protein response in immunity. *Nat Immunol* 15:910–919. <https://doi.org/10.1038/ni.2991>.
 59. Smith A, Rodriguez L, Ghouayel ME, Nogales A, Chamberlain JM, Sortino K, Reilly E, Feng C, Topham DJ, Martínez-Sobrido L, Dewhurst S. 2020. A live attenuated influenza vaccine elicits enhanced heterologous protection when the internal genes of the vaccine are matched to those of the challenge virus. *J Virol* 94. <https://doi.org/10.1128/JVI.01065-19>.
 60. Nachbagger R, Feser J, Naficy A, Bernstein DI, Guptill J, Walter EB, Berlanda-Scorza F, Stadlbauer D, Wilson PC, Aydillo T, Behzadi MA, Bhavsar D, Bliss C, Capuano C, Carreño JM, Chromikova V, Claeys C, Coughlan L, Freyn AW, Gast C, Javier A, Jiang K, Mariottini C, McMahon M, McNeal M, Solórzano A, Strohmeier S, Sun W, Van der Wielen M, Innis BL, García-Sastre A, Palese P, Krammer F. 2021. A chimeric hemagglutinin-based universal influenza virus

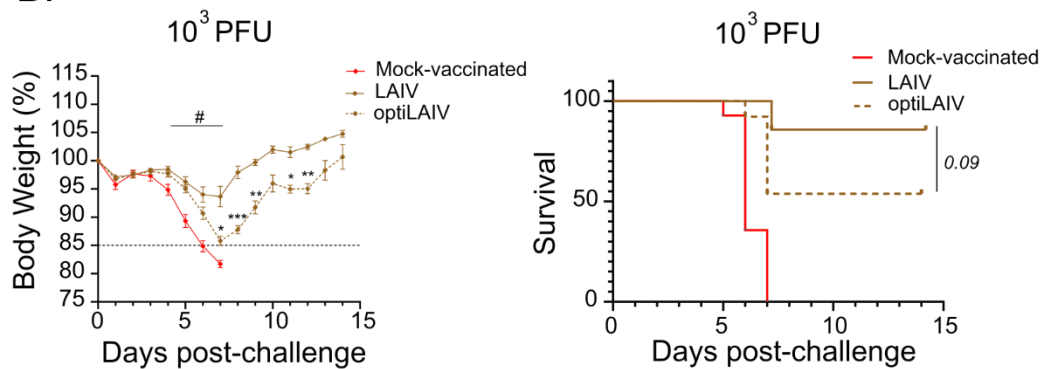
- vaccine approach induces broad and long-lasting immunity in a randomized, placebo-controlled phase I trial. *Nat Med* 27:106–114. <https://doi.org/10.1038/s41591-020-1118-7>.
61. Tillard C, Chazard E, Faure K, Bartolo S, Martinot A, Dubos F. 2021. Burden of influenza disease in children under 2 years of age hospitalized between 2011 and 2020 in France. *J Infect* <https://doi.org/10.1016/J.JINF.2021.11.006>.
 62. Matrajt L, Halloran ME, Antia R. 2020. Successes and failures of the live-attenuated influenza vaccine: can we do better? *Clin Infect Dis* 70: 1029–1037. <https://doi.org/10.1093/cid/ciz358>.
 63. Leuridan E, Van Damme P. 2007. Passive transmission and persistence of naturally acquired or vaccine-induced maternal antibodies against measles in newborns. *Vaccine* 25:6296–6304. <https://doi.org/10.1016/j.vaccine.2007.06.020>.
 64. Leuridan E, Hens N, Hutse V, Aerts M, Van Damme P. 2011. Kinetics of maternal antibodies against rubella and varicella in infants. *Vaccine* 29: 2222–2226. <https://doi.org/10.1016/j.vaccine.2010.06.004>.
 65. Kelvin AA, Zambon M. 2019. Influenza imprinting in childhood and the influence on vaccine response later in life. *Euro Surveill* 24. <https://doi.org/10.2807/1560-7917.ES.2019.24.48.1900720>.
 66. Huber VC, McCullers JA. 2006. Live attenuated influenza vaccine is safe and immunogenic in immunocompromised ferrets. *J Infect Dis* 193:677–684. <https://doi.org/10.1086/500247>.
 67. Hoffmann E, Neumann G, Kawaoka Y, Hobom G, Webster RG. 2000. A DNA transfection system for generation of influenza A virus from eight plasmids. *Proc Natl Acad Sci U S A* 97:6108–6113. <https://doi.org/10.1073/pnas.100133697>.
 68. Quinlivan M, Zamarin D, García-Sastre A, Cullinane A, Chambers T, Palese P. 2005. Attenuation of equine influenza viruses through truncations of the NS1 protein. *J Virol* 79:8431–8439. <https://doi.org/10.1128/JVI.79.13.8431-8439.2005>.
 69. Martínez-Sobrido L, García-Sastre A. 2010. Generation of recombinant influenza virus from plasmid DNA. *J Vis Exp* 5–9.
 70. Gauth CR, Smith TF. 1968. Replication and plaque assay of influenza virus in an established line of canine kidney cells. *Appl Microbiol* 16:588–594. <https://doi.org/10.1128/am.16.4.588-594.1968>.
 71. Gkoutidi AO, Garnier L, Dubrot J, Angelillo J, Harlé G, Brighthouse D, Wrobel LJ, Pick R, Scheiermann C, Swartz MA, Hugues S. 2021. MHC Class II antigen presentation by lymphatic endothelial cells in tumors promotes intratumoral regulatory T cell-suppressive functions. *Cancer Immunol Res* 9:748–764. <https://doi.org/10.1158/2326-6066.CIR-20-0784>.

Figure S1

A. Homosubtypic Challenge



B.



C.

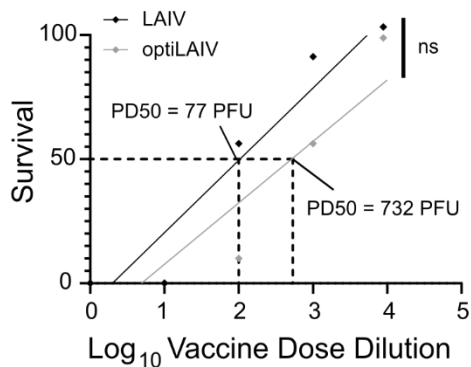


Figure S1: LAIV and optiLAIV body weight loss and survival in adult mice after challenge.

(A – B) Female 8-week-old mice vaccinated with 10² PFU (A) or 10³ PFU (B) of either LAIV or optiLAIV were challenged at day 21 post-vaccination with 20 PFU (10×LD₅₀) of A/Netherlands/602/2009 (H1N1) in 20 μL PBS under anaesthesia (n=14 per group).

Body weight (left panels) and survival (right panels) were monitored for 14 days post-challenge.

(C) PD_{50} was calculated according to Reed & Muench. Linear regression was used to determine statistical significance between the two PD_{50} .

The statistical significances between LAIV group and optiLAIV group were determined using two-way ANOVA with the Geisser-Greenhouse correction and post-hoc Dunn's multiple comparisons test for panels A and B and Mantel-Cox test for survival curve. *: comparison between LAIV and optiLAIV; #: comparison between mock and optiLAIV; *ns* = non-significant.

Graphs are representative of 3 independent experiments and indicate mean \pm SEM.

Figure S2

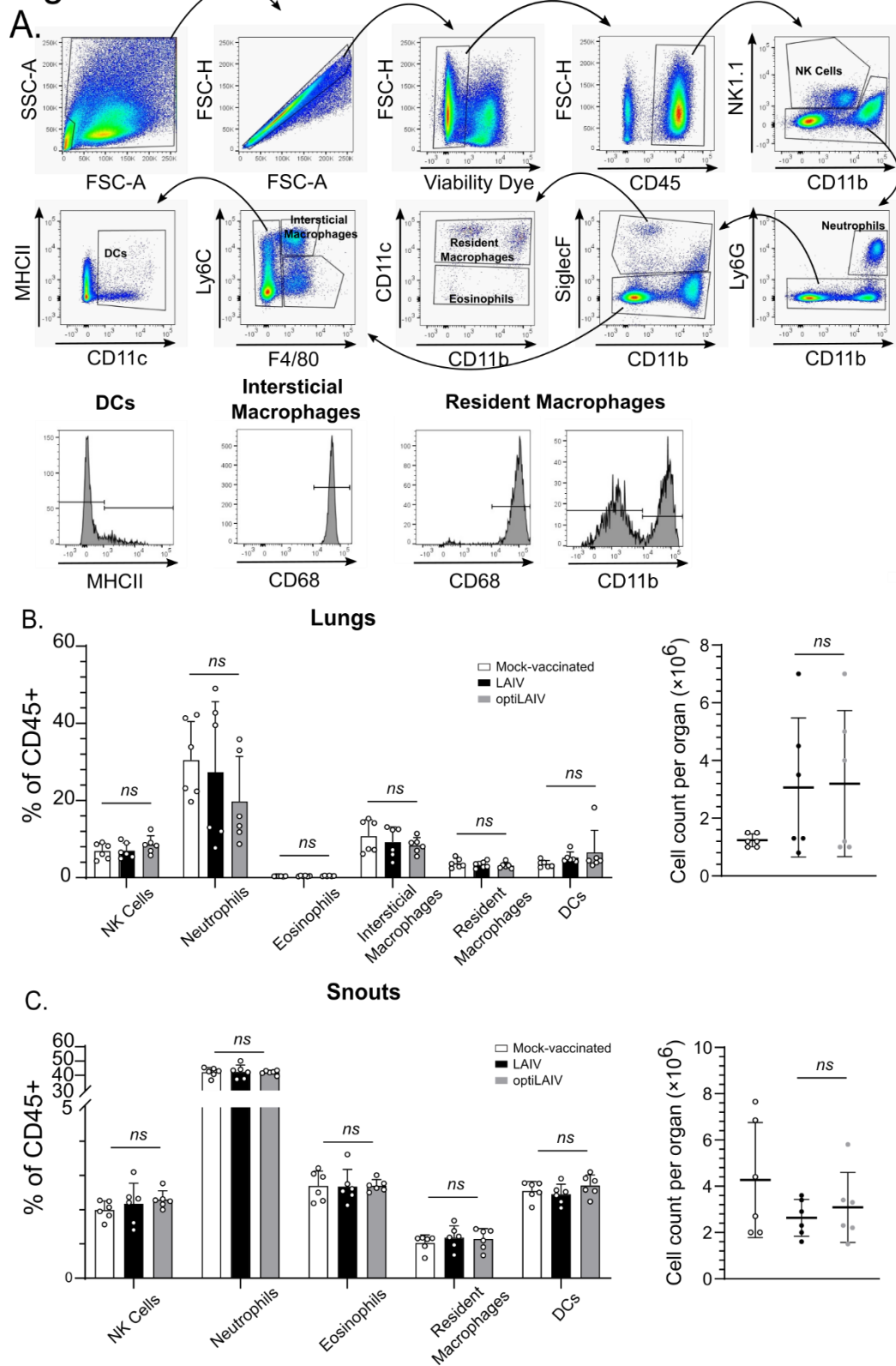


Figure S2: Cell infiltrates after LAIV administration in adult mice respiratory tract .

(A) Gating strategy (B-C) Female 8-weeks-old mice were vaccinated intranasally under anaesthesia with 10^5 PFU LAIV or optiLAIV in 25 μ L and at 4 days post-vaccination (B) lungs and (C) snouts were collected, homogenized and cells were stained for different surface markers to distinguish between different immune cell populations (left panels) and total cell number was determined counting cells manually (left panels). The statistical significances between LAIV group and optiLAIV group were determined using two-way ANOVA and post-hoc Tukey's multiple comparisons test for left panels and one-way ANOVA and post-hoc Tukey's multiple comparisons test for right panels. *ns* = non-significant. Graphs are representative of 2 independent experiments and indicate mean \pm SD.

Figure S3

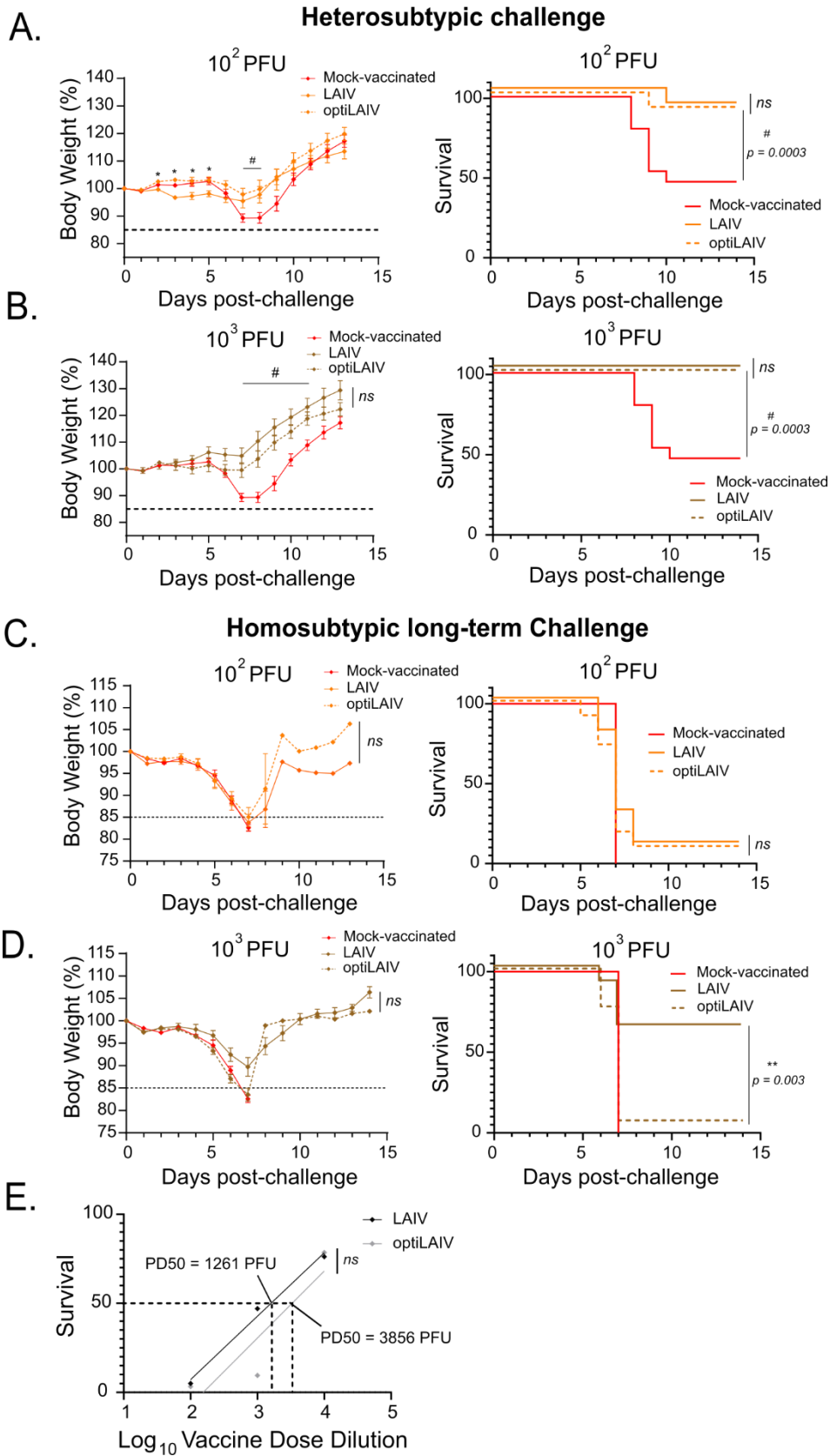


Figure S3: Body weight loss and survival after challenge in neonatal mice previously vaccinated with LAIV and optiLAIV.

(A – B) Seven-days-old mice were vaccinated intranasally with 10^2 PFU (A) or 10^3 PFU (B) of LAIV or optiLAIV in 5 μ L PBS. At day 21 post-vaccination, mice were challenged with 10^3 PFU ($20 \times LD_{50}$) of A/Vietnam/1203/2004 (H5N1) in 20 μ L PBS under anaesthesia (n=11 per group). Body weight (left panels) and survival (right panels) were monitored for 14 days post-challenge.

(C – D) Seven-days-old mice were vaccinated intranasally with 10^2 PFU (C) or 10^3 PFU (D) of LAIV or optiLAIV in 5 μ L PBS. At day 49 post-vaccination, mice were challenged with 20 PFU ($10 \times LD_{50}$) of A/Netherlands/602/2009 (H1N1) in 20 μ L PBS under anaesthesia (n=11-17 per group). Body weight (left panels) and survival (right panels) were monitored for 14 days post-challenge.

(E) PD_{50} was calculated according to Reed & Muench. Linear regression was used to determine statistical significance between the two PD_{50} .

The statistical significances between LAIV group and optiLAIV group were determined using two-way ANOVA with the Geisser-Greenhouse correction and post-hoc Dunn's multiple comparisons test for panels A-D and Mantel-Cox test for survival curve. *: comparison between LAIV and optiLAIV; #: comparison between mock and optiLAIV ; *ns* = non-significant.

Graphs are representative of 2 independent experiments and indicate mean \pm SEM.

Figure S4

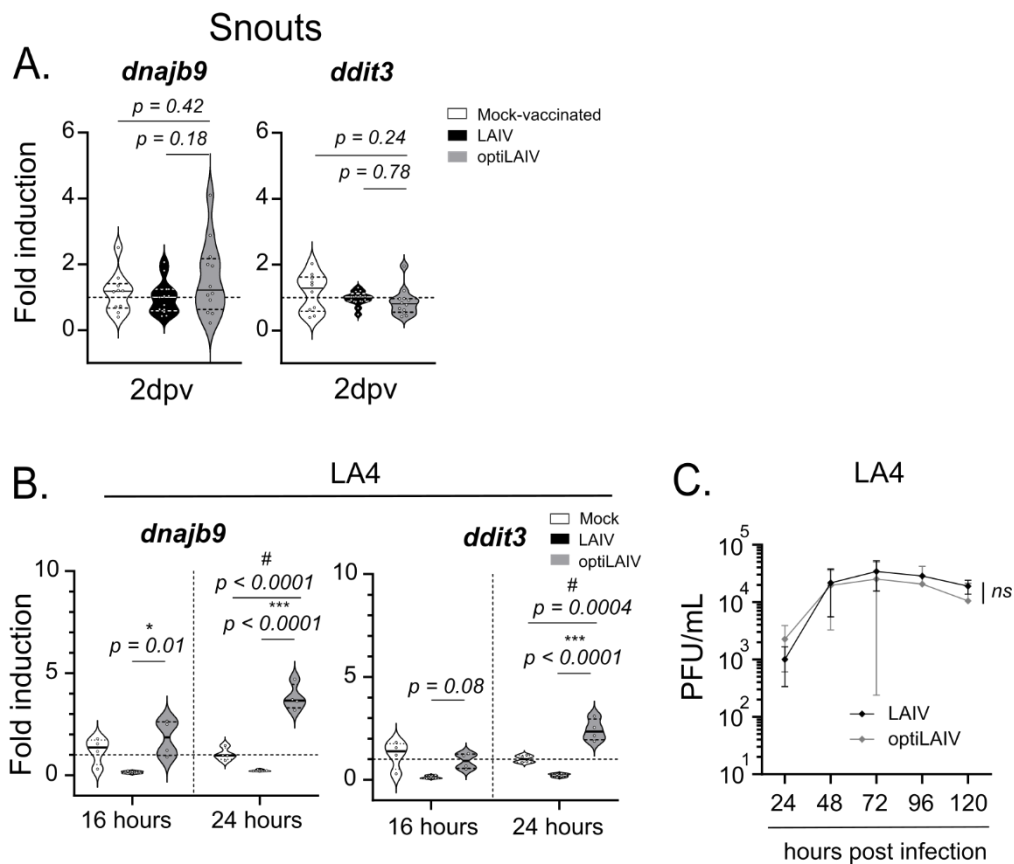


Figure S4: UPR-induced genes after LAIV and optiLAIV vaccination in neonatal snouts and murine lung cell lines.

(A) Seven-days-old mice ($n=11-12$) were vaccinated intranasally with 10^5 PFU of LAIV or optiLAIV in 5 μ L PBS. At 2 days post-vaccination snouts were harvested and RT-qPCR performed in isolated RNA for UPR-induced genes *Dnajb9* and *Ddit3*.

(B) LA4 cells were infected at a MOI of 5 with LAIV or optiLAIV and RT-qPCR for UPR-induced genes *Dnajb9* and *Ddit3* was performed in RNA lysates at 16h and 24h post infection.

(C) LA4 cells were infected at a MOI of 0.01 with either LAIV or optiLAIV. Supernatants were collected at indicated time post infection and viral titers determined by plaque assay.

The statistical significances between LAIV group and optiLAIV group were determined using one-way ANOVA and post-hoc Tukey's multiple comparisons test in panels A and B; two-way ANOVA with the Geisser-Greenhouse correction and post-hoc Dunn's multiple comparisons

test for panel C. *: comparison between LAIV and optiLAIV; #: comparison between mock and optiLAIV; *ns* = non-significant. Graphs are representative of 2-3 independent experiments and indicate mean \pm SD.

Figure S5

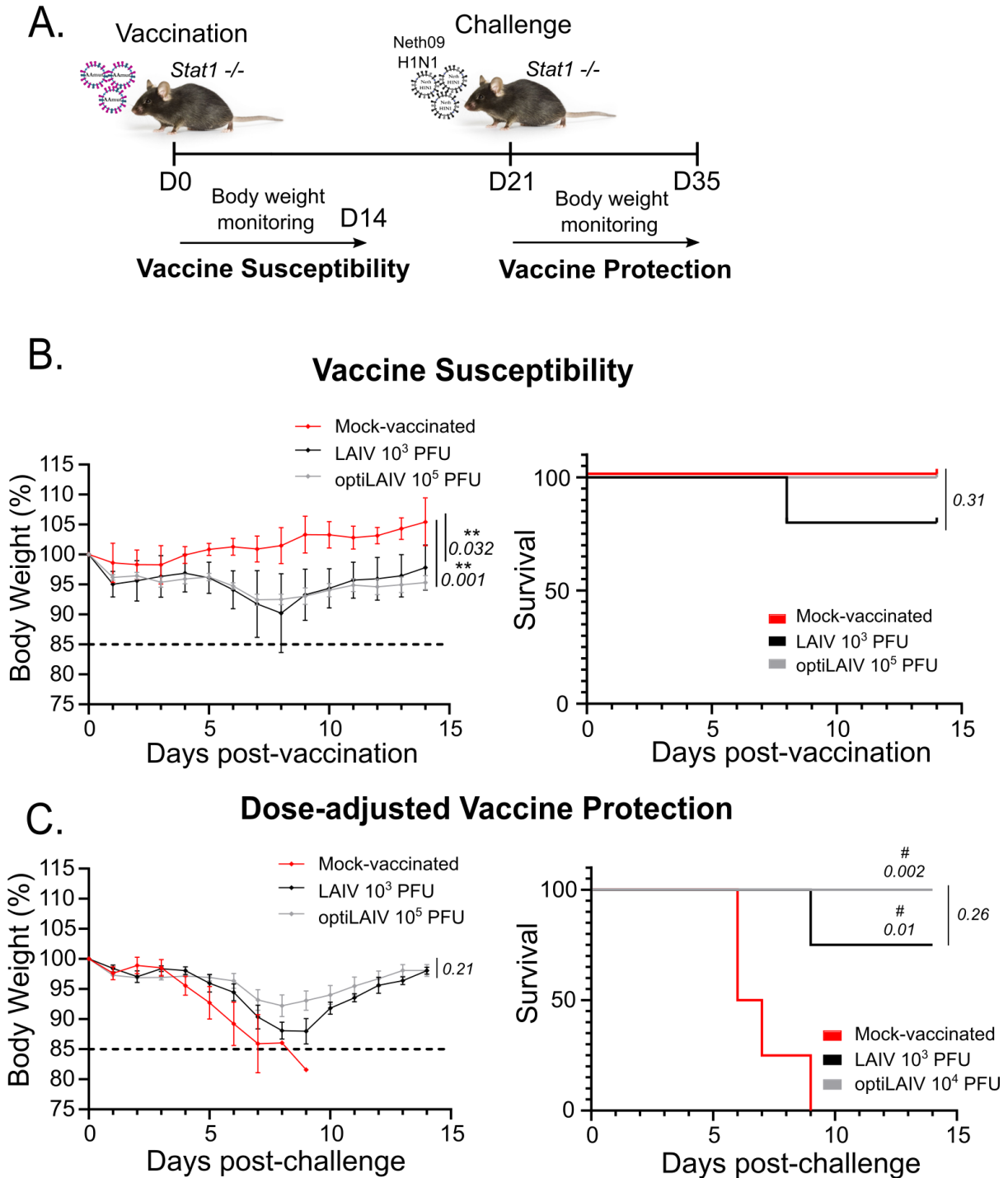


Figure S5. optiLAIV protects stat1^{-/-} mice against homosubtypic challenge.

(A) Scheme of mouse immunization and challenge.

(B) Eight-weeks-old Stat1^{-/-} mice were vaccinated intranasally under anaesthesia with 10³ PFU LAIV or 10⁵ PFU optiLAIV in 25 µL and body weight (left panel) and survival (right panel) were monitored for 14 days post-vaccination (n=4 for mock-vaccinated group; n=5 per vaccinated group).

(C) Female 8-weeks-old mice vaccinated with 10³ PFU of LAIV or 10⁵ PFU of optiLAIV were challenged at day 21 post-vaccination with 20 PFU (10×LD₅₀) of mouse adapted A/Netherlands/602/2009 (H1N1) in 25 µL PBS under light anaesthesia (n=4 in mock-vaccinated and LAIV group and n=5 in optiLAIV group). Body weight (left panel) and survival (right panel) were monitored for 14 days post-challenge. The statistical significances between LAIV group and optiLAIV group were determined using; two-way ANOVA with the Geisser-Greenhouse correction and post-hoc Dunn's multiple comparisons and Mantel-Cox long-rank test for survival curve. p-values are indicated in the figure. Graphs indicate mean ± SEM . Black dotted line represents 15% body weight loss cut-off.

3.1.2. Complementary Unpublished Results

3.1.2.1. Results

LAIV brings the advantage of triggering mucosal immunity. In order to explore the mechanisms of protection elicited by optiLAIV in comparison to LAIV we explored the humoral and cellular response to LAIV in neonatal mice.

- Humoral response to LAIV and optiLAIV

Mucosal surfaces are important entry points for a variety of pathogens. Hence, the mucosal response is an important compartment of the immune system to prevent transmission of influenza viruses. We tested the capacity of optiLAIV to induce IgAs in the BALs of vaccinated neonatal animals at 24-26 days post vaccination. We were not able to detect binding IgA antibodies to IAV in neither of the vaccinated groups (data not shown). In parallel, we also evaluated the ability of optiLAIV to induce serum IgGs compared to LAIV. According to our results, both vaccines induce similar levels of IgG binding antibodies against IAV (Figure 9). In addition, we found no serum neutralizing antibodies in vaccinated mice with either LAIV or optiLAIV (data not shown).

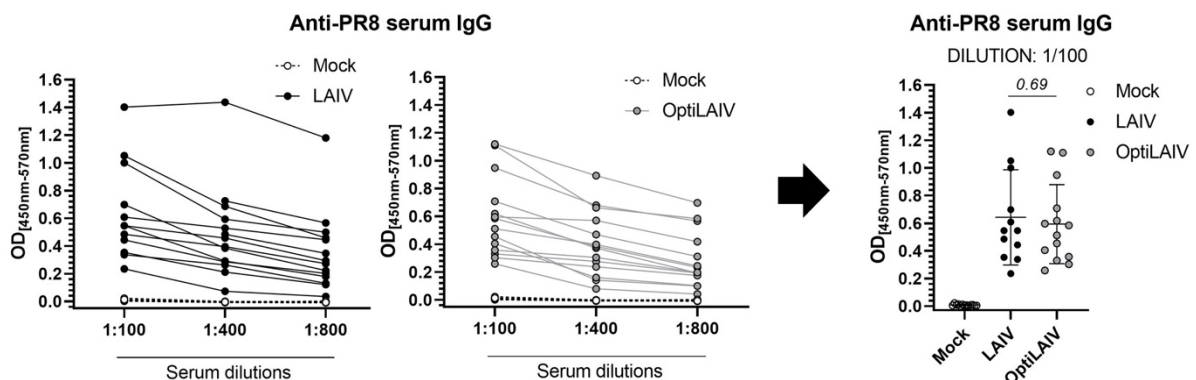


Figure 9: LAIV and optiLAIV induce IgG binding antibodies in serum. Seven-days-old mice were vaccinated intranasally with 10^4 PFU LAIV or optiLAIV in 5 μ L or mock-vaccinated. Sera from LAIV and optiLAIV mice 24 days post vaccination (n = 6 mice/group) or 26 days post vaccination (n = 8 mice/group) were tested for binding IgGs to PR8 virus by ELISA. The statistical significances between LAIV group and optiLAIV group were determined using multiple t-test. p-values are indicated in the figure. Each graph represents one independent experiment.

3.1.2.2. Materials and Methods

- ELISA

Blood samples and BALs were collected on day 24 after vaccination centrifuged at 10'000 rpm for 5 minutes at room temperature and supernatants were frozen at -20°C . Anti-PR8 binding antibodies in serum and BAL were determined by an ELISA assay adapted from [Wolf et al 2011 – J Clin Invest]. To determine virus-specific IgG and IgA, 96-well plates were coated overnight at 4°C with egg-grown PR8 virus (10^7 PFU/well) or allantoic fluid (as controls) diluted in carbonate buffer (pH = 9.6). Wells were blocked with PBS supplemented

with 1% bovine serum albumin (Gibco) and 0.05% Tween-20 and incubated at 37°C for 1h. Plates were washed three times with PBS and 0.05% Tween-20. Samples were serial-diluted (2-fold) 4-times in blocking buffer and 100 µL were added to each well and incubated for 2h at RT. Plates were washed three times with PBS and 0.05% Tween-20 and 100 µL of secondary antibody anti-mouse IgG conjugated with HRP (1:2'000) or anti-mouse IgA conjugated with HRP (1:2'000) were added in blocking buffer. Plates were washed five times with PBS and 0.05% Tween-20 and 100µL of 3,3',5,5' – tetramethylbenzidine (TMB) substrate solution was added to each well for 30 mins at RT in the dark. The reaction was stopped by adding 50 µL of 2M sulphuric acid to each well. The optical intensity (OD_{450nm} and OD_{570nm}) was determined with an ELISA reader and calculated using SoftMax Pro software. OD_{450nm-570nm} was determined and values from allantoic fluid coated wells were subtracted from all the other groups.

- **Microneutralization assay**

Influenza-specific reactivity of serum antibodies was determined using an adapted microneutralization assay. Briefly, serum was treated with receptor-destroying enzyme from cholera filtrate (Cholera filtrate sigma C8772) overnight at 37 °C, heat-inactivated at 56 °C for 30 minutes and 2.5% citrate in PBS was added for a final dilution of 1:10. Serial dilutions (1:2) were performed in infection media (Dulbecco's Modified Eagle Medium (Gibco) supplemented with 0.2 % (v/v) bovine serum albumin (Gibco) and 100U/ml Pen/Strep) and incubated with 4'500 PFU of A/Netherlands/2009 virus for 1h at RT. PBS-washed MDCK cells (4 × 10⁴ cells/well) were exposed to serum-virus mixtures for 45 min at 37 °C with 5% CO₂. The inoculum was removed, washed and cells were incubated overnight in infection media supplemented with 1 µg/mL of N-tosyl-L-phenylalanine chloromethyl ketone (TPCK)-treated trypsin at 37 °C with 5% CO₂. Cells were fixed for 1h at RT with 4% paraformaldehyde (PFA) and stained using a solution of 16% Metanol and Crystal Violet and neutralization titers were calculated.

3.2. A single respiratory tract infection early in life reroutes healthy microbiome development and affects adult metabolism in a preclinical animal model

3.2.1. Published Results

Soner Yildiz^{#, 1}, Beryl Mazel-Sanchez^{#, 1}, Joao P P Bonifacio^{#, 1}, Mirco Schmolke^{2, 3}

¹*Department of Microbiology and Molecular Medicine, Faculty of Medicine, University of Geneva, Geneva, Switzerland*

²*Department of Microbiology and Molecular Medicine, Faculty of Medicine, University of Geneva, Geneva, Switzerland. mirco.schmolke@unige.ch*

³*Geneva Center for Inflammation Research, Geneva, Switzerland. mirco.schmolke@unige.ch*

[#]*Contributed equally*

Status:

Manuscript published in NPJ Biofilms Microbiomes – PMID: 35780244

Summary:

The second part of my thesis addressed the role of acute respiratory infections as a driver of dysbiosis during microbiota development and resulting consequences for the host. Previous results published by our group showed a transient gut dysbiosis after IAV infection in adult mice⁴²⁹. Thus, we hypothesised that during infancy, a subclinical IAV infection could disturb microbiota development with long-term implications in host physiology. Using a neonatal mouse model, we assessed the small intestine microbiota composition after IAV H5N1 infection up to 56 days post infection. At 7 days post infection, we observed a decrease in the number of different species of bacteria, although microbiota abundance was similar between mock and infected animals. On the contrary, at 56 days post infection, a significant decrease in bacterial abundance was observed in infected animals despite an unchanged alpha diversity. Interestingly, at this time point IAV imprinted animals had an enrichment of Enterobacteriales and a reduction of Clostridiales, an observation previously described in pathological dysbiosis leading to obesity. Accordingly, these changes in microbiota were accompanied by an increased body weight in male mice when compared to mock imprinted animals. In line with these findings, imprinted animals had lower energy expenditure compared to mock and a slight increase in total fat mass. Cohousing experiments abrogated the body weight differences while a high-fat-high-sucrose diet enhanced the phenotype, suggesting a microbiota-dependent effect. Our data suggests that an acute respiratory infection during the critical period of microbiota maturation induces long-term dysbiosis with possible consequences on host metabolic processes.



Personal Contribution:

This work was part of a project started by the co-author Soner Yildiz, in which my contributions were most helpful to construct a coherent publication. In detail, I designed and performed all the experiments related to GPR41/43 knockout mice and the weaning response (additional data to the publication). I also participated in the writing of the first draft, interpretation of the data previously generated and figures construction. Finally, I performed all the experiments and analysis after peer-review pertaining LefSe and PCoA analysis together with the respective statistical tests (Figures 1e, 1f, 2f, S2b, S2c, S3b, S3c, S5 and Supplementary Tables), additional qPCR and animal experiments (Figure S2d) and refinement of figure legends, the methods section and rebuttal letter.

BRIEF COMMUNICATION OPEN



A single respiratory tract infection early in life reroutes healthy microbiome development and affects adult metabolism in a preclinical animal model

Soner Yildiz^{1,3}, Beryl Mazel-Sanchez^{1,3} , Joao P. P. Bonifacio^{1,3} and Mirco Schmolke^{1,2} ✉

In adult animals, acute viral infections only temporarily alter the composition of both respiratory and intestinal commensal microbiota, potentially due to the intrinsic stability of this microbial ecosystem. In stark contrast, commensal bacterial communities are rather vulnerable to perturbation in infancy. Animal models proved that disruption of a balanced microbiota development e.g., by antibiotics treatment early in life, increases the probability for metabolic disorders in adults. Importantly, infancy is also a phase in life with high incidence of acute infections. We postulated that acute viral infections in early life might pose a similarly severe perturbation and permanently shape microbiota composition with long-term physiological consequences for the adult host. As a proof of concept, we infected infant mice with a sub-lethal dose of influenza A virus. We determined microbiota composition up to early adulthood (63 days) from small intestine by 16S rRNA gene-specific next-generation sequencing. Infected mice underwent long-lasting changes in microbiota composition, associated with increase in fat mass. High-fat-high-glucose diet promoted this effect while co-housing with mock-treated animals overwrote the weight gain. Our data suggest that in the critical phase of infancy even a single silent viral infection could cast a long shadow and cause long-term microbiota perturbations, affecting adult host physiology.

npj Biofilms and Microbiomes (2022)8:51; <https://doi.org/10.1038/s41522-022-00315-x>

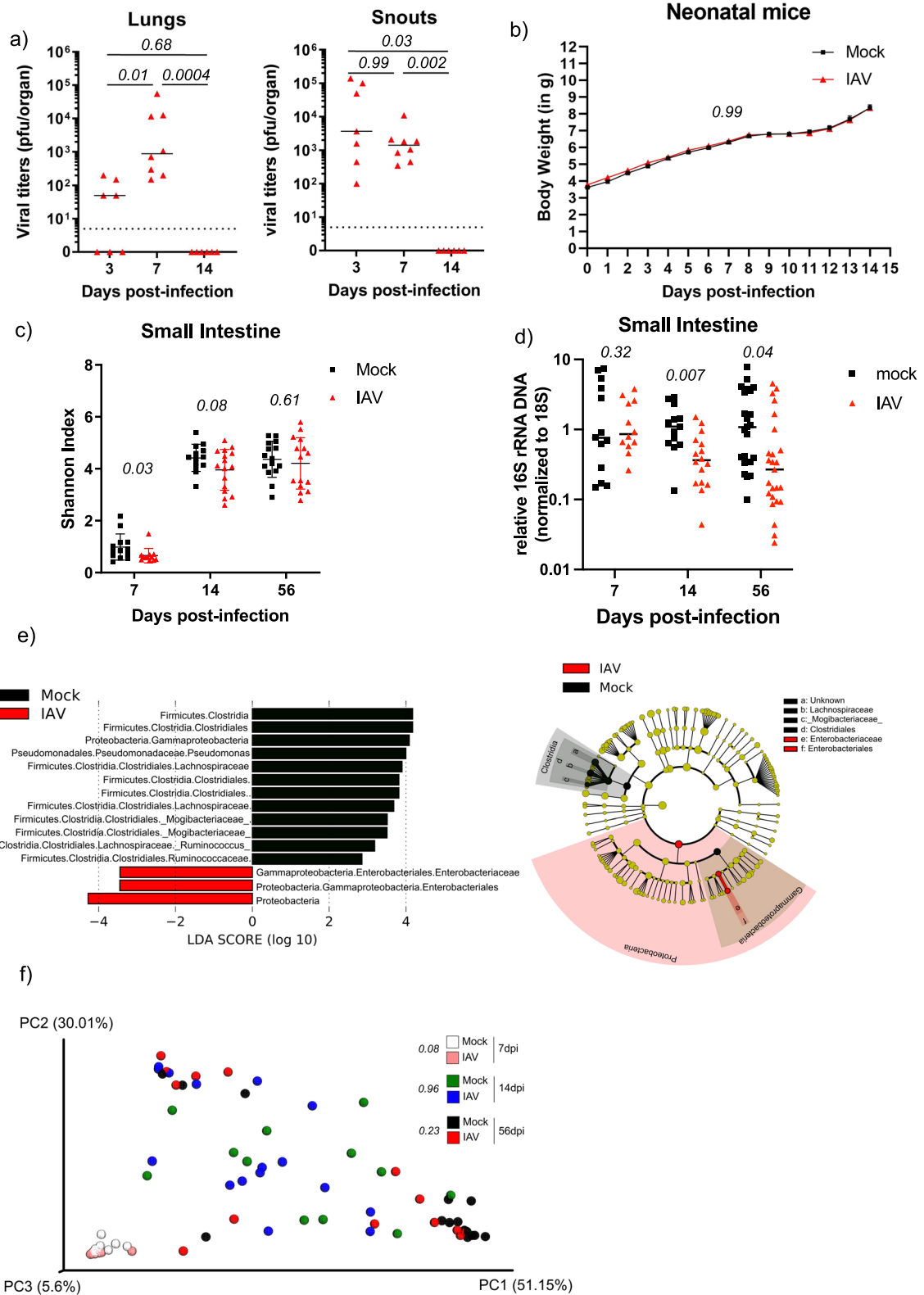
The establishment of a stable adult-like intestinal microbiota takes three to four years in humans (reviewed in¹). In laboratory mice, this phase takes about three weeks², due to the higher developmental speed, and is largely driven by the change in nutrition from milk to solid chow. Interference with microbial ecology in this early phase, e.g., by administering antibiotics (ABX), results in a long-term dysbiotic state and increased incidence of obesity and type II diabetes both in humans^{3,4} and mice⁵. Of note, the time frame between ABX treatment and clinical readout was limited in human observational studies to a maximum of 12 years.

Infancy is also a phase in human life with increased incidence of acute infections. From previous experiments we knew, that an established and robust adult intestinal microbiota, returns to baseline after undergoing qualitative and quantitative changes in consequence of an acute infection, e.g., with influenza A virus^{6–9}. We hypothesized that a single acute infection event, might be sufficient to permanently perturb commensal bacterial composition, when occurring in a dynamic and vulnerable phase of microbiota development. As a proof of concept, we demonstrate here that infant mice infected with influenza A virus (IAV) undergo a microbiota imprinting event, with an elevated risk for long-lasting qualitative and quantitative changes in intestinal microbiota composition and overall animal growth.

Infection of 7d-old (D7), infant C57BL/6J mice with a single sublethal dose (40pfu) of influenza A virus A/Viet Nam/1203/2004 Halo¹⁰, which resulted in robust viral replication restricted to the upper and lower respiratory tract (as determined by plaque assay (Fig. 1a and Fig. S1a), had no measurable impact on early life body weight development (Fig. 1b). This dose was previously used to sub-lethally infect adult animals⁶ and surprisingly did not cause

differences in weight gain here infant mice. Our finding contrasts observations made with mouse-adapted H1N1 virus, which is more lethal in neonate mice¹¹. We thus consider our model as a subclinical infection model, mimicking a mild childhood disease in humans. Viral titers were cleared by 14d post-infection, comparable to viral kinetics in adult animals⁶. We next used 16S rRNA gene-specific next-generation sequencing (NGS) as described previously⁶ on total DNA from small intestinal tissue homogenates from day 7, 14, and 56-post viral infection. Mice were infected in at least two independent experiments with at least two independent cages per run. In adult animals, we previously described quantitative reduction of small intestinal microbiota in IAV-infected animals, associated with a reduced alpha diversity and a shift in beta diversity. At the same time, we did not find changes in fecal microbiota diversity⁶. Similar to these results from adult mice infected with IAV, infant mice displayed significantly reduced alpha diversity 7d post-infection, but not at later time points (Fig. 1c). Additionally, we found overall ~5-fold reduced 16S/18S levels⁶ in the small intestine of D56 mice infected with IAV in infancy, indicating a long-term reduction in bacterial colonization by viral imprinting (Fig. 1d). Of note by D14 post-infection we already determined a reduced 16S/18S ratio, suggesting that this development starts during or right after clearance of the virus. When comparing microbiota composition on day 7-post infection, we found predominance of Bacilli both in mock-treated and IAV-infected animals, which is likely a consequence of breast milk-based nutrition (Fig. S2a). The drop in alpha diversity and the relative overrepresentation of Lactobacilli could be explained by a loss of low abundance populations, present in mock-treated mice (Fig. S2a/b). 14 days post-treatment (age 21d) mice showed diversified intestinal microbiota, with all major classes present in

¹Department of Microbiology and Molecular Medicine, Faculty of Medicine, University of Geneva, Geneva, Switzerland. ²Geneva Center for Inflammation Research, Geneva, Switzerland. ³These authors contributed equally: Soner Yildiz, Beryl Mazel-Sanchez, Joao P. P. Bonifacio. ✉email: mirco.schmolke@unige.ch



adult microbiota (Fig. S2a), most likely to the introduction of solid food into the diet and the lack of continuous milk intake. LefSe analysis¹² revealed significant increase in Gammaproteobacteria in IAV-infected mice at this stage (Fig. S2c). By day 56-post infection (9-week-old mice) we found Enterobacteriaceae significantly increased in IAV-infected mice. Conversely, in mock-treated

animals several groups of Firmicutes (mainly of the class Clostridia) were enriched. (Fig. 1e) Intriguingly, in mice, Enterobacteriaceae are favored under high-fat diet conditions¹³ or after low dose penicillin treatment, which both lead to obesity in mice⁵. In line with our findings from adult mice, in two American studies, populations of obese patients had enriched Enterobacteriaceae

Fig. 1 Neonatal IAV infection changes microbiota composition in adult mice. Seven-days-old mice were infected intranasally with PBS or 40 pfu of VN/1203 in 5 μ L of PBS. **a** At 3-, 7- and 14 dpi viral titers in lungs and snouts for IAV infected mice were determined by plaque assay. Each dot represents one animal ($n = 7-8$) and the median titer is represented by a black dash. Limit of detection is represented by a black dashed line. Statistical significance between groups was determined by Kruskal–Wallis test. P -values are indicated. **b** Body weight was followed for 14 days after infection and values for male mice are plotted as mean \pm SEM ($n = 29$ for mock-treated and $n = 38$ for IAV-infected). Statistical significance between groups was determined by 2-way Anova test. P -value is indicated. **c** Individual Shannon H-index of small intestine microbiota at 7, 14, and 56dpi of mock-treated (black squares) and IAV-infected mice (red triangles) are depicted for indicated days of sampling. Mean \pm SD per experimental group are shown. Statistical significance between groups was determined by unpaired students' t -test. P -values are indicated. **d** Normalized individual 16S/18S qPCR results (n-fold relative to mean of mock samples) in small intestine at 7, 14, and 56 dpi are depicted for mock-infected (black squares) and IAV-infected (red triangles). Mean \pm SD per experimental group are shown. Statistical significance between groups was determined by unpaired students' t -test. **e** LefSe analysis of the composition of the microbiota in small intestines of mock-treated and IAV-infected mice based on 16S rRNA gene sequencing of samples collected at 56dpi. Linear discriminant analysis scores (LDA) are indicated for different taxonomic groups significantly overrepresented ($p < 0.05$) in mock-treated or IAV infected mice. ($n = 15$). Kruskal–Wallis statistical test was performed as described previously¹². Cladograms of OTUs, as annotated by Qiime1, that are differentially represented in small intestine samples taken from mock and IAV infected animals on the right-hand side. Overrepresented taxonomy groups are given on legends next to the corresponding cladogram. **f** Scaled 3D principal coordinates analysis (PCoA) plots using a weighted-UniFrac distance matrix from small intestine microbiota of mock-treated or IAV-infected mice at indicated time points post-infection. Each symbol represents one individual mouse. Percentages explain variation in PC1 (x-axis), PC2 (y-axis) and PC3 (z-axis). PERMANOVA and PERMDISP statistical tests were performed and p -values are indicated in the figure and listed in Supplementary Table 1.

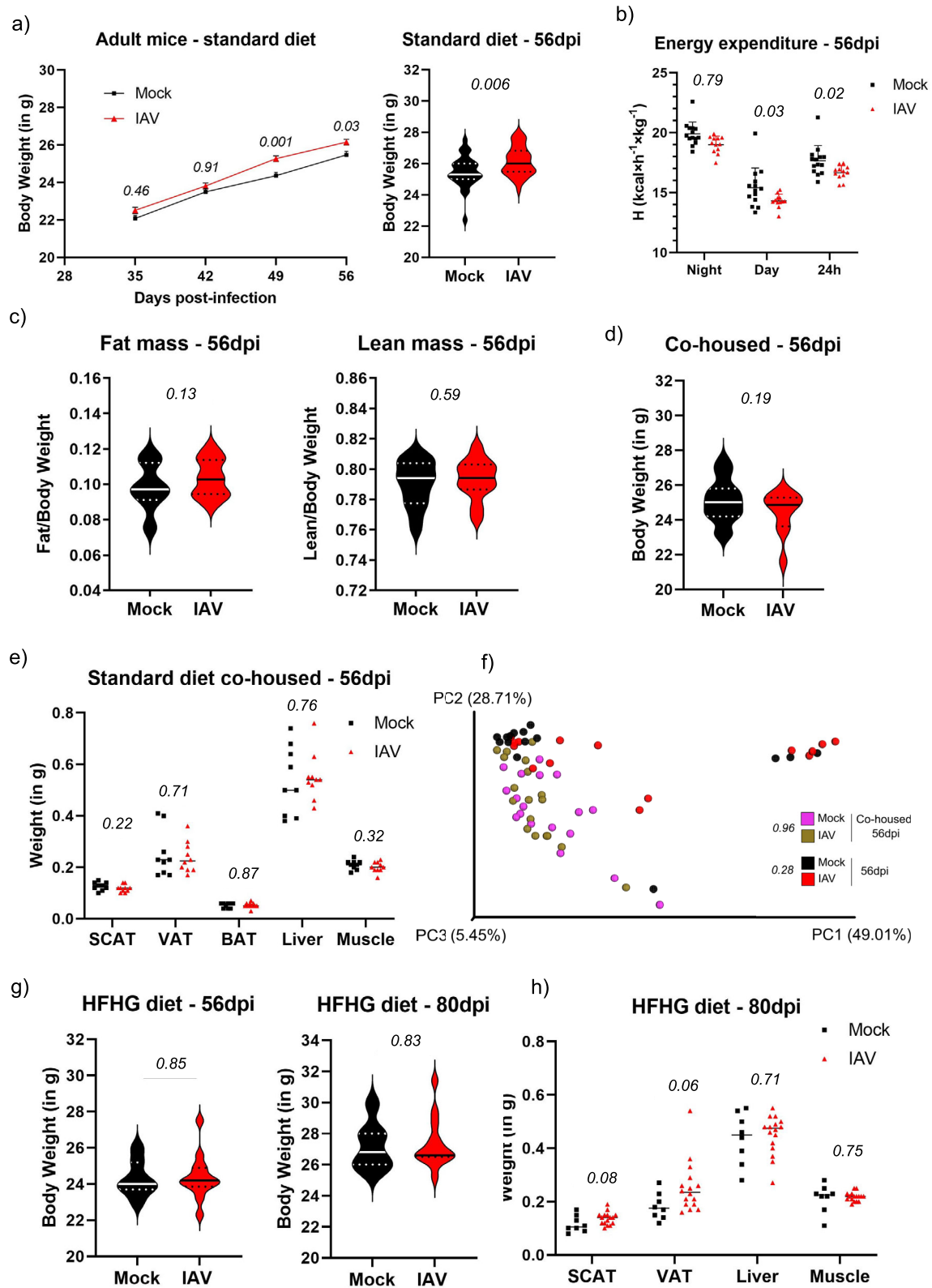
and decreased Clostridia¹⁴. In accordance with the compositional data, weighed PCoA analysis revealed a more dispersed beta diversity for mock-treated animals on D7 post-infection (Fig. 1f). By D14 post-infection, no obvious differences between the two mouse groups were apparent. Interestingly, a higher divergence along PC1 and PC2 was found for IAV-infected animals on D56 post-infection, which does not reach statistical significance, probably as a consequence of the large variance within this group (see Permadisp analysis in Supplementary Table 1). A direct comparison of D56 mock and IAV treated mice by Permanova analysis indicated a p -value of 0.178. Since we cannot monitor the severity of the infection in the young mice, due to lack of clinical signs, we propose that variability of infection could explain why few of the infected animals cluster with the majority of the mock-treated mice (bottom right corner of the graph in Fig. 1f). While IAV does not replicate in the intestine an increased interferon response was proposed to trigger microbiota changes in the intestinal tract after IAV infection⁸. We confirmed the absence of viral RNA in the small intestine by highly sensitive qPCR (Fig. S2d). Intriguingly we found 2fold-increased levels of IL28 mRNA but no changes in IP10 mRNA in the intestine of mice infected with IAV (Fig. S2e). This could explain the alterations of microbiota diversity and composition. At this stage, we speculate that the loss of rare OTUs might create a bottleneck early in life, which results in different trajectory of microbial community development. Likely, both direct and indirect mechanism play a role in this alteration. Obviously, this would open a therapeutic window for correction of infection-dependent microbiota depletion, e.g., by targeted application of probiotics. Strikingly, as previously shown in adult animals⁶, fecal microbiota were completely resistant to infection-related imprinting effects as shown by indistinguishable alpha and beta diversity and only minor differences in composition (Fig. S3a–c).

Intestinal microbiota are a driving force of host physiology (reviewed in¹⁵). In adult mice, acute IAV infection causes metabolic changes in adipose tissues, which eventually last until after IAV clearance¹⁶. We thus asked whether the long-term changes in small intestinal microbiota composition after early-life infection indeed affect the metabolism of adult mice. A striking observation arose from adult body weight curves. While there was overall no difference in the weight development of infected vs. mock-treated mice, gender-stratified data revealed a clear increase of absolute body weight in adult male mice infected with IAV in early in life starting around D42 post-infection (Fig. 2a), adding up to a median of about 3% body weight gain by D56 post-infection. We observed overall a similar tendency but with more variation in body weight among female mice, potentially due to the unsynchronized hormonal cycle of these animals (Fig. S4a). It

further has to be taken into account, that female mice respond generally weaker to e.g., diet-induced weight gain¹⁷. Hence, we focused on male mice to further address the observed weight gain phenotype. Since both decreased activity or increased food uptake or processing could be a reason for the increase weight, we performed metabolic phenotyping of individually caged male mice 56d post-infection using TSE Labmaster system (TSE Systems, Germany). We found no difference in movement patterns, food, and water intake, or fatty acid oxidation¹⁸, which could have explained increased body weight (Fig. S4b–f). Similarly, caloric uptake, as determined by bomb calorimetry of consumed food and shed fecal matter, yielded no differences between the two mouse groups (Fig. S4g). We did, however, observe a decrease in specific energy expenditure (determined by indirect calorimetry¹⁹) after IAV infection, both during day- and night-time which could explain in part the increase body weight (Fig. 2b). We next determined lean and fat mass by Echo-MRI, and found a tendency for increased total fat mass in previously IAV-infected mice ($p = 0.13$) (Fig. 2c). Acute IAV infection was recently shown to affect white fat browning¹⁶. However, analysis of fat browning-related marker genes did not reveal important differences in mRNA expression as determined by specific qPCR (Fig. S4h). This makes involvement of reduced-fat browning in weight gain unlikely.

In order to address if intestinal microbiota were responsible for the weight gain, we co-housed mice in parallel to non-co-housed experiments described before, which were either treated with PBS or IAV in infancy, in equal proportion, after weaning and after viral clearance and followed weight gain until nine weeks of age. Importantly, we did not observe differences in median weight gain between PBS treated and IAV infected animals (Fig. 2d) or differences in selected organ weights (Fig. 2e), implicating that exchange of microbiota with PBS treated animals could compensate for the effects by IAV infection early in life. Co-housing resulted indeed in a significantly distinct microbiota as indicated by the shift in beta diversity away from both non-co-housed IAV-infected mice (Fig. 2f). Importantly, towards the non-co-housed mock-treated mice these differences were not significant. There was no difference in beta diversity between cohoused IAV infected and mock-treated mice, confirming the successful exchange of intestinal microbiota between infected and mock-treated mice. Accordingly, we did not find major differences in the compositional data (Fig. S5 and Supplementary Table 2). This implicates that microbiota exchange with mock animals can override the IAV-caused dysbiosis even after viral clearance.

Finally, we asked, if mice, which underwent an IAV infection in infancy were more prone to diet-induced alterations of body mass. We hence fed a high fat/high glucose (HFHG) diet ad libitum



from 35d post-infection onwards to IAV infected or PBS treated mice. While the overall body mass did not differ between PBS treated and infected mice on D56 or D80 post-infection (Fig. 2g), we found an increase in visceral and subcutaneous fat in adult mice (D80 post-infection), which were infected with IAV in infancy

(Fig. 2h) with about 30% median effect size in VAT. This suggests that early life infections could sensitize to adulthood food-induced gain of fat mass in specific depots. The mechanistic link between the altered microbiota after early life IAV infection and the metabolic changes will require additional investigations.

Fig. 2 IAV related imprinting causes long term metabolic changes. **a** Body weight was monitored for each mouse weekly for 56 days after infection and values of male mice are plotted as mean \pm SEM – left panel. Individual weight values of male mock-treated ($n = 29$) and IAV-infected mice ($n = 38$) at 56dpi are shown—right panel. Statistical significance between groups was determined by unpaired student's *t*-test (left panel) and two-way ANOVA (right panel). **b** Energy expenditure in calories (H) for individual male mice at 56dpi from mock-treated (black squares) and IAV-infected groups (red triangles) are depicted for indicated periods of the day. Mean \pm SD are represented. **c** Fat mass (left panel) and lean mass (right panel) of individual male mock-treated mice ($n = 14$) or male IAV-infected mice ($n = 12$) was measured by EchoMRI at 56dpi. **d** Individual weight values of male mock-treated ($n = 15$) and male IAV-infected co-housed mice ($n = 10$) at 56dpi are shown. **e** Individual organs weight from mock-treated ($n = 9$) and IAV-infected co-housed mice ($n = 10$) at 56dpi are depicted by different organ/tissue. Median is represented by a black dash for each group. Statistical significance between groups was determined by unpaired student's *t*-tests. **f** Scaled 3D principal coordinates analysis (PCoA) plots using a weighted-UniFrac distance matrix from small intestine microbiota of co-housed mock-treated or IAV-infected mice and single housed mock-treated or IAV-infected mice at 56 post-infection. Each symbol represents one individual mouse and single-housed mice data are the same as in Fig. 1f. Percentages explain variation in PC1 (x-axis), PC2 (y-axis) and PC3 (z-axis). PERMDISP statistical tests were performed and *p*-values are indicated in the figure and listed in Supplementary Table 1. **g** Individual weight values of male mock-treated ($n = 7$) and male IAV-infected mice ($n = 13$) at 56dpi (left panel) or 80dpi (right panel) fed a high fat/high glucose (HFHG) diet are shown. Statistical significance between groups was determined by unpaired student's *t*-tests. **h** Individual organs weight from mock-treated ($n = 8$) and IAV-infected mice ($n = 16$) fed a high fat/high glucose (HFHG) diet at 80dpi are depicted by different organ/tissue. SCAT subcutaneous adipose tissue, VAT visceral adipose tissue, BAT brown adipose tissue. Median is represented by a black dash for each group. Statistical significances were determined by two-way ANOVA. *p*-values are indicated in the graphs.

While we cannot provide a detailed mechanism at this stage, we believe that our proof of principle study demonstrates that a single acute infection early in life could cause sufficient perturbation of intestinal microbiota development to provoke long-lasting changes in commensal bacterial composition and their function in host metabolism. Beyond changes in the host metabolism, early life infections could also affect other microbiome-driven processes of the host organism.

Limitations of this study: While mice are frequently used as a model system to study pathological effects of microbiota changes, they differ in many ways from humans. Microbiota compositions is substantially different^{20,21}, mice are coprophagic allowing easier exchange of intestinal microbiota between cage mates^{22,23}, mice have a faster aging rate and a substantially increased metabolic rate as compared to humans. Since we cannot sample small intestinal content from mice longitudinally, we can only provide snap-shots of microbiota dynamics, without the option of following the development within each animal.

We nonetheless believe that for our proof-of-principle study the mouse model remains useful. IAV-caused microbiota changes were also described in adult human patients²⁴. Association studies in humans would be required to prove, if severe childhood infections could have long-lasting impact on microbiota composition and host physiology.

METHODS

Animal experiments, metabolic phenotyping, and organ collection

C57BL/6J mice (male/female, 7–8 weeks of age) were purchased as breeders from Charles River Laboratories (France). Animals were housed at specific pathogen free (SPF)/biosafety level 2 (BSL2) animal facility of Central Medical University (CMU) at University of Geneva under a strict 12-hour light/dark cycle and fed ad libitum with standard chow diet (RM3 (E) FG, 3 Special Diets Service, UK) unless otherwise stated. Breeding couples were time-mated and 7-day old pups, born in house to IAV naive parents, were used for the experiments indicated in this study. At age 21d, pups were weaned and housed separately based on sex and experimental group. All animals were introduced to a new clean cage with fresh bedding and enrichment every two weeks.

For infection, 7-day-old pups were inoculated with 5 μ l of PBS (1X) or IAV A/Viet Nam/1203/2004 (VN/1203, 40 pfu) HALo¹⁰ (low pathogenic version) through intranasal route without anesthesia. Body weights of the animals were followed daily for two weeks following infection, then weekly up to 56 days post-infection, if not every two days for animals under HFHG diet.

For physiological and metabolic phenotyping¹⁸, 56-day-old mice (either mock-treated or IAV infected at 7-day of age), were individually introduced into TSE Labmaster/Phenomaster (TSE Systems, Germany). Animals were adapted to the caging conditions for two days. Experimental data were gathered for 3 days following the adaptation period. Energy expenditure was calculated based on V_{O_2} and V_{CO_2} from individually housed mice¹⁹.

At 42 days post-infection, animals were introduced to clean cages in pairs. Food intake and feces production over 48 hours were measured for each cage. Fecal pellets were subsequently collected, vacuum-dried, and grounded to fine powder. Caloric content of food and feces was measured by an oxygen bomb calorimeter (Parr, 6100, USA)²⁵. Average caloric uptake of two animals was calculated based on caloric content of consumed food and excreted feces. At 56 days post-infection, body composition of the animals, i.e., fat mass, lean mass, and free fluids, were analyzed through the use of EchoMRI-700 (EchoMRI, Houston, USA), without anesthesia.

For experiments including high caloric diet, animals were fed HFHG diet (HCD), (22.1 MJ/kg Gross Energy; 45 kJ% Fat, 20 kJ% Protein, 35 kJ% Carbohydrates, D12451, Ssniff, Germany) for 3 weeks starting from 35 days post-infection, at age of 6 weeks.

Upon reaching experimental endpoints, animals were euthanized using controlled CO₂ exposure. Organs were sampled following euthanasia using sterile tools, sterilized between groups, under aseptic conditions. Tissue samples were collected from visceral adipose tissue (epididymal WAT, unilateral), subcutaneous adipose tissue (inguinal WAT, unilateral), liver (medial lobe), or muscle (quadriceps, unilateral). Samples were weighed where necessary and immediately stored at -80°C to be used in viral titer determination, metabolic processing or extraction of DNA. Fecal pellets were freshly sampled on the day indicated before euthanasia. Infectious virus particles in indicated organs were quantified by standard plaque assay on MDCK cells²⁶. Briefly, organ homogenates were precleared using 2000 \times g centrifugation at 4 $^{\circ}\text{C}$. Supernatants were serially diluted and transferred to confluent monolayers of MDCK cells. These were subsequently overlaid with 2% agar-containing medium to limit free viral diffusion and allow plaque formation. Plaques were stained with crystal violet solution and counted to determine infectious virus titers.

All animal procedures were in accordance with federal regulations of the Bundesamt für Lebensmittelsicherheit und Veterinärwesen (BLV) Switzerland (Tierschutzgesetz) and approved by cantonal authorities (License number: GE/159/17).

Quantitative PCR for viral genomic RNA and host mRNA

Total tissue RNA was isolated using Trizol (Invitrogen). By reverse transcription (Superscript III) using either a vRNA-specific reverse primers for IAV²⁷ or oligo dT primer we generated cDNA according to the manufacturer's protocol. Quantitative PCR was performed using SYBR-Green. Primers for brownning-related genes were previously published²⁸. 16S and 18S specific qPCRs were described earlier⁶ (16S_F: 5'- TCC TACGGGAGGCAGCAGT -3'; 16S_R: 5'- GGACTACCAGGGTATCTAATCTT -3'; 18S_F: 5'- GTAACCCGTTGAACCCATT -3'; 18S_R: 5'- CCATCCAATCGGTAG TAGCG -3'; M1_F: 5'- AGATGAGTCTTCAACCGAGGTCG -3'; M1_R: 5'- TGCA AAAACATCTTCAAGTCTCTG -3'; IP-10_F: 5'- TTCACCATGTGCCATGCC -3'; IP-10_R: 5'- GAACTGACGAGCCTGAGCTAGG -3'; IL28_F: 5'- GTTCAAGTC TCTGTCCCAAAA -3'; IL28_R: 5'- GTGGGAAGTGCACCTCATGT -3'; PRDM16-F: 5'-CAGCACGGTGAAGCCATTC-3', PRDM16-R: 5'-GCGTGCATCCG CTTGTG-3'; UCP1_F: 5'- CACCTTCCCCTGGACACT -3'; UCP1_R: 5'- CCCTAG GACACCTTTATACCTAATGG -3'; TBX1_F: 5'-

CIDE-A_F: 5'- TGACATTCATGGGATTGCAGAC -3'; CIDE-A_R: 5'- GGCCAG TTGTGATGACTAAGAC -3'). Samples were measured in technical triplicates. Fold changes were determined based on the $2^{-\Delta\Delta\text{CT}}$ method²⁹.

Bacteria DNA Extraction, Library construction, and Bioinformatic analysis

Total DNA extraction from small intestine and fecal pellets was performed using QIAGEN Pathogen Cador Mini kit (USA) and PowerLyzer PowerSoil DNA isolation kit (MoBio, QIAGEN, USA), respectively, according to manufacturer's instructions with slight modifications^{6,30}, together process matched control tubes. DNA preps were used either for 16S rRNA DNA quantification or library preparation for analysis of bacterial composition³⁰. QIIME1³¹ was used for bioinformatics analysis of the sequences generated through Illumina (USA) sequencing through a pre-defined pipeline^{6,32–40}.

Statistics

In order to determine statistical significance, we applied unpaired students' t-test for parametric comparison of two experimental groups, or Kruskal-Wallis or 2-way Anova for comparison of longitudinal data sets, and multiple corrected t-tests for comparison of more than two parameters from the same two experimental samples, using Graph Pad Prism 7.0. T Statistical tests are indicated in each figure legend. Analysis of microbiome composition was performed using LefSe¹². Statistical analysis of beta diversity was done with PERMANOVA and PERMADISP^{41,42}.

DATA AVAILABILITY

NGS sequencing data are deposited under NCBI Bioproject PRJNA768309. Material is available through the lead contact.

Received: 19 October 2021; Accepted: 15 June 2022;

Published online: 02 July 2022

REFERENCES

- Arrieta, M. C., Stiemsma, L. T., Amenogbe, N., Brown, E. M. & Finlay, B. The intestinal microbiome in early life: health and disease. *Front Immunol.* **5**, 427 (2014).
- Al Nabhani, Z. et al. A weaning reaction to microbiota is required for resistance to immunopathologies in the adult. *Immunity* **50**, 1276–1288 (2019). e1275.
- Boursi, B., Mamtani, R., Haynes, K. & Yang, Y. X. The effect of past antibiotic exposure on diabetes risk. *Eur. J. Endocrinol.* **172**, 639–648 (2015).
- Azad, M. B., Bridgman, S. L., Becker, A. B. & Kozyrskyj, A. L. Infant antibiotic exposure and the development of childhood overweight and central adiposity. *Int J. Obes. (Lond.)* **38**, 1290–1298 (2014).
- Cox, L. M. et al. Altering the intestinal microbiota during a critical developmental window has lasting metabolic consequences. *Cell* **158**, 705–721 (2014).
- Yildiz, S., Mazel-Sanchez, B., Kandasamy, M., Manicassamy, B. & Schmolke, M. Influenza A virus infection impacts systemic microbiota dynamics and causes quantitative enteric dysbiosis. *Microbiome* **6**, 9 (2018).
- Groves, H. T. et al. Respiratory disease following viral lung infection alters the murine gut microbiota. *Front Immunol.* **9**, 182 (2018).
- Deriu, E. et al. Influenza virus affects intestinal microbiota and secondary salmonella infection in the gut through Type I interferons. *PLoS Pathog.* **12**, e1005572 (2016).
- Sencio, V. et al. Gut Dysbiosis during influenza contributes to pulmonary pneumococcal superinfection through altered short-chain fatty acid production. *Cell Rep.* **30**, 2934–2947 (2020). e2936.
- Steel, J. et al. Live attenuated influenza viruses containing NS1 truncations as vaccine candidates against H5N1 highly pathogenic avian influenza. *J. Virol.* **83**, 1742–1753 (2009).
- Lines, J. L., Hoskins, S., Hollifield, M., Cauley, L. S. & Garvy, B. A. The migration of T cells in response to influenza virus is altered in neonatal mice. *J. Immunol.* **185**, 2980–2988 (2010).
- Segata, N. et al. Metagenomic biomarker discovery and explanation. *Genome Biol.* **12**, R60 (2011).
- Singh, R. P., Halaka, D. A., Hayouka, Z. & Tirosh, O. High-fat diet induced alteration of mice microbiota and the functional ability to utilize fructooligosaccharide for ethanol production. *Front Cell Infect. Microbiol.* **10**, 376 (2020).
- Peters, B. A. et al. A taxonomic signature of obesity in a large study of American adults. *Sci. Rep.* **8**, 9749 (2018).
- Miller, B. M., Liou, M. J., Lee, J. Y. & Baumler, A. J. The longitudinal and cross-sectional heterogeneity of the intestinal microbiota. *Curr. Opin. Microbiol.* **63**, 221–230 (2021).
- Ayari, A. et al. Influenza infection rewires energy metabolism and induces browning features in adipose cells and tissues. *Commun. Biol.* **3**, 237 (2020).
- Hong, J., Stubbins, R. E., Smith, R. R., Harvey, A. E. & Nunez, N. P. Differential susceptibility to obesity between male, female and ovariectomized female mice. *Nutr. J.* **8**, 11 (2009).
- Tschop, M. H. et al. A guide to analysis of mouse energy metabolism. *Nat. Methods* **9**, 57–63 (2011).
- Even, P. C. & Nadkarni, N. A. Indirect calorimetry in laboratory mice and rats: principles, practical considerations, interpretation, and perspectives. *Am. J. Physiol. Regul. Integr. Comp. Physiol.* **303**, R459–R476 (2012).
- Hugenholtz, F. & de Vos, W. M. Mouse models for human intestinal microbiota research: a critical evaluation. *Cell Mol. Life Sci.* **75**, 149–160 (2018).
- Nguyen, T. L., Vieira-Silva, S., Liston, A. & Raes, J. How informative is the mouse for human gut microbiota research? *Dis. Model Mech.* **8**, 1–16 (2015).
- Ebino, K. Y., Yoshinaga, K., Saito, T. R. & Takahashi, K. W. A simple method for prevention of coprophagy in the mouse. *Lab Anim.* **22**, 1–4 (1988).
- Bogatyrev, S. R., Rolando, J. C. & Ismagilov, R. F. Self-reinoculation with fecal flora changes microbiota density and composition leading to an altered bile-acid profile in the mouse small intestine. *Microbiome* **8**, 19 (2020).
- Qin, N. et al. Influence of H7N9 virus infection and associated treatment on human gut microbiota. *Sci. Rep.* **5**, 14771 (2015).
- Chevalier, C. et al. Gut microbiota orchestrates energy homeostasis during cold. *Cell* **163**, 1360–1374 (2015).
- Anchisi, S., Goncalves, A. R., Mazel-Sanchez, B., Cordey, S. & Schmolke, M. Influenza a virus genetic tools: from clinical sample to molecular clone. *Methods Mol. Biol.* **1836**, 33–58 (2018).
- Hoffmann, E., Stech, J., Guan, Y., Webster, R. G. & Perez, D. R. Universal primer set for the full-length amplification of all influenza A viruses. *Arch. Virol.* **146**, 2275–2289 (2001).
- Fabbiano, S. et al. Caloric restriction leads to browning of white adipose tissue through Type 2 immune signaling. *Cell Metab.* **24**, 434–446 (2016).
- Livak, K. J. & Schmittgen, T. D. Analysis of relative gene expression data using real-time quantitative PCR and the 2(-Delta Delta C(T)) Method. *Methods* **25**, 402–408 (2001).
- Yildiz, S. et al. Respiratory tissue-associated commensal bacteria offer therapeutic potential against pneumococcal colonization. *Elife* **9**, <https://doi.org/10.7554/eLife.53581> (2020).
- Caporaso, J. G. et al. QIIME allows analysis of high-throughput community sequencing data. *Nat. Methods* **7**, 335–336 (2010).
- Edgar, R. C., Haas, B. J., Clemente, J. C., Quince, C. & Knight, R. UCHIME improves sensitivity and speed of chimera detection. *Bioinformatics* **27**, 2194–2200 (2011).
- DeSantis, T. Z. et al. Greengenes, a chimera-checked 16S rRNA gene database and workbench compatible with ARB. *Appl Environ. Microbiol.* **72**, 5069–5072 (2006).
- Caporaso, J. G. et al. PyNAST: a flexible tool for aligning sequences to a template alignment. *Bioinformatics* **26**, 266–267 (2010).
- Wang, Q., Garrity, G. M., Tiedje, J. M. & Cole, J. R. Naive Bayesian classifier for rapid assignment of rRNA sequences into the new bacterial taxonomy. *Appl Environ. Microbiol.* **73**, 5261–5267 (2007).
- Chao, A. Nonparametric estimation of the classes in a population. *Scand. J. Stat.* **11**, 265–270 (1984).
- Aronesty, E. Comparison of sequencing utility programs. *Open Bioinform. J.* **7**, 1–8 (2013).
- Colwell, R. C. et al. Models and estimators linking individual-based and sample-based rarefaction, extrapolation and comparison of assemblages. *J. Plant Ecol.* **5**, 3–21 (2012).
- Shannon, C. E. A mathematical theory of communication. *Bell Syst. Tech. J.* **27**, 623–656 (1948).
- Lozupone, C. & Knight, R. UniFrac: a new phylogenetic method for comparing microbial communities. *Appl Environ. Microbiol.* **71**, 8228–8235 (2005).
- Anderson, M. Permutational Multivariate Analysis of Variance (PERMANOVA). <https://doi.org/10.1002/9781118445112.stat07841> (2017).
- Anderson, M. J., Ellingsen, K. E. & McArdle, B. H. Multivariate dispersion as a measure of beta diversity. *Ecol. Lett.* **9**, 683–693 (2006).

ACKNOWLEDGEMENTS

This project was funded by the Swiss National Fund (SNF 310030_182475) granted to MS. We would like to express our gratitude to the excellent service provided by the animal care takers of the CMU and to the genomics core facility Ige3 of the CMU. We thank Dr. N. Hulo for his advice on statistical analysis.

AUTHOR CONTRIBUTIONS

S.Y., B.M.S., J.P.P.B., M.S.: Conceptualized study, performed experiment, analyzed and interpreted data, wrote the manuscript. S.Y., B.M.S., and J.P.P.B. contributed equally to this manuscript. M.S. acquired funding for this project.

COMPETING INTERESTS

The authors declare no competing interests.

ADDITIONAL INFORMATION

Supplementary information The online version contains supplementary material available at <https://doi.org/10.1038/s41522-022-00315-x>.

Correspondence and requests for materials should be addressed to Mirco Schmolke.

Reprints and permission information is available at <http://www.nature.com/reprints>

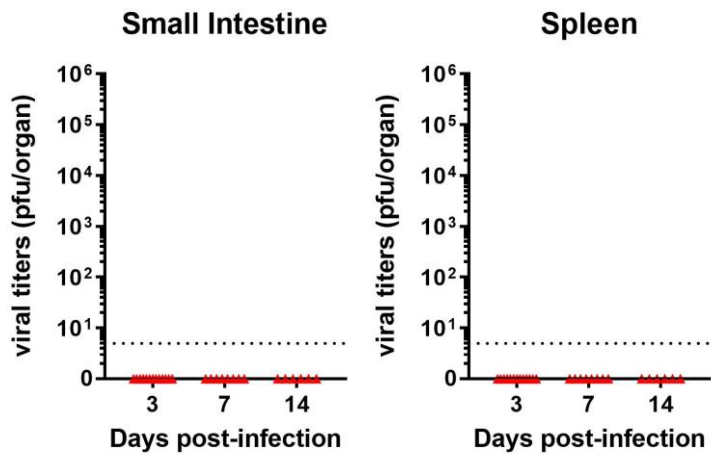
Publisher's note Springer Nature remains neutral with regard to jurisdictional claims in published maps and institutional affiliations.



Open Access This article is licensed under a Creative Commons Attribution 4.0 International License, which permits use, sharing, adaptation, distribution and reproduction in any medium or format, as long as you give appropriate credit to the original author(s) and the source, provide a link to the Creative Commons license, and indicate if changes were made. The images or other third party material in this article are included in the article's Creative Commons license, unless indicated otherwise in a credit line to the material. If material is not included in the article's Creative Commons license and your intended use is not permitted by statutory regulation or exceeds the permitted use, you will need to obtain permission directly from the copyright holder. To view a copy of this license, visit <http://creativecommons.org/licenses/by/4.0/>.

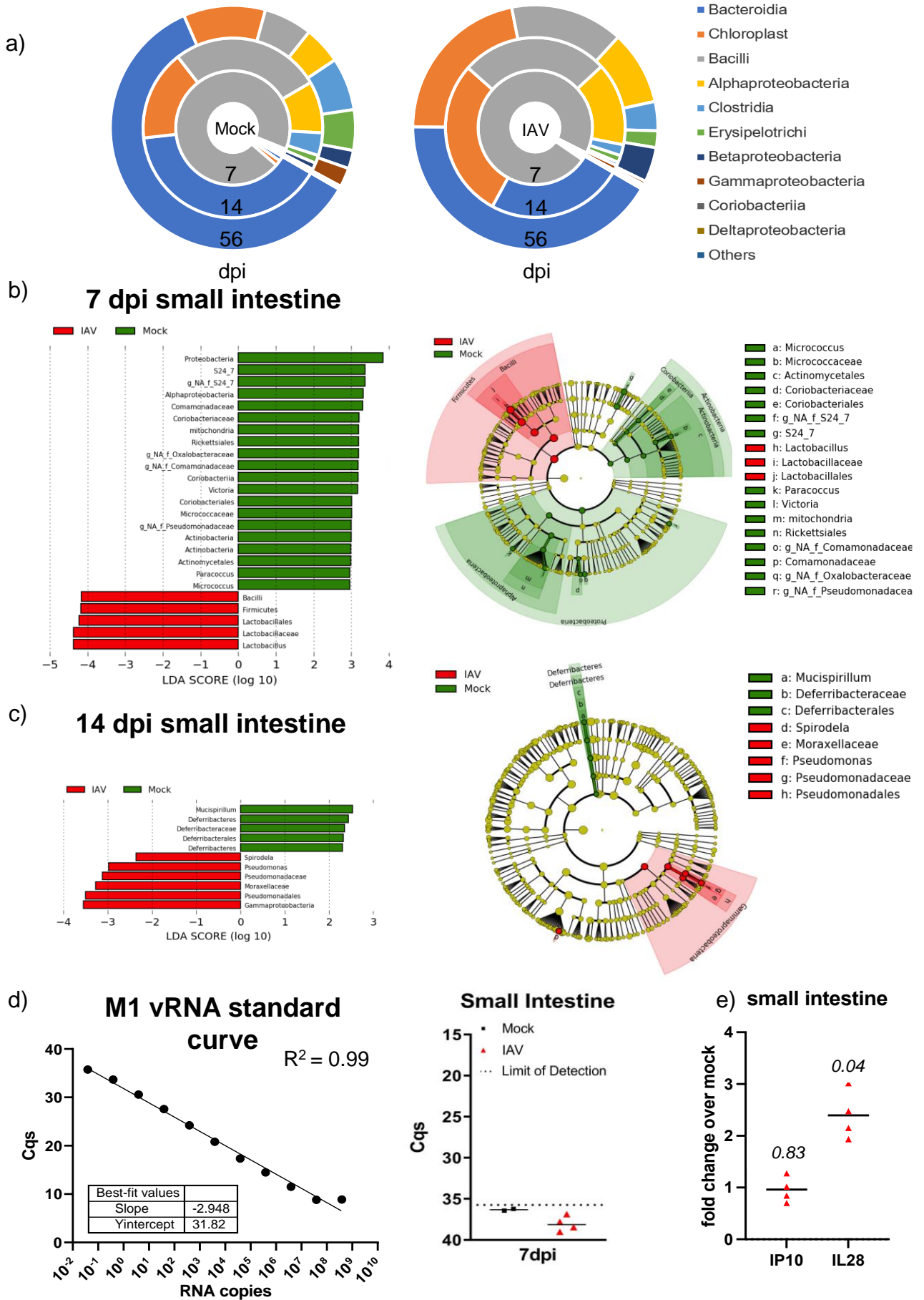
© The Author(s) 2022

Supplementary Figures



Supplementary Figure 1: IAV titers in small intestine and spleen

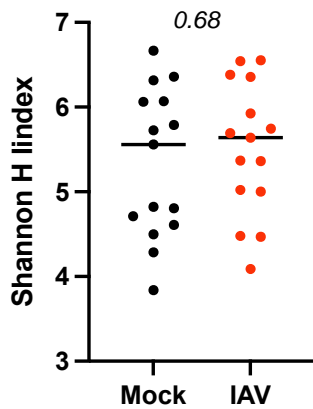
Seven-days-old mice were infected intranasally with PBS or 40 pfu of VN/1203 in 5 μ L. (a) At 3, 7 and 14 days post-infection (dpi) viral titers in intestine (left panel) and spleen (right panel) for IAV infected mice were determined by plaque assay. Limit of detection is represented by a black dashed line. No statistical testing was performed.



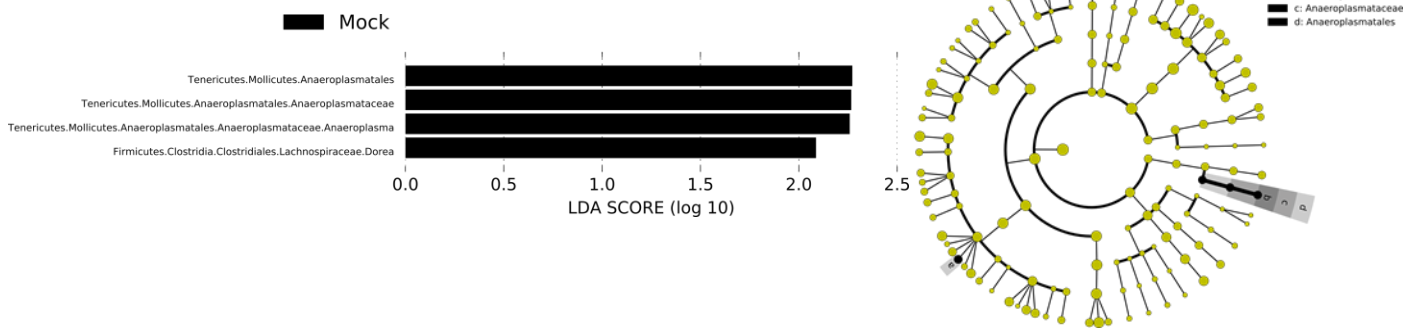
Supplementary Figure 2: microbiota composition in small intestine

(a) Microbiota composition in the small intestine of IAV or mock treated animals on D56 post infection. Mean relative bacterial abundance as analyzed by Qiime1 is plotted for each group at class level (%). (b/c) LefSe analysis of the composition of the microbiota in small intestines of mock-treated and IAV-infected mice based on 16S rRNA gene sequencing of samples collected at day 7 post-infection (b) or day 14 post-infection (c). Linear discriminant analysis (LDA) scores for significantly overrepresented ($p < 0.05$) taxonomic groups of microbiota from IAV-infected or mock-treated mice are plotted on a genus-level resolution for each group (n=12-16). Cladograms of OTUs, as annotated by Qiime1, that are differentially represented in small intestine samples taken from mock and IAV infected animals at 7 (b) or 14 (c) post-infection are shown on the right-hand side. Kruskal-Wallis statistical test was performed as described previously. Overrepresented taxonomy groups are given on legends next to the corresponding cladogram. (d) Quantitative PCR for genomic RNA of IAV in small intestine. Standard curve on the left-hand side, correlating viral RNA copies with PCR cycles (Cqs). qPCR result from small intestinal samples of mock treated mice (n=2) or IAV infected mice (n=4). Limit of detection indicated by dotted line. (e) Relative gene expression as quantified by RT-qPCR from small intestinal samples of IAV-infected (n=4) and mock-treated (n=2) animals. Statistical significance between mock and IAV groups for each gene was tested by unpaired t-test. P-values are indicated.

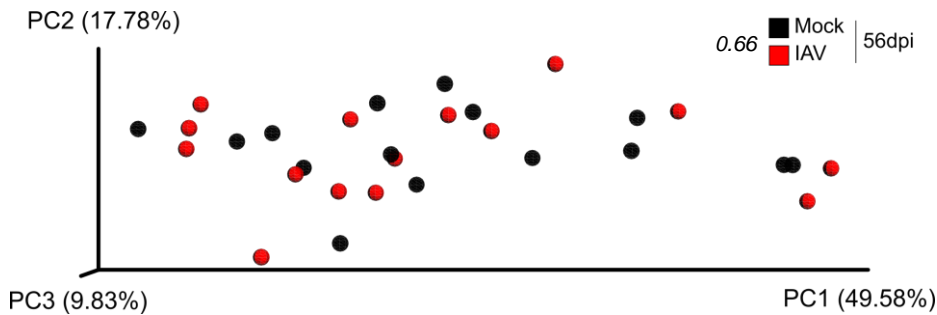
a) **Faeces**



b) **Faeces – 56dpi**



c) **Faeces**



Supplementary Figure 3: microbiota composition and diversity in feces

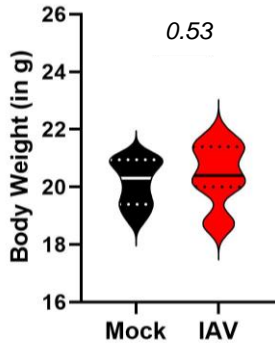
(a) Individual Shannon H-index of feces microbiota at 56dpi of mock-treated (black squares) and IAV-infected mice (red triangles). Mean \pm SD per experimental group is shown. (b) LefSe analysis of microbiota abundance in faeces of mock-treated and IAV-infected mice was determined based on 16S rRNA gene sequencing of samples collected at 56 days post-infection. LDA scores for significantly overrepresented ($p < 0.05$) groups are plotted on a genus level resolution for each group ($n = 15$). Cladograms of OTUs, as annotated by Qiime1, that are differentially represented in faeces samples taken from mock and IAV infected animals at 56 days post-infection are shown on the right-hand side. Kruskal-Wallis statistical test was performed as described previously. Overrepresented taxonomy groups are given on legends next to the corresponding cladogram. (c) Scaled 3D principal coordinates analysis (PCoA) plots using a weighted-UniFrac distance matrix from faeces microbiota of mock-treated or IAV-infected mice at 56 days post-infection. Each symbol represents one individual mouse. Percentages explain variation in PC1 (x-axis), PC2 (y-axis) and PC3 (z-axis). PERMANOVA statistical test was performed and p-value is indicated in the figure.

Supplementary Figure 4: Female mice body weight and metabolic phenotyping of IAV-imprinted adult male mice

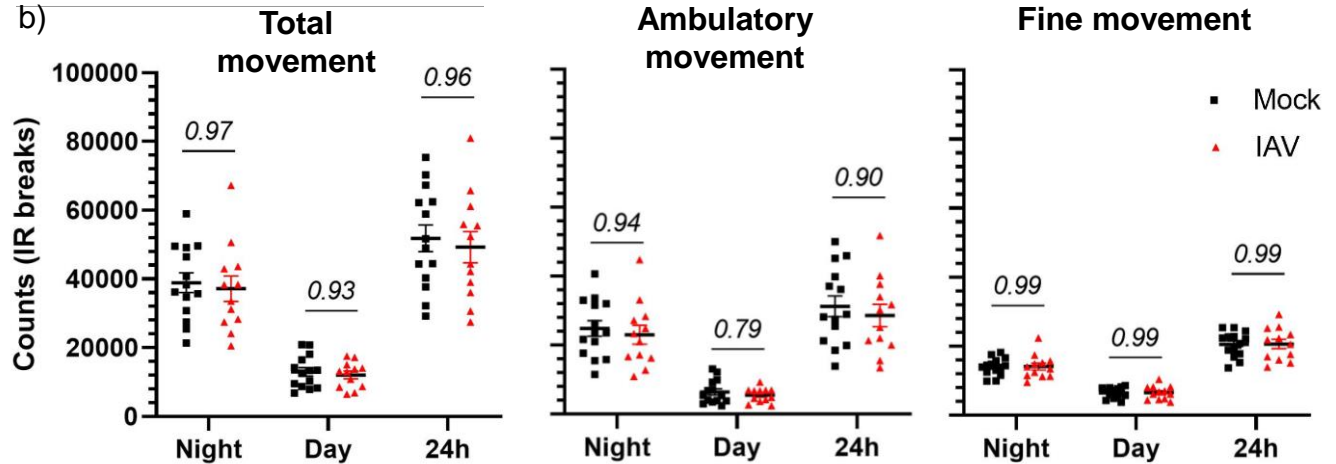
Seven-days-old mice were infected intranasally with PBS or 40 pfu of VN/1203 in 5 μ L. (a) Individual weight values of female mock-treated (n = 9) and IAV-infected mice (n=15) at 56dpi are shown. Home cage activity as recorded by TSE Labmaster/Phenomaster for different periods of the day. Each bar represents mean \pm SEM of mock-treated male mice (n=14) or IAV-infected male mice (n=12) (b) Ambulatory activity. (c) Respiratory exchange ratio. (d) Fatty acid oxidation. (e) Food intake. (f) Water intake. (g) Caloric uptake of mock-treated (n = 12) and IAV-infected mice (n=12) at 42dpi was calculated based on caloric content of consumed food and excreted feces and depicted as energy consumption in kcal. Each symbol represents the average of two mice. Statistical significances were determined using unpaired t-test (panel a and g), 2-way Anova (panel b-f), or multiple t-tests (panel h). P-values are indicated in each panel.

Standard diet – 56dpi (females)

a)

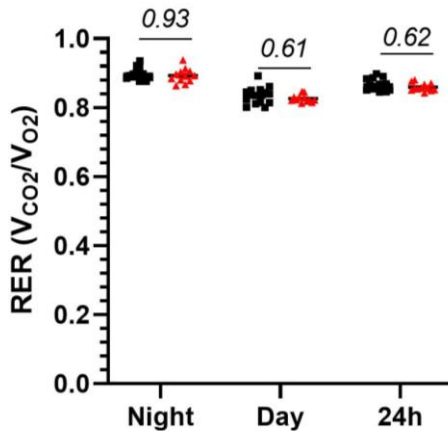


b)



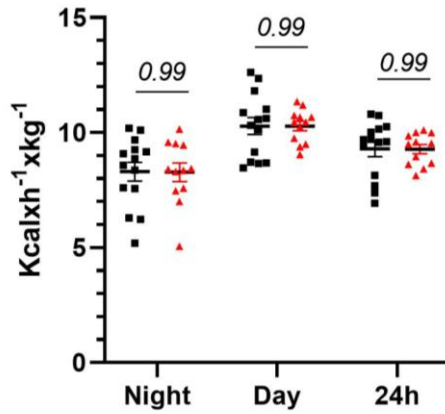
c)

Respiratory Exchange Ratio



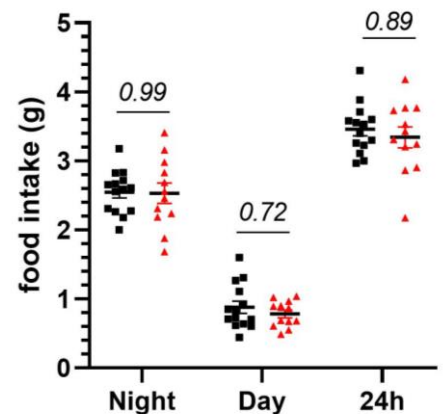
d)

Fatty acid oxidation



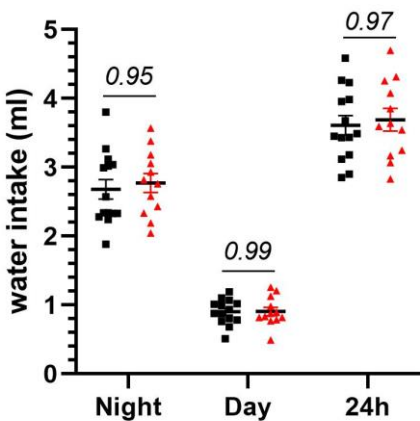
e)

Food intake



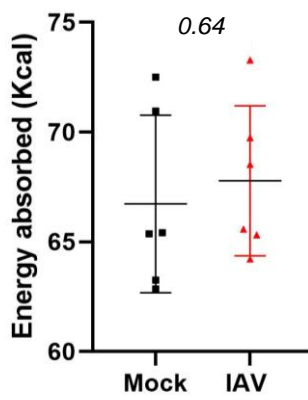
f)

Water intake



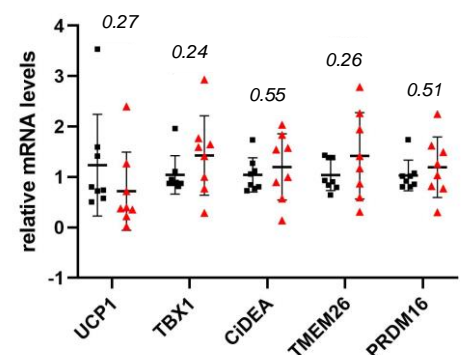
g)

Standard diet – 42dpi

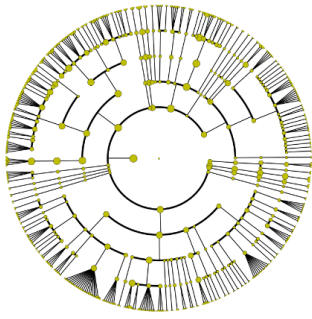


h)

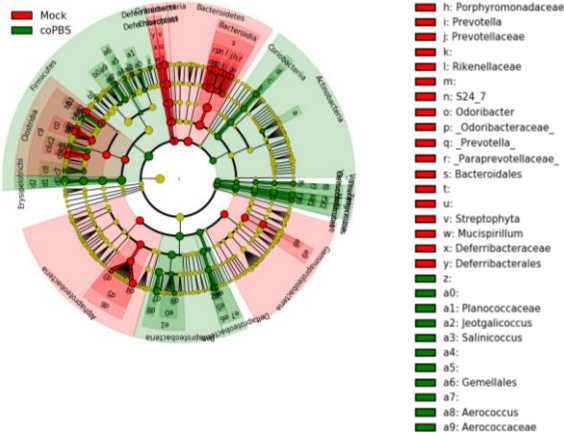
Gene expression in WAT



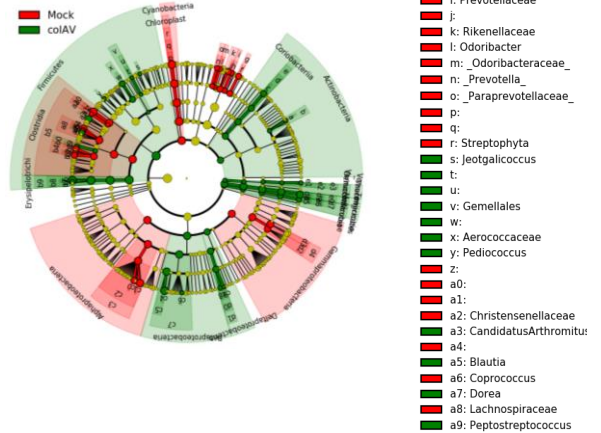
coMock vs colAV



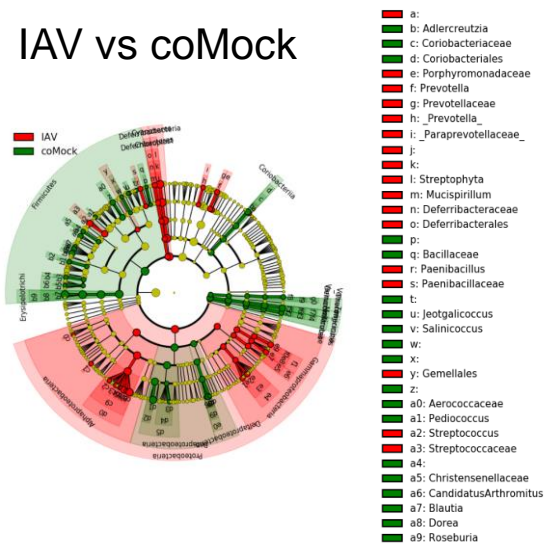
Mock vs coMock



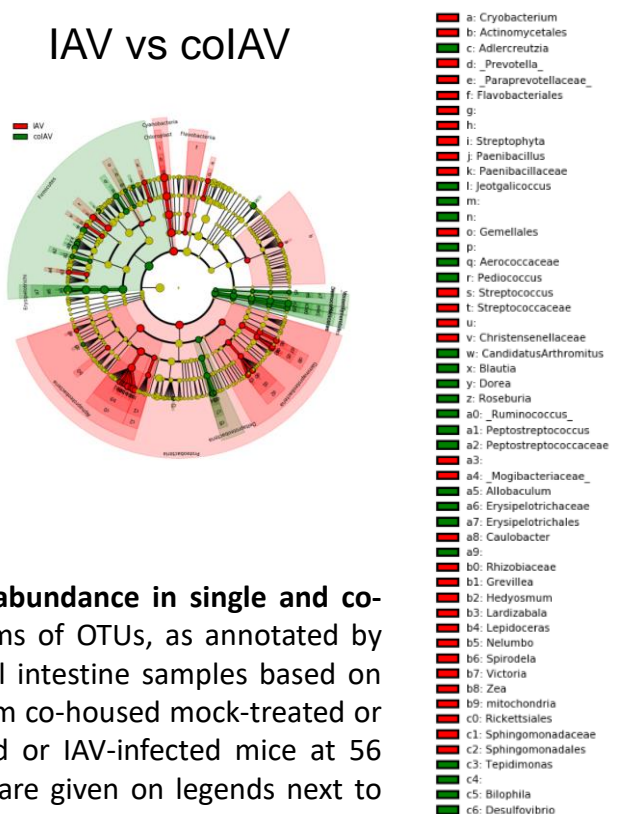
Mock vs colAV



IAV vs coMock



IAV vs colAV



Supplementary Figure 5: Differential microbiota abundance in single and co-housed mice treated with IAV or mock Cladograms of OTUs, as annotated by Qiime1, that are differentially represented in small intestine samples based on LDA scores. Small intestine samples were taken from co-housed mock-treated or IAV-infected mice and single housed mock-treated or IAV-infected mice at 56 post-infection. Overrepresented taxonomy groups are given on legends next to the corresponding cladogram. Blank legends correspond to unknown genus.

Supplementary Tables

Supplementary Table 1: Statistical test of PCoA. PERMDISP analysis for direct comparison of indicated data sets from Figure 1f resulted in displayed p-values.

PERMDISP						
<i>p-value</i>						
	IAV_14dpi	IAV_56dpi	IAV_7dpi	Mock_14dpi	Mock_56dpi	Mock_7dpi
IAV_14dpi		0.0390	0.0010	0.9640	0.8740	0.0010
IAV_56dpi	0.0315		0.0010	0.0320	0.2310	0.0010
IAV_7dpi	<0.0001	<0.0001		0.0010	0.0050	0.0800
Mock_14dpi	0.9619	0.0289	<0.0001		0.8450	0.0010
Mock_56dpi	0.8630	0.2331	0.0044	0.8521		0.0070
Mock_7dpi	<0.0001	<0.0001	0.0988	<0.0001	0.0057	

method name	PERMANOVA
test statistic name	pseudo-F
sample size	30
number of groups	2
test statistic	1.657099606
p-value	0.178
number of permutations	999

Supplementary Table 2: Statistical test of PCoA. PERMDISP analysis for direct comparison of indicated data sets from Figure 2f resulted in displayed p-values.

PERMDISP				
<i>p-value</i>				
	colAV	coPBS	IAV_56dpi	Mock_56dpi
colAV		0.961	0.002	0.396
coPBS	0.964		0.002	0.389
IAV_56dpi	0.003	0.004		0.283
Mock_56dpi	0.365	0.385	0.274	

3.2.2. Complementary Unpublished Results

3.2.2.1. Results

- IAV causes long term dysbiosis in GPR41/43 knockout mice

SCFA are secondary metabolites released by fermenting bacteria, e.g. in the intestine. They act systemically via GPR41 and GPR43 receptors and activate pathways of host metabolism involved in lipogenesis, glycogenesis and hormonal regulation. In order to evaluate the contribution of SCFA to the weight gain observed in adulthood we performed the same set of experiments in GPR41 and GPR43 double-knockout mice. We hypothesized that a long-term dysbiosis caused by IAV infection would still happen, however without the down-stream effect on mice physiology, i.e. increased body weight. First, we assessed, if our sublethal infection model was comparable between double-knockout and *wild-type* mice by assessing viral titers and body weight gain after infection. We saw no significant differences in body weight gain and viral titers at 7 days post infection were higher compared to *wild-type* animals, confirming the onset of an acute sublethal infection (Published Figure 1a,b and Figure 10A). Next, we assessed small intestine microbiota composition at 56 days post infection (Figure 10B). Compared to *wild-type* animals, GPR41/43^{-/-} mice had a distinct intestinal flora characterized by a pronounced presence of Erysipelotrichi and Verrucomicrobiae classes. Moreover, when comparing mock- to IAV-imprinted double-knockout mice, we observed a significant enrichment of Cyanobacteria and a decrease of Bacilli corroborating to a long-term dysbiosis provoked by IAV infection (Figure 10C). Interestingly, no effect on body weight of these animals was observed, which suggests an effect mediated by SCFAs (Figure 10D).

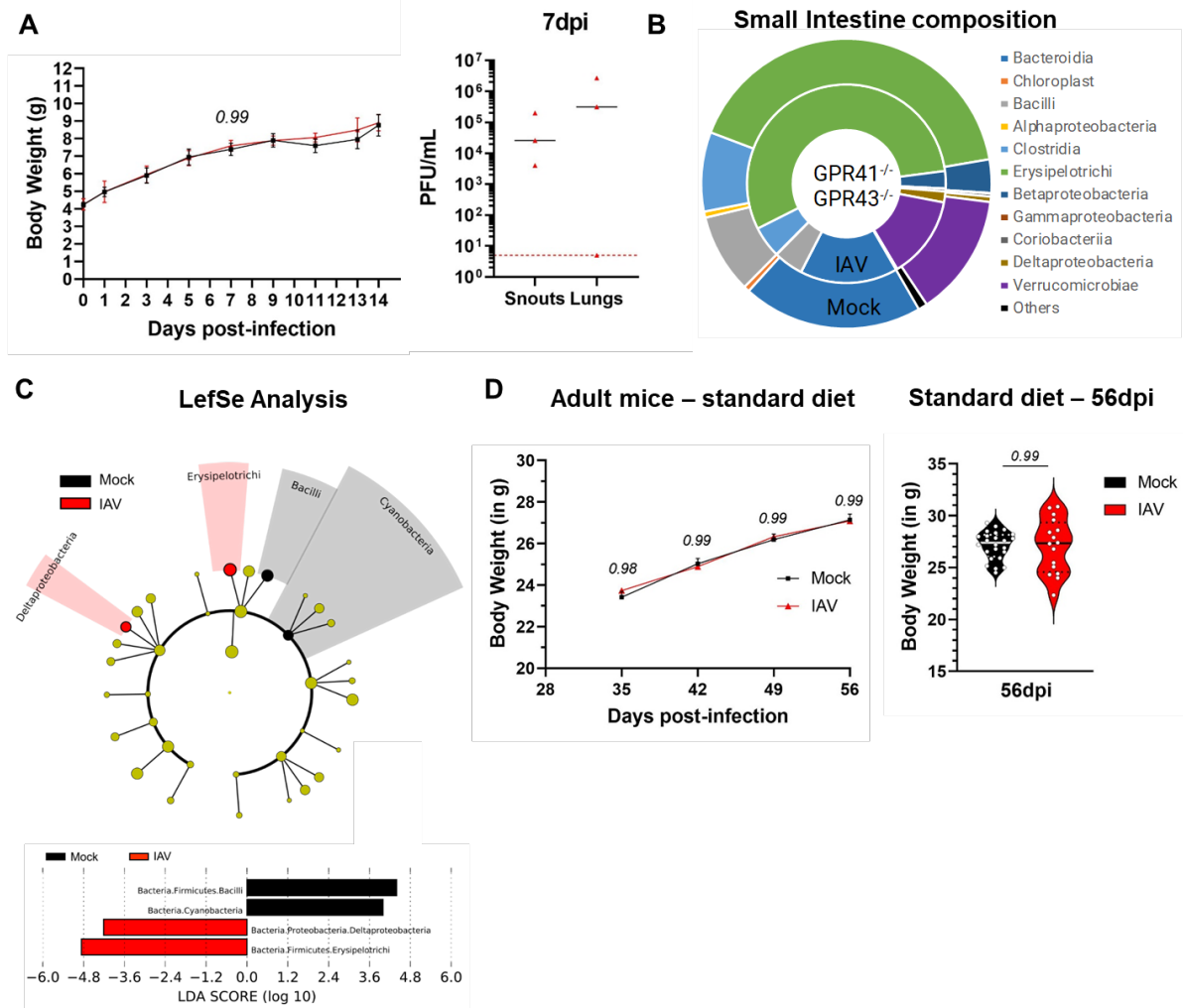


Figure 10: Neonatal IAV infection long-term dysbiosis does not affect body weight in adult GPR41/43^{-/-} mice. Seven-days-old GPR41/43^{-/-} mice were infected intranasally with PBS or 150 PFU of VN/1203 in 5 μ L of PBS. (A) left panel - At 7 dpi viral titers in lungs and snouts for IAV infected mice were determined by plaque assay. Each dot represents one animal (n = 3) and the median titer is represented by a black dash. Limit of detection is represented by a red dashed line. Right panel - Body weight was monitored for 14 days after infection and values for male mice are plotted as mean \pm SEM (n = 24 for mock-treated and n = 16 for IAV-infected). Statistical significance between groups was determined by 2-way ANOVA and post hoc Šídák's multiple comparisons test. P-values are indicated in the figure. (B) Microbiota composition in the small intestine of IAV or mock treated animals at 56dpi. Mean relative bacterial abundance as analyzed by Qiime1 is plotted for each group at class level (in %). (C) LefSe analysis of the composition of the microbiota in small intestines of mock-treated and IAV-infected mice based on 16S rRNA gene sequencing of samples collected at 56dpi. Cladograms of OTUs, as annotated by Qiime1, that are differentially represented in small intestine samples of mock (n=17) and IAV-imprinted (n=14) animals. Linear discriminant analysis scores (LDA) are indicated for different taxonomic groups significantly overrepresented (p < 0.05). Kruskal–Wallis statistical test was performed. (D) left panel - Body weight was monitored for each mouse weekly for 56 days after infection and values of male mice are plotted as mean \pm SEM. Right panel - Individual weight values of male mock-treated (n = 24) and IAV infected mice (n = 16) at 56dpi are shown. Statistical significance between groups was determined by two-way ANOVA (left panel) and unpaired student's t-test (right panel). P-values are indicated in the figure.

Early life interventions causing gut microbiota dysbiosis have been shown to imprint the host immune system and exacerbate pathological outcomes later in life. This happens by interfering with the weaning reaction, an inflammatory response to rapid microbiota changes in the intestine after the sudden exposure to solid food. Since the host response to our model of IAV infection coincides with the weaning period, we asked if it would affect the weaning response and contribute to the long-term dysbiosis and increased body weight observed in IAV-imprinted animals. To answer this question, we evaluated the expression of TNF- α and IFN- γ in the ileum of mock and imprinted animals at 21 days of age (Figure 11A). Our results confirm previous published data, with a significant increase of these two cytokines compared to basal levels at 11 days of age in the mock-imprinted group. However, no significant differences were observed when comparing mock- and IAV-imprinted animals, showing that early life IAV infections do not affect the weaning response (Figure 11B).

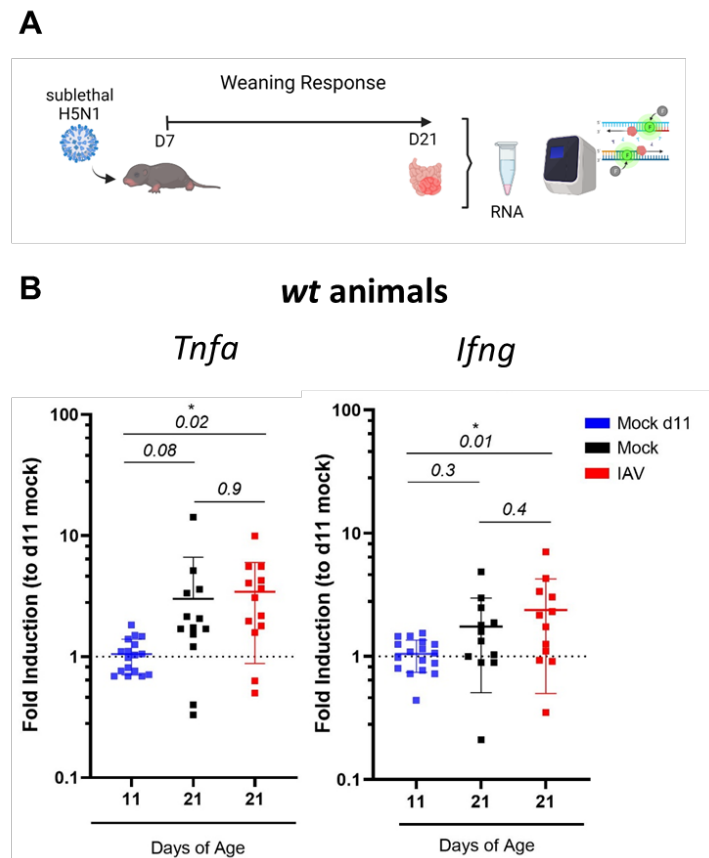


Figure 11: Neonatal IAV infection does not affect the weaning response. (A) Schematic representation of the experimental design to evaluate the weaning response. (B) Seven days old mice were inoculated intranasally with PBS or 150 PFU of H5N1 in 5 μ L PBS. At day 11 and day 21 of age the distal ileum was harvested and RT-qPCR was performed in isolated RNA for the indicated genes. Mean \pm SD per experimental group is shown. Statistical significance between groups was determined by one-way ANOVA and post-hoc Tukey's multiple comparisons test. P-values are indicated in the figure. Graphs are representative of 4 independent experiments and each dot represents one animal (n = 12-17).

- IAV imprinting does not affect humoral responses after vaccination

Differences in host microbiota composition have been shown to modulate vaccine responses. To evaluate if long-term dysbiosis by IAV infection would impair vaccine responses we followed the antibody responses after immunization with Infanrix (Figure 12A). This vaccine is administered via the intramuscular route and induces systemic IgG responses. Indeed, our results show an increase in IgG titers against two of the antigens present in the vaccine formulation (diphtheria and filamentous hemagglutinin (FHA)) after 14 and 28 days post vaccination. However, no significant differences between mock- and IAV-imprinted animals were observed (Figure 12B).

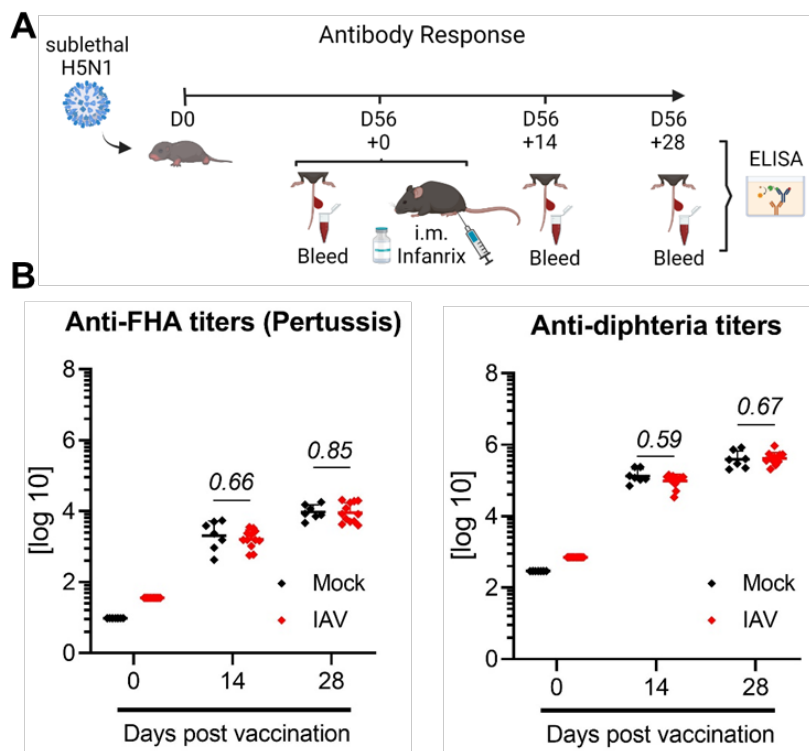


Figure 12: Neonatal IAV infection long-term dysbiosis does not affect antibody responses. (A) Schematic representation of the experimental design to evaluate antibody responses after vaccination. (B) Seven days old mice were infected intranasally with PBS or 150 PFU of VN/1203 in 5 μ L of PBS. At 56dpi mice were immunized i.m. with 1/5 dose of Infanrix. FHA-specific (Left panel) or Diphtheria-specific (Right panel) IgG serum antibody titers were assessed 14 and 28 days post vaccination. The graphs show the mean log₁₀ IgG titers (\pm SEM) of individual mouse sera from mock group (n = 7) and IAV imprinted group (n=12). IgG titers from pre-immunization serum (day 0) was calculated by pooling samples from all animals for each respective group. Statistical significance between groups was determined by 2-way ANOVA and post hoc Šídák's multiple comparisons test. P-values are indicated in the figures.

- IAV imprinting causes long-term dysbiosis in lung microbiota

IAV infections were previously shown by our group to cause a transient dysbiosis in the lung microbiota of adult mice. Based on this observation we asked if an early life infection could affect the lung microbiota composition. As a final result, we evaluated lung microbiota

composition along the development of *wild-type* mice infected with IAV at 7 days of age (Figure 13A). Compared to mock-imprinted animals, IAV-imprinted animals had significant compositional changes in lung microbiota at several time points after infection (Figure 13B). We observed significant differences in the Bacteroidia class after short periods post infection, with enrichment at day 7 post infection and decrease at 14 days post infection, compared to mock animals. Moreover, at 56 days post infection, when infection is long resolved, we still observed significant compositional changes in Bacilli, with enrichment of this class in IAV-imprinted animals. The data presented for the lung microbiota dysbiosis after neonatal IAV infection is still explorative and a former PhD student (Soner Yildiz) performed the experimental procedures. For these results, I executed the bioinformatic analysis and the construction of the images.

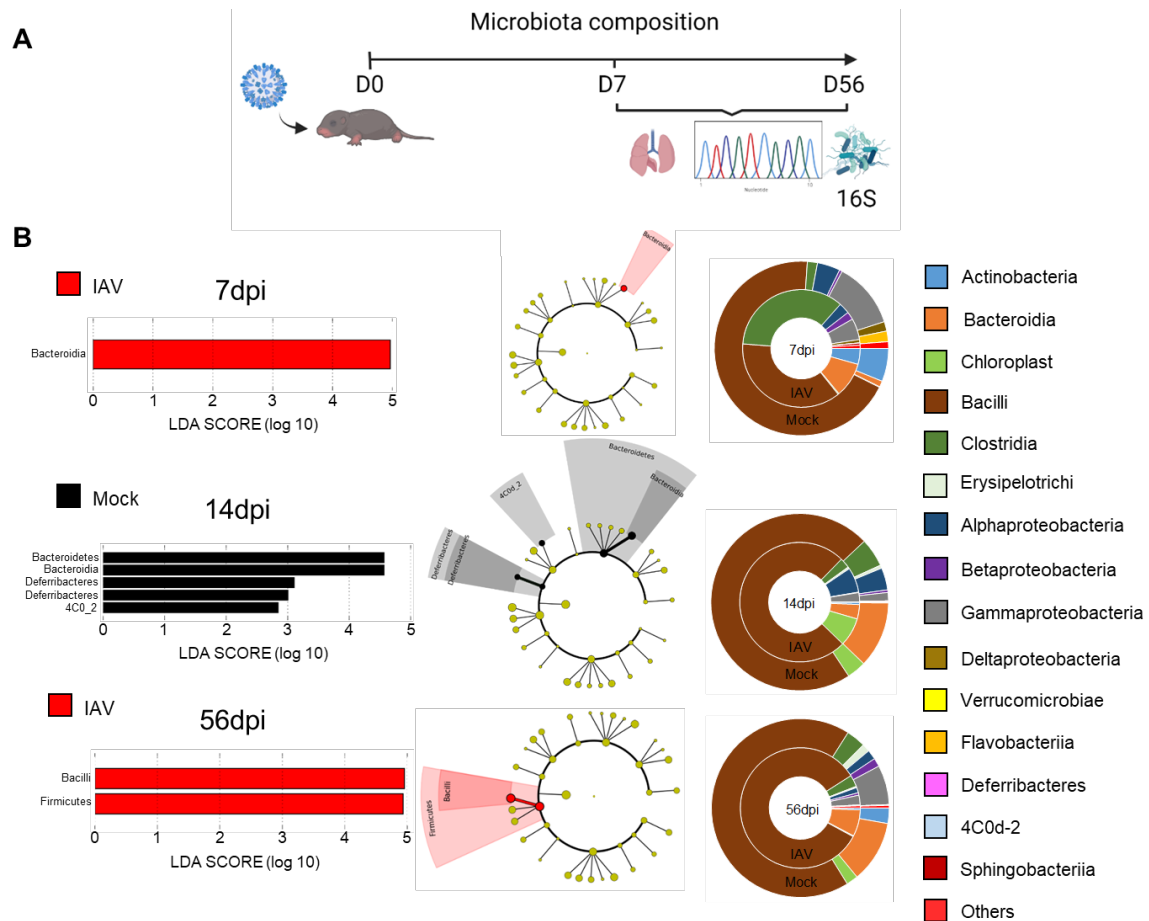


Figure 13: Neonatal IAV infection changes lung microbiota composition in adult mice. (A) Schematic representation of the experimental design to evaluate lung microbiota composition. (B) LefSe analysis of the composition of the microbiota in lungs of mock-treated and IAV-infected mice based on 16S rRNA gene sequencing of samples collected at 7, 14 and 56dpi. From left to right: Linear discriminant analysis scores (LDA) are indicated for different taxonomic groups significantly overrepresented ($p < 0.05$ after Kruskal–Wallis statistical test) in lung samples of mock and IAV-imprinted animals; Cladograms of OTUs, as annotated by Qiime1, that are differentially represented according to LDA scores; Microbiota composition at class level plotted as mean relative abundance as analyzed by Qiime1 for each group.

3.2.2.2. Materials and Methods

All the animal experiments on GRP41/43^{-/-} animals and the bioinformatics analysis were performed according to the materials and methods of the attached publication, except A/Viet Nam/1203/2004 HALo inoculation which was increased to 150 PFU due to a change in viral stocks.

- **Animals**

All animal procedures were in accordance with federal regulations of the Bundesamt für Lebensmittelsicherheit und Veterenärwesen (BLV) Switzerland (Tierschutzgesetz) and approved by an institutional review board and the cantonal authorities (license number GE45). C57BL/6J GRP41 and GPR43 double-knockout (GRP41/43^{-/-}) were generated by artificial insemination with sperm from a double knockout animal on a C57BL/6J background. Heterozygous offspring were backcrossed until we obtained double knockout homozygous offspring confirmed by genotyping. GRP41/43^{-/-} animals were housed under a strict 12 h light/dark cycle and fed ad libitum before entering an experiment or the breeding process. Breeding cages were checked three times a day during labor period and time of birth was recorded for each dam. Litters born on the same day were divided into equal groups and left with the lactating parent until weaning at 21 days of age. After weaning, males and females were separated in groups of 4-5 animals/cage.

- **RT-qPCR**

At 11 and 21 days of age (14dpi), animals were euthanized using controlled CO₂ exposure. The 5 cm of the distal ileum were sampled following euthanasia using sterile tools, sterilized between groups, under aseptic conditions in RNA protect (QIAGEN) and incubated overnight at RT. On the following day, samples were transferred into Trizol and stored at -70°C until further analysis. Total tissue RNA was isolated using Trizol (Invitrogen). cDNA was synthesised using M-MLV Reverse transcriptase (Promega #M170A) according to manufacturer's instructions using 500 ng of RNA as starting material and oligo dT as primers. To perform qPCR, 1 µL of cDNA was mixed with 10 µl of 2X SYBRGreen (KAPA Biosystems), 1 µl of each respective forward (10 µM) and reverse (10 µM) primers in a final volume of 20 µl with RNase, DNase Free Molecular Biology Grade Water (Amimed, BioConcept, Switzerland). Quantitative PCR was performed following a thermal cycling protocol of an initial denaturation step at 95°C for 5 min, followed by 40 cycles of denaturation at 95°C for 30 s and annealing/extension at 60°C for 60s. After each reaction melting curves were determined for each primer set to confirm the correct amplification of the target gene. Ct

values were normalized to Hprt gene and fold induction was calculated using $2^{\Delta\Delta Ct}$ method to samples from day 11 animals.

Primers:

18S_F:5'-GTAACCCGTTGAACCCCAT-3'; 18S_R:5'-CCATCCAATCGGTAGTAGCG-3'; TNF-a_F:5'-GGTCCCAAAGGGATGAGAAGTT-3'; TNF-a_R:5'-GGTTGTCTTTGAGATCCATGCCG-3'; IFN-g_F:5'-TGGAGGAACTGGCAAAAGGATG-3'; IFN-g_R:5'-GGACCTGTGGGTTGTTGACCTCAAA-3'; Hprt_F:5'-CTGGTGAAAAGGACCTCTCGAAG-3'; Hprt_R:5'-CAGTTTCACTAATGACACAAACG-3';

- Immunization and antibody response

At 56 days post infection, animals were weighed, marked and injected intramuscularly with 1/5 dose of the human dose of Infanrix hexa vaccine (GSK Lot: A21CD120B) diluted in 100 μ L PBS. Each mouse was administered 50 μ L in each hind limb. Blood samples were harvested on the respective days by tail bleeding as previously described (Bonifacio et al). Briefly, mice were placed in a plexiglass restrainer and an orthogonal incision was made on the left veins of the tail. Blood was collected in 1,5 mL polystyrene tubes and incubated at room temperature for 30 minutes to 1 hour to allow coagulation. Samples were centrifuged at $10,000 \times g$ for 5 minutes at room temperature and supernatants collected into fresh tubes and stored at $-20^\circ C$ to be used in ELISA assays

- ELISA assay

Diphtheria and pertussis (FHA) antigen-specific antibody titers were determined by ELISAs according to (Auderset 2019 Frontiers immunology). Briefly, 96-well plates (Nunc MaxiSorp™; ThermoFischer Scientific) were coated with Diphtheria antigen diluted 1:10'000 (FA229295) or FHA (1 μ g/ml). Wells were incubated with 2-fold serial dilutions of individual or pooled mouse prior to incubation with secondary horseradish peroxidase (HRP) conjugated anti-mouse IgG (Invitrogen). The optical density of each well was measured at 405 nm and the data analyzed with SoftMax Pro software. IgG titers were expressed as Log10 in reference to a standard curve using reference anti-serum.

3.3. Visualization of respiratory commensal bacteria in context of their natural host environment

3.3.1. Published Results

Joao P. P. Bonifacio and Mirco Schmolke*

Microbiology and Molecular Medicine Department, University of Geneva, Geneva, Switzerland

*Correspondence: *Mirco Schmolke*

Status:

Manuscript published in *Frontiers Microbiology* – PMID: 34149669

Summary:

The aim of this work was to adapt an RNA in situ hybridization (ISH) technique named RNAScope, to visualize tissue-associated commensal microbiota in the lungs. We performed frontal sections of specific pathogen-free (SPF) mice lungs embedded in paraffin and used the 16S RNA gene as target for probe hybridization. Based on a previous publication from our group, we designed a probe to specifically hybridize with the 16S RNA sequence of the gram-positive bacteria *Lactobacillus murinus*. This strain was isolated and cultured from SPF animal housed in our facility and was shown to represent over 95% of the tissue-associated flora of the lungs (Yildiz & Bonifacio et al 2020). We show that a standard colouring method to stain for gram-positive bacteria (Giemsa staining) was not able to detect the presence of intact bacteria associated with the tissue. In contrast, our adapted RNA ISH protocol detected tissue-associated *Lactobacillus murinus*. Moreover, we resolved the spatial distribution of tissue-associated microbiota and found most bacteria located in medium and large airways in between the epithelial cell layer. The specificity of the assay was also assessed in tissue sections from germ-free mice, in which the signal from our probe was absent. Overall, this technique offers advantages over standard staining protocols and is able to detect low-density commensal bacteria in the lungs. In addition, it also provides valuable information on the spatial localization of commensal bacteria in this tissue, which contributes to our understanding of lung microbiota dynamics.

Personal Contribution:

For this publication, I performed all the experimental setup and design. I also performed the acquisition, analysis, interpretation and construction of the images. In addition, I wrote the first draft of the manuscript and contributed to the final revisions together with Mirco Schmolke.



Visualization of Respiratory Commensal Bacteria in Context of Their Natural Host Environment

Joao P. P. Bonifacio and Mirco Schmolke*

Microbiology and Molecular Medicine Department, University of Geneva, Geneva, Switzerland

Commensal microbes are an integral component of mammalian physiology. 16S rRNA gene-specific next generation sequencing from DNA of total organs, swabs or lavages has revolutionized the characterization of bacterial communities in virtually every ecological niche of the body. Culturomics, next allowed the isolation and characterization of commensal bacteria in the lab and the establishment of artificial communities of bacteria, which were eventually reintroduced in model organisms. Spatial organization of microbiota within a given host environment is critical to the physiological or pathological phenotypes provoked by commensal microbiota. *In situ* hybridization (ISH) is a complementary technique to sequencing and culturing to visualize the presence of individual bacterial operational taxonomic unit (OTUs) in context of the colonized organ. We recently applied highly sensitive *in situ* RNA hybridization to detection of commensal bacteria in low abundance respiratory tract samples of mice housed under specific pathogen free conditions. This technique allows species-specific detection of living bacteria using RNAScope™ technology, while preserving the natural environment of the organ. We here provide a detailed step-by-step protocol describing the detection of commensal lung bacteria in respiratory tissue.

Keywords: *L. murinus*, lung tissue, microbiome, commensal bacteria, *in situ* hybridization, RNAScope

OPEN ACCESS

Edited by:

George Tsiamis,
University of Patras, Greece

Reviewed by:

Rabia Khan,
University of Oslo, Norway
Byron Brehm-Stecher,
Iowa State University, United States

*Correspondence:

Mirco Schmolke
mirco.schmolke@unige.ch

Specialty section:

This article was submitted to
Systems Microbiology,
a section of the journal
Frontiers in Microbiology

Received: 10 March 2021

Accepted: 11 May 2021

Published: 04 June 2021

Citation:

Bonifacio JPP and Schmolke M
(2021) Visualization of Respiratory
Commensal Bacteria in Context
of Their Natural Host Environment.
Front. Microbiol. 12:678389.
doi: 10.3389/fmicb.2021.678389

INTRODUCTION

Characterization of bacterial communities in various ecological niches of human or animal bodies largely relies today on 16S rRNA gene specific next generation sequencing. This highly sensitive and valuable technique allows quasi unbiased quantification and identification of bacteria from DNA of swabs, lavages or total tissue samples (Human Microbiome Project Consortium, 2012). It does, however, not distinguish between living and dead bacteria and resolution of spatial organization of the identified bacteria within a given niche is limited to the choice of organ section used for DNA isolation. Complementary analysis of shotgun DNA sequencing allows deeper insight into the physiological state of a given group of living bacteria under changing environmental conditions (Westermann et al., 2016; Griesenauer et al., 2019; Becattini et al., 2021) since bacterial RNA is rather short-lived. Culturomics, that is the isolation and amplification of bacteria by using multiple growth conditions, allows further detailed characterization of bacterial species which were previously considered unculturable (Sibley et al., 2011; Browne et al., 2016). As a complement to these techniques we present here a protocol for RNA-based *in situ* hybridization to detect commensal or pathogenic bacteria in a sensitive fashion in context of the host organ. Previous

studies have used fluorescent based approaches to determine spatial organization of commensal microbiota in the intestine and lung (Yun et al., 2014; Tropini et al., 2017; Welch et al., 2017) using phylum specific probes. We extended this approach recently to the respiratory tract of mice, which displays 10^4 to 10^5 -fold less bacterial content than the intestine (Yildiz et al., 2020). This technique allowed us to identify tissue associated bacteria in the large airways of the lung, with probes detecting all eubacteria or only specific species. We here provide a detailed step-by-step protocol describing the detection of commensal lung bacteria in respiratory tissue, which could easily be adapted to other tissues or other host species.

MATERIALS AND EQUIPMENT

Animals

Animals should be housed and treated according the respective national animal welfare guidelines. Hygiene standards of the respective animal facility will largely contribute to the colonization of the investigated animals (Laukens et al., 2015; Rausch et al., 2016). We base this protocol on specific pathogen free housed mice, but we see no limitations on extending it to conventionally housed or wild animals.

Extraction and Fixation of Mouse Lung Tissue

Scissors (F.S.I.), micro-dissecting forceps (F.S.I.) Falcon 15-mL conical centrifuge polypropylene tubes (Thermo Fisher Scientific), Paraformaldehyde 4% (Merck), Ethanol 70%.

Paraffinization and Histological Cuts

Cooling block grid (Leica), histology cassettes (Leica) microscope slides (Thermo Fisher Scientific), microtome (Leica RM2235), Paraplast (Leica), Ethanol with 2% methyl ethyl ketone (MEK) (Biosystems), Histo-Sav (Mallinckrodt Baker).

Deparaffinization

Histological grade xylene, ethanol 99.9 grade, Fume-hood, x8 50-mL beakers, dry oven.

RNAscope—ISH

RNA Scope kit (ADC) containing: RNAscope Hydrogen Peroxide, RNAscope 10X Target Retrieval, RNAscope 50X Wash Buffer, RNAscope Protease Plus, RNAscope Hydrophobic pen, RNAscope probes (#475131 or #451961), RNAscope AMP1-6 Reagents, RNAscope Fast Red-A, RNAscope Fast Red-B, RNAscope EcoMount. Lysozyme (40 μ g/mL), 5X SSC Buffer (optional), Meyer's Solutions (Sigma), Ammonia, Histological grade xylene, Steam Cooker (e.g., Tefal Vitacuisine Compact VS4003 digitale steam cooker Art. #IP095536), Coverslips, Dry Oven, HybEZ Oven, Slide's Rack for washing.

Visualization

Brightfield Olympus BX61VS120 with a motorized stage (Olympus LifeSciences) equipped with Plan Apo N 2 \times /0.08 and

U Plan S Apo 100 \times /1.4 Oil objectives and a Pike F505C VC50 detector (Allied Vision Technology).

METHODS

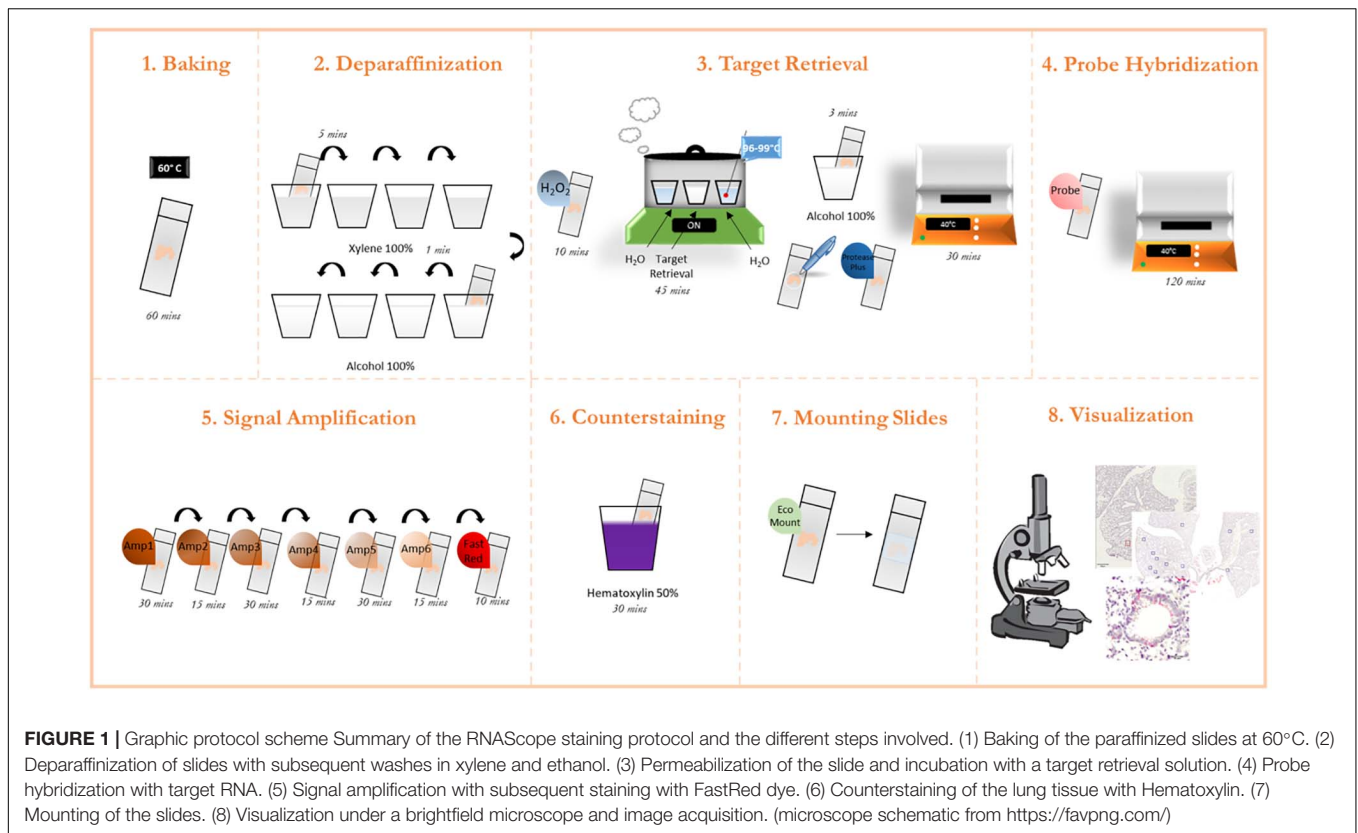
This methodology was adapted from the protocol guidelines provided by the ACD RNAscope platform (ACD, 2021). Furthermore, the company provides step-by-step short videos on each step of the process under “training videos” tab. A graphical overview of the process is presented in **Figure 1**.

Animal Husbandry

Germ free animals with C57BL/6J background were generated and maintained by the Clean Mouse Facility of Department of Biomedical Research of the University of Bern kindly provided by Dr. Mercedes Gomez and Prof Sigfried Hapfelmeier. They were born and raised in flexible film isolators in at the University of Bern, transferred aseptically into sterile IVC cages provided with sterile food and water *ad libitum*. Seven to eight weeks colonized C57BL/6J mice were housed in a specific pathogen-free and climate-controlled animal facility at the University of Geneva. Mice were provided with water and pelleted diet *ad libitum*. All cages were provided with environmental enrichment in the form of nesting material and mouse houses. Procedures and experimentation were carried out in accordance with federal regulations of the Bundesamt für Lebensmittelsicherheit und Veterenärwesen (BLV) Switzerland (Tierschutzgesetz) and approved by an institutional review board and the cantonal authorities. Animal license GE/159/17.

Extraction and Fixation of Mouse Lung Tissue

- 1.1 Euthanize animals (here done by controlled CO₂ exposure). Confirm death by controlling from absence of reflex after pinching the footpad of the hind limbs.
- 1.2 Place the animal on the back and attach it with needles to a preparation board.
- 1.3 Wet the fur of the chest and abdomen with 70% ethanol. Avoid spilling ethanol in mouth or nose of the animal.
- 1.4 Lift the fur at the level of the lower tip of the sternum and make a horizontal incision.
- 1.5 Remove the fur from the mid abdomen to the neck by extending the cut along the lower end of the rib cage, followed by two lateral upward cuts toward the front limbs.
- 1.6 Flush fur attached to the exposed chest muscle tissue with 70% ethanol or sterile isotonic saline solution.
- 1.7 Make a small horizontal incision below the sternum and extend to this cut along the lower end of the rib cage.
- 1.8 Carefully puncture the diaphragm to collapse the lungs and open the rib cage by two lateral cuts toward the front limbs.
- 1.9 Carefully remove the lungs from the chest cavity. Pay attention not to put too much pressure with the forceps to the lung to avoid tissue damage.
- 1.10 Disconnect the attached connective tissue the trachea and the heart with scissors.



1.11 Immerse lungs in prepared 50 ml tubes with in PBS with 4%v/v freshly prepared paraformaldehyde solution (see “Materials” section) and stored at room temperature for 24 h. Make sure that the organ is fully immersed in the fixative. This can be achieved e.g., by adding the lid of a 15 ml tube upside down into the 50 ml tube, to hold the lung below the air-liquid interface. Of note, inflation of the lung with fixative is not recommended, since it could flush commensal bacteria out of their natural niche and might lead to artificial location in the organ.

Paraffin Embedding

- 2.1 After fixation place lungs in cassettes, orient them properly according to the envisioned cutting program and dehydrate as follows.
- 2.2 Immerse lungs fully in 70% ethanol for 2 h at RT.
- 2.3 After 2 h Immerse Lungs fully a second time in 70% ethanol for 2 h at RT.
- 2.4 Immerse lungs fully in 90% ethanol for 1 h at RT.
- 2.5 Immerse lungs fully in 95% ethanol for 1 h at RT.
- 2.6 Immerse lungs fully in 100% ethanol for three consecutive steps of 30 min.
- 2.7 Transfer lungs into Histo-SAV I (Mallinckrodt Baker) for 30 min.
- 2.8 Immerse lungs fully in Histo-SAV II (Mallinckrodt Baker) for 30 min.
- 2.9 Immerse lungs fully in Histo-SAV III (Mallinckrodt Baker) for 30 min.
- 2.10 Transfer lungs into paraffin I for 2 h.
- 2.11 Transfer lungs into paraffin II for 4 h.
- 2.12 After hardening, cut paraffin blocks into 1 μM frontal sections using a microtome (Leica RM2235 Rotary Microtome).
- 2.13 Perform five consecutive transversal cuts at four different depths (1, 51, 101, and 151 μm). Cutting could be adapted according to experimental goals.
- 2.14 Transfer two consecutive slices of each depth onto one microscope slide and leave them to dry overnight at RT. Slides can be left either unstained or stained e.g., with Giemsa.
- 2.15 Submerge the slides in 20% Giemsa dye (Mallinckrodt Baker) diluted in distilled water.
- 2.16 Quickly dip the slides in 0.2% acetic acid (Sigma Aldrich) diluted in distilled water (organ samples should turn pink).
- 2.17 Quickly dip the slides in ethanol 90% (organ samples should turn blue).
- 2.18 Submerge the slides in isopropanol (Fluka) for 2 min.
- 2.19 Quickly dip the slides in ethanol 100%.
- 2.20 Quickly dip the slides in Histo-Sav (Mallinckrodt Baker).
- 2.21 Mount the slides following the protocol provided by UltraKit (Mallinckrodt Baker).
- 2.22 Place the slides containing the organ cuts in a dry oven for 1 h at 60°C to dry.
- 2.23 Place eight 50-mL beakers under a fume-hood and filled with either histological grade xylene or ethanol 99.9 grade (four beakers for each solution).x

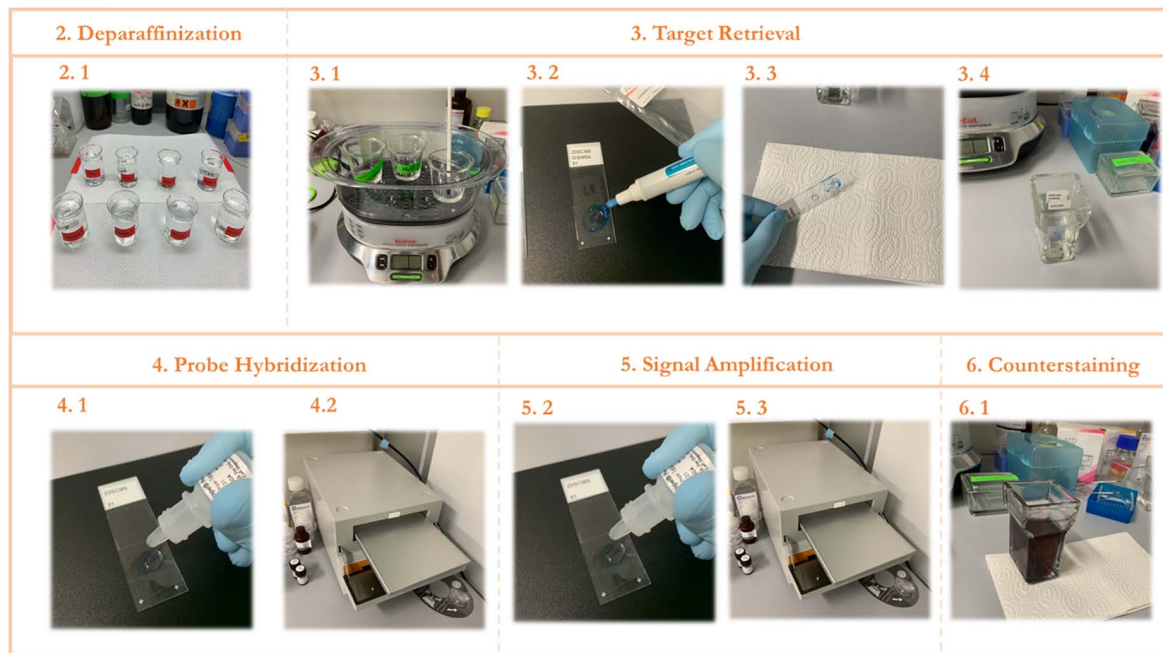


FIGURE 2 | STEP-BY-STEP Visual protocol scheme. (1) Visual summary of the RNAScope staining protocol and the different steps involved. (2) Deparaffinization of slides with subsequent washes in xylene and ethanol. (3) Permeabilization of the slide and incubation with a target retrieval solution and subsequent hydrophobic barrier and washing. (4) Probe hybridization with target RNA. (5) Signal amplification with subsequent staining with FastRed dye. (6) Counterstaining of the lung tissue with Hematoxylin.

- 2.24 Dip the dried microscope slides first into each xylene-containing beaker for 5 min each.
- 2.25 Continue with the ethanol-containing beakers for 1 min each and leave to air dry. Deparaffinized slides were used for the RNAScope procedure described in the next section (see also **Figures 2–2.1**).

In situ Hybridization

- 3.1 Target Retrieval
- 3.1.1 Lay the slides in the HyBEZ tray and add enough drops of RNAScope Hydrogen Peroxide to cover the samples on each slide.
- 3.1.2 Incubate at room temperature for 10 min.
- 3.1.3 Tap the slides on top of absorbent paper to remove excess liquid and immediately submerge the slides in a reservoir containing distilled water.
- 3.1.4 Lift the slides up and down for a proper wash.
- 3.1.5 Repeat the washing step.
- 3.1.6 Place two reservoirs containing RNAScope 1X Target Retrieval Reagent and Distilled water in a steam cooker (Tefal, #IP095536) machine set at 99°C.
- 3.1.7 Add slides to the distilled water container for 10 seconds and move them into the container with RNAScope 1X Target Retrieval Reagent.
- 3.1.8 Monitor the temperature with a thermometer.
- 3.1.9 Cover the steam cooker and incubate for 45 min (refer to **Figures 2–3.1**). *This incubation time is susceptible to changes according to the samples.*
- 3.1.10 Meanwhile, pre-warm HyBEZ Oven at 40°C for 10 min.
- 3.1.11 Remove slides from steam cooker and wash with distilled water.
- 3.1.12 Move the slides to a container with Ethanol 99.9 grade for 3 min.
- 3.1.13 Dry the slides in a dry oven at 60°C.
- 3.1.14 Using the hydrophobic pen, draw a circular barrier around the samples on each slide and let it dry completely at room temperature for 5 min (refer to **Figures 2–3.2**).
- 3.1.15 Lay the slides in the HyBEZ tray and add enough drops of RNAScope Protease Plus to cover the samples on each slide.
- 3.1.16 Incubate at 40°C inside the tray of the HyBEZ Oven for 30 min. *This incubation time is susceptible to changes according to the samples.*
- 3.1.17 Tap the slides on top of absorbent paper to remove excess liquid and immediately submerge the slides in a reservoir containing distilled water (refer to **Figures 2–3.3, 2–3.4**).
- 3.1.18 Lift the slides up and down for a proper wash.
- 3.1.19 Lay the slides in the HyBEZ tray and add enough drops of Lysozyme (40 µg/mL) to cover the samples on each slide (optional).
- 3.1.20 Incubate at 40°C inside the tray of the HyBEZ Oven for 90 min (optional).
- 3.1.21 Tap the slides on top of absorbent paper to remove excess liquid and immediately submerge the slides in a reservoir containing distilled water.
- 3.1.22 Lift the slides up and down for a proper wash.

Probe Hybridization

- 3.2.1 Pre-warm the HyBEZ Oven at 40°C and the RNAScope probes at 37°C for 10 min.
- 3.2.2 Tap the slides on top of absorbent paper to remove excess liquid and lay them in the HyBEZ tray.
- 3.2.3 Add enough drops of the appropriate probe to cover the samples on each slide (refer to **Figures 2–4.1**).
- 3.2.4 Incubate at 40°C inside the tray of the HyBEZ Oven for 2 h (refer to **Figures 2–4.2**).
- 3.2.5 One at a time, tap the slides on top of absorbent paper to remove excess liquid and place it back on the tray.
- 3.2.6 Submerge the slides in a container filled with 1X Wash Buffer and lift them up and down for a proper wash.
- 3.2.7 Repeat the washing step.
- 3.2.8 Optional Step: Place the slides in a container with 5X SSC Buffer and leave them overnight.
- 3.2.9 Remove excess liquid by tapping the slide on top of absorbent paper and place them back on the tray.

Signal Amplification

The next steps consist on the amplification of the probe signal by adding AMP1-4 reagents and incubating them at 40°C inside the tray of HyBEZ Oven at 40°C.

Note: Always add enough drops of each reagent to cover the samples on the slides and remove excess liquid after incubation.

- 3.3.1 Add AMP 1 Reagent and incubate for 30 min (refer to **Figures 2–5.1, 2–5.2**).
- 3.3.2 Wash the slides twice with 1X Wash buffer.
- 3.3.3 Add AMP 2 Reagent and incubate for 15 min.
- 3.3.4 Wash the slides twice with 1X Wash buffer.
- 3.3.5 Add AMP 3 Reagent and incubate for 30 min.
- 3.3.6 Wash the slides twice with 1X Wash buffer.
- 3.3.7 Add AMP 4 Reagent and incubate for 15 min.
- 3.3.8 Wash the slides twice with 1X Wash buffer.

The next steps consist on the final amplification of the probe signal by adding AMP5-6 reagents and incubating them at room temperature.

- 3.3.9 Add AMP 5 Reagent and incubate for 30 min. *This incubation time can be modulated to adjust probe signal intensity.*
- 3.3.10 Wash the slides twice with 1X Wash buffer.
- 3.3.11 Add AMP 6 Reagent and incubate for 15 min.
- 3.3.12 Wash the slides twice with 1X Wash buffer.
- 3.3.13 Meanwhile, prepare a solution of Fast RED (A + B) by adding: 1 volume of Fast RED-B and 60 volumes of Fast RED-A.
- 3.3.14 Pipette enough volume of Fast RED mix to cover the samples in each slide (~300 µL per slide) and incubate for 10 min at room temperature.
- 3.3.15 Tap the slides on top of absorbent paper to remove excess liquid and lay them in the HyBEZ tray.
- 3.3.16 Rinse the slides with distilled water.

Counterstaining

- 4.1 Submerge the slides in a container filled with Meyer's solution diluted 1:2 for 2 min at room temperature (refer to **Figures 2–6.1**) *This dilution can be modulated to adjust staining intensity.*
- 4.2 Wash the slides with distilled water until the water is clear and has no traces of Meyer's solution.
- 4.3 Submerge the slides in 0.02% ammonia diluted in distilled water and move the slides up and down a few times until the sample turns blue.
- 4.4 Wash the slides with distilled water.
- 4.5 Dry the slides at 60°C for at least 15 min or air dry until all visible liquid is evaporated.
- 4.6 Briefly dip the slides into a 50-mL beaker containing fresh histological grade xylene and add 1–2 drops of EcoMount (Vectamount) while the slides are still wet.
- 4.7 Cover the sample with a coverslip carefully to prevent formation of air bubbles and let it air-dry.

Visualization

A large variety of imaging systems can be used for visualization. The following steps are thus solely to indicate a technical guidance and should be adapted to the existing infrastructure in each laboratory.

- 5.1 Visualize slides using a Olympus VS120 brightfield microscope (Olympus) and QuPath-0.2.1 Software.
- 5.2 Screen slides first with a 2× magnification for a quick visual scan of the overall distribution of positive signal (red-pink staining).
- 5.3 Choose a one random field from each slice and scanned again with the 100×/1.4 Oil objective using a multifocal approach. The VS-ASW creates a focus map with multiple coordinates defined by the user. This allows the optimal Z-position to be determined and saved on various parts of the sample, allowing a height profile of the sample to be compiled before detailed scan acquisition.
- 5.4 Process and analyze an average of 5–8 fields per sample at higher resolution. *This value can be adapted to the experimental requirements of each user.*
- 5.5 Determine positive staining of red-pink punctate dots around epithelial cells of airway ducts.

RESULTS

In order to get an impression of the quality of tissue slices we performed Giemsa staining (**Figure 3**).

Technically this should allow the detection of bacteria in tissue (Tian et al., 2011; Morris et al., 2019), however, the density of flora and the nature of the bacteria could be limiting this staining technique.

Generally, the consultation of experienced histo-pathologists is advised in order to evaluate the quality of tissue slices.

The specific colorimetric staining for Panbacteria or *L. murinus* used here will provide a bright red-pink coloration of bacterial clusters (black arrows) attached to the medium or large

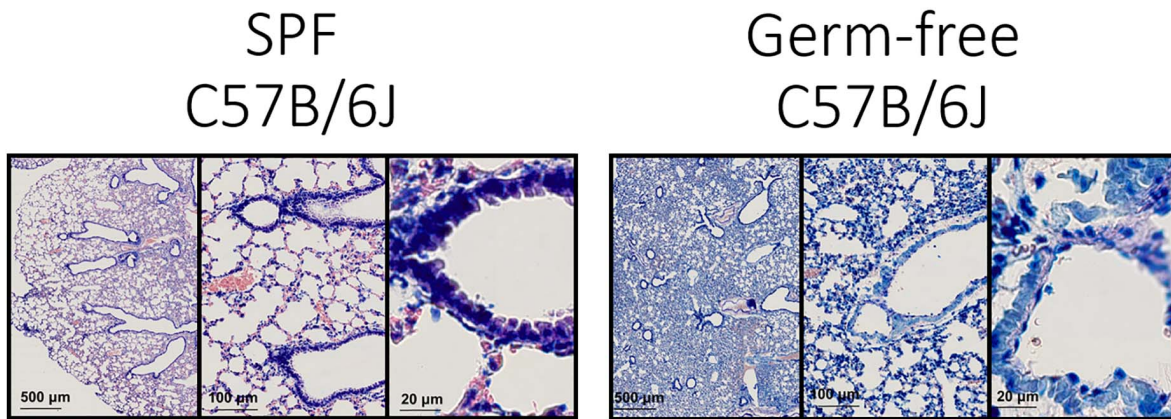


FIGURE 3 | Lung architecture with Giemsa staining—Sections obtained by performing transversal cuts of whole lung and visualized under a brightfield microscope with a 100×/1.4 Oil objective.

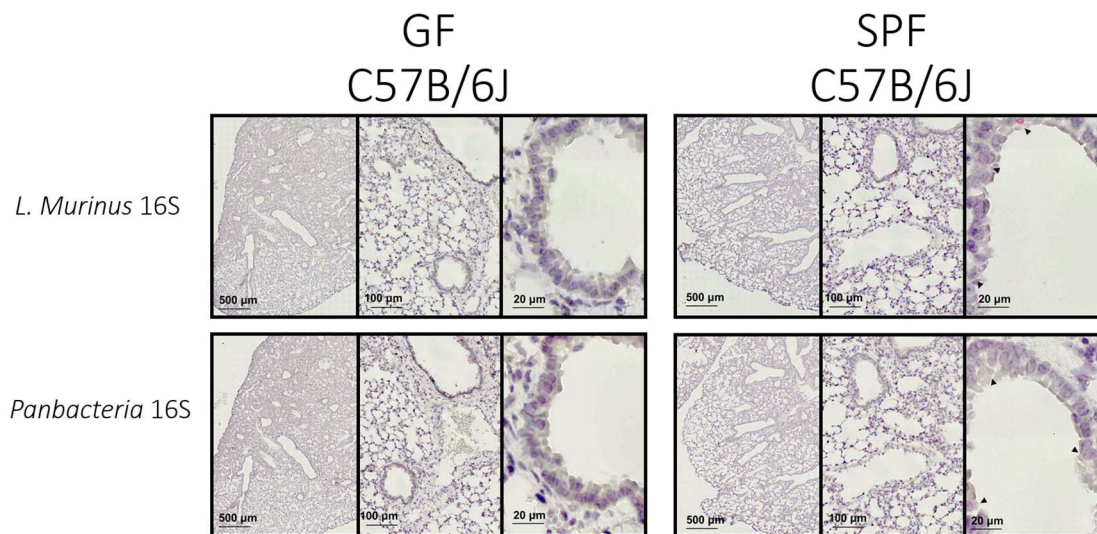


FIGURE 4 | *L. murinus* and panbacteria visualization in lung sections of SPF and GF mice—Sections obtained by performing transversal cuts of whole lung and visualized under a brightfield microscope with a 100×/1.4 Oil objective. Black arrows indicate the presence of target RNA: *L. murinus* (top panel) or Panbacteria (lower panel).

airways (**Figure 4**–right panel). When adapted to other tissues, the density and location of commensal bacteria could differ (Welch et al., 2017). We recommend staining of consecutive slides with two probes (here Panbacteria and species specific) to independently confirm the presence of commensals. As a negative control we used lung tissue from axenic mice (**Figure 4**–left panel), which should remain free of staining. Alternatively, gnotobiotic animals lacking a certain species of bacteria could also be used as a negative control for the species-specific staining.

Conventionally housed mice or «wild» mice derived tissues would probably show a different distribution and colonization density with commensal bacteria. From previous experiments we know that the lung of SPF housed mice (in our facility) contains about 10^5 CFU of bacteria when plated in rich chocolate agar or

Columbia agar (Yildiz et al., 2020), most of which are *L. murinus* based on NGS data. 16S rRNA specific qPCR for this commensal revealed approximately 10^7 genome equivalents. The discrepancy could be based on dead bacteria. Regardless, these numbers could be used as proxy for minimum colonization density required for successful ISH approaches.

Critical Steps and Troubleshooting

- It is important to always use freshly prepared histological grade xylene, ethanol 99.9 grade and Meyer's solution.
- The efficiency of the staining process primarily depends on the target retrieval step, which allows the permeabilization of the tissue granting the probe access to the target.

- The temperature of the steam cooker is crucial to be maintained constant (between 96 and 99°C) throughout the target retrieval incubation. The use of a thermometer on the steam cooker helps monitoring the temperature with the specified machine.
- We tried an additional stage of permeabilization since gram-positive bacteria such as *L. murinus* are known to have a thicker cell wall. For that we introduced a lysozyme incubation step for 90 min at 40°C. However, this additional exposure did not improve staining results (data not shown).
- Another important point during the staining process is the adjustment of the time of incubation during the signal amplification step. Amp5 incubation can be left for longer or shorter times for intensity regulation of the probe signal. On the same note, Meyer's solution dilution can also be adjusted for a stronger counterstaining of the tissue slice. The fine-tuning of both these steps is helpful if the probe intensity is faint and contributes to a better contrast between counterstaining and target signal.

DISCUSSION

In this article we presented a general pipeline for ISH allowing visualization of commensal bacteria in an environment of low-colonization density. Combined with specific probes, detection of a given bacterial species in context of its natural organ context is possible. The technique provides a high signal to noise ratio as shown by the lack of background staining in axenic animals. In contrast to hybridization approaches targeting bacterial DNA (Choi et al., 2015), it further allows detection of mostly living bacteria since the targets are short lived bacterial RNAs. Similar approaches were already used to detect pathogenic bacteria in the densely colonized digestive tract of pigs (Jonach et al., 2014) or in human feces (Harmsen et al., 2002). As for metagenomic approaches the targeted bacterium does not require to be culturable. Nevertheless, FISH and ISH techniques are limited to a rather small number of targets, thus we propose this technique as complementary to genomic (Barfod et al., 2013; Pendleton et al., 2017) and culturomic approaches (Sibley et al., 2011; Browne et al., 2016).

We chose a colorimetric approach in order to better visualize the proximity to the host tissue (Yildiz et al., 2020), but in general fluorophore-labeled probes could also be used as shown in a recent study using pan-eubacteria specific fluorescent probes to detect lung commensal bacteria (Yun et al., 2014).

In a recently published study we estimated the total genome copy number of *L. murinus* in the lung of a SPF housed mouse as 10^7 , based on specific qPCR data (Yildiz et al., 2018). NGS data from the same study showed predominance of Lactobacilli in the lung (90–95%). In comparison to the fecal matter of ASF a systematic screen would be required to estimate the sensitivity of ISH for detection of very low abundant commensal bacteria. According to the above-mentioned relative abundance of Lactobacilli in the SPF house mouse lungs, we

would expect a substantially reduced signal for the less abundant lung commensals (at least a factor of 10–20-fold reduction).

An interesting future expansion of this technique would be the combined detection of bacterial RNA and host RNA, to visualize, e.g., host responses of cells in the direct environment of commensal or pathogenic bacteria. Using distinct fluorescently labeled probes, such a staining is perfectly in accordance with the here proposed techniques and would require only little adaptation. In context of cancer diagnostics, a similar approach was used to confirm the presence of the bacteria strain *Acidovorax* as a potential biomarker for lung cancer (Greathouse et al., 2020). This approach would be complementary to dual RNAseq techniques, used to characterize interaction networks between bacteria and host from total organ homogenates (Westermann et al., 2016; Griesenauer et al., 2019).

A combination of several probes for the detection of multiple bacterial species in more complexly colonized animal would equally be of interest. For the intestinal tract FISH was already used to establish a biogeographical map indicating microbiota distribution on phylum level (Tropini et al., 2017; Welch et al., 2017). In mice with defined microbiota (Brugiroux et al., 2016), this approach would obviously be easier than in wild mice. Association of bacterial localization with metabolic function by metabolomic approaches (Marion et al., 2020) would be an additional, exciting approach to combine ISH for commensal bacteria with.

In combination with 16S specific rRNA gene NGS and metagenomic shot gun approaches we propose the use of complementing FISH or ISH approaches to localize commensal bacteria of interest in organ context.

DATA AVAILABILITY STATEMENT

The original contributions presented in the study are included in the article/supplementary material, further inquiries can be directed to the corresponding author/s.

ETHICS STATEMENT

The animal study was reviewed and approved by the Direction de l'expérimentation animale, University of Geneva and SCAV Canton Geneva.

AUTHOR CONTRIBUTIONS

JPPB performed the ISH experiments and optimized the technique for detection of bacteria in lung tissue. Both authors wrote the article and approved the submitted version.

FUNDING

This work was supported by the Swiss National Science Fund (155959 and 182475).

REFERENCES

- ACD (2021). *Introduction to RNAscope® ISH Technology in Any Species, Any Tissue*. London: ACD.
- Barfod, K. K., Roggenbuck, M., Hansen, L. H., Schjørring, S., Larsen, S. T., Sørensen, S. J., et al. (2013). The murine lung microbiome in relation to the intestinal and vaginal bacterial communities. *BMC Microbiol.* 13:303. doi: 10.1186/1471-2180-13-303
- Becattini, S., Sorbara, M. T., Kim, S. G., Littmann, E. L., Dong, Q., Walsh, G., et al. (2021). Rapid transcriptional and metabolic adaptation of intestinal microbes to host immune activation. *Cell Host Microbe* 29, 378.e5–393.e5. doi: 10.1016/j.chom.2021.01.003
- Browne, H. P., Forster, S. C., Anonye, B. O., Kumar, N., Neville, B. A., Stares, M. D., et al. (2016). Culturing of “unculturable” human microbiota reveals novel taxa and extensive sporulation. *Nature* 533, 543–546. doi: 10.1038/nature17645
- Brugiroux, S., Beutler, M., Pfann, C., Garzetti, D., Ruscheweyh, H. J., Ring, D., et al. (2016). Genome-guided design of a defined mouse microbiota that confers colonization resistance against *Salmonella enterica* serovar Typhimurium. *Nat. Microbiol.* 2:16215. doi: 10.1038/nmicrobiol.2016.215
- Choi, Y. S., Kim, Y. C., Baek, K. J., and Choi, Y. (2015). In situ detection of bacteria within paraffin-embedded tissues using a digoxin-labeled DNA probe targeting 16s rRNA. *J. Vis. Exp.* 2015, 1–6. doi: 10.3791/52836
- Greathouse, K. L., White, J. R., Vargas, A. J., Bliskovsky, V. V., Beck, J. A., Von Muhlinen, N., et al. (2020). Author correction: interaction between the microbiome and TP53 in human lung cancer. *Genome Biology* 21, 1–16. doi: 10.1186/s13059-018-1501-6
- Griesenauer, B., Tran, T. M., Fortney, K. R., Janowicz, D. M., Johnson, P., Gao, H., et al. (2019). Determination of an interaction network between an extracellular bacterial pathogen and the human host. *mBio* 10:e001193-19. doi: 10.1128/mBio.01193-19
- Harmsen, H. J. M., Raangs, G. C., He, T., Degener, J. E., and Welling, G. W. (2002). Extensive set of 16S rRNA-based probes for detection of bacteria in human feces. *Appl. Environ. Microbiol.* 68, 2982–2990. doi: 10.1128/AEM.68.6.2982-2990.2002
- Human Microbiome Project Consortium (2012). Structure, function and diversity of the healthy human microbiome. *Nature* 486, 207–214. doi: 10.1201/9781482293289-58
- Jonach, B., Boye, M., Stockmarr, A., and Jensen, T. K. (2014). Fluorescence in situ hybridization investigation of potentially pathogenic bacteria involved in neonatal porcine diarrhea. *BMC Vet. Res.* 10:1–8. doi: 10.1186/1746-6148-10-68
- Laukens, D., Brinkman, B. M., Raes, J., De Vos, M., and Vandenabeele, P. (2015). Heterogeneity of the gut microbiome in mice: guidelines for optimizing experimental design. *FEMS Microbiol. Rev.* 40, 117–132. doi: 10.1093/femsre/fuv036
- Marion, S., Desharnais, L., Studer, N., Dong, Y., Notter, M. D., Poudel, S., et al. (2020). Biogeography of microbial bile acid transformations along the murine gut. *J. Lipid Res.* 61, 1450–1463. doi: 10.1194/jlr.RA120001021
- Morris, G. B., Ridgway, E. J., and Suvarna, S. K. (2019). Traditional stains and modern techniques for demonstrating microorganisms in histology. *Bancroft's Theory Pract. Histol. Tech.* 2019, 254–279. doi: 10.1016/B978-0-7020-6864-5.00016-5
- Pendleton, K. M., Erb-Downward, J. R., Bao, Y., Branton, W. R., Falkowski, N. R., Newton, D. W., et al. (2017). Rapid pathogen identification in bacterial pneumonia using real-time metagenomics. *Am. J. Respir. Crit. Care Med.* 196, 1610–1612. doi: 10.1164/rccm.201703-0537LE
- Rausch, P., Basic, M., Batra, A., Bischoff, S. C., Blaut, M., Clavel, T., et al. (2016). Analysis of factors contributing to variation in the C57BL/6J fecal microbiota across German animal facilities. *Int. J. Med. Microbiol.* 306, 343–355. doi: 10.1016/j.ijmm.2016.03.004
- Sibley, C. D., Grinwis, M. E., Field, T. R., Eshaghurshan, C. S., Faria, M. M., Dowd, S. E., et al. (2011). Culture enriched molecular profiling of the cystic fibrosis airway microbiome. *PLoS One* 6:e0022702. doi: 10.1371/journal.pone.0022702
- Tian, G., Qiu, Y., Qi, Z., Wu, X., Zhang, Q., Bi, Y., et al. (2011). Histopathological observation of immunized rhesus macaques with plague vaccines after subcutaneous infection of yersinia pestis. *PLoS One* 6:e0019260. doi: 10.1371/journal.pone.0019260
- Tropini, C., Earle, K. A., Huang, K. C., and Sonnenburg, J. L. (2017). The gut microbiome: connecting spatial organization to function. *Cell Host Microbe* 21, 433–442. doi: 10.1016/j.chom.2017.03.010
- Welch, J. L. M., Hasegawa, Y., McNulty, N. P., Gordon, J. I., and Borisy, G. G. (2017). Spatial organization of a model 15-member human gut microbiota established in gnotobiotic mice. *Proc. Natl. Acad. Sci. U.S.A.* 114, E9105–E9114. doi: 10.1073/pnas.1711596114
- Westermann, A. J., Förstner, K. U., Amman, F., Barquist, L., Chao, Y., Schulte, L. N., et al. (2016). Dual RNA-seq unveils noncoding RNA functions in host-pathogen interactions. *Nature* 529, 496–501. doi: 10.1038/nature16547
- Yildiz, S., Bonifacio Lopes, J. P. P., Bergé, M., González-Ruiz, V., Baud, D., Kloehn, J., et al. (2020). Respiratory tissue-associated commensal bacteria offer therapeutic potential against pneumococcal colonization. *eLife* 9:53581. doi: 10.7554/ELIFE.53581
- Yildiz, S., Mazel-Sanchez, B., Kandasamy, M., Manicassamy, B., and Schmolke, M. (2018). Influenza A virus infection impacts systemic microbiota dynamics and causes quantitative enteric dysbiosis. *Microbiome* 6, 1–17. doi: 10.1186/s40168-017-0386-z
- Yun, Y., Srinivas, G., Kuenzel, S., Linnenbrink, M., Alnahas, S., Bruce, K. D., et al. (2014). Environmentally determined differences in the murine lung microbiota and their relation to alveolar architecture. *PLoS One* 9:e0113466. doi: 10.1371/journal.pone.0113466

Conflict of Interest: The authors declare that the research was conducted in the absence of any commercial or financial relationships that could be construed as a potential conflict of interest.

Copyright © 2021 Bonifacio and Schmolke. This is an open-access article distributed under the terms of the Creative Commons Attribution License (CC BY). The use, distribution or reproduction in other forums is permitted, provided the original author(s) and the copyright owner(s) are credited and that the original publication in this journal is cited, in accordance with accepted academic practice. No use, distribution or reproduction is permitted which does not comply with these terms.

4. Discussion

4.1. Optimizing the live attenuated influenza A vaccine (LAIV) backbone for high-risk patient groups

Influenza vaccines are the best cost-effective way to prevent influenza disease and decrease the burden associated with this respiratory disease. Inactivated influenza vaccines are safe and capable of inducing robust antibody responses, however vaccine effectiveness remains suboptimal. On the other hand, LAIVs induce broad cellular immunity and potent mucosal responses, but are limited to the use in healthy subjects from 2 to 49 years old due to safety concerns. In this thesis, we demonstrated a strategy to further attenuate the currently licensed LAIV backbone with the intention to expand its application to high-risk population groups. This is not the first attempt to increase the safety profile of an attenuated influenza vaccine. Mutations in PA-X and NS1 of the LAIV backbone have been shown to decrease vaccine virus replication in the upper respiratory tract of mice^{441,442,438}. Moreover, several other strategies rely on sophisticated alternative mechanisms of attenuation that are applicable to other influenza strains^{443,444}. For instance, codon deoptimization strategies were shown to attenuate the A/PR/8/34 (H1N1) strain by decreasing the expression level of the viral proteins encoded by the deoptimized segments. When administered to mice, this virus conferred cross protection against lethal challenges with two mouse-adapted H3N2 strains. Similarly, a new technology called proteolysis-targeting chimeric (PROTAC) was published recently. Genetically engineered PROTAC strains contain a conditionally removable proteasome-targeting domain that allows specific viral proteins to be degraded in vivo resulting in attenuated viruses still able to induce robust antibody and cellular responses⁴⁴⁵. All these approaches present additional LAIV platforms capable of inducing strong and cross-protective responses and underscore the need for novel strategies to tackle influenza burden in human populations^{446,447}. Among them, our study represents one of the first to address the potential implications of a safer LAIV in susceptible patient groups.

Live attenuated vaccines (LAVs) bring the advantage of triggering mucosal immunity. They replicate at the local site of infection and induce potent IgA and memory T cell responses with the potential to block infection and limit transmission. In our neonatal mice model, we did not observe induction of IgAs in broncho-alveolar lavages from LAIV or optiLAIV vaccination. This could be due to the immature state of the immune system. It is known that during infancy, vaccination induces weak plasma cell and germinal center B cell responses^{448,449}.

LAIV efficacy studies in animal models have shown a correlation between vaccine replication and the ability to induce protective responses. This is most likely from an increased antigen availability due to higher vaccine virus replication⁴⁵⁰. We showed that despite lower replication and faster clearance from the URT of neonatal mice when compared to LAIV, optiLAIV equally protected these animals, even when the challenge was performed more than one month after vaccination. We propose that an increased immunogenicity of optiLAIV could explain this observation. The use of adjuvants in inactivated vaccines relies on the same principal: increasing vaccine efficacy by enhancing immunogenicity using the same or lower antigen doses. For example, the addition of AS03, a squalene-based adjuvant, to the formulation of a monovalent IIV increased strain-specific and broad heterosubtypic antibodies after vaccination, compared to the same dose without adjuvant⁴⁵¹. Mechanistically, AS03 acts by destabilizing the lipid metabolism of macrophages and inducing ER stress and the unfolded protein response^{452,453}. In turn, this response was shown to enhance antigen delivery, immune cell recruitment, the stimulation of local immune cells, and induction of high affinity antigen-specific antibody responses^{454,455}. Our results showed that, compared to LAIV, optiLAIV upregulated genes downstream of the UPR in infected lung cells from human and mice origin, but also in macrophages derived from human peripheral blood monocyctic cells (PBMCs) (data not shown). This is in line with the mechanism of action of the AS03 adjuvant and corroborates the increased immunogenicity of optiLAIV. Although we only provide circumstantial evidence, follow up studies could strengthen our hypothesis by using conditional knockout mice lacking key elements of the UPR⁴⁵⁶.

Both HA and NA were shown to activate this pathway, and different degrees of activation were observed for NA from different strains⁴⁵⁷. It would be interesting to assess if an optiLAIV candidate expressing HA and NA variants that do not induce the UPR would still maintain its enhanced attenuated phenotype and adjuvanticity. If not, implementing optiLAIV would mean that, during vaccine strain selection, WHO guidelines would have to consider the ability of the HA and NA strain used to induce this pathway. Nevertheless, alternative strategies to exploit UPR activation by the vaccine strains exist and could be employed. For example, decreasing glycosylation sites in HA globular domain increased their ability to induce UPR signaling⁴⁵⁸.

The use of adjuvants is common practice to increase immunogenicity of vaccine formulations, with the exception of LAVs. This is due to the fact that LAVs already contain multiple immunostimulatory molecules capable of inducing potent immune responses, i.e. PAMPs, and are a self-amplifying antigen source. Interestingly, our study suggests that it might

be possible to modulate the intrinsic adjuvant properties of these vaccine platforms and further enhance immunogenicity via the UPR activation. One mechanism to trigger the UPR signaling is via accumulation of misfolded proteins in host cells. Since this is a common feature for several viral pathogens⁴⁵⁹, other live attenuated viral vaccine vectors could benefit from this strategy. Varicella-zoster virus (VZV)^{460,461}, Adenovirus (ADNV)^{462,463} and Cytomegalovirus (CMV)^{464,465} represent other examples of viruses that can modulate the UPR and are used as live attenuated vaccine vectors, highlighting the breadth of candidates our strategy could be applied to. Moreover, it has been shown that during rotavirus replication cycle, UPR activation is interrupted at the translational level by the viral nonstructural protein NSP3 of the virus⁴⁶⁶. Modifying this function of NSP3 in the oral rotavirus vaccine strain and evaluating efficacy and safety could be an interesting way of testing the transferability of our strategy to other platforms.

The ability of LAVs to induce local mucosal and cellular immunity could act in synergy with inactivated vaccines (IVs) which trigger mostly systemic humoral responses. In addition, LAVs are associated with blocking infection and transmission while IVs are associated with better protection against disease. A ‘prime and boost’ strategy has been suggested to exploit the combination of both types of immune response. In animal models, prime and boost regimens with different combinations of IIV and LAIV were shown to induce higher antibody titers against conserved epitopes, memory T cells and better heterologous protection^{467–469}. Boosting with an LAIV can redirect the recall response of the immune system towards internal proteins, induce mucosal immunity and deliver antigens for longer periods. Moreover, in this scenario, using optiLAIV could have the added benefit of including a broader range of target populations.

Another important effect of LAVs is the induction of trained immunity. Trained immunity is defined as a long-term change in the functional properties of innate immune cells by epigenetic reprogramming. By mimicking a natural infection and promoting a strong immune response, it is postulated that live vaccines can induce epigenetic rewiring in innate immune cells and promote sustained changes in their transcriptional programs lasting for months. BCG, measles, oral polio and smallpox vaccines have all shown beneficial, non-specific effects due to trained immunity⁴⁷⁰. In the case of BCG vaccine, protection against all-cause mortality in neonates⁴⁷¹ and protection against non-related pathogenic infections such as yellow fever⁴⁷² or malaria⁴⁷³ have been observed. Although there is no clinical evidence for LAIV and trained immunity, one study reported an indirect effect of this vaccine on all-cause medically attended acute respiratory illness⁴⁷⁴. Moreover, an ongoing prospective cohort study

is aiming to evaluate the effects of LAIV in all-cause mortality and cardiovascular mortality⁴⁷⁵. In mice, it was shown that LAIV protected against subsequential RSV infection without any RSV-specific antibody responses⁴⁷⁶, although the effect was only sustained for a few days. Altogether, these studies point towards non-specific effects of LAIV which in combination with prime-boost strategies and a broader application in high-risk groups, could not only mitigate the burden of influenza, but also, significantly reduce the incidence of other diseases⁴⁷⁷.

The currently licensed LAIV contains a quadrivalent formulation with two IAV caAnnArbor expressing H1N1 and H3N2 subtypes and two attenuated IBV lineages present in one single dose. In our study we used the caAnnArbor strain expressing IAV PR8 HA and NA(H1N1) as a model for the LAIV used in humans. This approach serves the purpose of characterizing this vaccine *in vitro* and *in vivo* using a mouse model, however, it falls short on the ability to measure vaccine interference from the other strains present in the vaccine. Vaccine viral interference was suggested as major contributors for the low vaccine effectiveness observed in the 2015/2016 influenza season based on *in vitro* replication studies⁴⁷⁸, although no significant clinical evidence was found to support this⁴⁷⁹. Moreover, our *in vivo* model uses naïve mice and does not address the impact of pre-existing immunity to IAV and the possible interference with LAIV replication and efficacy, as reported in other studies⁴⁸⁰⁻⁴⁸⁴. It would be interesting in follow up studies to explore the effects of a quadrivalent formulation and pre-existing immunity in the safety and efficacy of optiLAIV.

4.2.A single respiratory tract infection early in life reroutes healthy microbiome development and affects adult metabolism in a preclinical animal model

Interventions during childhood have the potential to impact the development of a healthy microbiota with physiological implications in adult life. Antibiotic treatment, exposure to environmental factors and diet are strong modulators of microbiota by depleting, introducing and favoring the growth of particular strains in the community. In our study, we showed that a subclinical IAV infection during childhood is also capable of inducing a state of dysbiosis lasting until adulthood in mice. We observed an enrichment of Enterobacteriales and an underrepresentation of Clostridiales. Moreover, the dysbiosis state was more pronounced in tissue-associated microbiota of the small intestine whereas in the fecal microbiota only minor changes in low abundance families were observed (although an underrepresentation of the same member of the Clostridiales family was also seen in feces). Interestingly, we also report that male mice imprinted by an early life IAV infection have increased body weight in adulthood and are more susceptible to develop heavier adipose depots upon a high sugar high fat diet. This is in line with an altered microbiota since co-housing experiments abrogated this effect. In humans, a decreased representation of Clostridiales and enrichment in Enterobacteriales have been observed in obese patients⁴⁸⁵. Enterobacteriales are gram-negative bacteria exhibiting high endotoxin activity and are thought to be a source of low-grade increase in plasma LPS. Termed metabolic endotoxemia, this process has been suggested as a mediator of metabolic syndromes commonly observed in obese patients⁴⁸⁶. Our data suggests that a subclinical viral infection has the potential to cause long-term impacts in the microbiota composition with effects on host physiology. This is also true for other viral pathogens. Other groups reported an association between early life exposure to rhinoviruses and adenovirus and dysbiosis and increased susceptibility to respiratory tract infections years later⁴⁸⁷.

The idea of viral infections in early life as modulators of host microbiota development is particularly interesting given that childhood viral infections are frequent and often underreported. Although a subclinical viral infection does not affect the microbiota in the same degree as antibiotic interventions, the constant pressure/impact caused by repetitive viral infections could deviate microbiota development into a pathology-associated community. In fact, the Anna Karenina principle (AKP) theory beautifully describes this phenomenon. According to its definition, healthy microbiota communities are alike, and each disease-associated community is unique in its own way^{488,489}. Thus, microbiota stressors that provoke stochastic perturbations in microbiota composition, i.e. mild viral infections, need not shift the

community to a predefined disease-like composition. Instead, they would only need to tweak the natural progress of a healthy/symbiotic microbiota which would be sufficient to result in a dysbiotic community. Interestingly, this observation is reflected in our data. By evaluating β -diversity over time in mock- and IAV-imprinted animals, we observed that at 7 days post infection, microbiota communities from both groups were very similar and closely distributed along the principal component analysis plot. This is most likely due to the small impact of a mild respiratory tract infection in the gut microbiota as observed in respiratory syncytial virus (RSV) and SARS-CoV2 asymptomatic infections^{490,491}. As the mice developed and went through stronger disturbances known to affect their microbiota, i.e. the introduction of solid food, at 14 days post infection we observed a higher β -diversity. This was characterized by a bigger scattering of each sample for both groups, although they still presented overlapping distributions. Interestingly, mock-imprinted adult animals (56 days post infection) showed more alike communities characterized by a lower β -diversity (closer distribution of the mock-imprinted samples in the plot). In contrast, IAV-imprinted animals had more dissimilar communities with higher β -diversity (dispersed distribution of the IAV-imprinted samples in the plot), reflecting the AKP theory. It would be interesting to assess viral replication or the degree of the immune response in the IAV-imprinted animals with microbiota communities resembling mock-imprinted animal communities. This could indicate if the degree of dysbiosis correlates to the severity of IAV infection. Moreover, following up microbiota composition at later time points and evaluating if β -diversity of IAV-imprinted microbiota communities would increase, could strengthen the claims of an AKP effect.

The effects of dysbiosis in human health are usually associated with a change in SCFAs metabolism. It was shown that pathologic imprinting of the microbiota can modulate SCFA levels in plasma and impair normal functions of distal organs and immune cells. Upon IAV infection, gut microbiota changes decrease butyrate levels and impair the killing activity of macrophages in the lungs. In turn, mice are more susceptible to secondary bacterial infections⁴³¹. Moreover, SCFA administration in mice has been shown to induce adipogenesis, promote insulin resistance and regulate energy metabolism through engagement with GPR43 receptor, leading to fat accumulation in adipose tissues^{492,493}. Accordingly, we show that the increased body weight in male mice imprinted with IAV seems to be mediated by SCFA, since in the absence of these metabolite receptors (GPR41 and GPR43), the effect was abrogated, even though the long term dysbiosis was still present. The underlying mechanism is still elusive and other factors could explain the absence of a phenotype in these animals. For example, the baseline weight of GPR41 and GPR43 double knockouts was increased by 10% compared to

wild-type animals. Since the difference in body weight loss between mock and imprinted animals was less than 3%, this effect could have been overruled by the baseline differences between knockout and *wild type* animals. Moreover, the baseline microbiota of *wild-type* and knockout animals was different which could also contribute to the loss of body weight differences. An experiment co-housing IAV-imprinted *wild-type* and knockout animals and comparing their body weight to co-housed mock-imprinted *wild-type* and knockout animals, could address this possible cofounder. Nonetheless, we cannot rule out an effect mediated by SCFAs. In addition, measuring SCFAs in the intestinal flushes of IAV-imprinted GPR41/43^{-/-} animals showed a slight decrease in butyrate levels compared to mock-imprinted animals (data not shown). Although it did not reach significance, this result indicates a possible link between dysbiosis and SCFA metabolism. However, more experiments need to be done to evaluate if this effect is true for *wild-type* animals.

The consequences of long-term dysbiosis have been shown to affect vaccine responses. Antibiotic treated mice had impaired antibody titers to 13 different vaccines currently approved for human use⁴⁹⁴. In addition, an extensive review gathered epidemiological evidence on the association between fecal microbiota and vaccine responses and showed an increased ratio of Enterobacteriaceae to Bacteroides in recipients with enhanced antibody responses⁴⁹⁵. According to our findings, we did not observe a significant difference in antibody titers to a childhood vaccine. Since our study model uses a subclinical IAV infection as a driver of dysbiosis, the long-term effects in host physiology might be small. Indeed, the body weight differences observed were mild (3% of total body weight). With that in mind, we believe that evaluating the immune response to a mucosal vaccine would be of interest in a follow-up study and more likely to be affected by the dysbiosis caused by IAV imprinting. Two interesting candidates would be the BCG vaccine and the oral rotavirus vaccine which have been shown to elicit different magnitudes of immune responses based on microbiota differences both in mice and in human studies⁴¹⁵.

Previous studies have shown the ability of respiratory infections to modulate the microbiota of the respiratory tract. Our group showed that upon a severe IAV infection the growth of an *Escherichia coli* strain is favored over the predominant resident population of *Lactobacillus murinus*⁴⁹⁶. This disbalance contributes to the increased susceptibility of IAV-infected mice to secondary bacterial infections, in line with the functional role of the lung microbiota in maintaining health. According to our results, IAV infections in early life also shape the lung microbiota as the mouse develops, with an enrichment of Bacilli observed in adulthood. It would be interesting to explore if these changes are a consequence of direct viral-

bacterial interactions in the respiratory tract. In fact, it has been shown that in the lung, RSV and IAV can directly interact with the bacterial surface of *Streptococcus pneumoniae*, *Moraxella catarrhalis*, *Haemophilus influenzae* and *Staphylococcus aureus* and increase bacterial attachment to the respiratory epithelia⁴⁹⁷⁻⁴⁹⁹. A good starting point to follow-up on this idea would be to visualize the spatial distribution of commensals and how the dynamics of an acute respiratory infection overlap in niches colonized by bacteria in the lung. Our adapted in situ RNA hybridization technique would be useful in this regard. Moreover, coupling our compositional data with metagenomic, proteomic and metabolomic approaches could reveal important functional roles of the lung microbiota and provide a better insight on the possible physiological consequences of this dysbiosis.

4.3. General Discussion

The quest to find the perfect vaccine against influenza remains one of the most challenging aspects of vaccine research. Apart from all the hurdles posed by the complex biology of the virus and the socio-economic aspects of implementing effective vaccination programs, there is still a multitude of intrinsic factors affecting the individual responses to vaccination. The host microbiota is one of these factors with growing evidence linking the quality of antibody responses to different microbiota compositions⁴¹⁵. For example, an increase in the relative abundance of Proteobacteria in fecal microbiota significantly correlated to higher antibody titers after rotavirus vaccination⁵⁰⁰. Although causal relationships are still missing, there is reasonable biological plausibility. Commensal bacteria can imprint the immune system of the host by direct interaction with the mucosal compartment of the immune system and/or by production of secondary metabolites implicated in immune regulation. This was observed in a study performed in mice where the presence of commensal bacteria expressing flagellin induced higher antibody titers against IIV compared to antibiotic-treated and germ-free mice. Mechanistically, the authors showed that TLR5-mediated sensing of flagellin promoted plasma cell differentiation and stimulated lymph node macrophages to produce plasma cells growth factors⁵⁰¹. Interestingly, not only does the microbiota modulate vaccine responses, the administration of vaccines also affects microbiota composition. This was shown within the first year of life, where administration of a pneumococcal conjugate vaccine correlated to an increased diversity and stability of the URT microbiota⁵⁰². Altogether, these lines of evidence suggest that the crosstalk between vaccines and microbiota represents an important phenomenon that has been ignored for years. Modulating such interactions should be explored to enhance the effectiveness of LAIV and at the same time extend its non-specific benefits on other health outcomes.

In this thesis we presented a strategy to optimize the LAIV and explore its application in high-risk patient groups, particularly in very young children. In addition, we observed that an early life subclinical infection with IAV caused long-term dysbiosis with consequences in host physiology. Taken together, these findings could pave the way to explore undiscovered effects of LAIV in early life. Administering LAIV could be used to elicit protection against influenza virus but also to shape early microbiota communities favoring beneficial outcomes later in life. Preliminary evidence has been reported in this direction by showing a modest increase in nasopharyngeal pneumococcal carriage and density following LAIV vaccination in young children^{503,504}. Although these studies raise concerns regarding the consequences of an increased prevalence of *Streptococcus pneumoniae* and *Staphylococcus aureus* colonization of the URT, they mostly focus on pathobionts and do not report on the composition of other potentially beneficial commensals. Moreover, they lack longitudinal follow up without any evidence for long-term consequences of this vaccine. Based on our results, it would be interesting to see in a follow-up study, if the long-term effects observed with our subclinical IAV infection would still happen with optiLAIV. Understanding the underlying mechanisms of how IAV infection causes long-term dysbiosis can guide concomitant interventions to LAIV administration in order to modulate the microbiota development. One such intervention could be the delivery of probiotics in parallel to vaccination to promote the expansion of a healthy gut microbiota.

With this report, we would like to bring the attention of the microbiome research community to the possibility of a live attenuated influenza vaccine to modulate the human microbiota, when administered in early life. It would be of great interest to us and others to better understand the relationship between live attenuated influenza vaccine and the human microbiota. We think that further research could lead to new strategies that could enhance the vast beneficial effects of LAIV and that the microbiota holds the key to achieve such purpose.

5. List of Abbreviations

Abbreviation	Description
IAV	Influenza A Virus
IBV	Influenza B Virus
ICV	Influenza C Virus
IDV	Influenza D Virus
HA	Hemagglutinin
NA	Neuraminidase
WHO	World Health Organization
HI	Hemagglutination inhibition
CDC	Center for Disease Control and Prevention
URT	Upper Respiratory Tract
LRT	Lower Respiratory Tract
NP	Nucleoprotein
FluPol	Influenza Viral polymerase
PB1	Polymerase Basic Protein 1
PB2	Polymerase Basic Protein 2
PA	Acidic Polymerase
vRNP	Viral Ribonucleoprotein
M1	Matrix Protein 1
M2	Matrix Protein 2
NS1	Non-structural Protein 1
FP	Fusion Peptide
mRNA	Messenger RNA
HPAI	Highly Pathogenic Avian Influenza
TM	Transmembrane
RBD	RNA-binding Domain
ED	Effector Domain
RIG-I	Retinoic Acid-inducible Gene I
dsRNA	Double-stranded RNA
TRIM25	Tripartite Motif Containing 25
NF- κ B	Nuclear Factor kappa-light-chain-enhancer of Activated B Cells
PI3K	Phosphatidylinositol-3-kinase
PKR	RNA-binding Protein Kinase

CPSF30	Cleavage and Polyadenylation Specificity Factor 30
STAT-1	Signal Transducer and Activator of Transcription 1
IFNR	Interferon Receptor
UPR	Unfolded Protein Response
GISRS	Global Influenza Surveillance and Response System
ICU	Intensive Care Unite
PID	Primary Immunodeficiency
SoT	Solid Organ Transplant
HSCT	Hematopoietic Stem Cell Transplant
OAS	Original Antigenic Sin
PAMPs	Pathogen Associated Molecular Patterns
PRRs	Pattern Recognition Receptors
TLRs	Toll-like Receptors
NLRs	NOD-like Receptors
RLRs	RIG-like Receptors
CLRs	C-type lectin Receptors
ALRs	AIM2-like Receptors
IFNs	Interferons
ISGs	Interferon-stimulated Genes
ER	Endoplasmic Reticulum
BiP	Binding Immunoglobulin Protein
NK	Natural Killer
DCs	Dendritic Cells
ADCC	Antibody-dependent Cellular Cytotoxicity
TNF- α	Tumor Necrosis Factor alpha
IL-6	Interleukin 6
IL-1 β	Interleukin 1 beta
IL-18	Interleukin 18
APCs	Antigen Presenting Cells
Ig	Immunoglobulins
IgMs	Immunoglobulin M
PCs	Plasma Cells
IgG	Immunoglobulin G
IgA	Immunoglobulin A

CTLs	Cytotoxic T Lymphocytes
Th	T-helper
IL-2	Interleukin 2
M2e	M2 ectodomain
MDCKs	Madin-Darby Canine Kidney
IIV	Inactivated Influenza Vaccines
WPVs	Whole Particle Vaccines
SV	Split Virion
SU	Subunit
LAIV	Live Attenuated Influenza Vaccines
MDV	Master Donor Virus
ts	Temperature Sensitive
ca	Cold Adapted
att	Attenuated
NIAID	National Institute of Allergy and Infectious Disease
UIV	Universal Influenza Vaccine
HMP	Human Microbiome Project
rRNA	Ribosomal RNA
HMOs	Human Milk Oligosaccharides
GI	Gastro-intestinal
COPD	Chronic Obstruction of Pulmonary Disease
BAL	Bronco-alveolar Lavage
GF	Germ-free
SCFAs	Short-chain Fatty Acids
CNS	Central Nervous System
GAP	Goblet Cell-associated Antigen Passage
GALT	Gut-associated Lymphoid Tissue
Tregs	T regulatory Cells
GPR41	G-protein Coupled Receptor 41
GPR43	G-protein Coupled Receptor 43
HDAC	Histone Deacetylases
BCG	Bacillus Calmette-Guérin
RCTs	Randomized Clinical Trials
optiLAIV	Optimized LAIV

FHA	Filamentous Hemagglutinin
LDA	Linear Discriminant Analysis
ISH	In Situ Hybridization
SPF	Specific Pathogen-free
PROTAC	Proteolysis-targeting Chimeric
LAV	Live Attenuated Vaccines
PBMCs	Peripheral Blood Monocytic Cells
VZV	Varicella-zoster Virus
ADNV	Adenovirus
CMV	Cytomegalovirus
IVs	Influenza Vaccines
AKP	Anna Karenina Principle
RSV	Respiratory Syncytial Virus

6. List of Figures and Tables

INTRODUCTION

TABLE 1: HEMAGGLUTININ AND NEURAMINIDASE SUBTYPES AND THE SPECIES IN WHICH THEY HAVE BEEN DETECTED.....	12
FIGURE 1: STRUCTURE AND MORPHOLOGY OF IAV GENOME	13
FIGURE 2: INFLUENZA A VIRUS REPLICATION CYCLE	15
FIGURE 3: LINEAR AND 3D STRUCTURE OF INFLUENZA HA AND NA	17
FIGURE 4: INFLUENZA PANDEMICS TIMELINE	20
FIGURE 5: ANTIGENICITY OF IAV	31
FIGURE 6: HUMAN MICROBIOTA DEVELOPMENT.....	38
FIGURE 7: MICROBIOTA DISTRIBUTION ALONG THE GUT AND LUNGS.....	41
FIGURE 8: HOST MICROBIOTA EFFECTOR MECHANISMS IMPLICATED IN HEALTH AND DISEASE	44

RESULTS

FIGURE 9: LAIV AND OPTILAIV INDUCE IGG BINDING ANTIBODIES IN SERUM.....	78
FIGURE 10: NEONATAL IAV INFECTION LONG-TERM DYSBIOSIS DOES NOT AFFECT BODY WEIGHT IN ADULT GPR41/43^{-/-} MICE	96
FIGURE 11: NEONATAL IAV INFECTION DOES NOT AFFECT THE WEANING RESPONSE.	97
FIGURE 12: NEONATAL IAV INFECTION LONG-TERM DYSBIOSIS DOES NOT AFFECT ANTIBODY RESPONSES..	98
FIGURE 13: NEONATAL IAV INFECTION CHANGES LUNG MICROBIOTA COMPOSITION IN ADULT MICE	99

7. References

1. Monto, A. S. & Fukuda, K. Lessons From Influenza Pandemics of the Last 100 Years. *Clinical Infectious Diseases* **70**, 951–957 (2020).
2. Sederdahl, B. K. & Williams, J. v. Epidemiology and Clinical Characteristics of Influenza C Virus. *Viruses* **12**, (2020).
3. Weekly U.S. Influenza Surveillance Report | CDC. <https://www.cdc.gov/flu/weekly/index.htm>.
4. Flu News Europe: Weekly influenza updates. <https://www.ecdc.europa.eu/en/seasonal-influenza/surveillance-and-disease-data/flu-news-europe>.
5. Nyirenda, M., Omori, R., Tessmer, H. L., Arimura, H. & Ito, K. Estimating the Lineage Dynamics of Human Influenza B Viruses. *PLoS One* **11**, (2016).
6. A revision of the system of nomenclature for influenza viruses: a WHO memorandum - PubMed. <https://pubmed.ncbi.nlm.nih.gov/6969132/>.
7. A revised system of nomenclature for influenza viruses - PubMed. <https://pubmed.ncbi.nlm.nih.gov/5316848/>.
8. Schild, G. C., Winter, W. D. & Brand, C. M. Serological Diagnosis of Human Influenza Infections by Immunoprecipitin Techniques. *Bull. Org. mond. Sante* **1**, 465–471 (1971).
9. Hornbeck, P. Double-Immunodiffusion Assay for Detecting Specific Antibodies. *Curr Protoc Immunol* **00**, 2.3.1-2.3.4 (1991).
10. Antigenic Characterization | CDC. <https://www.cdc.gov/flu/about/professionals/antigenic.htm>.
11. Nobusawa, E. *et al.* Comparison of complete amino acid sequences and receptor-binding properties among 13 serotypes of hemagglutinins of influenza A viruses. *Virology* **182**, 475–485 (1991).
12. Europe, S. Influenza virus characterisation. (2019).
13. Bagheri, M. *et al.* European External Influenza Virus Quality Assessment Programme European External Influenza Virus Quality Assessment Programme-2020 data. doi:10.2900/588058.
14. Harrington, W. N., Kackos, C. M. & Webby, R. J. The evolution and future of influenza pandemic preparedness. *Experimental & Molecular Medicine* **2021 53:5** **53**, 737–749 (2021).
15. Influenza A Subtypes and the Species Affected | Seasonal Influenza (Flu) | CDC. <https://www.cdc.gov/flu/other/animal-flu.html>.

16. Kwon, E., Cho, M., Kim, H. & Son, H. S. A Study on Host Tropism Determinants of Influenza Virus Using Machine Learning. *Curr Bioinform* **15**, 121–134 (2019).
17. Ghosh, S. Sialic acid and biology of life: An introduction. *Sialic Acids and Sialoglycoconjugates in the Biology of Life, Health and Disease* 1 (2020) doi:10.1016/B978-0-12-816126-5.00001-9.
18. A, V. *et al.* Essentials of Glycobiology. *Cold Spring Harbor (NY)* **039**, 2015–2017 (2009).
19. Couceiro, J. N. S. S., Paulson, J. C. & Baum, L. G. Influenza virus strains selectively recognize sialyloligosaccharides on human respiratory epithelium; the role of the host cell in selection of hemagglutinin receptor specificity. *Virus Res* **29**, 155–165 (1993).
20. Costa, T. *et al.* Distribution patterns of influenza virus receptors and viral attachment patterns in the respiratory and intestinal tracts of seven avian species. *Vet Res* **43**, 28 (2012).
21. Ma, W. *et al.* North American Triple Reassortant and Eurasian H1N1 Swine Influenza Viruses Do Not Readily Reassort to Generate a 2009 Pandemic H1N1-Like Virus. *mBio* **5**, (2014).
22. Ma, W. *et al.* Viral reassortment and transmission after co-infection of pigs with classical H1N1 and triple-reassortant H3N2 swine influenza viruses. *J Gen Virol* **91**, 2314 (2010).
23. Ayora-Talavera, G. Sialic acid receptors: focus on their role in influenza infection. *J Receptor Ligand Channel Res* **10**, 1–11 (2018).
24. Trebbien, R., Larsen, L. E. & Viuff, B. M. Distribution of sialic acid receptors and influenza A virus of avian and swine origin in experimentally infected pigs. *Virol J* **8**, 434 (2011).
25. Ito, T. *et al.* Molecular basis for the generation in pigs of influenza A viruses with pandemic potential. *J Virol* **72**, 7367–7373 (1998).
26. Suzuki, Y. *et al.* Sialic acid species as a determinant of the host range of influenza A viruses. *J Virol* **74**, 11825–11831 (2000).
27. Bisht, K. & Velthuis, A. J. W. te. Decoding the Role of Temperature in RNA Virus Infections. *mBio* (2022) doi:10.1128/MBIO.02021-22.
28. Tong, S. *et al.* A distinct lineage of influenza A virus from bats. *Proc Natl Acad Sci U S A* **109**, 4269–4274 (2012).
29. Massin, P., van der Werf, S. & Naffakh, N. Residue 627 of PB2 is a determinant of cold sensitivity in RNA replication of avian influenza viruses. *J Virol* **75**, 5398–5404 (2001).

30. Kasloff, S. B. & Weingartl, H. M. Swine alveolar macrophage cell model allows optimal replication of influenza A viruses regardless of their origin. *Virology* **490**, 91–98 (2016).
31. Long, J. S., Mistry, B., Haslam, S. M. & Barclay, W. S. Host and viral determinants of influenza A virus species specificity. *Nature Reviews Microbiology* *2018 17:2* **17**, 67–81 (2018).
32. Zhang, H. Tissue and host tropism of influenza viruses: Importance of quantitative analysis. *Sci China Ser C-Life Sci* **52**, 1101–1110 (2009).
33. Stanley, W. M. THE SIZE OF INFLUENZA VIRUS. *J Exp Med* **79**, 267–283 (1944).
34. Badham, M. D. & Rossman, J. S. Filamentous Influenza Viruses. *Curr Clin Microbiol Rep* **3**, 155–161 (2016).
35. Becker, T., Elbahesh, H., Reperant, L. A., Rimmelzwaan, G. F. & Osterhaus, A. D. M. E. Influenza Vaccines: Successes and Continuing Challenges. *J Infect Dis* **224**, S405–S419 (2021).
36. Eisfeld, A. J., Neumann, G. & Kawaoka, Y. At the centre: influenza A virus ribonucleoproteins. *Nature Reviews Microbiology* *2014 13:1* **13**, 28–41 (2014).
37. Kosik, I. & Yewdell, J. W. Influenza Hemagglutinin and Neuraminidase: Yin–Yang Proteins Coevolving to Thwart Immunity. *Viruses* **11**, (2019).
38. Nayak, D. P., Balogun, R. A., Yamada, H., Zhou, Z. H. & Barman, S. Influenza virus morphogenesis and budding. *Virus Res* **143**, 147–161 (2009).
39. Plotch, S. J., Bouloy, M., Ulmanen, I. & Krug, R. M. A unique cap(m7GpppXm)-dependent influenza virion endonuclease cleaves capped RNAs to generate the primers that initiate viral RNA transcription. *Cell* **23**, 847–858 (1981).
40. Poon, L. L. M., Pritlove, D. C., Fodor, E. & Brownlee, G. G. Direct evidence that the poly(A) tail of influenza A virus mRNA is synthesized by reiterative copying of a U track in the virion RNA template. *J Virol* **73**, 3473–3476 (1999).
41. Nuwarda, R. F., Alharbi, A. A. & Kayser, V. An Overview of Influenza Viruses and Vaccines. *Vaccines* *2021, Vol. 9, Page 1032* **9**, 1032 (2021).
42. Turrell, L., Lyall, J. W., Tiley, L. S., Fodor, E. & Vreede, F. T. The role and assembly mechanism of nucleoprotein in influenza A virus ribonucleoprotein complexes. *Nat Commun* **4**, (2013).
43. Miyamoto, S. *et al.* Migration of Influenza Virus Nucleoprotein into the Nucleolus Is Essential for Ribonucleoprotein Complex Formation. *mBio* **13**, (2022).
44. Chlanda, P. *et al.* Structural Analysis of the Roles of Influenza A Virus Membrane-Associated Proteins in Assembly and Morphology. *J Virol* **89**, 8957–8966 (2015).

45. Rossman, J. S. & Lamb, R. A. Influenza virus assembly and budding. *Virology* **411**, 229–236 (2011).
46. Stieneke-Grober, A. *et al.* Influenza virus hemagglutinin with multibasic cleavage site is activated by furin, a subtilisin-like endoprotease. *EMBO J* **11**, 2407–2414 (1992).
47. Böttcher-Friebertshäuser, E. *et al.* Cleavage of influenza virus hemagglutinin by airway proteases TMPRSS2 and HAT differs in subcellular localization and susceptibility to protease inhibitors. *J Virol* **84**, 5605–5614 (2010).
48. Taubenberger, J. K. Influenza virus hemagglutinin cleavage into HA1, HA2: no laughing matter. *Proc Natl Acad Sci U S A* **95**, 9713–9715 (1998).
49. Neumann, G. & Kawaoka, Y. Transmission of Influenza A Viruses. *Virology* **0**, 234 (2015).
50. van Reeth, K. The post-2009 influenza pandemic era: time to revisit antibody immunodominance. *J Clin Invest* **128**, 4751–4754 (2018).
51. Neu, K. E., Henry Dunand, C. J. & Wilson, P. C. Heads, stalks and everything else: how can antibodies eradicate influenza as a human disease? *Curr Opin Immunol* **42**, 48 (2016).
52. Steel, J. *et al.* Influenza virus vaccine based on the conserved hemagglutinin stalk domain. *mBio* **1**, (2010).
53. Graves, P. N., Schulman, J. L., Young, J. F. & Palese, P. Preparation of influenza virus subviral particles lacking the HA1 subunit of hemagglutinin: unmasking of cross-reactive HA2 determinants. *Virology* **126**, 106–116 (1983).
54. Throsby, M. *et al.* Heterosubtypic neutralizing monoclonal antibodies cross-protective against H5N1 and H1N1 recovered from human IgM⁺ memory B cells. *PLoS One* **3**, (2008).
55. Ekiert, D. C. *et al.* Antibody recognition of a highly conserved influenza virus epitope. *Science* **324**, 246–251 (2009).
56. Krammer, F. Novel universal influenza virus vaccine approaches. *Curr Opin Virol* **17**, 95 (2016).
57. Creytens, S., Pascha, M. N., Ballegeer, M., Saelens, X. & de Haan, C. A. M. Influenza Neuraminidase Characteristics and Potential as a Vaccine Target. *Front Immunol* **12**, 4848 (2021).
58. Yang, X. *et al.* A beneficiary role for neuraminidase in influenza virus penetration through the respiratory mucus. *PLoS One* **9**, (2014).

59. Zanin, M. *et al.* Pandemic Swine H1N1 Influenza Viruses with Almost Undetectable Neuraminidase Activity Are Not Transmitted via Aerosols in Ferrets and Are Inhibited by Human Mucus but Not Swine Mucus. *J Virol* **89**, 5935–5948 (2015).
60. Sakai, T., Nishimura, S. I., Naito, T. & Saito, M. Influenza A virus hemagglutinin and neuraminidase act as novel motile machinery. *Sci Rep* **7**, (2017).
61. Palese, P., Tobita, K., Ueda, M. & Compans, R. W. Characterization of temperature sensitive influenza virus mutants defective in neuraminidase. *Virology* **61**, 397–410 (1974).
62. Chen, Y. Q. *et al.* Influenza Infection in Humans Induces Broadly Cross-Reactive and Protective Neuraminidase-Reactive Antibodies. *Cell* **173**, 417-429.e10 (2018).
63. Pichlmair, A. *et al.* RIG-I-mediated antiviral responses to single-stranded RNA bearing 5'-phosphates. *Science* **314**, 997–1001 (2006).
64. Gack, M. U. *et al.* Influenza A virus NS1 targets the ubiquitin ligase TRIM25 to evade recognition by the host viral RNA sensor RIG-I. *Cell Host Microbe* **5**, 439–449 (2009).
65. Wang, X. *et al.* Influenza A virus NS1 protein prevents activation of NF-kappaB and induction of alpha/beta interferon. *J Virol* **74**, 11566–11573 (2000).
66. Zhirnov, O. P., Konakova, T. E., Wolff, T. & Klenk, H.-D. NS1 protein of influenza A virus down-regulates apoptosis. *J Virol* **76**, 1617–1625 (2002).
67. Li, S., Min, J. Y., Krug, R. M. & Sen, G. C. Binding of the influenza A virus NS1 protein to PKR mediates the inhibition of its activation by either PACT or double-stranded RNA. *Virology* **349**, 13–21 (2006).
68. Ayllon, J. & García-Sastre, A. The ns1 protein: A multitasking virulence factor. *Curr Top Microbiol Immunol* **386**, 73–107 (2015).
69. Ji, Z. X., Wang, X. Q. & Liu, X. F. NS1: A Key Protein in the “Game” Between Influenza A Virus and Host in Innate Immunity. *Front Cell Infect Microbiol* **11**, 638 (2021).
70. Kathum, O. A. *et al.* Phosphorylation of influenza A virus NS1 protein at threonine 49 suppresses its interferon antagonistic activity. *Cell Microbiol* **18**, 784–791 (2016).
71. Hale, B. G., Randall, R. E., Ortin, J. & Jackson, D. The multifunctional NS1 protein of influenza A viruses. *Journal of General Virology* **89**, 2359–2376 (2008).
72. Hale, B. G. *et al.* Inefficient Control of Host Gene Expression by the 2009 Pandemic H1N1 Influenza A Virus NS1 Protein. *J Virol* **84**, 6909 (2010).
73. García-Sastre, A. *et al.* Influenza A Virus Lacking the NS1 Gene Replicates in Interferon-Deficient Systems. *Virology* **252**, 324–330 (1998).

74. García-Sastre, A. *et al.* The role of interferon in influenza virus tissue tropism. *J Virol* **72**, 8550–8558 (1998).
75. Mazel-Sanchez, B. *et al.* Influenza A viruses balance ER stress with host protein synthesis shutoff. *Proc Natl Acad Sci U S A* **118**, e2024681118 (2021).
76. Matrosovich, M. *et al.* Early alterations of the receptor-binding properties of H1, H2, and H3 avian influenza virus hemagglutinins after their introduction into mammals. *J Virol* **74**, 8502–8512 (2000).
77. Tumpey, T. M. *et al.* A two-amino acid change in the hemagglutinin of the 1918 influenza virus abolishes transmission. *Science* **315**, 655–659 (2007).
78. Webster, R. G. & Govorkova, E. A. Continuing challenges in influenza. *Ann N Y Acad Sci* **1323**, 115 (2014).
79. Francis, M. E., King, M. L. & Kelvin, A. A. Back to the Future for Influenza Preimmunity—Looking Back at Influenza Virus History to Infer the Outcome of Future Infections. *Viruses* 2019, Vol. 11, Page 122 **11**, 122 (2019).
80. The Deadliest Flu: The Complete Story of the Discovery and Reconstruction of the 1918 Pandemic Virus | Pandemic Influenza (Flu) | CDC. <https://www.cdc.gov/flu/pandemic-resources/reconstruction-1918-virus.html>.
81. M’ikanatha, N. M. The Pandemic Century: One Hundred Years of Panic, Hysteria and Hubris. *Emerg Infect Dis* **26**, 1349 (2020).
82. Morens, D. M., Taubenberger, J. K. & Fauci, A. S. Predominant Role of Bacterial Pneumonia as a Cause of Death in Pandemic Influenza: Implications for Pandemic Influenza Preparedness. *J Infect Dis* **198**, 962 (2008).
83. Worobey, M., Han, G. Z. & Rambaut, A. Genesis and pathogenesis of the 1918 pandemic H1N1 influenza a virus. *Proc Natl Acad Sci U S A* **111**, 8107–8112 (2014).
84. Antonovics, J., Hood, M. E. & Baker, C. H. Was the 1918 flu avian in origin? *Nature* 2006 440:7088 **440**, E9–E9 (2006).
85. Patrono, L. v. *et al.* Archival influenza virus genomes from Europe reveal genomic variability during the 1918 pandemic. *Nature Communications* 2022 13:1 **13**, 1–9 (2022).
86. Rozo, M. & Gronvall, G. K. The Reemergent 1977 H1N1 Strain and the Gain-of-Function Debate. *mBio* **6**, (2015).
87. Gao, G. F. & Sun, Y. P. It is not just AIV: from avian to swine-origin influenza virus. *Sci China Life Sci* **53**, 151–153 (2010).

88. Newman, A. P. *et al.* Human case of swine influenza A (H1N1) triple reassortant virus infection, Wisconsin. *Emerg Infect Dis* **14**, 1470–1472 (2008).
89. Smith, G. J. D. *et al.* Origins and evolutionary genomics of the 2009 swine-origin H1N1 influenza A epidemic. *Nature* **459**, 1122–1125 (2009).
90. Dawood, F. S. *et al.* Estimated global mortality associated with the first 12 months of 2009 pandemic influenza A H1N1 virus circulation: a modelling study. *Lancet Infect Dis* **12**, 687–695 (2012).
91. al Hajjar, S. & McIntosh, K. The first influenza pandemic of the 21st century. *Ann Saudi Med* **30**, 1 (2010).
92. Fisman, D. N. *et al.* Older age and a reduced likelihood of 2009 H1N1 virus infection. *N Engl J Med* **361**, 2000–2001 (2009).
93. Hancock, K. *et al.* Cross-reactive antibody responses to the 2009 pandemic H1N1 influenza virus. *N Engl J Med* **361**, 1945–1952 (2009).
94. Global Influenza Programme. <https://www.who.int/teams/global-influenza-programme/surveillance-and-monitoring/burden-of-disease>.
95. Harfoot, R. & Webby, R. J. H5 influenza, a global update. *J Microbiol* **55**, 196–203 (2017).
96. Public Health England. Weekly national Influenza and COVID-19 surveillance report Executive summary - Week 29 2021. (2021).
97. The next pandemic: H5N1 and H7N9 influenza? | Gavi, the Vaccine Alliance. <https://www.gavi.org/vaccineswork/next-pandemic/h5n1-and-h7n9-influenza>.
98. Miller, B. J. Why unprecedented bird flu outbreaks sweeping the world are concerning scientists. *Nature* **606**, 18–19 (2022).
99. Govindaraj, G. *et al.* Economic impacts of avian influenza outbreaks in Kerala, India. *Transbound Emerg Dis* **65**, e361–e372 (2018).
100. Ramos, S., Maclachlan, M. & Melton, A. A Report from the Economic Research Service A Report from the Economic Research Service Impacts of the 2014-2015 Highly Pathogenic Avian Influenza Outbreak on the U.S. Poultry Sector. 282–284 (2017).
101. Lv, J. *et al.* Aerosol Transmission of Coronavirus and Influenza Virus of Animal Origin. *Front Vet Sci* **8**, 109 (2021).
102. Ding, S., Teo, Z. W., Wan, M. P. & Ng, B. F. Aerosols from speaking can linger in the air for up to nine hours. *Build Environ* **205**, 108239 (2021).
103. Carrat, F. *et al.* Time lines of infection and disease in human influenza: a review of volunteer challenge studies. *Am J Epidemiol* **167**, 775–785 (2008).

104. Hayward, A. C. *et al.* Comparative community burden and severity of seasonal and pandemic influenza: results of the Flu Watch cohort study. *Lancet Respir Med* **2**, 445–454 (2014).
105. Shah, N. S. *et al.* Bacterial and viral co-infections complicating severe influenza: Incidence and impact among 507 U.S. patients, 2013–14. *J Clin Virol* **80**, 12–19 (2016).
106. Kalil, A. C. & Thomas, P. G. Influenza virus-related critical illness: Pathophysiology and epidemiology. *Crit Care* **23**, 1–7 (2019).
107. Sanders, C. J. *et al.* Compromised respiratory function in lethal influenza infection is characterized by the depletion of type I alveolar epithelial cells beyond threshold levels. *Am J Physiol Lung Cell Mol Physiol* **304**, (2013).
108. Gounder, A. P. & Boon, A. C. M. Influenza Pathogenesis: The role of host factors on severity of disease. *J Immunol* **202**, 341 (2019).
109. Schrauwen, E. J. A. *et al.* Determinants of virulence of influenza A virus. *Eur J Clin Microbiol Infect Dis* **33**, 479 (2014).
110. Kash, J. C. & Taubenberger, J. K. The Role of Viral, Host, and Secondary Bacterial Factors in Influenza Pathogenesis. *Am J Pathol* **185**, 1528 (2015).
111. Conenello, G. M., Zamarin, D., Perrone, L. A., Tumpey, T. & Palese, P. A single mutation in the PB1-F2 of H5N1 (HK/97) and 1918 influenza A viruses contributes to increased virulence. *PLoS Pathog* **3**, 1414–1421 (2007).
112. van Riel, D. *et al.* H5N1 virus attachment to lower respiratory tract. *Science (1979)* **312**, 399 (2006).
113. JH, B. *et al.* Avian influenza A (H5N1) infection in humans. *N Engl J Med* **353**, 1374–1385 (2005).
114. Watanabe, T. & Kawaoka, Y. Pathogenesis of the 1918 Pandemic Influenza Virus. *PLoS Pathog* **7**, (2011).
115. Lu, P., Zhou, B., Yuan, J. & Yang, G. Human Infected H5N1 Avian Influenza. *Radiology of Influenza* 67 (2016) doi:10.1007/978-94-024-0908-6_10.
116. To, K.-F. *et al.* Pathology of Fatal Human Infection Associated With Avian Influenza A H5N1 Virus. *J Med Virol* **63**, 242–246 (2001).
117. Martínez, A. *et al.* Risk factors associated with severe outcomes in adult hospitalized patients according to influenza type and subtype. *PLoS One* **14**, (2019).
118. Mertz, D. *et al.* Populations at risk for severe or complicated influenza illness: systematic review and meta-analysis. *BMJ* **347**, (2013).

119. Risk groups for severe influenza. <https://www.ecdc.europa.eu/en/seasonal-influenza/prevention-and-control/vaccines/risk-groups>.
120. Harboe, Z. B. *et al.* Effect of influenza vaccination in solid organ transplant recipients: A nationwide population-based cohort study. *American Journal of Transplantation* (2022) doi:10.1111/AJT.17055.
121. Pitman, R. J., White, L. J. & Sculpher, M. Estimating the clinical impact of introducing paediatric influenza vaccination in England and Wales. *Vaccine* **30**, 1208–1224 (2012).
122. Charu, V. *et al.* Influenza-related mortality trends in Japanese and American seniors: evidence for the indirect mortality benefits of vaccinating schoolchildren. *PLoS One* **6**, (2011).
123. Esposito, S. *et al.* Clinical and economic impact of influenza vaccination on healthy children aged 2–5 years. *Vaccine* **24**, 629–635 (2006).
124. Gama de Sousa, S. *et al.* The Japanese experience with vaccinating schoolchildren against influenza. *N Engl J Med* **344**, 249–251 (2001).
125. Uyeki, T. M. High-risk Groups for Influenza Complications. *JAMA* **324**, 2334–2334 (2020).
126. People at Higher Risk of Flu Complications | CDC. <https://www.cdc.gov/flu/highrisk/index.htm>.
127. Wang, X. *et al.* Global burden of respiratory infections associated with seasonal influenza in children under 5 years in 2018: a systematic review and modelling study. *Lancet Glob Health* **8**, e497–e510 (2020).
128. Izurieta, H. S. *et al.* Influenza and the rates of hospitalization for respiratory disease among infants and young children. *N Engl J Med* **342**, 232–239 (2000).
129. Neuzil, K. M. *et al.* Burden of interpandemic influenza in children younger than 5 years: a 25-year prospective study. *J Infect Dis* **185**, 147–152 (2002).
130. Ruf, B. R. & Knuf, M. The burden of seasonal and pandemic influenza in infants and children. *Eur J Pediatr* **173**, 265 (2014).
131. Hauge, S. H., Bakken, I. J., de Blasio, B. F. & Håberg, S. E. Risk conditions in children hospitalized with influenza in Norway, 2017–2019. *BMC Infect Dis* **20**, 1–9 (2020).
132. Sachedina, N. & Donaldson, L. J. Paediatric mortality related to pandemic influenza A H1N1 infection in England: An observational population-based study. *The Lancet* **376**, 1846–1852 (2010).
133. Coates, B. M., Staricha, K. L., Wiese, K. M. & Ridge, K. M. Influenza A Virus Infection, Innate Immunity, and Childhood. *JAMA Pediatr* **169**, 956 (2015).

134. Crowe, J. E. & Williams, J. v. Immunology of viral respiratory tract infection in infancy. *Paediatr Respir Rev* **4**, 112–119 (2003).
135. Esposito, S. *et al.* Viral shedding in children infected by pandemic A/H1N1/2009 influenza virus. *Virol J* **8**, 1–4 (2011).
136. Ng, S. *et al.* The Timeline of Influenza Virus Shedding in Children and Adults in a Household Transmission Study of Influenza in Managua, Nicaragua. *Pediatr Infect Dis J* **35**, 583 (2016).
137. Worby, C. J. *et al.* On the relative role of different age groups in influenza epidemics. *Epidemics* **13**, 10–16 (2015).
138. Meng, X. *et al.* Epidemiological and Clinical Characteristics of Influenza Outbreaks Among Children in Chongqing, China. *Front Public Health* **10**, 710 (2022).
139. Jackson, C., Vynnycky, E., Hawker, J., Olowokure, B. & Mangtani, P. School closures and influenza: Systematic review of epidemiological studies. *BMJ Open* **3**, e002149 (2013).
140. Cauchemez, S. *et al.* Closure of schools during an influenza pandemic. *Lancet Infect Dis* **9**, 473–481 (2009).
141. Davis, L. E., Caldwell, G. G., Lynch, R. E., Bailey, R. E. & Chin, T. D. Y. HONG KONG INFLUENZA: THE EPIDEMIOLOGIC FEATURES OF A HIGH SCHOOL FAMILY STUDY ANALYZED AND COMPARED WITH A SIMILAR STUDY DURING THE 1957 ASIAN INFLUENZA EPIDEMIC. *Am J Epidemiol* **92**, 240–247 (1970).
142. Viboud, C. *et al.* Risk factors of influenza transmission in households. *The British Journal of General Practice* **54**, 684 (2004).
143. Macias, A. E. *et al.* The disease burden of influenza beyond respiratory illness. *Vaccine* **39**, A6 (2021).
144. Collins, J. P. *et al.* Outcomes of Immunocompromised Adults Hospitalized With Laboratory-confirmed Influenza in the United States, 2011–2015. *Clin Infect Dis* **70**, 2121 (2020).
145. Kumar, D. *et al.* Outcomes from pandemic influenza A H1N1 infection in recipients of solid-organ transplants: a multicentre cohort study. *Lancet Infect Dis* **10**, 521–526 (2010).
146. Weigt, S. S., Gregson, A. L., Deng, J. C., Lynch, J. P. & Belperio, J. A. Respiratory viral infections in hematopoietic stem cell and solid organ transplant recipients. *Semin Respir Crit Care Med* **32**, 471–493 (2011).

147. Nanishi, E. *et al.* A nationwide survey of common viral infections in childhood among patients with primary immunodeficiency diseases. *J Infect* **73**, 358–368 (2016).
148. Ison, M. G. Respiratory viral infections in the immunocompromised. *Curr Opin Pulm Med* **28**, 205–210 (2022).
149. Memoli, M. J. *et al.* The Natural History of Influenza Infection in the Severely Immunocompromised vs Nonimmunocompromised Hosts. *Clin Infect Dis* **58**, 214 (2014).
150. Czaja, C. A. *et al.* Age-Related Differences in Hospitalization Rates, Clinical Presentation, and Outcomes Among Older Adults Hospitalized With Influenza—U.S. Influenza Hospitalization Surveillance Network (FluSurv-NET). *Open Forum Infect Dis* **6**, (2019).
151. McElhaney, J. E. *et al.* The immune response to influenza in older humans: Beyond immune senescence. *Immunity and Ageing* **17**, 1–10 (2020).
152. Zhang, A., Stacey, H. D., Mullarkey, C. E. & Miller, M. S. Original Antigenic Sin: How First Exposure Shapes Lifelong Anti-Influenza Virus Immune Responses. *The Journal of Immunology* **202**, 335–340 (2019).
153. Franceschi, C. & Campisi, J. Chronic inflammation (inflammaging) and its potential contribution to age-associated diseases. *J Gerontol A Biol Sci Med Sci* **69 Suppl 1**, S4–S9 (2014).
154. Frasca, D. & Blomberg, B. B. Inflammaging decreases adaptive and innate immune responses in mice and humans. *Biogerontology* **17**, 7 (2016).
155. Solana, R. *et al.* Innate immunosenescence: effect of aging on cells and receptors of the innate immune system in humans. *Semin Immunol* **24**, 331–341 (2012).
156. Pillai, P. S. *et al.* Mx1 reveals innate pathways to antiviral resistance and lethal influenza disease. *Science* **352**, 463 (2016).
157. Molony, R. D. *et al.* Aging impairs both primary and secondary RIG-I signaling for interferon induction in human monocytes. *Sci Signal* **10**, (2017).
158. Hatzifoti, C. & Heath, A. W. Influenza in the Elderly. *Microbiology and Aging* 113 (2009) doi:10.1007/978-1-59745-327-1_6.
159. Liu, S. L. *et al.* Pandemic influenza A(H1N1) 2009 virus in pregnancy. *Rev Med Virol* **23**, 3–14 (2013).
160. Rogers, V. L. *et al.* Presentation of Seasonal Influenza A in Pregnancy: 2003-2004 Influenza Season. *Obstetrics and Gynecology* **115**, 924–929 (2010).

161. Schanzer, D. L., Tam, T. W. S., Langley, J. M. & Winchester, B. T. Influenza-attributable deaths, Canada 1990-1999. *Epidemiol Infect* **135**, 1109–1116 (2007).
162. Dawood, F. S. *et al.* Incidence of influenza during pregnancy and association with pregnancy and perinatal outcomes in three middle-income countries: a multisite prospective longitudinal cohort study. *Lancet Infect Dis* **21**, 97–106 (2021).
163. Wang, R., Yan, W., Du, M., Tao, L. & Liu, J. The effect of influenza virus infection on pregnancy outcomes: A systematic review and meta-analysis of cohort studies. *International Journal of Infectious Diseases* **105**, 567–578 (2021).
164. Influenza (Flu) Vaccine and Pregnancy | CDC. <https://www.cdc.gov/vaccines/pregnancy/hcp-toolkit/flu-vaccine-pregnancy.html>.
165. Doss, M. *et al.* Interactions of α -, β -, and θ -Defensins with Influenza A Virus and Surfactant Protein D. *The Journal of Immunology* **182**, 7878–7887 (2009).
166. Holly, M. K., Diaz, K. & Smith, J. G. Annual Review of Virology Defensins in Viral Infection and Pathogenesis. (2017) doi:10.1146/annurev-virology.
167. Tecle, T., White, M. R., Gantz, D., Crouch, E. C. & Hartshorn, K. L. Human neutrophil defensins increase neutrophil uptake of influenza A virus and bacteria and modify virus-induced respiratory burst responses. *J Immunol* **178**, 8046–8052 (2007).
168. Li, D. & Wu, M. Pattern recognition receptors in health and diseases. *Signal Transduction and Targeted Therapy* **2021 6:1 6**, 1–24 (2021).
169. Iwasaki, A. & Pillai, P. S. Innate immunity to influenza virus infection. *Nature Reviews Immunology* **2014 14:5 14**, 315–328 (2014).
170. Mifsud, E. J., Kuba, M., Barr, I. G. & Valkenburg, S. Innate Immune Responses to Influenza Virus Infections in the Upper Respiratory Tract. (2021) doi:10.3390/v13102090.
171. Zhang, L. & Wang, A. Virus-induced ER stress and the unfolded protein response. *Front Plant Sci* **3**, (2012).
172. Chan, S. W. The unfolded protein response in virus infections. *Front Microbiol* **5**, (2014).
173. Hassan, I. H. *et al.* Influenza A viral replication is blocked by inhibition of the inositol-requiring enzyme 1 (IRE1) stress pathway. *J Biol Chem* **287**, 4679–4689 (2012).
174. Roberson, E. C. *et al.* Influenza induces endoplasmic reticulum stress, caspase-12-dependent apoptosis, and c-Jun N-terminal kinase-mediated transforming growth factor- β release in lung epithelial cells. *Am J Respir Cell Mol Biol* **46**, 573–581 (2012).

175. George, S. T. *et al.* Neutrophils and Influenza: A Thin Line between Helpful and Harmful. *Vaccines* 2021, Vol. 9, Page 597 **9**, 597 (2021).
176. Tate, M. D. *et al.* Neutrophils Ameliorate Lung Injury and the Development of Severe Disease during Influenza Infection. *The Journal of Immunology* **183**, 7441–7450 (2009).
177. Zhu, L. *et al.* High Level of Neutrophil Extracellular Traps Correlates With Poor Prognosis of Severe Influenza A Infection. **00**, 1–10 (2017).
178. Narasaraju, T. *et al.* Excessive Neutrophils and Neutrophil Extracellular Traps Contribute to Acute Lung Injury of Influenza Pneumonitis. *Am J Pathol* **179**, 199 (2011).
179. Tang, B. M. *et al.* Neutrophils-related host factors associated with severe disease and fatality in patients with influenza infection. *Nature Communications* 2019 10:1 **10**, 1–13 (2019).
180. Prager, I. & Watzl, C. Mechanisms of natural killer cell-mediated cellular cytotoxicity. *J Leukoc Biol* **105**, 1319–1329 (2019).
181. Schultz-Cherry, S. Role of nk cells in influenza infection. *Curr Top Microbiol Immunol* **386**, 109–120 (2015).
182. Carlin, L. E., Hemann, E. A., Zacharias, Z. R., Heusel, J. W. & Legge, K. L. Natural Killer Cell Recruitment to the Lung During Influenza A Virus Infection Is Dependent on CXCR3, CCR5, and Virus Exposure Dose. *Front Immunol* **9**, (2018).
183. Gazit, R. *et al.* Lethal influenza infection in the absence of the natural killer cell receptor gene *Ncr1*. *Nat Immunol* **7**, 517–523 (2006).
184. Zhou, G., Juang, S. W. W. & Kane, K. P. NK cells exacerbate the pathology of influenza virus infection in mice. *Eur J Immunol* **43**, 929–938 (2013).
185. Somerville, L., Cardani, A. & Braciale, T. J. Alveolar Macrophages in Influenza A Infection Guarding the Castle with Sleeping Dragons. *Infect Dis Ther* **1**, (2020).
186. Schneider, C. *et al.* Alveolar macrophages are essential for protection from respiratory failure and associated morbidity following influenza virus infection. *PLoS Pathog* **10**, (2014).
187. Purnama, C. *et al.* Transient ablation of alveolar macrophages leads to massive pathology of influenza infection without affecting cellular adaptive immunity. *Eur J Immunol* **44**, 2003–2012 (2014).
188. Kim, H. M. *et al.* The severe pathogenicity of alveolar macrophage-depleted ferrets infected with 2009 pandemic H1N1 influenza virus. *Virology* **444**, 394–403 (2013).

189. Cardani, A., Boulton, A., Kim, T. S. & Braciale, T. J. Alveolar Macrophages Prevent Lethal Influenza Pneumonia By Inhibiting Infection Of Type-1 Alveolar Epithelial Cells. *PLoS Pathog* **13**, (2017).
190. Tate, M. D., Pickett, D. L., van Rooijen, N., Brooks, A. G. & Reading, P. C. Critical role of airway macrophages in modulating disease severity during influenza virus infection of mice. *J Virol* **84**, 7569–7580 (2010).
191. Ichinohe, T., Lee, H. K., Ogura, Y., Flavell, R. & Iwasaki, A. Inflammasome recognition of influenza virus is essential for adaptive immune responses. *Journal of Experimental Medicine* **206**, 79–87 (2009).
192. Pang, I. K., Ichinohe, T. & Iwasaki, A. IL-1R signaling in dendritic cells replaces pattern-recognition receptors in promoting CD8⁺ T cell responses to influenza A virus. *Nat Immunol* **14**, 246–253 (2013).
193. Braciale, T. J., Sun, J. & Kim, T. S. Regulating the adaptive immune response to respiratory virus infection. *Nature Reviews Immunology* 2012 12:4 **12**, 295–305 (2012).
194. Kopf, M., Brombacher, F. & Bachmann, M. F. Role of IgM antibodies versus B cells in influenza virus-specific immunity. doi:10.1002/1521-4141(200208)32:8.
195. Baumgarth, N. *et al.* B-1 and B-2 cell-derived immunoglobulin M antibodies are nonredundant components of the protective response to influenza virus infection. *J Exp Med* **192**, 271–280 (2000).
196. Cerutti, A., Chen, K. & Chorny, A. Immunoglobulin responses at the mucosal interface. *Annu Rev Immunol* **29**, 273–293 (2011).
197. Renegar, K. B., Small, P. A., Boykins, L. G. & Wright, P. F. Role of IgA versus IgG in the Control of Influenza Viral Infection in the Murine Respiratory Tract. *The Journal of Immunology* **173**, 1978–1986 (2004).
198. Seibert, C. W. *et al.* Recombinant IgA is sufficient to prevent influenza virus transmission in guinea pigs. *J Virol* **87**, 7793–7804 (2013).
199. Choi, A. *et al.* Non-sterilizing, Infection-Permissive Vaccination With Inactivated Influenza Virus Vaccine Reshapes Subsequent Virus Infection-Induced Protective Heterosubtypic Immunity From Cellular to Humoral Cross-Reactive Immune Responses. *Front Immunol* **11**, 1166 (2020).
200. Abreu, R. B., Clutter, E. F., Attari, S., Sautto, G. A. & Ross, T. M. IgA Responses Following Recurrent Influenza Virus Vaccination. *Front Immunol* **11**, 902 (2020).
201. Qin, T. *et al.* Mucosal Vaccination for Influenza Protection Enhanced by Catalytic Immune-Adjuvant. *Advanced Science* **7**, 2000771 (2020).

202. la Gruta, N. L. & Turner, S. J. T cell mediated immunity to influenza: mechanisms of viral control. *Trends Immunol* **35**, 396–402 (2014).
203. Graham, M. B. & Braciale, T. J. Resistance to and recovery from lethal influenza virus infection in B lymphocyte-deficient mice. *J Exp Med* **186**, 2063–2068 (1997).
204. Kägi, D. *et al.* Fas and perforin pathways as major mechanisms of T cell-mediated cytotoxicity. *Science* **265**, 528–530 (1994).
205. Pipkin, M. E. *et al.* Interleukin-2 and inflammation induce distinct transcriptional programs that promote the differentiation of effector cytolytic T cells. *Immunity* **32**, 79–90 (2010).
206. Harty, J. T., Tvinnereim, A. R. & White, D. W. CD8+ T cell effector mechanisms in resistance to infection. *Annu Rev Immunol* **18**, 275–308 (2000).
207. Topham, D. J., Tripp, R. A. & Doherty, P. C. CD8+ T cells clear influenza virus by perforin or Fas-dependent processes. *The Journal of Immunology* **159**, (1997).
208. Alonso, G. T., Fomin, D. S. & Rizzo, L. V. Human follicular helper T lymphocytes critical players in antibody responses. *Einstein (Sao Paulo)* **19**, eRB6077 (2021).
209. Helper T Cells and Lymphocyte Activation - Molecular Biology of the Cell - NCBI Bookshelf. <https://www.ncbi.nlm.nih.gov/books/NBK26827/>.
210. Pizzolla, A. & Wakim, L. M. Memory T Cell Dynamics in the Lung during Influenza Virus Infection. *The Journal of Immunology* **202**, 374–381 (2019).
211. McKinstry, K. K., Strutt, T. M. & Swain, S. L. Hallmarks of CD4 T cell immunity against influenza. *J Intern Med* **269**, 507 (2011).
212. Zens, K. D. & Farber, D. L. Memory CD4 T cells in influenza. *Curr Top Microbiol Immunol* **386**, 399–421 (2015).
213. McMaster, S. R. *et al.* Memory T Cells Generated by Prior Exposure to Influenza Cross React with the Novel H7N9 Influenza Virus and Confer Protective Heterosubtypic Immunity. *PLoS One* **10**, e0115725 (2015).
214. Jazayeri, S. D. & Poh, C. L. Development of Universal Influenza Vaccines Targeting Conserved Viral Proteins. *Vaccines (Basel)* **7**, (2019).
215. Sautto, G. A., Kirchenbaum, G. A. & Ross, T. M. Towards a universal influenza vaccine: Different approaches for one goal. *Viol J* **15**, 1–12 (2018).
216. Xie, X. *et al.* Influenza vaccine with consensus internal antigens as immunogens provides cross-group protection against influenza A viruses. *Front Microbiol* **10**, 1630 (2019).

217. Doud, M. B. & Bloom, J. D. Accurate Measurement of the Effects of All Amino-Acid Mutations on Influenza Hemagglutinin. *Viruses* **8**, (2016).
218. Koel, B. F. *et al.* Substitutions near the receptor binding site determine major antigenic change during influenza virus evolution. *Science* **342**, 976–979 (2013).
219. Krammer, F. The human antibody response to influenza A virus infection and vaccination. *Nature Reviews Immunology* 2019 *19*:6 **19**, 383–397 (2019).
220. Jang, Y. H. & Seong, B. L. Immune Responses Elicited by Live Attenuated Influenza Vaccines as Correlates of Universal Protection against Influenza Viruses. *Vaccines* 2021, *Vol. 9*, Page 353 **9**, 353 (2021).
221. Hobson, D., Curry, R. L., Beare, A. S. & Ward-Gardner, A. The role of serum haemagglutination-inhibiting antibody in protection against challenge infection with influenza A2 and B viruses. *J Hyg (Lond)* **70**, 767 (1972).
222. Danier, J. *et al.* Association Between Hemagglutination Inhibition Antibody Titers and Protection Against Reverse-Transcription Polymerase Chain Reaction–Confirmed Influenza Illness in Children 6–35 Months of Age: Statistical Evaluation of a Correlate of Protection. *Open Forum Infect Dis* **9**, (2022).
223. Black, S. *et al.* Hemagglutination inhibition antibody titers as a correlate of protection for inactivated influenza vaccines in children. *Pediatr Infect Dis J* **30**, 1081–1085 (2011).
224. Thornlow, D. N. *et al.* Altering the Immunogenicity of Hemagglutinin Immunogens by Hyperglycosylation and Disulfide Stabilization. *Front Immunol* **12**, 4137 (2021).
225. Neiryneck, S. *et al.* A universal influenza A vaccine based on the extracellular domain of the M2 protein. *Nat Med* **5**, 1157–1163 (1999).
226. Turley, C. B. *et al.* Safety and immunogenicity of a recombinant M2e-flagellin influenza vaccine (STF2.4xM2e) in healthy adults. *Vaccine* **29**, 5145–5152 (2011).
227. Zhong, W. *et al.* Serum antibody response to matrix protein 2 following natural infection with 2009 pandemic influenza A(H1N1) virus in humans. *J Infect Dis* **209**, 986–994 (2014).
228. Tao, W. *et al.* Consensus M2e peptide conjugated to gold nanoparticles confers protection against H1N1, H3N2 and H5N1 influenza A viruses. *Antiviral Res* **141**, 62–72 (2017).
229. Krammer, F. The Quest for a Universal Flu Vaccine: Headless HA 2.0. *Cell Host Microbe* **18**, 395–397 (2015).

230. Liao, H. Y. *et al.* Chimeric hemagglutinin vaccine elicits broadly protective CD4 and CD8 T cell responses against multiple influenza strains and subtypes. *Proc Natl Acad Sci U S A* **117**, 17757–17763 (2020).
231. Isakova-Sivak, I. & Rudenko, L. The future of haemagglutinin stalk-based universal influenza vaccines. *Lancet Infect Dis* **22**, 926–928 (2022).
232. Dhar, N. *et al.* Hemagglutinin Stalk Antibody Responses Following Trivalent Inactivated Influenza Vaccine Immunization of Pregnant Women and Association With Protection From Influenza Virus Illness. *Clin Infect Dis* **71**, 1072–1079 (2020).
233. Shu, L. L., Bean, W. J. & Webster, R. G. Analysis of the evolution and variation of the human influenza A virus nucleoprotein gene from 1933 to 1990. *J Virol* **67**, 2723–2729 (1993).
234. Yin, Y. *et al.* Protein transduction domain-mediated influenza NP subunit vaccine generates a potent immune response and protection against influenza virus in mice. *Emerg Microbes Infect* **9**, 1933 (2020).
235. Evans, T. G. *et al.* Efficacy and safety of a universal influenza A vaccine (MVA-NP+M1) in adults when given after seasonal quadrivalent influenza vaccine immunisation (FLU009): a phase 2b, randomised, double-blind trial. *Lancet Infect Dis* **22**, 857–866 (2022).
236. Nguyen, Q. T. & Choi, Y. K. Targeting Antigens for Universal Influenza Vaccine Development. *Viruses* **13**, (2021).
237. Putri, W. C. W. S., Muscatello, D. J., Stockwell, M. S. & Newall, A. T. Economic burden of seasonal influenza in the United States. *Vaccine* **36**, 3960–3966 (2018).
238. Disease Burden of Flu | CDC. <https://www.cdc.gov/flu/about/burden/index.html>.
239. 2020-2021 Flu Season Summary | CDC. <https://www.cdc.gov/flu/season/faq-flu-season-2020-2021.htm>.
240. Estimated Influenza Illnesses, Medical visits, and Hospitalizations Averted by Vaccination in the United States — 2019–2020 Influenza Season | CDC. <https://www.cdc.gov/flu/about/burden-averted/2019-2020.htm>.
241. Logsdon, S. L., von Tiehl, K. F. & Assa’ad, A. H. Effect of Egg Allergy on Influenza Vaccination. *Journal of Allergy and Clinical Immunology* **127**, AB33–AB33 (2011).
242. Liang, W. *et al.* Egg-adaptive mutations of human influenza H3N2 virus are contingent on natural evolution. *PLoS Pathog* **18**, e1010875 (2022).

243. de Lejarazu-Leonardo, R. O. *et al.* Estimation of Reduction in Influenza Vaccine Effectiveness Due to Egg-Adaptation Changes—Systematic Literature Review and Expert Consensus. *Vaccines (Basel)* **9**, 1255 (2021).
244. Manini, I. *et al.* Flucelvax (Optaflu) for seasonal influenza. *Expert Rev Vaccines* **14**, 789–804 (2015).
245. Yang, L. P. H. Recombinant trivalent influenza vaccine (Flublok®): A review of its use in the prevention of seasonal influenza in adults. *Drugs* **73**, 1357–1366 (2013).
246. Leuridan, E., Hens, N., Hutse, V., Aerts, M. & van Damme, P. Kinetics of maternal antibodies against rubella and varicella in infants. *Vaccine* **29**, 2222–2226 (2011).
247. Niewiesk, S. Maternal Antibodies: Clinical Significance, Mechanism of Interference with Immune Responses, and Possible Vaccination Strategies. *Front Immunol* **5**, (2014).
248. Hasan, N. H., Ignjatovic, J., Peaston, A. & Hemmatzadeh, F. Avian Influenza Virus and DIVA Strategies. *Viral Immunol* **29**, 198–211 (2016).
249. Co, M. D. T. *et al.* In vitro evidence that commercial influenza vaccines are not similar in their ability to activate human T cell responses. *Vaccine* **27**, 319–327 (2009).
250. Talbot, H. K. *et al.* Clinical Effectiveness of Split-Virion Versus Subunit Trivalent Influenza Vaccines in Older Adults. *Clin Infect Dis* **60**, 1170 (2015).
251. Gemmill, I. & Young, K. Summary of the NACI literature review on the comparative effectiveness of subunit and split virus inactivated influenza vaccines in older adults. *Canada Communicable Disease Report* **44**, 129–133 (2018).
252. Koroleva, M. *et al.* Heterologous viral protein interactions within licensed seasonal influenza virus vaccines. *npj Vaccines* 2020 5:1 **5**, 1–10 (2020).
253. Jennings, R. *et al.* Inactivated influenza virus vaccines in man: a comparative study of subunit and split vaccines using two methods for assessment of antibody responses. *Vaccine* **2**, 75–80 (1984).
254. Kang, S. *et al.* Comparison of Split versus Subunit Seasonal Influenza Vaccine in Korean Children over 3 to under 18 Years of Age. *Pediatric Infection & Vaccine* **26**, 161–169 (2019).
255. Morales, A. *et al.* A randomized controlled trial comparing split and subunit influenza vaccines in adults in Colombia. *Medicina (B Aires)* **63**, 197–204 (2003).
256. Dong, P. *et al.* [Comparative study on safety and immunogenicity between influenza subunit vaccine and split vaccine]. *Zhonghua Liu Xing Bing Xue Za Zhi* **24**, 570–3 (2003).

257. Arunachalam, A. B., Post, P. & Rudin, D. Unique features of a recombinant haemagglutinin influenza vaccine that influence vaccine performance. *npj Vaccines* 2021 6:1 **6**, 1–8 (2021).
258. Cox, M. M. J., Izikson, R., Post, P. & Dunkle, L. Safety, efficacy, and immunogenicity of Flublok in the prevention of seasonal influenza in adults. *Ther Adv Vaccines* **3**, 97–108 (2015).
259. Khurana, S. *et al.* Repeat vaccination reduces antibody affinity maturation across different influenza vaccine platforms in humans. *Nature Communications* 2019 10:1 **10**, 1–15 (2019).
260. Maassab, H. F. & Bryant, M. L. The development of live attenuated cold-adapted influenza virus vaccine for humans. *Rev Med Virol* **9**, 237–244 (1999).
261. Jin, H., Zhou, H., Lu, B. & Kemble, G. Imparting Temperature Sensitivity and Attenuation in Ferrets to A/Puerto Rico/8/34 Influenza Virus by Transferring the Genetic Signature for Temperature Sensitivity from Cold-Adapted A/Ann Arbor/6/60. *J Virol* **78**, 995 (2004).
262. Belshe, R. B. *et al.* Live attenuated versus inactivated influenza vaccine in infants and young children. *N Engl J Med* **356**, 685–696 (2007).
263. Ashkenazi, S. *et al.* Superior relative efficacy of live attenuated influenza vaccine compared with inactivated influenza vaccine in young children with recurrent respiratory tract infections. *Pediatr Infect Dis J* **25**, 870–879 (2006).
264. Banovic, T. *et al.* Disseminated varicella infection caused by varicella vaccine strain in a child with low invariant natural killer T cells and diminished CD1d expression. *J Infect Dis* **204**, 1893–1901 (2011).
265. Jean-Philippe, P. *et al.* Severe varicella caused by varicella-vaccine strain in a child with significant T-cell dysfunction. *Pediatrics* **120**, (2007).
266. Kamboj, M. & Sepkowitz, K. A. Risk of transmission associated with live attenuated vaccines given to healthy persons caring for or residing with an immunocompromised patient. *Infect Control Hosp Epidemiol* **28**, 702–707 (2007).
267. Poliomyelitis: Vaccine derived polio. <https://www.who.int/news-room/questions-and-answers/item/poliomyelitis-vaccine-derived-polio>.
268. Buonagurio, D. A. *et al.* Genetic and phenotypic stability of cold-adapted influenza viruses in a trivalent vaccine administered to children in a day care setting. *Virology* **347**, 296–306 (2006).

269. Vesikari, T. *et al.* A randomized, double-blind study of the safety, transmissibility and phenotypic and genotypic stability of cold-adapted influenza virus vaccine. *Pediatr Infect Dis J* **25**, 590–595 (2006).
270. Belshe, R. B., Ambrose, C. S. & Yi, T. Safety and efficacy of live attenuated influenza vaccine in children 2-7 years of age. *Vaccine* **26 Suppl 4**, (2008).
271. Belshe, R. B. *et al.* Live attenuated versus inactivated influenza vaccine in infants and young children. *N Engl J Med* **356**, 685–696 (2007).
272. Influenza vaccine effectiveness. <https://www.ecdc.europa.eu/en/seasonal-influenza/prevention-and-control/vaccine-effectiveness>.
273. Vaccine Effectiveness: How Well Do Flu Vaccines Work? | CDC. <https://www.cdc.gov/flu/vaccines-work/vaccineeffect.htm>.
274. Rose, A. *et al.* Interim 2019/20 influenza vaccine effectiveness: six European studies, September 2019 to January 2020. *Eurosurveillance* **25**, (2020).
275. Wiedermann, U., Garner-Spitzer, E. & Wagner, A. Primary vaccine failure to routine vaccines: Why and what to do? *Hum Vaccin Immunother* **12**, 239–243 (2016).
276. Clemens, E. B., van de Sandt, C., Wong, S. S., Wakim, L. M. & Valkenburg, S. A. Harnessing the Power of T Cells: The Promising Hope for a Universal Influenza Vaccine. *Vaccines (Basel)* **6**, (2018).
277. Segerstrom, S. C. & Miller, G. E. Psychological stress and the human immune system: a meta-analytic study of 30 years of inquiry. *Psychol Bull* **130**, 601–630 (2004).
278. Sheridan, P. A. *et al.* Obesity is associated with impaired immune response to influenza vaccination in humans. *Int J Obes (Lond)* **36**, 1072–1077 (2012).
279. Lewnard, J. A. & Cobey, S. Immune History and Influenza Vaccine Effectiveness. *Vaccines (Basel)* **6**, (2018).
280. Alharbi, M. H. & Kribs, C. M. A Mathematical Modeling Study: Assessing Impact of Mismatch Between Influenza Vaccine Strains and Circulating Strains in Hajj. *Bull Math Biol* **83**, (2021).
281. Paules, C. I., Sullivan, S. G., Subbarao, K. & Fauci, A. S. Chasing Seasonal Influenza - The Need for a Universal Influenza Vaccine. *N Engl J Med* **378**, 7–9 (2018).
282. Krammer, F. *et al.* Influenza. *Nature Reviews Disease Primers* **2018 4:1 4**, 1–21 (2018).
283. Tricco, A. C. *et al.* Comparing influenza vaccine efficacy against mismatched and matched strains: a systematic review and meta-analysis. *BMC Med* **11**, 153 (2013).

284. Belongia, E. A. *et al.* Effectiveness of inactivated influenza vaccines varied substantially with antigenic match from the 2004-2005 season to the 2006-2007 season. *J Infect Dis* **199**, 159–167 (2009).
285. Corder, B. N., Bullard, B. L., Poland, G. A. & Weaver, E. A. A Decade in Review: A Systematic Review of Universal Influenza Vaccines in Clinical Trials during the 2010 Decade. *Viruses* **12**, (2020).
286. Immunogenicity and Safety of a Single 0.5 mL Dose of Inflexal V With a 0.25 mL 2-dose Regimen of Inflexal V - Full Text View - ClinicalTrials.gov. <https://clinicaltrials.gov/ct2/show/NCT01229397?term=NCT01229397&draw=2&rank=1>.
287. Mischler, R. & Metcalfe, I. C. Inflexal®V a trivalent virosome subunit influenza vaccine: Production. *Vaccine* **20**, (2002).
288. Grant, E. *et al.* Nucleoprotein of influenza A virus is a major target of immunodominant CD8+ T-cell responses. *Immunol Cell Biol* **91**, 184–194 (2013).
289. Francis, J. N. *et al.* A novel peptide-based pan-influenza A vaccine: a double blind, randomised clinical trial of immunogenicity and safety. *Vaccine* **33**, 396–402 (2015).
290. del Campo, J. *et al.* OVX836 a recombinant nucleoprotein vaccine inducing cellular responses and protective efficacy against multiple influenza A subtypes. *NPJ Vaccines* **4**, (2019).
291. Thompson, M. G. *et al.* Effectiveness of seasonal trivalent influenza vaccine for preventing influenza virus illness among pregnant women: a population-based case-control study during the 2010-2011 and 2011-2012 influenza seasons. *Clin Infect Dis* **58**, 449–457 (2014).
292. Beck, C. R. *et al.* Influenza vaccination for immunocompromised patients: summary of a systematic review and meta-analysis. *Influenza Other Respir Viruses* **7 Suppl 2**, 72–75 (2013).
293. Demicheli, V. *et al.* Vaccines for preventing influenza in the elderly. *Cochrane Database Syst Rev* **2**, (2018).
294. Machado, M. A. de A. *et al.* Relative effectiveness of influenza vaccines in elderly persons in the United States, 2012/2013-2017/2018 seasons. *npj Vaccines* **2021 6:1 6**, 1–6 (2021).
295. Orrico-Sánchez, A., Valls-Arévalo, Á., Garcés-Sánchez, M., Álvarez Aldeán, J. & Ortiz de Lejarazu Leonardo, R. Efficacy and effectiveness of influenza vaccination in healthy

- children. A review of current evidence. *Enferm Infecc Microbiol Clin* (2022) doi:10.1016/J.EIMC.2022.02.005.
296. Jefferson, T., Rivetti, A., di Pietrantonj, C. & Demicheli, V. Vaccines for preventing influenza in healthy children. *Cochrane Database Syst Rev* **2**, (2018).
297. Costantino, C. & Vitale, F. Influenza vaccination in high-risk groups: a revision of existing guidelines and rationale for an evidence-based preventive strategy. *J Prev Med Hyg* **57**, E13 (2016).
298. Sung, L. C. *et al.* Influenza vaccination reduces hospitalization for acute coronary syndrome in elderly patients with chronic obstructive pulmonary disease: a population-based cohort study. *Vaccine* **32**, 3843–3849 (2014).
299. Tanner, A. R., Dorey, R. B., Brendish, N. J. & Clark, T. W. Influenza vaccination: protecting the most vulnerable. *European Respiratory Review* **30**, 1–9 (2021).
300. Gibson, E. *et al.* Economic evaluation of pediatric influenza immunization program compared with other pediatric immunization programs: A systematic review. <http://dx.doi.org/10.1080/21645515.2015.1131369> **12**, 1202–1216 (2016).
301. Hurwitz, E. S. *et al.* Effectiveness of influenza vaccination of day care children in reducing influenza-related morbidity among household contacts. *JAMA* **284**, 1677–1682 (2000).
302. Ting, E. E. K., Sander, B. & Ungar, W. J. Systematic review of the cost-effectiveness of influenza immunization programs. *Vaccine* **35**, 1828–1843 (2017).
303. Lynch, S. v. & Pedersen, O. The Human Intestinal Microbiome in Health and Disease. *N Engl J Med* **375**, 2369–2379 (2016).
304. Fan, Y. & Pedersen, O. Gut microbiota in human metabolic health and disease. *Nature Reviews Microbiology* *2020 19:1* **19**, 55–71 (2020).
305. Blaser, M. J. *et al.* Lessons learned from the prenatal microbiome controversy. *Microbiome* **9**, 1–7 (2021).
306. Sprockett, D., Fukami, T. & Relman, D. A. Role of priority effects in the early-life assembly of the gut microbiota. *Nat Rev Gastroenterol Hepatol* **15**, 197 (2018).
307. Korpela, K. & de Vos, W. M. Early life colonization of the human gut: microbes matter everywhere. *Curr Opin Microbiol* **44**, 70–78 (2018).
308. Ferretti, P. *et al.* Mother-to-Infant Microbial Transmission from Different Body Sites Shapes the Developing Infant Gut Microbiome. *Cell Host Microbe* **24**, 133-145.e5 (2018).

309. Roswall, J. *et al.* Developmental trajectory of the healthy human gut microbiota during the first 5 years of life. *Cell Host Microbe* **29**, 765-776.e3 (2021).
310. Rautava, S. Early-life antibiotic exposure, the gut microbiome, and disease in later life. *The Human Microbiome in Early Life* 135–153 (2021) doi:10.1016/B978-0-12-818097-6.00006-7.
311. Robertson, R. C., Manges, A. R., Finlay, B. B. & Prendergast, A. J. The Human Microbiome and Child Growth – First 1000 Days and Beyond. *Trends Microbiol* **27**, 131–147 (2019).
312. Risnes, K. R., Belanger, K., Murk, W. & Bracken, M. B. Antibiotic Exposure by 6 Months and Asthma and Allergy at 6 Years: Findings in a Cohort of 1,401 US Children. *Am J Epidemiol* **173**, 310–318 (2011).
313. Palleja, A. *et al.* Recovery of gut microbiota of healthy adults following antibiotic exposure. *Nature Microbiology* 2018 3:11 **3**, 1255–1265 (2018).
314. Sommer, F., Anderson, J. M., Bharti, R., Raes, J. & Rosenstiel, P. The resilience of the intestinal microbiota influences health and disease. *Nature Reviews Microbiology* 2017 15:10 **15**, 630–638 (2017).
315. Hill, L. *et al.* The neonatal microbiome in utero and beyond: Perinatal influences and long-term impacts. *Journal of Laboratory Medicine* **45**, 275–291 (2021).
316. Jian, C. *et al.* Early-life gut microbiota and its connection to metabolic health in children: Perspective on ecological drivers and need for quantitative approach. *EBioMedicine* **69**, (2021).
317. Lederberg, J. & Mccray, A. T. COMMENTARY 'Ome Sweet 'Omics-A Genealogical Treasury of Words.
318. Liang, G. & Bushman, F. D. The human virome: assembly, composition and host interactions. *Nature Reviews Microbiology* 2021 19:8 **19**, 514–527 (2021).
319. Cui, L., Morris, A. & Ghedin, E. The human mycobioime in health and disease. *Genome Med* **5**, 1–12 (2013).
320. NIH Human Microbiome Project - About the Human Microbiome. <https://www.hmpdacc.org/overview/>.
321. Jovel, J. *et al.* Characterization of the gut microbiome using 16S or shotgun metagenomics. *Front Microbiol* **7**, 459 (2016).
322. Mosca, A., Leclerc, M. & Hugot, J. P. Gut microbiota diversity and human diseases: Should we reintroduce key predators in our ecosystem? *Front Microbiol* **7**, 455 (2016).

323. Lloyd-Price, J. *et al.* Multi-omics of the gut microbial ecosystem in inflammatory bowel diseases. *Nature* 2019 569:7758 **569**, 655–662 (2019).
324. Duvallet, C., Gibbons, S. M., Gurry, T., Irizarry, R. A. & Alm, E. J. Meta-analysis of gut microbiome studies identifies disease-specific and shared responses. *Nat Commun* **8**, (2017).
325. Abt, M. C., McKenney, P. T. & Pamer, E. G. Clostridium difficile colitis: pathogenesis and host defence. *Nat Rev Microbiol* **14**, 609–620 (2016).
326. Khan, I. *et al.* Alteration of Gut Microbiota in Inflammatory Bowel Disease (IBD): Cause or Consequence? IBD Treatment Targeting the Gut Microbiome. *Pathogens* **8**, (2019).
327. Xu, Z. *et al.* Gut microbiota in patients with obesity and metabolic disorders — a systematic review. *Genes & Nutrition* 2021 17:1 **17**, 1–18 (2022).
328. Eckburg, P. B. *et al.* Diversity of the human intestinal microbial flora. *Science* **308**, 1635–1638 (2005).
329. Huttenhower, C. *et al.* Structure, function and diversity of the healthy human microbiome. *Nature* 2012 486:7402 **486**, 207–214 (2012).
330. Qin, J. *et al.* A human gut microbial gene catalogue established by metagenomic sequencing. *Nature* 2010 464:7285 **464**, 59–65 (2010).
331. Blakeley-Ruiz, J. A. *et al.* Metaproteomics reveals persistent and phylum-redundant metabolic functional stability in adult human gut microbiomes of Crohn’s remission patients despite temporal variations in microbial taxa, genomes, and proteomes. *Microbiome* **7**, (2019).
332. Henrick, B. M. *et al.* Colonization by *B. infantis* EVC001 modulates enteric inflammation in exclusively breastfed infants. *Pediatric Research* 2019 86:6 **86**, 749–757 (2019).
333. Thongaram, T., Hoeflinger, J. L., Chow, J. M. & Miller, M. J. Human milk oligosaccharide consumption by probiotic and human-associated bifidobacteria and lactobacilli. *J Dairy Sci* **100**, 7825–7833 (2017).
334. Henrick, B. M. *et al.* Bifidobacteria-mediated immune system imprinting early in life. *Cell* **184**, 3884-3898.e11 (2021).
335. Zhang, A., Sun, H., Yan, G., Wang, P. & Wang, X. Metabolomics for Biomarker Discovery: Moving to the Clinic. *Biomed Res Int* **2015**, (2015).

336. Avuthu, N. & Guda, C. Meta-Analysis of Altered Gut Microbiota Reveals Microbial and Metabolic Biomarkers for Colorectal Cancer. *Microbiol Spectr* (2022) doi:10.1128/SPECTRUM.00013-22.
337. Sender, R., Fuchs, S. & Milo, R. Revised Estimates for the Number of Human and Bacteria Cells in the Body. *PLoS Biol* **14**, e1002533 (2016).
338. Nardone, G. & Compare, D. The human gastric microbiota: Is it time to rethink the pathogenesis of stomach diseases? *United European Gastroenterol J* **3**, 255 (2015).
339. Stearns, J. C. *et al.* Bacterial biogeography of the human digestive tract. *Scientific Reports 2011 1:1* **1**, 1–9 (2011).
340. Almeida, A. *et al.* A new genomic blueprint of the human gut microbiota. *Nature 2019 568:7753* **568**, 499–504 (2019).
341. Rangel, I. *et al.* The relationship between faecal-associated and mucosal-associated microbiota in irritable bowel syndrome patients and healthy subjects. *Aliment Pharmacol Ther* **42**, 1211–1221 (2015).
342. Zoetendal, E. G. *et al.* Mucosa-associated bacteria in the human gastrointestinal tract are uniformly distributed along the colon and differ from the community recovered from feces. *Appl Environ Microbiol* **68**, 3401–3407 (2002).
343. Pereira, F. C. & Berry, D. Microbial nutrient niches in the gut. *Environ Microbiol* **19**, 1366–1378 (2017).
344. Whiteside, S. A., McGinniss, J. E. & Collman, R. G. The lung microbiome: progress and promise. *J Clin Invest* **131**, (2021).
345. Man, W. H., de Steenhuijsen Piters, W. A. A. & Bogaert, D. The microbiota of the respiratory tract: gatekeeper to respiratory health. *Nat Rev Microbiol* **15**, 259 (2017).
346. Kumpitsch, C., Koskinen, K., Schöpf, V. & Moissl-Eichinger, C. The microbiome of the upper respiratory tract in health and disease. *BMC Biology 2019 17:1* **17**, 1–20 (2019).
347. Cao, W. *et al.* Characteristics of the bacterial microbiota in the upper respiratory tract of children. *European Archives of Oto-Rhino-Laryngology* **279**, 1081–1089 (2022).
348. Lighthart, B. Mini-review of the concentration variations found in the alfresco atmospheric bacterial populations. *Aerobiologia 2000 16:1* **16**, 7–16 (2000).
349. Charlson, E. S. *et al.* Assessing bacterial populations in the lung by replicate analysis of samples from the upper and lower respiratory tracts. *PLoS One* **7**, (2012).
350. Bassis, C. M. *et al.* Analysis of the upper respiratory tract microbiotas as the source of the lung and gastric microbiotas in healthy individuals. *mBio* **6**, (2015).

351. Weiser, J. N., Ferreira, D. M. & Paton, J. C. Streptococcus pneumoniae: transmission, colonization and invasion. *Nat Rev Microbiol* **16**, 355 (2018).
352. Pecora, D. v. A Comparison of Transtracheal Aspiration with Other Methods of Determining the Bacterial Flora of the Lower Respiratory Tract. <http://dx.doi.org/10.1056/NEJM196309262691304> **269**, 664–666 (2010).
353. Hilty, M. *et al.* Disordered microbial communities in asthmatic airways. *PLoS One* **5**, (2010).
354. Whiteside, S. A., McGinniss, J. E. & Collman, R. G. The lung microbiome: progress and promise. *J Clin Invest* **131**, (2021).
355. Lee, S. H. *et al.* Characterization of microbiome in bronchoalveolar lavage fluid of patients with lung cancer comparing with benign mass like lesions. *Lung Cancer* **102**, 89–95 (2016).
356. Wang, Z. *et al.* Multi-omic meta-analysis identifies functional signatures of airway microbiome in chronic obstructive pulmonary disease. *ISME J* **14**, 2748–2765 (2020).
357. Pragman, A. A. *et al.* Chronic obstructive pulmonary disease upper airway microbiota alpha diversity is associated with exacerbation phenotype: a case-control observational study. *Respir Res* **20**, (2019).
358. Dickson, R. P. Approaches to Sampling the Respiratory Microbiome. 3–19 (2022) doi:10.1007/978-3-030-87104-8_1.
359. Charlson, E. S. *et al.* Topographical continuity of bacterial populations in the healthy human respiratory tract. *Am J Respir Crit Care Med* **184**, 957–963 (2011).
360. Rutgers, S. R. *et al.* Comparison of induced sputum with bronchial wash, bronchoalveolar lavage and bronchial biopsies in COPD. *Eur Respir J* **15**, 109–115 (2000).
361. Carney, S. M. *et al.* Methods in lung microbiome research. *Am J Respir Cell Mol Biol* **62**, 283–299 (2020).
362. Dickson, R. P. & Cox, M. J. Sampling. *ERS Monograph* **2019**, 1–17 (2019).
363. Yu, G. *et al.* Characterizing human lung tissue microbiota and its relationship to epidemiological and clinical features. *Genome Biol* **17**, 1–12 (2016).
364. Carney, S. M. *et al.* Methods in lung microbiome research. *Am J Respir Cell Mol Biol* **62**, 283–299 (2020).
365. Brüssow, H. Problems with the concept of gut microbiota dysbiosis. *Microb Biotechnol* **13**, 423–434 (2020).

366. Walter, J., Armet, A. M., Finlay, B. B. & Shanahan, F. Establishing or Exaggerating Causality for the Gut Microbiome: Lessons from Human Microbiota-Associated Rodents. *Cell* **180**, 221–232 (2020).
367. Parsonnet, J. *et al.* Helicobacter pylori Infection and the Risk of Gastric Carcinoma. <http://dx.doi.org/10.1056/NEJM199110173251603> **325**, 1127–1131 (2010).
368. Gupta, S., Allen-Vercoe, E. & Petrof, E. O. Fecal microbiota transplantation: in perspective. *Therap Adv Gastroenterol* **9**, 229–239 (2016).
369. Smith, K., McCoy, K. D. & Macpherson, A. J. Use of axenic animals in studying the adaptation of mammals to their commensal intestinal microbiota. *Semin Immunol* **19**, 59–69 (2007).
370. Zheng, D., Liwinski, T. & Elinav, E. Interaction between microbiota and immunity in health and disease. *Cell Research* **2020 30:6** **30**, 492–506 (2020).
371. Arrieta, M. C., Walter, J. & Finlay, B. B. Human Microbiota-Associated Mice: A Model with Challenges. *Cell Host Microbe* **19**, 575–578 (2016).
372. Ridaura, V. K. *et al.* Gut microbiota from twins discordant for obesity modulate metabolism in mice. *Science* **341**, (2013).
373. Eberl, C. *et al.* Reproducible Colonization of Germ-Free Mice With the Oligo-Mouse-Microbiota in Different Animal Facilities. *Front Microbiol* **10**, 2999 (2020).
374. van der Waaij, D., Berghuis-de Vries, J. M. & Lekkerkerk-Van Der Wees, J. E. C. Colonization resistance of the digestive tract in conventional and antibiotic-treated mice. *J Hyg (Lond)* **69**, 405–411 (1971).
375. Stecher, B. & Hardt, W. D. Mechanisms controlling pathogen colonization of the gut. *Curr Opin Microbiol* **14**, 82–91 (2011).
376. Natividad, J. M. M. *et al.* Differential induction of antimicrobial REGIII by the intestinal microbiota and Bifidobacterium breve NCC2950. *Appl Environ Microbiol* **79**, 7745–7754 (2013).
377. Lécuyer, E. *et al.* Segmented Filamentous Bacterium Uses Secondary and Tertiary Lymphoid Tissues to Induce Gut IgA and Specific T Helper 17 Cell Responses. *Immunity* **40**, 608–620 (2014).
378. Robak, O. H. *et al.* Antibiotic treatment-induced secondary IgA deficiency enhances susceptibility to Pseudomonas aeruginosa pneumonia. *J Clin Invest* **128**, 3535–3545 (2018).
379. Grünewald, T. & Ruf, B. R. Clostridium difficile infection. *Nurs Older People* **22**, 335–348 (2010).

380. Britton, R. A. & Young, V. B. Role of the intestinal microbiota in resistance to colonization by *Clostridium difficile*. *Gastroenterology* **146**, 1547–1553 (2014).
381. Rupnik, M., Wilcox, M. H. & Gerding, D. N. *Clostridium difficile* infection: new developments in epidemiology and pathogenesis. *Nat Rev Microbiol* **7**, 526–536 (2009).
382. Rea, M. C. *et al.* Thuricin CD, a posttranslationally modified bacteriocin with a narrow spectrum of activity against *Clostridium difficile*. *Proc Natl Acad Sci U S A* **107**, 9352–9357 (2010).
383. Wilson, K. H. & Perini, F. Role of competition for nutrients in suppression of *Clostridium difficile* by the colonic microflora. *Infect Immun* **56**, 2610–2614 (1988).
384. Raplee, I. *et al.* Emergence of nosocomial associated opportunistic pathogens in the gut microbiome after antibiotic treatment. *Antimicrob Resist Infect Control* **10**, 1–11 (2021).
385. Tacconelli, E. *et al.* Antibiotic Usage and Risk of Colonization and Infection with Antibiotic-Resistant Bacteria: a Hospital Population-Based Study. *Antimicrob Agents Chemother* **53**, 4264 (2009).
386. Buffie, C. G. & Pamer, E. G. Microbiota-mediated colonization resistance against intestinal pathogens. *Nature Reviews Immunology* *2013 13:11* **13**, 790–801 (2013).
387. Silva, Y. P., Bernardi, A. & Frozza, R. L. The Role of Short-Chain Fatty Acids From Gut Microbiota in Gut-Brain Communication. *Front Endocrinol (Lausanne)* **11**, 25 (2020).
388. Rachid, R., Stephen-Victor, E. & Chatila, T. A. The microbial origins of food allergy. *Journal of Allergy and Clinical Immunology* **147**, 808–813 (2021).
389. Roediger, W. E. W. Role of anaerobic bacteria in the metabolic welfare of the colonic mucosa in man. *Gut* **21**, 793–798 (1980).
390. Chambers, E. S., Preston, T., Frost, G. & Morrison, D. J. Role of Gut Microbiota-Generated Short-Chain Fatty Acids in Metabolic and Cardiovascular Health. *Curr Nutr Rep* **7**, 198 (2018).
391. Frampton, J., Murphy, K. G., Frost, G. & Chambers, E. S. Short-chain fatty acids as potential regulators of skeletal muscle metabolism and function. *Nature Metabolism* *2020 2:9* **2**, 840–848 (2020).
392. He, J. *et al.* Short-Chain Fatty Acids and Their Association with Signalling Pathways in Inflammation, Glucose and Lipid Metabolism. *Int J Mol Sci* **21**, 1–16 (2020).
393. Mora, S. & Fullerton, R. Effects of Short Chain Fatty Acids on Glucose and Lipid metabolism in Adipocytes. *The FASEB Journal* **29**, 672.5 (2015).

394. Yao, Y. *et al.* The role of short-chain fatty acids in immunity, inflammation and metabolism. *Crit Rev Food Sci Nutr* **62**, 1–12 (2022).
395. Albillos, A., de Gottardi, A. & Rescigno, M. The gut-liver axis in liver disease: Pathophysiological basis for therapy. *J Hepatol* **72**, 558–577 (2020).
396. Carabotti, M., Scirocco, A., Maselli, M. A. & Severi, C. The gut-brain axis: interactions between enteric microbiota, central and enteric nervous systems. *Annals of Gastroenterology: Quarterly Publication of the Hellenic Society of Gastroenterology* **28**, 203 (2015).
397. Dang, A. T. & Marsland, B. J. Microbes, metabolites, and the gut–lung axis. *Mucosal Immunology* 2019 12:4 **12**, 843–850 (2019).
398. Brown, A. J. *et al.* The Orphan G protein-coupled receptors GPR41 and GPR43 are activated by propionate and other short chain carboxylic acids. *J Biol Chem* **278**, 11312–11319 (2003).
399. Singh, N. *et al.* Activation of Gpr109a, receptor for niacin and the commensal metabolite butyrate, suppresses colonic inflammation and carcinogenesis. *Immunity* **40**, 128–139 (2014).
400. Kimura, I. *et al.* Short-chain fatty acids and ketones directly regulate sympathetic nervous system via G protein-coupled receptor 41 (GPR41). *Proc Natl Acad Sci U S A* **108**, 8030–8035 (2011).
401. Samuel, B. S. *et al.* Effects of the gut microbiota on host adiposity are modulated by the short-chain fatty-acid binding G protein-coupled receptor, Gpr41. *Proc Natl Acad Sci U S A* **105**, 16767–16772 (2008).
402. Lu, Z. *et al.* GPR40 deficiency is associated with hepatic FAT/CD36 upregulation, steatosis, inflammation, and cell injury in C57BL/6 mice. *Am J Physiol Endocrinol Metab* **320**, E30–E42 (2021).
403. Maslowski, K. M. *et al.* Regulation of inflammatory responses by gut microbiota and chemoattractant receptor GPR43. *Nature* **461**, 1282–1286 (2009).
404. Pan, P. *et al.* Loss of FFAR2 promotes colon cancer by epigenetic dysregulation of inflammation suppressors. *Int J Cancer* **143**, 886–896 (2018).
405. BAUER, H., HOROWITZ, R. E., LEVENSON, S. M. & POPPER, H. The response of the lymphatic tissue to the microbial flora. Studies on germfree mice. *Am J Pathol* **42**, 471–83 (1963).
406. Kunisawa, J. *et al.* Microbe-dependent CD11b⁺ IgA⁺ plasma cells mediate robust early-phase intestinal IgA responses in mice. *Nat Commun* **4**, (2013).

407. Cahenzli, J., Köller, Y., Wyss, M., Geuking, M. B. & McCoy, K. D. Intestinal microbial diversity during early-life colonization shapes long-term IgE levels. *Cell Host Microbe* **14**, 559–570 (2013).
408. Hapfelmeier, S. *et al.* Reversible microbial colonization of germ-free mice reveals the dynamics of IgA immune responses. *Science* **328**, 1705–1709 (2010).
409. Knoop, K. A. *et al.* Microbial antigen encounter during a preweaning interval is critical for tolerance to gut bacteria. *Sci Immunol* **2**, (2017).
410. al Nabhani, Z. *et al.* A Weaning Reaction to Microbiota Is Required for Resistance to Immunopathologies in the Adult. *Immunity* **50**, 1276-1288.e5 (2019).
411. Olszak, T. *et al.* Microbial exposure during early life has persistent effects on natural killer T cell function. *Science* **336**, 489–493 (2012).
412. Knoop, K. A., McDonald, K. G., McCrate, S., McDole, J. R. & Newberry, R. D. Microbial sensing by goblet cells controls immune surveillance of luminal antigens in the colon. *Mucosal Immunol* **8**, 198–210 (2015).
413. Gonçalves, E. *et al.* Host Transcriptome and Microbiota Signatures Prior to Immunization Profile Vaccine Humoral Responsiveness. *Front Immunol* **12**, 1552 (2021).
414. Lynn, M. A. *et al.* Early-Life Antibiotic-Driven Dysbiosis Leads to Dysregulated Vaccine Immune Responses in Mice. *Cell Host Microbe* **23**, 653-660.e5 (2018).
415. Lynn, D. J., Benson, S. C., Lynn, M. A. & Pulendran, B. Modulation of immune responses to vaccination by the microbiota: implications and potential mechanisms. *Nature Reviews Immunology* 2021 22:1 **22**, 33–46 (2021).
416. Zhao, T. *et al.* Influence of gut microbiota on mucosal IgA antibody response to the polio vaccine. *npj Vaccines* 2020 5:1 **5**, 1–9 (2020).
417. Huda, M. N. *et al.* Bifidobacterium Abundance in Early Infancy and Vaccine Response at 2 Years of Age. *Pediatrics* **143**, (2019).
418. Zimmermann, P. & Curtis, N. The influence of probiotics on vaccine responses - A systematic review. *Vaccine* **36**, 207–213 (2018).
419. Frank, D. N. *et al.* Molecular-phylogenetic characterization of microbial community imbalances in human inflammatory bowel diseases. *Proc Natl Acad Sci U S A* **104**, 13780–13785 (2007).
420. Abrahamsson, T. R. *et al.* Low gut microbiota diversity in early infancy precedes asthma at school age. *Clin Exp Allergy* **44**, 842–850 (2014).

421. Giongo, A. *et al.* Toward defining the autoimmune microbiome for type 1 diabetes. *ISME J* **5**, 82–91 (2011).
422. Arslan, N. Obesity, fatty liver disease and intestinal microbiota. *World J Gastroenterol* **20**, 16452–16463 (2014).
423. Gupta, A., Singh, V. & Mani, I. Dysbiosis of human microbiome and infectious diseases. (2022) doi:10.1016/BS.PMBTS.2022.06.016.
424. Libertucci, J. & Young, V. B. The role of the microbiota in infectious diseases. *Nature Microbiology* *2018 4:1* **4**, 35–45 (2018).
425. Mizutani, T., Ishizaka, A., Koga, M., Tsutsumi, T. & Yotsuyanagi, H. Role of Microbiota in Viral Infections and Pathological Progression. *Viruses* *2022, Vol. 14, Page 950* **14**, 950 (2022).
426. al Khatib, H. A. *et al.* Profiling of intestinal microbiota in patients infected with respiratory influenza a and b viruses. *Pathogens* **10**, (2021).
427. Lv, Z., Xiong, D., Shi, J., Long, M. & Chen, Z. The Interaction Between Viruses and Intestinal Microbiota: A Review. *Curr Microbiol* **78**, 3597–3608 (2021).
428. Gu, S. *et al.* Alterations of the Gut Microbiota in Patients With Coronavirus Disease 2019 or H1N1 Influenza. *Clinical Infectious Diseases* **71**, 2669–2678 (2020).
429. Yildiz, S., Mazel-Sanchez, B., Kandasamy, M., Manicassamy, B. & Schmolke, M. Influenza A virus infection impacts systemic microbiota dynamics and causes quantitative enteric dysbiosis. *Microbiome* **6**, 1–17 (2018).
430. Groves, H. T. *et al.* Respiratory disease following viral lung infection alters the murine gut microbiota. *Front Immunol* **9**, 182 (2018).
431. Sencio, V. *et al.* Gut Dysbiosis during Influenza Contributes to Pulmonary Pneumococcal Superinfection through Altered Short-Chain Fatty Acid Production. *Cell Rep* **30**, 2934-2947.e6 (2020).
432. Zhang, Q. *et al.* Influenza infection elicits an expansion of gut population of endogenous *Bifidobacterium animalis* which protects mice against infection. *Genome Biol* **21**, 1–26 (2020).
433. Hernández-Terán, A. *et al.* Microbiota composition in the lower respiratory tract is 1 associated with severity in patients with acute respiratory 2 distress by influenza 3. doi:10.1101/2021.12.07.21267419.
434. Gu, L. *et al.* Dynamic Changes in the Microbiome and Mucosal Immune Microenvironment of the Lower Respiratory Tract by Influenza Virus Infection. *Front Microbiol* **10**, 2491 (2019).

435. Sommariva, M. *et al.* The lung microbiota: role in maintaining pulmonary immune homeostasis and its implications in cancer development and therapy. *Cell Mol Life Sci* **77**, 2739–2749 (2020).
436. Yang, D., Xing, Y., Song, X. & Qian, Y. The impact of lung microbiota dysbiosis on inflammation. *Immunology* **159**, 156 (2020).
437. Wei, C. J. *et al.* Next-generation influenza vaccines: opportunities and challenges. *Nat Rev Drug Discov* **19**, 239–252 (2020).
438. Hilimire, T. A., Nogales, A., Chiem, K., Ortego, J. & Martinez-sobrido, L. Increasing the Safety Profile of the Master Donor Live Attenuated Influenza Vaccine. *Pathogens* **2020**, Vol. 9, Page 86 **9**, 86 (2020).
439. Deriu, E. *et al.* Influenza Virus Affects Intestinal Microbiota and Secondary Salmonella Infection in the Gut through Type I Interferons. *PLoS Pathog* **12**, e1005572 (2016).
440. Wang, J. *et al.* Respiratory influenza virus infection induces intestinal immune injury via microbiota-mediated Th17 cell-dependent inflammation. *Journal of Experimental Medicine* **211**, 2683–2683 (2014).
441. Mueller, S. *et al.* Live attenuated influenza virus vaccines by computer-aided rational design. *Nat Biotechnol* **28**, 723–726 (2010).
442. Yang, C., Skiena, S., Futcher, B., Mueller, S. & Wimmer, E. Deliberate reduction of hemagglutinin and neuraminidase expression of influenza virus leads to an ultraproductive live vaccine in mice. *Proc Natl Acad Sci U S A* **110**, 9481–9486 (2013).
443. Steel, J. *et al.* Live attenuated influenza viruses containing NS1 truncations as vaccine candidates against H5N1 highly pathogenic avian influenza. *J Virol* **83**, 1742–1753 (2009).
444. Wang, L. *et al.* Generation of a Live Attenuated Influenza Vaccine that Elicits Broad Protection in Mice and Ferrets. *Cell Host Microbe* **21**, 334–343 (2017).
445. Si, L. *et al.* Generation of a live attenuated influenza A vaccine by proteolysis targeting. *Nature Biotechnology* **2022** 40:9 **40**, 1370–1377 (2022).
446. Rockman, S., Laurie, K. L., Parkes, S., Wheatley, A. & Barr, I. G. New Technologies for Influenza Vaccines. *Microorganisms* **8**, 1–20 (2020).
447. Blanco-Lobo, P., Nogales, A., Rodríguez, L. & Martínez-Sobrido, L. Novel Approaches for The Development of Live Attenuated Influenza Vaccines. *Viruses* **11**, (2019).
448. Basha, S., Surendran, N. & Pichichero, M. Immune responses in neonates. *Expert Rev Clin Immunol* **10**, 1171–1184 (2014).

449. Mohr, E. & Siegrist, C. A. Vaccination in early life: standing up to the challenges. *Curr Opin Immunol* **41**, 1–8 (2016).
450. Lau, Y.-F., Santos, C., Torres-Vélez, F. J. & Subbarao, K. The Magnitude of Local Immunity in the Lungs of Mice Induced by Live Attenuated Influenza Vaccines Is Determined by Local Viral Replication and Induction of Cytokines. *J Virol* **85**, 76–85 (2011).
451. Goll, J. B. *et al.* The antibody landscapes following AS03 and MF59 adjuvanted H5N1 vaccination. *npj Vaccines* *2022 7:1* **7**, 1–11 (2022).
452. Givord, C. *et al.* Activation of the endoplasmic reticulum stress sensor IRE1 α by the vaccine adjuvant AS03 contributes to its immunostimulatory properties. *npj Vaccines* *2018 3:1* **3**, 1–12 (2018).
453. Orr, M. T. & Fox, C. B. AS03 stresses out macrophages: Commentary on ‘Activation of the endoplasmic reticulum stress sensor IRE1 α by the vaccine adjuvant AS03 contributes to its immunostimulatory properties’. *npj Vaccines* *2018 3:1* **3**, 1–2 (2018).
454. Garçon, N., Vaughn, D. W. & Didierlaurent, A. M. Development and evaluation of AS03, an Adjuvant System containing α -tocopherol and squalene in an oil-in-water emulsion. <http://dx.doi.org/10.1586/erv.11.192> **11**, 349–366 (2014).
455. Morel, S. *et al.* Adjuvant System AS03 containing α -tocopherol modulates innate immune response and leads to improved adaptive immunity. *Vaccine* **29**, 2461–2473 (2011).
456. Bommiasamy, H. & Popko, B. Animal Models in the Study of the Unfolded Protein Response. *Methods Enzymol* **491**, 91 (2011).
457. Mazel-Sanchez, B. *et al.* Influenza A viruses balance ER stress with host protein synthesis shutoff. *Proc Natl Acad Sci U S A* **118**, (2021).
458. Hrinčius, E. R. *et al.* Acute Lung Injury Results from Innate Sensing of Viruses by an ER Stress Pathway. *Cell Rep* **11**, 1591 (2015).
459. Prasad, V. & Greber, U. F. The endoplasmic reticulum unfolded protein response – homeostasis, cell death and evolution in virus infections. *FEMS Microbiol Rev* **45**, 1–19 (2021).
460. Carpenter, J. E. & Grose, C. Varicella-zoster virus glycoprotein expression differentially induces the unfolded protein response in infected cells. *Front Microbiol* **5**, (2014).
461. Gabutti, G., Bolognesi, N., Sandri, F., Florescu, C. & Stefanati, A. Varicella zoster virus vaccines: an update. *Immunotargets Ther* **8**, 15 (2019).

462. Prasad, V. *et al.* The UPR sensor IRE1 α and the adenovirus E3-19K glycoprotein sustain persistent and lytic infections. *Nat Commun* **11**, (2020).
463. Chang, J. Adenovirus Vectors: Excellent Tools for Vaccine Development. *Immune Netw* **21**, 1–11 (2021).
464. Stahl, S. *et al.* Cytomegalovirus downregulates IRE1 to repress the unfolded protein response. *PLoS Pathog* **9**, (2013).
465. Liu, J., Jaijyan, D. K., Tang, Q. & Zhu, H. Promising Cytomegalovirus-Based Vaccine Vector Induces Robust CD8⁺ T-Cell Response. *Int J Mol Sci* **20**, (2019).
466. Trujillo-Alonso, V., Maruri-Avidal, L., Arias, C. F. & López, S. Rotavirus Infection Induces the Unfolded Protein Response of the Cell and Controls It through the Nonstructural Protein NSP3. *J Virol* **85**, 12594 (2011).
467. Nachbagauer, R., Krammer, F. & Albrecht, R. A. A Live-Attenuated Prime, Inactivated Boost Vaccination Strategy with Chimeric Hemagglutinin-Based Universal Influenza Virus Vaccines Provides Protection in Ferrets: A Confirmatory Study. *Vaccines* 2018, Vol. 6, Page 47 **6**, 47 (2018).
468. Yan, L. M. *et al.* Combined use of live-attenuated and inactivated influenza vaccines to enhance heterosubtypic protection. *Virology* **525**, 73 (2018).
469. Jang, H. *et al.* Efficacy and synergy of live-attenuated and inactivated influenza vaccines in young chickens. *PLoS One* **13**, e0195285 (2018).
470. Benn, C. S., Netea, M. G., Selin, L. K. & Aaby, P. A small jab - a big effect: nonspecific immunomodulation by vaccines. *Trends Immunol* **34**, 431–439 (2013).
471. Jensen, K. J. *et al.* Seasonal variation in the non-specific effects of BCG vaccination on neonatal mortality: three randomised controlled trials in Guinea-Bissau. *BMJ Glob Health* **5**, e001873 (2020).
472. Arts, R. J. W. *et al.* BCG Vaccination Protects against Experimental Viral Infection in Humans through the Induction of Cytokines Associated with Trained Immunity. *Cell Host Microbe* **23**, 89-100.e5 (2018).
473. Walk, J. *et al.* Outcomes of controlled human malaria infection after BCG vaccination. *Nat Commun* **10**, (2019).
474. Piedra, P. A. *et al.* Trivalent live attenuated intranasal influenza vaccine administered during the 2003-2004 influenza type A (H3N2) outbreak provided immediate, direct, and indirect protection in children. *Pediatrics* **120**, (2007).

475. Liu, R. *et al.* Association between influenza vaccination, all-cause mortality and cardiovascular mortality: a protocol for a living systematic review and prospective meta-analysis. *BMJ Open* **12**, e054171 (2022).
476. Lee, Y. J. *et al.* Non-specific effect of vaccines: Immediate protection against respiratory syncytial virus infection by a live attenuated influenza vaccine. *Front Microbiol* **9**, 83 (2018).
477. Palgen, J. L. *et al.* Optimize Prime/Boost Vaccine Strategies: Trained Immunity as a New Player in the Game. *Front Immunol* **12**, 554 (2021).
478. Hawksworth, A. *et al.* Replication of live attenuated influenza vaccine viruses in human nasal epithelial cells is associated with H1N1 vaccine effectiveness. *Vaccine* **38**, 4209–4218 (2020).
479. Bandell, A., Woo, J. & Coelingh, K. Protective efficacy of live-attenuated influenza vaccine (multivalent, Ann Arbor strain): a literature review addressing interference. <http://dx.doi.org/10.1586/erv.11.73> **10**, 1131–1141 (2014).
480. Belshe, R. B. *et al.* Efficacy of vaccination with live attenuated, cold-adapted, trivalent, intranasal influenza virus vaccine against a variant (A/Sydney) not contained in the vaccine. *J Pediatr* **136**, 168–175 (2000).
481. Nolan, T. *et al.* Safety and immunogenicity of a live-attenuated influenza vaccine blended and filled at two manufacturing facilities. *Vaccine* **21**, 1224–1231 (2003).
482. Zangwill, K. M. *et al.* Prospective, randomized, placebo-controlled evaluation of the safety and immunogenicity of three lots of intranasal trivalent influenza vaccine among young children. *Pediatr Infect Dis J* **20**, 740–746 (2001).
483. Lee, M. S. *et al.* Measuring antibody responses to a live attenuated influenza vaccine in children. *Pediatr Infect Dis J* **23**, 852–856 (2004).
484. Roy, S., Williams, C. M., Wijesundara, D. K. & Furuya, Y. Impact of Pre-Existing Immunity to Influenza on Live-Attenuated Influenza Vaccine (LAIV) Immunogenicity. *Vaccines 2020, Vol. 8, Page 683* **8**, 683 (2020).
485. Peters, B. A. *et al.* A taxonomic signature of obesity in a large study of American adults. *Scientific Reports 2018 8:1* **8**, 1–13 (2018).
486. Boutagy, N. E., McMillan, R. P., Frisard, M. I. & Hulver, M. W. Metabolic endotoxemia with obesity: Is it real and is it relevant? *Biochimie* **124**, 11–20 (2016).
487. de Steenhuijsen Piters, W. A. A. *et al.* Early-life viral infections are associated with disadvantageous immune and microbiota profiles and recurrent respiratory infections. *Nature Microbiology 2022 7:2* **7**, 224–237 (2022).

488. Ma, Z. (Sam). Testing the Anna Karenina Principle in Human Microbiome-Associated Diseases. *iScience* **23**, 101007 (2020).
489. Zaneveld, J. R., McMinds, R. & Thurber, R. V. Stress and stability: applying the Anna Karenina principle to animal microbiomes. *Nature Microbiology* *2017 2:9* **2**, 1–8 (2017).
490. Yagi, K., Asai, N., Huffnagle, G. B., Lukacs, N. W. & Fonseca, W. Early-Life Lung and Gut Microbiota Development and Respiratory Syncytial Virus Infection. *Front Immunol* **13**, (2022).
491. Nashed, L. *et al.* Gut microbiota changes are detected in asymptomatic very young children with SARS-CoV-2 infection. *Gut* **71**, 2371–2373 (2022).
492. May, K. S. & den Hartigh, L. J. Modulation of Adipocyte Metabolism by Microbial Short-Chain Fatty Acids. *Nutrients* *2021, Vol. 13, Page 3666* **13**, 3666 (2021).
493. Hong, Y. H. *et al.* Acetate and propionate short chain fatty acids stimulate adipogenesis via GPCR43. *Endocrinology* **146**, 5092–5099 (2005).
494. Lynn, M. A. *et al.* Early-Life Antibiotic-Driven Dysbiosis Leads to Dysregulated Vaccine Immune Responses in Mice. *Cell Host Microbe* **23**, 653-660.e5 (2018).
495. Harris, V. C. *et al.* Significant Correlation Between the Infant Gut Microbiome and Rotavirus Vaccine Response in Rural Ghana. *J Infect Dis* **215**, 34–41 (2017).
496. Yildiz, S. *et al.* Respiratory tissue-associated commensal bacteria offer therapeutic potential against pneumococcal colonization. *Elife* **9**, 1–25 (2020).
497. Rowe, H. M. *et al.* Direct interactions with influenza promote bacterial adherence during respiratory infections. *Nature Microbiology* *2019 4:8* **4**, 1328–1336 (2019).
498. Avadhanula, V., Wang, Y., Portner, A. & Adderson, E. Nontypeable Haemophilus influenzae and Streptococcus pneumoniae bind respiratory syncytial virus glycoprotein. *J Med Microbiol* **56**, 1133–1137 (2007).
499. Hament, J. M. *et al.* Direct Binding of Respiratory Syncytial Virus to Pneumococci: A Phenomenon That Enhances Both Pneumococcal Adherence to Human Epithelial Cells and Pneumococcal Invasiveness in a Murine Model. *Pediatric Research* *2005 58:6* **58**, 1198–1203 (2005).
500. Harris, V. C. *et al.* Significant Correlation Between the Infant Gut Microbiome and Rotavirus Vaccine Response in Rural Ghana. *J Infect Dis* **215**, 34–41 (2017).
501. Oh, J. Z. *et al.* TLR5-mediated sensing of gut microbiota is necessary for antibody responses to seasonal influenza vaccination. *Immunity* **41**, 478–492 (2014).

502. Mika, M. *et al.* Influence of the pneumococcal conjugate vaccines on the temporal variation of pneumococcal carriage and the nasal microbiota in healthy infants: a longitudinal analysis of a case-control study. *Microbiome* **5**, 85 (2017).
503. Peno, C. *et al.* The effect of live attenuated influenza vaccine on pneumococcal colonisation densities among children aged 24–59 months in The Gambia: a phase 4, open label, randomised, controlled trial. *Lancet Microbe* **2**, e656–e665 (2021).
504. Thors, V. *et al.* The Effects of Live Attenuated Influenza Vaccine on Nasopharyngeal Bacteria in Healthy 2 to 4 Year Olds. A Randomized Controlled Trial. *Am J Respir Crit Care Med* **193**, 1401–1409 (2016).

8. Appendix - Contributions to Other Publications

8.1. Respiratory tissue-associated commensal bacteria offer therapeutic potential against pneumococcal colonization

Soner Yildiz^{#,1}, João P Pereira Bonifacio Lopes^{#,1}, Matthieu Bergé¹, Víctor González-Ruiz^{2,3}, Damian Baud¹, Joachim Kloehn¹, Inês Boal-Carvalho¹, Olivier P Schaeren^{4,5}, Michael Schotsaert⁶, Lucy J Hathaway⁴, Serge Rudaz^{2,3}, Patrick H Viollier¹, Siegfried Hapfelmeier⁴, Patrice Francois¹, Mirco Schmolke¹

¹*Department of Microbiology and Molecular Medicine, Faculty of Medicine, University of Geneva, Geneva, Switzerland.*

²*Analytical Sciences, School of Pharmaceutical Sciences, University of Geneva, University of Lausanne, Geneva, Switzerland.*

³*Swiss Centre for Applied Human Toxicology, Basel, Switzerland.*

⁴*Institute for Infectious Disease (IFIK), University of Bern, Bern, Switzerland.*

⁵*Graduate School GCB, University of Bern, Bern, Switzerland.*

⁶*Department of Microbiology, Icahn School of Medicine at Mount Sinai, New York, United States.*

[#]*Contributed equally.*

Status:

Manuscript published in eLife – PMID: 33287959

Summary:

Integrity of the microbiota is essential for a vast number of physiological processes. Importantly, commensal microbes provide a natural barrier against invading pathogens. In humans, influenza A virus (IAV) infection leads to increased susceptibility to secondary bacterial infections in the respiratory tract, in particular with *Staphylococcus aureus* and *Streptococcus pneumoniae*. In this work, we evaluated the role of the lung microbiota during IAV-induced bacterial superinfection using a mouse model. We identified *Lactobacillus murinus* as the predominant bacterial species in the healthy lung environment of specific pathogen-free (SPF) animals. Furthermore, we verified that *L. murinus*-conditioned media (LmCM) inhibits the growth of *S. pneumoniae in vitro* and limits the growth of pneumococcal chains. This effect was likely due to the presence of high levels of lactic acid in LmCM. Finally, we show that intranasal administration of *L. murinus* to IAV-infected mice, decreases the titers of *S. pneumoniae* in the lungs upon challenge. Thus, our results suggest that probiotics treatment could be used therapeutically to reduce the burden of secondary bacterial infections in IAV-infected individuals.

Personal Contribution:

For this work, I performed the quantification of *L. murinus* by qPCR in lung homogenates (Figures 3A and 3B and Figure 3 – supplement 1) together with the in situ hybridization of the RNA probes specific for the rRNA gene of *L. murinus* and panbacteria in lung tissue slices (Figure 3C). I also performed the pH and lactic acid measurements in BAL samples of SPF and GF mice (Figures 8A and 8D and Figure 8 – supplement 1A). Furthermore, I performed the animal work, qPCRs for pro-inflammatory cytokines and 16S DNA sequencing analysis of lung homogenates after IAV infection and *L. murinus* administration and constructed the images (Figure 8 – supplement 1B and C).

Respiratory tissue-associated commensal bacteria offer therapeutic potential against pneumococcal colonization

Soner Yildiz^{1†}, João P Pereira Bonifacio Lopes^{1†}, Matthieu Bergé¹, Víctor González-Ruiz^{2,3}, Damian Baud¹, Joachim Kloehn¹, Inês Boal-Carvalho¹, Olivier P Schaeren^{4,5}, Michael Schotsaert⁶, Lucy J Hathaway⁴, Serge Rudaz^{2,3}, Patrick H Viollier¹, Siegfried Hapfelmeier⁴, Patrice Francois¹, Mirco Schmolke^{1*}

¹Department of Microbiology and Molecular Medicine, Faculty of Medicine, University of Geneva, Geneva, Switzerland; ²Analytical Sciences, School of Pharmaceutical Sciences, University of Geneva, University of Lausanne, Geneva, Switzerland; ³Swiss Centre for Applied Human Toxicology, Basel, Switzerland; ⁴Institute for Infectious Disease (IFIK), University of Bern, Bern, Switzerland; ⁵Graduate School GCB, University of Bern, Bern, Switzerland; ⁶Department of Microbiology, Icahn School of Medicine at Mount Sinai, New York, United States

Abstract Under eubiotic conditions commensal microbes are known to provide a competitive barrier against invading bacterial pathogens in the intestinal tract, on the skin or on the vaginal mucosa. Here, we evaluate the role of lung microbiota in *Pneumococcus* colonization of the lungs. In eubiosis, the lungs of mice were dominantly colonized by *Lactobacillus murinus*. Differential analysis of 16S rRNA gene sequencing or *L. murinus*-specific qPCR of DNA from total organ homogenates vs. broncho alveolar lavages implicated tight association of these bacteria with the host tissue. Pure *L. murinus* conditioned culture medium inhibited growth and reduced the extension of pneumococcal chains. Growth inhibition in vitro was likely dependent on *L. murinus*-produced lactic acid, since pH neutralization of the conditioned medium aborted the antibacterial effect. Finally, we demonstrate that *L. murinus* provides a barrier against pneumococcal colonization in a respiratory dysbiosis model after an influenza A virus infection, when added therapeutically.

*For correspondence:
mirco.schmolke@unige.ch

†These authors contributed
equally to this work

Competing interests: The
authors declare that no
competing interests exist.

Funding: See page 20

Received: 13 November 2019

Accepted: 18 November 2020

Published: 08 December 2020

Reviewing editor: Peter
Turnbaugh, University of
California, San Francisco, United
States

© Copyright Yildiz et al. This
article is distributed under the
terms of the [Creative Commons
Attribution License](https://creativecommons.org/licenses/by/4.0/), which
permits unrestricted use and
redistribution provided that the
original author and source are
credited.

Introduction

Mucosal surfaces are major entry ports for microbial pathogens. In the densely colonized gut, commensal bacteria confer a prominent protective role against invading bacterial pathogens, in part by posing a competitive threshold within this ecological niche (Barthel et al., 2003). This biological barrier is absent in axenic mice and reduced in mice harboring a low-complexity microbiota colonized mice. Barrier function of the microbiota is consequently sensitive to antibiotics treatment in colonized conventionally housed mice (Barthel et al., 2003; Brugiroux et al., 2017). Skin microbiota poses a similar barrier against colonization by bacterial skin pathogens (reviewed in Parlet et al., 2019). In recent years, it became evident that the lower respiratory tract (LRT), previously considered quasi-sterile, also hosts a bacterial microbiota under healthy conditions (Dickson et al., 2015). Whether the bacterial LRT microbiota confers colonization resistance against bacterial pathogens, e.g. causing pneumonia, is unclear.

Recently, a number of groups, including ours, reported compositional changes in the intestinal and lower respiratory tract microbiota over the course of an IAV infection using a C57BL/6J mouse

model housed under specific pathogen-free (SPF) conditions (Deriu *et al.*, 2016; Groves *et al.*, 2018; Planet *et al.*, 2016; Yildiz *et al.*, 2018). This opened a temporarily limited window for *Salmonella enterica* serovar Typhimurium infection in the intestine, similarly as in mice orally treated with antibiotics (Deriu *et al.*, 2016; Yildiz *et al.*, 2018). We found only little qualitative or quantitative differences in respiratory microbiota of IAV infected mice by 16S rRNA gene-specific next generation sequencing and qPCR. Nevertheless, we observed enhanced secondary colonization with *Streptococcus pneumoniae* following IAV infections, as described previously (McCullers and Rehg, 2002). The outcome of these super-infections is determined by host factors, viral factors and factors of the bacterial pathogen (reviewed in McCullers, 2014).

IAV infections take place in the poly-microbial environment of the respiratory tract and bacterial colonization of the lung is important to prime alveolar macrophages (Abt *et al.*, 2012). However, the immediate role of the lung microbiota composition and complexity on invading bacterial pathogens is poorly investigated. We recently discovered a high content of Lactobacillaceae in the lung microbiota of healthy SPF housed mice, which was not reported before (Yildiz *et al.*, 2018). Here we identify these commensal bacteria as *Lactobacillus murinus*, most probably a strain of the altered Schaedler flora (ASF). We provide in vitro evidence that it can limit pneumococcal growth, e.g. through release of lactic acid and reduces of chain formation of pneumococcus. Importantly, therapeutic application of *L. murinus* after IAV infection reduced the burden of secondary pneumococcal pneumonia.

Results

***L. murinus* (ASF361) could be a major constituent of mouse lung microbiota in laboratory settings**

We previously demonstrated dominance of Lactobacillaceae in total lower respiratory tract (LRT) homogenates of SPF housed C57Bl/6J mice by 16S rRNA gene-specific NGS (Yildiz *et al.*, 2018). In order to characterize these Lactobacillaceae in greater detail, we independently isolated and characterized two clones of phenotypically dominant bacteria from LRT homogenates cultivated on Columbia agar plates. After whole genome sequencing and de novo assembly we determined the evolutionary relationships of the two isolates based on the 16S rRNA gene. The phylogeny presented in **Figure 1A** is based on the alignment of approximately 1400 nucleotides of the 16S rRNA gene. The lung-isolated strains clustered with *L. murinus* and were clearly separated from *L. animalis* and *L. apodemi* isolates. One likely source for *L. murinus* is the altered Schaedler flora (ASF), introduced in 1978 to standardize mouse model colonization (Dewhirst *et al.*, 1999; Schaedler *et al.*, 1965; Wymore Brand *et al.*, 2015) (indicated as *L. murinus* Schaedler in **Figure 1B**). Blasting of the de novo assembled genome against available genomes revealed that indeed *L. murinus* ASF361 was the best match to our *L. murinus* strain isolate (**Figure 1B**, z-score = 1, PRJNA591640 and **Supplementary file 1**). Alignment of the whole genome of our *Lactobacillus* isolate to the recently published reference genome of *L. murinus* ASF361 (Wannemuehler *et al.*, 2014) resulted in >99.5% sequence identity (**Figure 1C**).

The high prevalence of *L. murinus* in the murine LRT microbiota was not reported by other studies. Previous analyses of murine LRT microbiota by 16S rRNA gene NGS revealed a higher diversity with a balanced distribution of Actinobacteria, Bacteroidetes, Firmicutes and Proteobacteria (Barfod *et al.*, 2013; Poroyko *et al.*, 2015; Singh *et al.*, 2017; Yadava *et al.*, 2016). We speculated that differences in sampling techniques (bronchoalveolar lavage fluid (BALF) vs. partial organs vs. total organs) might introduce a potential sampling bias by avoiding or limiting tissue-associated bacteria. To resolve this discrepancy, we directly compared the compositional profile of LRT microbiota from bronchoalveolar lavage fluid (BALF), total organ after bronchoalveolar lavage or total organ without manipulation from SPF (individually ventilated cage) and conventionally (open cage) housed C57Bl/6J mice (see methods section for details). As demonstrated before (Yildiz *et al.*, 2018), we found predominantly Lactobacillaceae in total organ samples (**Figure 2A/B**). However, this family was poorly represented in BALF samples, indicating a tight association with lung tissue. Accordingly, alpha diversity was higher in BALF samples (**Figure 2C**) and the overall homogeneous composition of BALF microbiota confirmed previous analysis by other groups. Of note, total 16S copy numbers by qPCR on the same amount of input DNA were substantially higher in tissue-derived samples

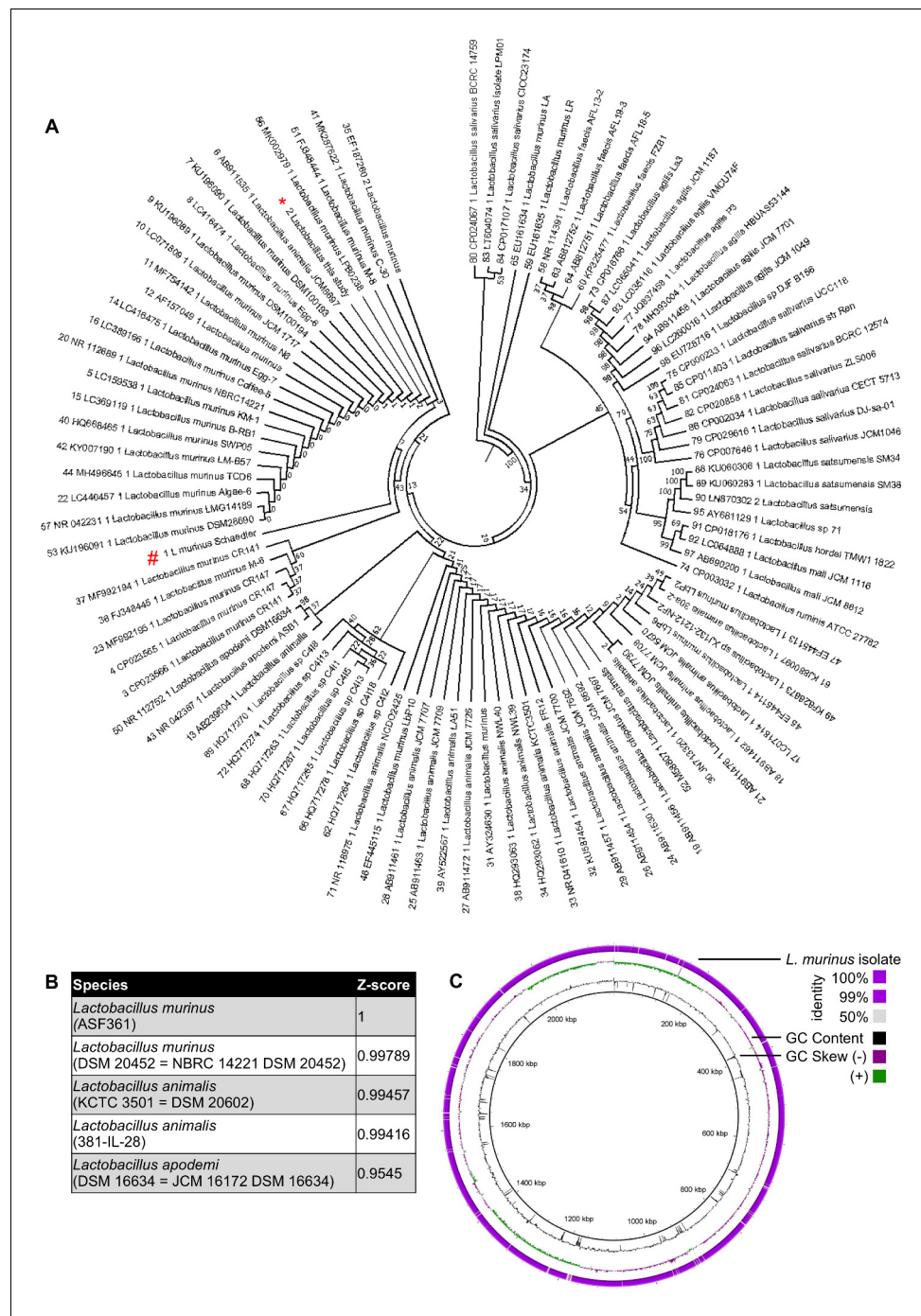


Figure 1. Lactobacillaceae isolate from total lung homogenates of mice is identified to be *Lactobacillus murinus*, a member of altered Scheadler Flora. (A) Phylogenetic tree of Lactobacillaceae isolate (indicated with red asterisk) to other known members of Lactobacillaceae family (*L. murinus* ASF361 is indicated with a red octothorpe). The phylogeny presented is based on the alignment of approximately 1400 nucleotides of the 16S rRNA gene. The phylogenetic analyses were generated with the neighbor-joining method. The percentage of replicate trees in which the associated taxa clustered together in the bootstrap test (100 replicates) is shown next to the branches. The trees are not rooted but drawn to scale with branch lengths in the same units as those of the evolutionary distances used to infer the phylogenetic tree. The evolutionary distances were computed using the Kimura 2-parameter method for 16S rRNA gene. The analysis included 17 sequences. Evolutionary analyses were conducted using MEGA6. All sequences are labeled according to strain name, species and accession number. (B) Genome of Lactobacillaceae isolate was aligned to reference genome database. Z-scores are calculated based on Average

Figure 1 continued on next page

Figure 1 continued

nucleotide identity. Top five hits are represented on the table. (C) Alignment between genome of *Lactobacillaceae* isolate and reference *L. murinus* genome from ASF 361. Genomic location, GC content, GC skew and sequence similarity given from most inner circle to most outer circle, respectively. The GC skew should not be considered since the nucleotide 0, origin of the genome, is not at the correct position due to the lack of closed genome of *L. murinus*.

(Figure 2—figure supplement 1A) than in BALF samples. Effectively, BALF samples were indistinguishable from blanks and background by 16S rRNA-specific qPCR. As a control for successful BAL procedure we included a qPCR for host 18S rRNA (Figure 2—figure supplement 1B) would be.

Regardless, the more sensitive NGS approach revealed OTUs in BALF (and tissue) samples, which were absent in blanks, such as Bacteroidia (Figure 2A). Beta-diversity (Weighted UniFrac) analysis revealed that BALF samples were found to be distinct in bacterial composition and abundance from tissue homogenates, resembling largely blank samples in SPF housed and separately positioned in CONV housed mice (Figure 2D). We next confirmed the presence of *L. murinus* in the lungs of SPF mice by two independent and species-specific techniques. First, we quantified *L. murinus* by specific primers using qPCR (Figure 3A). Genomic DNA from a defined amount of colony forming units of isolated *L. murinus* served as a standard to convert Ct values into cfu equivalents (Figure 3—figure supplement 1A). Four out of five SPF mice displayed DNA equivalent to $>10^7$ cfu/lung (Figure 3A and Figure 3—figure supplement 1B), which was about 100–1000 fold higher than the titers of live *L. murinus* determined by plating of lung homogenates (Yildiz et al., 2018) and potentially a result of dead *L. murinus*. In line with the 16S rRNA NGS data (Figure 2A) we did not detect *L. murinus* in DNA of BALF samples by *L. murinus*-specific qPCR, but in the majority of total lung DNA and DNA from lungs after BAL (Figure 3B). To gain insight into the anatomic distribution of *L. murinus* in the airways of mice, we performed highly sensitive RNAScope based ISH from frontal sections of total PFA fixed lungs (150 μ m depth from ventral side) using probes specific for eubacteria or *L. murinus*. Bright red staining for *L. murinus* was exclusively visible in the airway space of SPF mouse lungs, but not in the germfree control specimen (Figure 3C). *L. murinus* was predominantly found in large airways of the bronchi, but not in the trachea or the alveolar space (upper panels). Staining of adjacent slides for eubacteria (lower panels), revealed overall good correlation of *L. murinus*-specific staining with total eubacterial staining. This confirms our initial finding, that *L. murinus* dominates the bacterial flora. The RNAScope data further support that *L. murinus* is viable in the lung, since we detected short lived bacterial RNA. A limitation to these findings is that they are based on data from two laboratories within a single animal facility. Facility and vendor-specific confounding effects will require to be addressed in the future.

***L. murinus* inhibits growth of bacterial lung pathogens**

Direct competition of commensal microbiota with invading bacterial pathogens or already present pathobionts is believed to be a major host defense strategy against bacterial infections on mucosal surfaces. It was demonstrated for the intestine (Barthel et al., 2003; Brugiroux et al., 2017) and for the skin (Nakatsuji et al., 2017), but data from the LRT are currently not available. Mechanistically, commensal bacteria control outgrowth of pathobionts or invasion of pathogenic bacteria by different mechanisms: i.e. direct competition for nutrients and space, priming of innate immune cells, which are responsible for bacterial clearance and secretion of production/secretion of antibacterial metabolites (reviewed in Pickard et al., 2017).

Members of the family Lactobacillaceae were previously shown to inhibit growth of Gram-positive or Gram-negative bacteria in co-culture or by exposure to Lactobacillus conditioned medium (De Keersmaecker et al., 2006; Lu et al., 2009). Following a similar idea, we decided to first evaluate the effect of our *L. murinus* isolate on a common bacterial pathogen of the respiratory tract, *S. pneumoniae*, in an in vitro setting. Incompatibility of media requirements for efficient growth of these two bacteria did not allow us to perform co-culture studies. Instead, we used an experimental setup where *S. pneumoniae* was grown in presence of fresh MRS medium (FM) or *L. murinus* conditioned MRS medium (LmCM), both at a dilution of 1:10 with *S. pneumoniae* culture media (TSB). To further rule out that the antibacterial effects could merely be a consequence of depletion/reduction of nutrients in the growth media, we used a similarly prepared medium conditioned by control

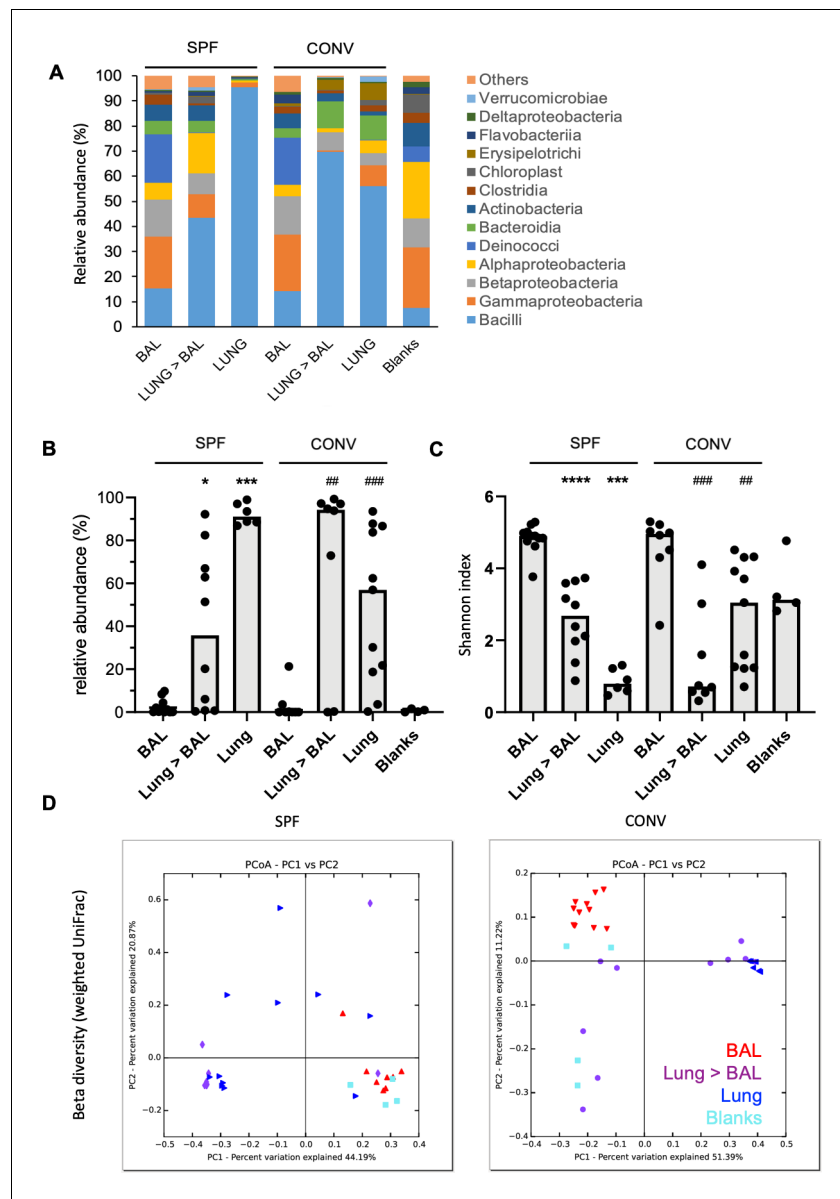


Figure 2. Bacilli class of bacteria is under-represented in bronchoalveolar lavage samples in mice in comparison to total lung homogenates. BALF, total lung homogenates after BAL procedure (Lung >BAL) or directly sampled total lung homogenates (Lung) of mice housed in specific pathogen-free environment (SPF) or housed conventionally (CONV) were prepped for bacterial 16S rRNA DNA libraries. Samples from mice housed in two different cages from two independent experiments for each group were pooled for analysis (SPF; n_{BAL} : 11, $n_{LUNG>BAL}$:10, n_{LUNG} :6, CONV; n_{BAL} : 8, $n_{LUNG>BAL}$:8, n_{LUNG} :11). Empty tubes were processed in parallel (Blank) for evaluation of contamination. **(A)** Mean relative abundance (%) of different taxonomical classes of bacteria in BAL, Lung >BAL, Lung and Blank samples. Color codes for each bacterial class are given next to the graph. Number of animals used for evaluation is indicated on the graph for each group (n). **(B)** Relative abundance (%) of Lactobacillus genus in BAL, Lung >BAL, Lung and Blank samples. Each circle represents an individual mouse. Medians of each group are depicted as gray columns. Mann-Whitney test is applied for statistical analysis (*: in comparison to BAL of SPF mice, #: in comparison to BAL of CONV mice). **(C)** Individual Shannon indices of BAL, Lung >BAL, Lungs, and Blank samples. Each black circle represents an individual mouse. Medians of each group are depicted as columns. Mann-Whitney test is applied for statistical analysis (*: in comparison to BAL of SPF mice, #: in comparison to BAL of CONV mice). **(D)** 2D PCoA plots (UniFrac, weighted) of BAL (red head-down triangles), Lung >BAL (purple circles), Lungs (blue head-left triangles), and blanks (turquoise squares).

The online version of this article includes the following figure supplement(s) for figure 2:

Figure supplement 1. Sensitivity controls for qPCR and 16S rRNA NGS.

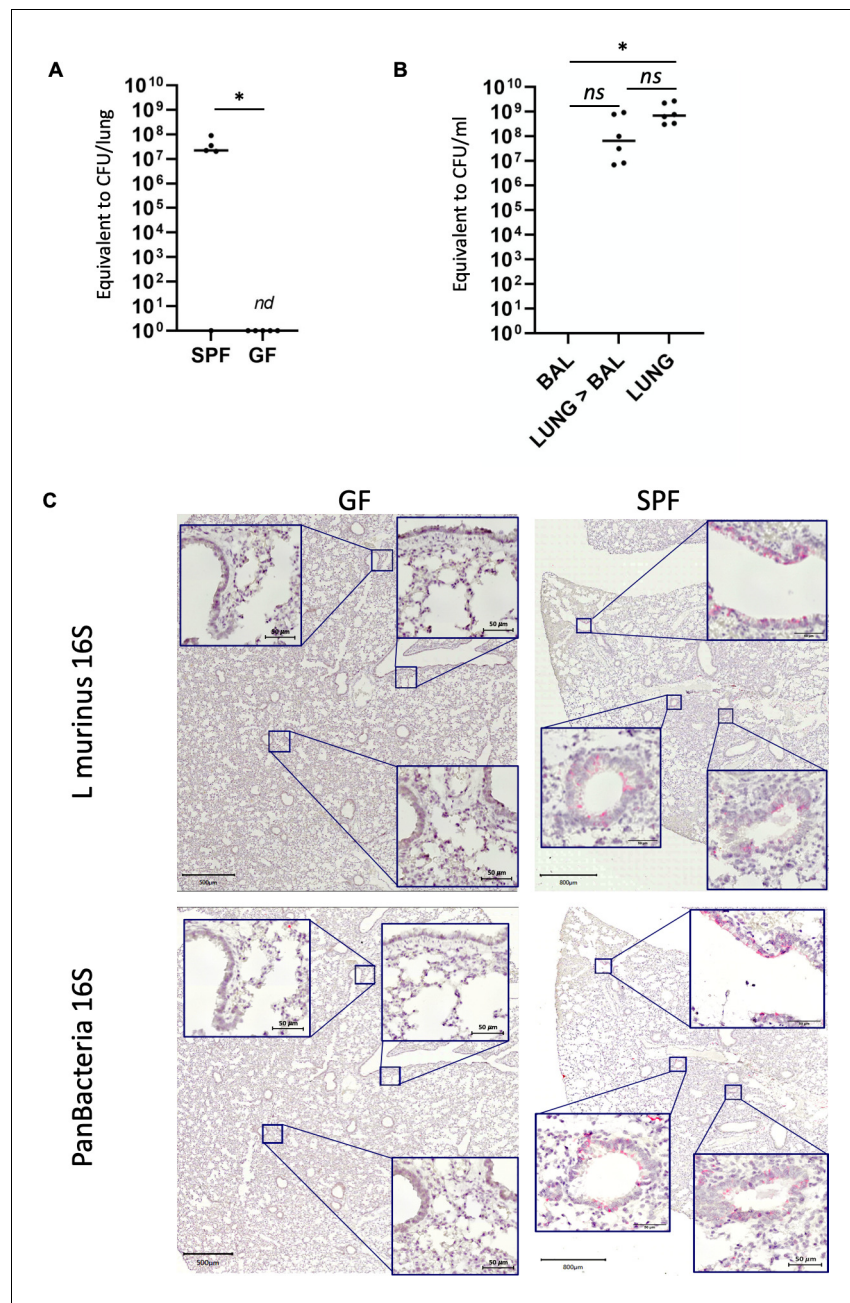


Figure 3. *L. murinus* is tightly associated with the respiratory tissue. (A) *L. murinus*-specific qPCR was used to determine genome copies of *L. murinus* in total lung DNA extracted from SPF mice (n = 5) or germ-free (GF) mice (n = 5). CT values were compared to standard of *L. murinus* genomes (see **Figure 3—figure supplement 3 and 1a**). 1/5 SPF mice and all GF mice revealed no specific amplicon (see also **Figure 3—figure supplement 3 and 1b**). Median value is indicated, each dot represents an individual mouse. (B) *L. murinus*-specific qPCR was used to determine genome copies of *L. murinus* in BALF (n = 11), Lungs after BAL (n = 10) and total lung (n = 6) DNA extracted from SPF mice. CT values were compared to standard of *L. murinus* genomes, median values are indicated (see **Figure 3—figure supplement 3 and 1a**). Kruskal–Wallis test was used to determine statistical significance in multiple comparisons with Dunn’s correction. (C) Tissue distribution of *L. murinus* (upper panels) or total bacteria (lower panels) was determined in consecutive tissue slides of SPF mouse lungs (left panels) or GF mouse lungs (right panels). Bacterial colonization is indicated by a bright red/pink staining. Slides were counter-stained with hematoxylin. Representative sections of n = 5 mice for each group are shown. The online version of this article includes the following figure supplement(s) for figure 3:

Figure supplement 1. Quality controls for *L. murinus* specific qPCR.

bacteria, *E. coli* (EcCM). This *E. coli* strain was previously isolated from the LRT of mice (Yildiz *et al.*, 2018) and characterized by whole genome sequencing. Phylogenetic analysis revealed close relationship with *E. coli* SJ7 (Figure 4—figure supplement 1 and PRJNA591640 and Supplementary file 2). Only LmCM inhibited growth of *S. pneumoniae* cultures that prevented reaching the same optical density, even after prolonged incubation, compared *S. pneumoniae* grown in FM or EcCM supplemented TSB (Figure 4A). This result could be explained by the production of a soluble killing factor by *L. murinus* acting on *S. pneumoniae* and/or the inhibition of *S. pneumoniae* growth and division, without affecting viability. To decipher between the two possibilities, we conducted efficiency of plating assays of serially diluted *S. pneumoniae* cultures grown for 6 hr in FM, LmCM, or EcCM and found a one log in magnitude reduction of viability with LmCM compared to the other conditions, confirming the reduction in bacterial growth (Figure 4B,C). This result suggests a soluble killing activity produced by *L. murinus* that acts on *S. pneumoniae*.

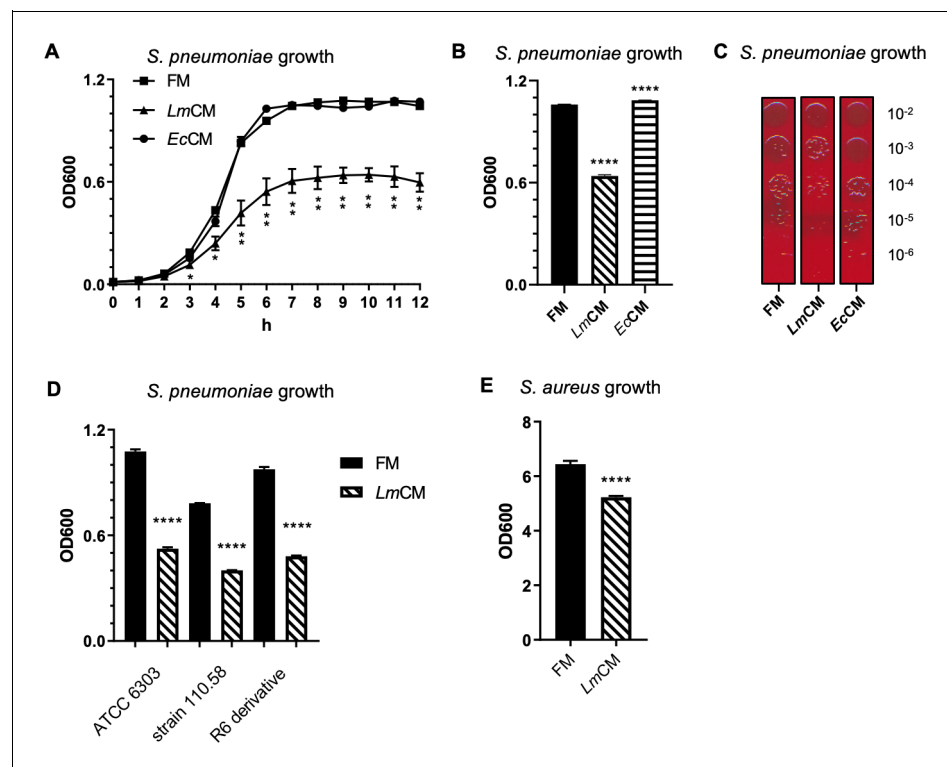


Figure 4. *L. murinus* conditioned media shows inhibitory role against *S. pneumoniae* growth in vitro. (A) *S. pneumoniae* cultures were grown in presence of fresh (FM) or *L. murinus* (LmCM) or *E. coli* (EcCM) conditioned media. Culture growth was followed hourly by optical density at 600 nm (OD600) for 12 hr. Pooled data from two independent experiments are given as mean \pm SD. Student t-test was applied for significance test. (B) *S. pneumoniae* cultures were grown for 6 hr in presence of FM, LmCM, or EcCM. Culture growth was measured by OD600. Representative data from two independent experiments are depicted as mean \pm sd (n = 3). Student t-test was applied for significance test in comparison to fresh media treated group. (C) Following incubation in presence of FM, LmCM, or EcCM for 6 hr (note, the same OD was taken for the efficiency of plating at the 6 hr time point), *S. pneumoniae* cultures are serially diluted and growth on fresh TSB agar plate with 5% sheep blood for 24 hr. Representative images are shown. (D) Different *S. pneumoniae* strains, that is the virulent encapsulated strain (ATCC6303), non-encapsulated clinical isolate (110.58) and a derivative of the non-encapsulated avirulent lab strain R6 (R-6 derivative), or (E) *Staphylococcus aureus* (USA300) cultures were grown in presence of FM, LmCM, or EcCM for 6 hr. Culture growth was measured by OD600. Representative data from two independent experiments are depicted as mean \pm SD. Student t-test was applied for significance test in comparison to fresh media group of each bacterial strain.

The online version of this article includes the following figure supplement(s) for figure 4:

Figure supplement 1. Phylogenetic tree of *E. coli* isolate to regular lab strains and other environmental isolates.

Next, we asked whether growth inhibition by *LmCM* exhibits strain-specific differences on *S. pneumoniae*. To this end, we tested the activity of *LmCM* on two additional strains of *S. pneumoniae*, i.e. the non-encapsulated clinical isolate (110.58) and a derivative of the non-encapsulated avirulent lab strain R6. Our results indicate that inhibition of *S. pneumoniae* by *LmCM* is strain independent and is not affected by capsule formation since both strains displayed similar sensitivity to *LmCM* as the virulent encapsulated strain (ATCC6303) (**Figure 4B–D**). Since a wide range of bacterial pathogens causes bacterial pneumonia, we wondered if the inhibition by *LmCM* is specific to *S. pneumoniae*. *Staphylococcus aureus*, another Gram -positive bacterium, is a highly prevalence pathobiont, colonizing the upper respiratory tract of ~30% of the human population and frequently leading to bacterial pneumonia (**Wertheim et al., 2005**). Despite the much faster in vitro growth rate, *LmCM* reduced optical density of *S. aureus* cultures (**Figure 4E**), implicating a broader acting mechanism against at least two distinct pathogenic bacteria.

Encapsulated *S. pneumoniae* forms linear chains in vitro and in vivo. Formation of chains was previously associated with tissue adhesion and pathogenicity in vivo (**Rodriguez et al., 2012**). We observed a significant decrease in median chain length of *S. pneumoniae* when grown in the presence of *LmCM* (**Figure 5A/B**). *EcCM*, however, did not affect *S. pneumoniae* growth and/or chain length. In order to narrow down the nature of the soluble inhibitor of *S. pneumoniae* growth, we first treated the *LmCM* with Proteinase K. This treatment had no effect on its *S. pneumoniae* growth inhibition (**Figure 5—figure supplement 1**), excluding e.g. the action of bacteriocins. Our results suggested the active compound affecting *S. pneumoniae* growth in vitro could be a small bacterial metabolite.

Secreted lactic acid is responsible for antibacterial effect of *L. murinus*

We first decided to identify metabolites specifically upregulated in *LmCM* as compared to control (Fresh media, FM) or *EcCM* with an untargeted multiplatform high-resolution mass spectrometry (HRMS) approach. 174 metabolite features that are at least 10-fold enriched in *LmCM* over in FM and not upregulated in *EcCM* (**Figure 5—figure supplement 1**) were detected. Two of these peaks were unambiguously identified by comparison to reference chemical standards: D-Glucosamine-6-phosphate and uridine-diphosphate-glucose. However, exposure of *S. pneumoniae* to these metabolites in concentrations up to 10 mM did not affect bacterial growth (**Figure 5—figure supplement**

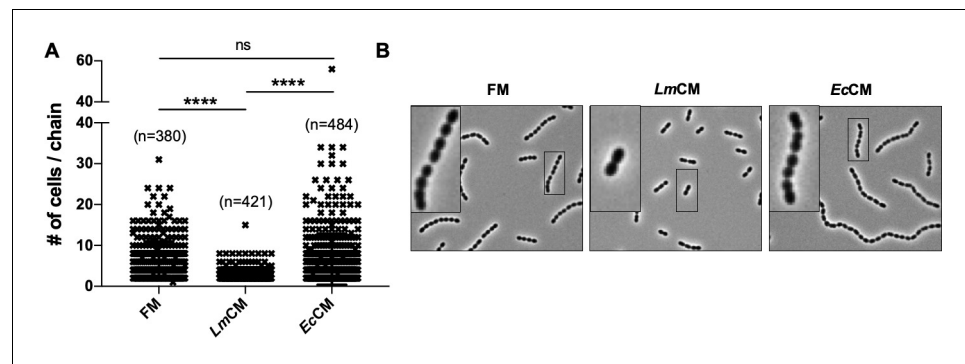


Figure 5. *LmCM* limits cellular chain length of *S. pneumoniae* cultures. *S. pneumoniae* cultures were grown to 0.6 OD₆₀₀ in presence of FM, *LmCM* or *EcCM*. Cellular chain lengths of bacterial cultures are quantified using light microscopy. Each symbol represents an individual multicellular *S. pneumoniae* chain. Data was pooled from three independent experiments. Number of chains evaluated for each group indicated on the graph (n). Student t-test is applied for statistical analysis. Representative images are shown.

The online version of this article includes the following figure supplement(s) for figure 5:

Figure supplement 1. Active substance in *LmCM* causing growth inhibition on *S. pneumoniae* is not protein in nature.

Figure supplement 2. Mass spectrometry identified hits from *LmCM* do not cause similar growth inhibition on *S. pneumoniae* cultures.

Figure supplement 3. *LmCM* dependent suppression of *S. pneumoniae* growth does not rely on reactive oxygen species.

2), making it unlikely that any of these putative *L. murinus* metabolites are responsible for the observed inhibition of *S. pneumoniae* growth. The chosen HRMS approach would not allow us to detect very low molecular weight metabolites such as reactive oxygen species or lactic acid, which were both previously described as metabolites produced by Lactobacillaceae with potential antibacterial action (Nardi et al., 2005). Some Lactobacillus species were previously reported to produce high levels of H₂O₂ when grown in presence of oxygen (Hertzberger et al., 2014; Kang et al., 2013; Marty-Teyssset et al., 2000). However, supernatants of *L. murinus* grown in hypoxia showed similar levels of growth inhibition (Figure 5—figure supplement 3A). Moreover, catalase treatment did not affect the growth arrest on *S. pneumoniae* seen with LmCM, while it completely abolished the effect of H₂O₂ (Figure 5—figure supplement 3B). These results excluded reactive oxygen species from the candidate list of active metabolites in LmCM.

Of note, LmCM had a pH of 4.5 (Figure 6A). We observed a full recovery of *S. pneumoniae* growth, when the LCM was pH neutralized with NaOH (Figure 6B). We thus speculated that indeed

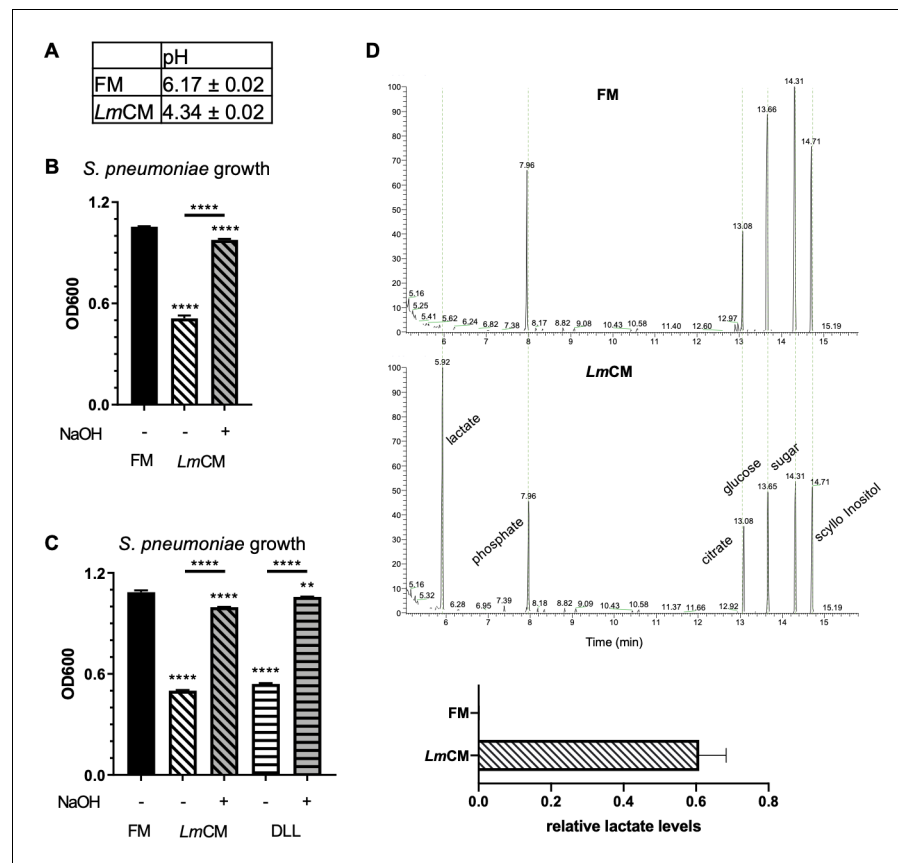


Figure 6. Lactic acid suppresses growth of *S. pneumoniae*. Lactic acid present in LmCM is responsible for growth inhibition in *S. pneumoniae* cultures. (A) pH measurements of fresh (FM) or *L. murinus* conditioned (LmCM) media. Data is pooled from three independent experiments and depicted as mean ± SD (n = 3). (B) *S. pneumoniae* cultures were grown for 6 hr in presence of FM, LmCM or pH adjusted LmCM (pH:~6.2, NaOH). Culture growth was measured by OD600. Representative data from two independent experiments are depicted as mean ± SD (n = 3). Student t-test was applied for significance test in comparison to fresh media treated group unless otherwise stated by the arrows. (C) Representative GC-MS total ion chromatograms of FM (dashed blue line) and LmCM (straight red line) are shown. Concentrations of Lactate in each media, calculated based on a standard curve acquired using DL-Lactic acid, depicted in the graph (Mean ± SD, n = 3). Student t-test was applied for significance test. (D) *S. pneumoniae* cultures were grown for 6 hr in presence of FM, LmCM, DL-Lactic acid (DLL, 100 mM) or pH adjusted LmCM (pH:~6.2, NaOH) and pH adjusted DLL (pH:~6.2, NaOH). Culture growth was measured by OD600. Representative data from two independent experiments are depicted as mean ± SD (n = 3). Student t-test was applied for significance test in comparison to fresh media treated group unless otherwise stated by the arrows.

lactic acid might be the compound responsible for the antimicrobial action of *LmCM*. An involvement of lactic acid would be in accordance with the rescue of *S. pneumoniae* growth after pH neutralization we observed earlier (**Figure 6A/B**). Indeed, quantification of lactic acid in *LmCM* by GC/MS revealed concentrations of approximately 100 μM (**Figure 6C**). In order to test if these concentrations are sufficient to explain the antibacterial effect of *LmCM*, we grew *S. pneumoniae* for 6 hr in TSB complemented with 100 μM DL-lactic acid. Indeed, we observed inhibition of *S. pneumoniae* growth at comparable levels to *LmCM* (**Figure 6D**), sustained over 24 hr (data not shown). These results suggest that lactic acid is the primary metabolite in *LmCM* causing growth arrest on *S. pneumoniae*.

The second phenotype induced by *LmCM*, the reduction of median chain length of *S. pneumoniae* cultures (see **Figure 4a**), was not affected by presence of lactic acid (**Figure 7A**). Accordingly, pH neutralization did not restore chain length (**Figure 7B**). This implies that the effect of lactic acid on *S. pneumoniae* growth in vitro is independent of the previously observed inhibition of chain length. In order to characterize the nature of the compound responsible for inhibition of chain extension we repeated the treatment of *LmCM* with protease K. Proteinase K completely abolished the reduced chain extension (**Figure 7C**), suggesting a secreted protein or peptide could be responsible for disrupting or preventing chain formation.

Probiotic treatment with *L. murinus* reduces outgrowth of *S. pneumoniae* in vivo

In order to provide evidence that lung resident *L. murinus* does indeed provide colonization resistance against respiratory bacterial pathogens we inoculated germ-free (GF) mice and colonized SPF mice with either sterile PBS or 10^5 cfu *L. murinus* and challenged them 72 hr later with 10^3 *S. pneumoniae* (ATCC 6303). 24 hr later we measured *S. pneumoniae* titers in total lung homogenates. To our great surprise we did not find increased susceptibility of GF mice to *S. pneumoniae* infection over colonized SPF mice (**Figure 8A**). In fact, GF mice were resistant to colonization, largely independent of *L. murinus* pretreatment. Resistance did not correlate with significantly lowered lung pH (**Figure 8B**). In colonized SPF mice, the pretreatment with *L. murinus* had a small but statistically non-significant effect on *S. pneumoniae* colonization (**Figure 8A**), which is likely due to the already present population of respiratory commensal *L. murinus*. Of note, *L. murinus* instillation did not alter body weight of the mice, which indicates no adverse effects by this probiotic treatment.

We thus decided to choose an alternative more realistic model, in which mice become more susceptible to *S. pneumoniae* colonization. Even in SPF mice, the colonization of the respiratory tract with low doses of *S. pneumoniae* is quite inefficient. This natural colonization threshold can be lowered by previous, sub-lethal IAV infection (**Figure 8B**), modeling the frequently observed secondary bacterial pneumonia in human IAV patients (**Morris et al., 2017**). In order to address if *L. murinus* could overcome the IAV mediated sensitization toward *S. pneumoniae* colonization, we established a respiratory probiotics treatment protocol (**Figure 8C**, probiotics treatment indicated by black arrow). When inoculating IAV infected mice on day 7-post infection (after onset of clinical signs of IAV infection) with *L. murinus* via the intranasal route, we observed a significant reduction BALF pH and diminished pneumococcal colonization on day 11-post IAV infection (24 hr post secondary *S. pneumoniae* challenge) (**Figure 8C/D**). Lactic acid levels in BALF of these mice were not changed compared to IAV infected and mock colonized controls (**Figure 8—figure supplement 1A**). We can currently not rule out that lactic acid is quickly taken up by the surrounding tissue or commensal bacteria. Importantly, treatment with *L. murinus* did not influence the overall pathology of IAV infection as indicated by similar weight loss in both experimental groups (**Figure 8—figure supplement 1C**). Lactobacilli were previously shown to modulate inflammatory signaling. An involvement of the innate host protein response was ruled out by specific qPCR for key cytokines involved in antibacterial signaling (**Figure 8—figure supplement 1B**). IAV infected mice showed a robust inflammatory response in their lungs on D10 post infection, which was non-significantly impacted by administration of *L. murinus*. Finally we tested by 16S rRNA gene-specific NGS, if *L. murinus* colonization of the lungs would alter the resident lung microbiota. Indeed, we found a mild increase in Bacilli in SPF mice colonized with *L. murinus* and a homogenous reduction of the remaining bacterial classes (**Figure 8—figure supplement 1C**). The overall composition of lung microbiota was however indistinguishable as indicated by largely overlapping clouds in the PCoA (**Figure 8—figure supplement**

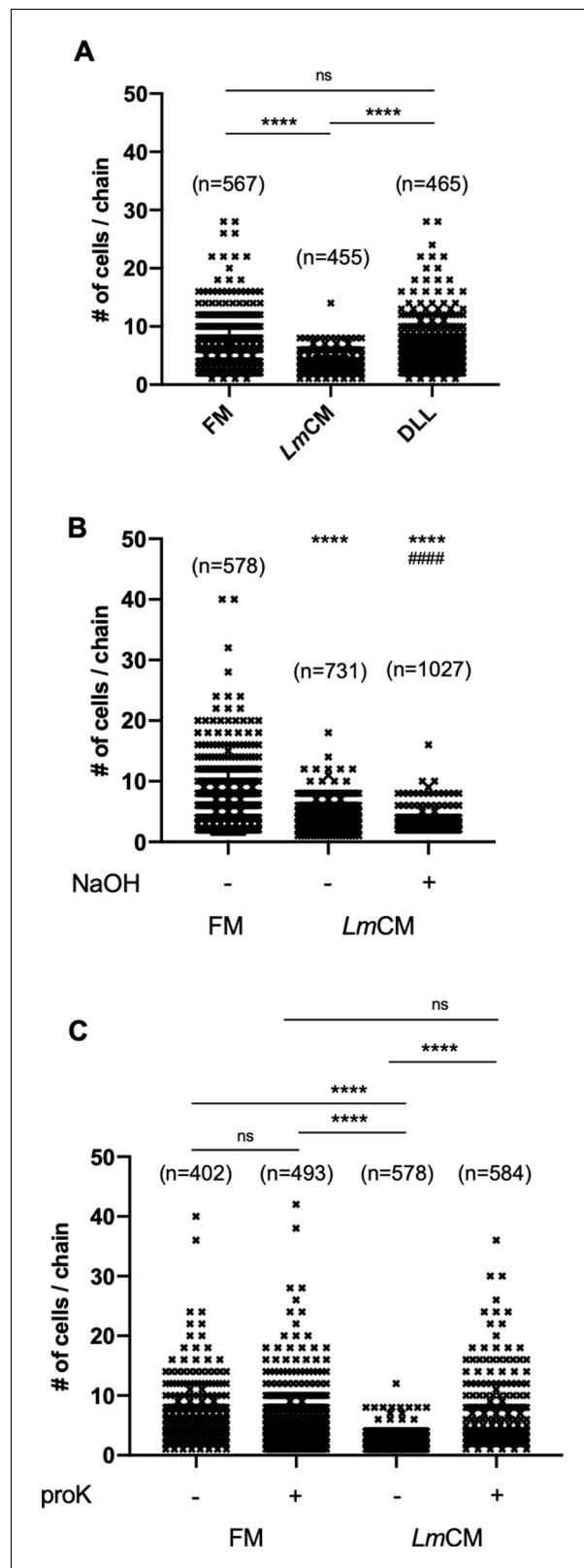


Figure 7. *L. murinus* secreted substance of protein origin is the cause of decrease in cellular chain length of *S. pneumoniae* cultures. *S. pneumoniae* cultures were grown to 0.6 OD₆₀₀ in presence of (A) FM, LmCM or DL-Lactic acid (DLL, ~100 mM), (B) FM, LmCM or pH adjusted LmCM (pH: ~6.2, NaOH) and (C) mock or proteinase K (proK) treated FM and LmCM. Cellular chain lengths of bacterial cultures are quantified using light microscopy. Each Figure 7 continued on next page

Figure 7 continued

symbol represents an individual multicellular *S. pneumoniae* chain. Data was pooled from three independent experiments. Number of chains evaluated for each group indicated on the graph (n). Student t-test is applied for statistical analysis.

1D). These data indicate that *L. murinus* could be a safe and directly acting antibacterial probiotic candidate for the respiratory tract.

Discussion

The benefit of bacterial colonization of mucosal surfaces has been the center of attention of numerous scientific studies in recent years, ranging from nutritional science, to immunology and even behavioral studies. Most studies focus on the highly colonized digestive tract, where exposure of various immune cell types results in peripheral education of adaptive immune cells and fine-tuning of immune responses. Beyond these indirect effects, bacterial microbiota is posing a direct competitive threshold to colonization or outgrowth of pathogenic bacteria on barrier tissues.

Gnotobiotic animals, with an increased resistance to bacterial colonization, were first introduced in the mid-1960s by Russel W. Schaedler. This original Schaedler flora was later revised and became the ASF. Since the 1980s, all major commercial vendors provided mice for barrier facilities by colonizing germ-free animals with this standardized mix of eight bacterial strains. There are however numerous reports on vendor-specific variations in the commensal microbiota ([Ericsson et al., 2015](#); [Guo et al., 2019](#); [Ivanov et al., 2009](#); [Ivanov et al., 2008](#)). Nevertheless, we believe our results are of importance for researchers working on lung physiology or pathology in commercially acquired mouse models.

In laboratory mice, *L. murinus*, as part of the ASF, was reported to colonize the intestine ([Almirón et al., 2013](#); [Hemme et al., 1980](#)), the oral cavity ([Blais and Lavoie, 1990](#); [Rodrigue et al., 1993](#)) and the vaginal tract ([Jerse et al., 2002](#)). In the lower respiratory tract *L. murinus* was to our best knowledge not reported as a dominant species, however Lactobacilli were previously found in high number in lung tissue microbiome ([Singh et al., 2017](#); [Zhang et al., 2018](#)). Our data implicate that the sampling technique is critical for the adequate quantification of this species in the lung, since they might have a tight association with the host tissue. A previous comparison of BALF (+ or - cells) with lung tissue (from the distal tips of the lung) revealed enrichment of Firmicutes in tissue ([Barfod et al., 2013](#)), independently confirming our observation. Even within BAL samples of human patients, it was previously reported that a substantial proportion of commensal bacteria is tightly associated with cells and thus easily lost during removal of these cells ([Dickson et al., 2014](#)). From conventionally housed mice in our own facility, we know that Lactobacilli are still overall dominant in the lung tissue microbiome after two weeks of open cage housing.

Lactobacilli display a number of antimicrobial and immune modulatory activities. Depending on the ecological niche and the Lactobacillus strain investigated, diverse phenotypes have been observed: Colonization of GF mice with Lactobacillus spp. was proposed to increased alveoli numbers per μm^2 and to enhanced mucus production after 16 weeks ([Yun et al., 2014](#)), comparable to non-SPF mice, albeit this was not independently confirmed by others. Intranasal application of *L. rhamnosus* GG or *L. paracasei* one reduces IL-5 and eotaxin production in the lung ([Pellaton et al., 2012](#)). Intranasal application of *L. rhamnosus* GG was recently shown to suppress allergic responses in mouse models ([Spacova et al., 2019](#)). Colonization with *L. murinus* H12 was recently described to protect neonatal rats from necrotizing enterocolitis ([Isani et al., 2018](#)).

Direct antibacterial effects were also previously reported. Lactobacilli produce antimicrobial peptides such as bacteriocins ([Elayaraja et al., 2014](#)) and metabolites that are antibacterial in nature such as reactive oxygen species and lactic acid ([Nardi et al., 2005](#)). Our data imply a direct function for lactic acid in the antagonism of pneumococcus growth. Lactic acid was shown to inhibit growth of various bacterial pathogens; *E. coli*, *S. enterica* Typhimurium serovar, *L. monocytogenes* ([De Keersmaecker et al., 2006](#); [Wang et al., 2015](#)). This action is assigned to two mechanisms: (1) its capacity to penetrate cytoplasmic membranes in its non-dissociated form, which results in lowered cytoplasmic pH and disruption of the proton gradient across the cytoplasmic membrane ([Alakomi et al., 2000](#)); 2) its capacity to permeabilize the cytoplasmic membrane, which was

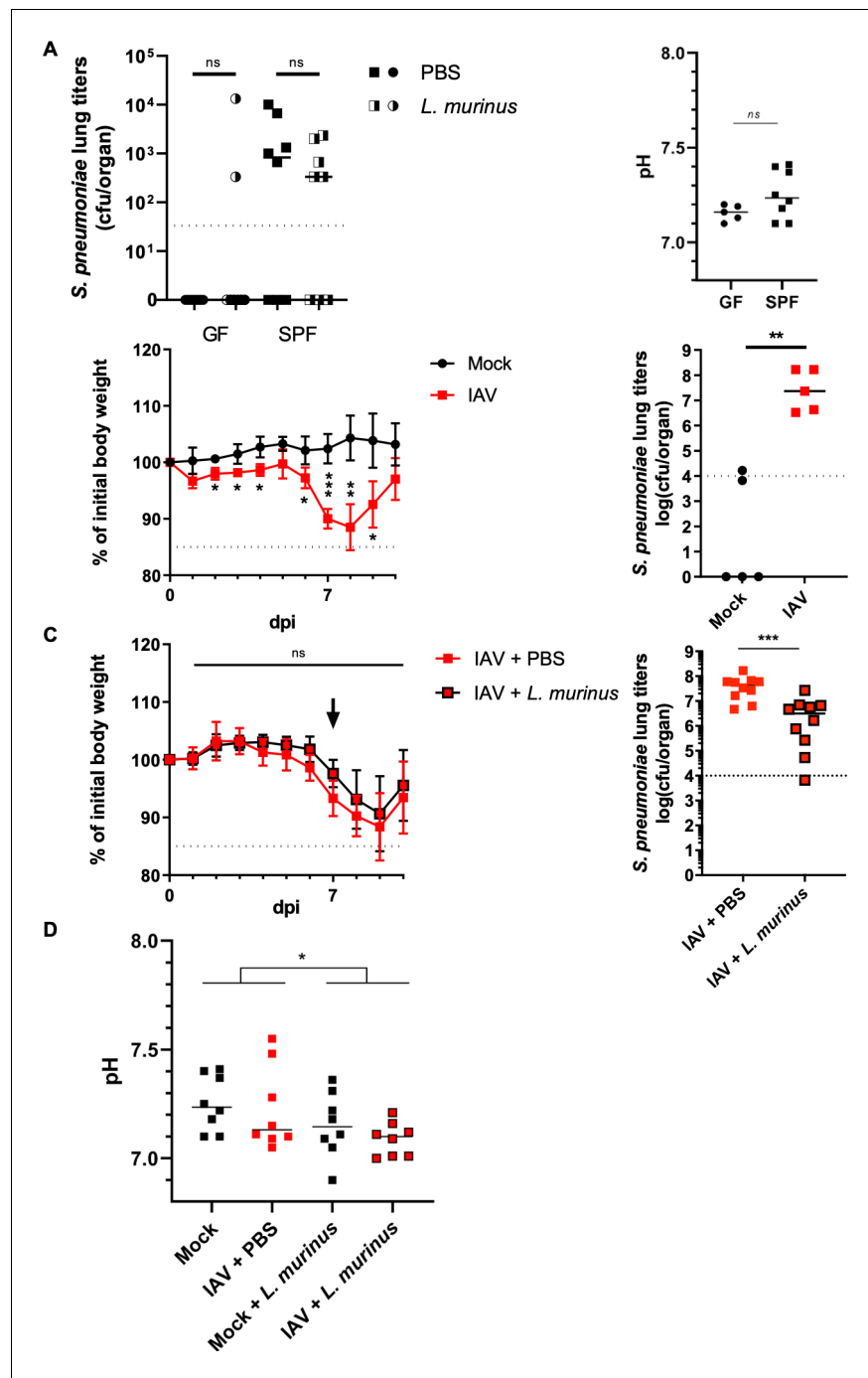


Figure 8. Therapeutic administration of *L. murinus* decreases *S. pneumoniae* titers in the lung of IAV infected mice. (A) Germ-free (GF) or specific pathogen-free (SPF) mice were intranasally administered with PBS or *L. murinus* (~10⁵ cfu/animal). Three days post-administration, mice were challenged with *S. pneumoniae* (~1500 cfu/animal). *S. pneumoniae* lung titers (cfu/organ) of *L. murinus* (half black/half white) or PBS (plain black) administered GF (circles) or SPF (squares) are quantified 24 hr post infection (n = 10). Medians are depicted by a black line for each group. Pooled data from two independent experiments are shown. BALF pH does not significantly differ between colonized and GF mice (right panel). Median pH values for indicated mice are shown. Each dot represents one animal. Mann-Whitney test is applied for statistical analysis. (B) Average relative initial body weight (%± SD) is depicted for mock treated (black line with circles) and IAV infected (red line with squares) mice (n = 5). Mice were challenged with *S. pneumoniae* (~1500 cfu/animal) 10 days post IAV infection. *S. pneumoniae* lung titers (cfu/organ) of mock treated (black circles) or IAV infected (red squares) are quantified 24 hr post infection (n = 5). Medians are depicted by a black line for each group. Student t-test was applied for significance test. (C) All mice

Figure 8 continued on next page

Figure 8 continued

are infected with IAV (40 pfu). Seven days post IAV infection, PBS (red line with red squares) or *L. murinus* ($\sim 10^5$ cfu/animal, black line with red squares) is intranasally administered to the animals. Average relative initial body weight (%) \pm SD is depicted for both group ($n = 10$). Mice were challenged with *S. pneumoniae* (~ 1500 cfu/animal) 10 days post IAV challenge. *S. pneumoniae* lung titers (cfu/organ) of IAV infected, PBS (red squares) or *L. murinus* administered (black rounded red squares) are quantified 24 hr post infection ($n = 10$). Medians are depicted by a black line for each group. Pooled data from two independent experiments are shown. Student t-test was applied for significance test. (D) pH of BALF from mock treated or *L. murinus* colonized mice 3 days post colonization and 10 days post IAV vaccination ($n = 7$ –8 animals/group).

The online version of this article includes the following figure supplement(s) for figure 8:

Figure supplement 1. Probiotic treatment with *L. murinus* does not alter lactic acid levels, inflammatory response or composition of commensal lung bacteria.

proposed to increase in turn the sensitivity of lactic acid exposed bacteria (mainly gram-negative) to other antimicrobial compounds (Alakomi et al., 2000). Lactic acid levels were however not changed in vivo after exogenous application of *L. murinus*. We can thus not rule out that lactate independent mechanisms, e.g. the in vitro observed reduction of *S. pneumoniae* chain length, come into play in vivo. Additionally, we found a protease sensitive reduction of chain extension. It is currently unclear if both phenotypes contribute to the in vivo colonization defect of *S. pneumoniae* after probiotics treatment with *L. murinus*. The antibacterial activity was not limited to *S. pneumoniae* but also affected *S. aureus*. Published reports indicate a broad antibacterial activity of *L. murinus* (Bilkova et al., 2011; Perelmuter et al., 2008). In our study the repressing effects on fast growing *S. aureus* were mild but evident. The antimicrobial effect of *L. murinus* on *S. aureus* growth depends on low pH as well (Bilkova et al., 2011).

Notably we found that germ-free mice were more difficult to colonize with *S. pneumoniae*. This appears as a contradiction to the hypothesis that lung microbiota poses a colonization barrier toward invading bacterial pathogens. An explanation to this dilemma could be that *S. pneumoniae* colonization requires yet unknown anatomical conditions induced by commensal lung microbiota. Future tests in antibiotic treated mice might resolve this phenomenon.

The majority of human lung microbiota studies rely on aspirates or endoscopic brushes. In a recent tissue-biopsy based human lung microbiota study (Yu et al., 2016), Firmicutes were found in all regions of the respiratory tract, albeit not to the same extent as shown here in SPF mice. We can moreover not rule out that other bacteria might produce lactic acid in the lung of humans to prevent colonization. One of the most prevalent KEGG pathways retrieved from the human tissue microbiome was carbohydrate metabolism (Yu et al., 2016), which includes the pathway involved in lactic acid generation. Under chronic inflammatory conditions as found in IPF patients, lactic acid levels in lungs are elevated albeit the source of this lactate could not be determined (Kottmann et al., 2012). In cystic fibrosis patients, neutrophils were identified as a source for lactic acid in sputum (Bensel et al., 2011). The contribution of commensal respiratory tract bacteria and host cells to anti-bacterial lactate production in healthy humans remains to be addressed.

Finally, we demonstrated here that lung resident commensals might be applicable as probiotics to counteract lung colonization by pathogenic bacteria, without major effects on lung commensals. In contrast to other *Lactobacillus* species (Ding et al., 2017) *L. murinus* is not immunogenic when administered orally in mice (Östberg et al., 2018). This was also confirmed here by overall similar levels of cytokine mRNAs involved in antibacterial signaling. However, it remains currently unclear through which mechanism IAV might weaken the commensal shield against colonization, or if the here demonstrated effect of probiotics treatment is solely based on alterations of the host immune response. Nevertheless, in the context of a lung environment prone to bacterial colonization, e.g. as we induced by IAV infection, this treatment could reduce the risk of superinfection or improve the clinical outcome. This is of special interest in elderly human patients with high susceptibility to respiratory tract infections and reduced lung microbiome complexity (Kovacs et al., 2017).

Conclusions

Lung tissue-associated microbiota of mice differ substantially from BALF microbiota, in containing large proportions of *L. murinus*. Future studies on respiratory microbiota should take this into

account. Under dysbiotic conditions, intranasal instillation of *L. murinus* decreases the burden of *S. pneumoniae* colonization. In light of the ongoing antibiotic resistance crisis, probiotic treatment of bacterial lung infection might offer therapeutic alternatives.

Materials and methods

Animal experiments

Power analysis (G*power 3.1) was used to estimate group size for mouse experiments was performed based on experimental variation obtained in a previous study aiming for a power of 0.95 (Yildiz *et al.*, 2018).

C57BL/6J mice (female, 7–8 weeks of age) were purchased from Charles River Laboratories (France) and housed under SPF/BSL2 conditions or under conventional non-SPF conditions with open cages. All animals were housed for 7 days to adjust to housing conditions under a strict 12 hr light/dark cycle and fed ad libitum. Conventionally housed animals were kept in open cages 14 days before experiments. germ-free animals with C57BL/6J background were generated by the Clean Mouse Facility of Department of Biomedical Research of the University of Bern. They were born and raised in flexible film isolators in the at University of Bern, transferred aseptically into sterile IVC cages provided with sterile food and water and kept in the BSL2 unit of the animal facility of the Centre Medical Universitaire, Geneva for the duration of the experiments. For inoculation with IAV, *S. pneumoniae* or *L. murinus*, mice were injected intraperitoneally with a mix of ketamine/xylazine (100 mg/kg and 5 mg/kg, respectively) in 200 μ l of sterile PBS. Upon reaching deep anesthesia, mice were inoculated with 40 μ l of PBS, virus or bacterial suspension via the intranasal route.

Body weights were measured daily during the light phase. Upon reaching experimental or humane endpoints (85% of initial body weight), animals were euthanized using controlled CO₂ exposure. Broncho alveolar lavages (BAL) or lungs were sampled immediately after euthanasia using sterile tools. BAL sampling was performed as previously described (Sun *et al.*, 2017) with some modifications. Briefly, mice were sacrificed by controlled CO₂ inhalation and fixed with needles to a Styrofoam panel. The skin from abdomen to neck was cut open to expose thoracic cage and neck. With a second set of sterile tools soft tissue around the neck was gently removed. Using forceps, approximately 10 cm sterile sewing thread was placed underneath the trachea. With sterile scissors the trachea was nicked and a 22G \times 1' Exel Safelet Catheter was inserted no more than 0.5 cm. The inner cannula was removed and the catheter was tied to trachea with a double knot in the sewing thread. 1 ml of PBS, or saline (0.9%) in experiments for pH or lactate measurements, was slowly introduced into the lung through the catheter with a 1 ml syringe, incubated for 10 s and aspirated back to the syringe. This procedure was repeated two more times, using a new sterile syringe in every step. Retrieved liquid was collected in a screw cap tube. Tools were changed in between organs and experimental groups to avoid cross contamination. BAL or lung samples were immediately stored at -80°C until extraction of DNA.

In situ hybridization

Lungs were collected under sterile conditions from five SPF and five germ-free C57BL/6J mice, fixed in paraformaldehyde 4% solution and embedded in paraffin and sliced at two different depth levels (51 μ M and 101 μ M), using a standard microtome (1 μ M thickness).

In situ detection of *L. murinus* 16S rRNA was performed using the RNAscope 2.5 HD Assay - RED (Advanced Cell Diagnostics) according to the manufacturer's protocol. Briefly, lung slides were deparaffinized by submerging the slides four rounds in 100% xylol and subsequently four rounds in 96% ethanol solutions. Slides were dried at 60°C. An incubation with hydrogen peroxide was performed for 10 min and target retrieval was achieved by incubating the slides with RNAscope 1x Target Retrieval Reagent for 45 min at 95°C. Tissue was permeabilized using RNAscope protease plus (Advanced Cell Diagnostics). Probe hybridization was performed with a specific RNA probe for the 16S rRNA of *L. murinus* or 16S rRNA Panbacteria (#475131 or #451961 Advanced Cell Diagnostics) for 2 hr at 40°C. Signal amplification was achieved by incubating the tissues at 40°C with AMP solutions provided by the kit and a final Fast Red dye incubation for 10 min. Slides were counter-stained with hematoxylin and EcoMount solution was added to preserve the coloration. Slides were visualized under Olympus VS120 brightfield microscope (Zeiss) under a 100x/1.4 Oil objective and

processed using QuPath-0.2.1 Software. Random fields were picked from each slide and evaluated at 100x magnification. An average of 5–8 fields per sample were analyzed and positive staining was determined by red/pink punctate dots around epithelial cells of large airways.

Bacteria

L. murinus and *Escherichia coli* isolates were grown from serially diluted lung homogenates on Columbia agar + 5% sheep blood plates (bioMerieux, France) at 37°C under aerobic conditions. *L. murinus* was cultured in vitro at 37°C with 5% CO₂ in static liquid broth or solid plates of MRS media (bioMerieux, France), prepared according to manufacturer's instructions. *E. coli* was grown in standard LB broth with agitation (250 rpm) or on LB plates, with antibiotic where indicated, at 37°C, except for conditioned media experiments where MRS media instead of LB were used in the same incubation settings. For experiments using *L. murinus* conditioned media (LmCM) and *E. coli* conditioned media (EcCM), overnight cultures were adjusted to 0.1 optical density at OD600 nm in MRS media. To grow *L. murinus* anaerobically, cultures were prepared as described above except in air-sealed plastic containers containing atmosphere generator, GenBox Anaer (bioMerieux, France). After 8 hr of incubation, bacteria were pelleted by centrifugation at 4000 x g at 4°C for 10 min. Supernatants were filtered through a 0.22 µm PVDF syringe-top filters (Merck Millipore, Ireland). Similarly processed fresh MRS media (FM) used as a negative control. *Streptococcus pneumoniae* strains, i.e. antigenic type 3 (ATCC-6303, LGC, Germany), Swiss non-encapsulated nasopharyngeal pneumococcal isolate 110.58 (MLST 344) and R6-derivative strain, were cultivated on Trypticase soy agar plates (bioMerieux, France) with 5% sheep blood (bioMerieux, France) at 37°C with 5% CO₂. Liquid cultures were grown directly from frozen stocks in Trypticase soy broth (bioMerieux, France) at 37°C with 5% CO₂ in static culture up to 0.5 optical density (OD600 nm). Then, cultures were diluted in Trypticase soy broth (bioMerieux, France) to 0.01 OD600, mixed with FM, LmCM, or EcCM in 1:10 ratio and incubated for 6 hr until experimental end point unless otherwise stated. Hydrogen peroxide (H₂O₂), UDP-glucose, glucosamine 6 P and DL-Lactic acid were purchased from Sigma-Aldrich (Switzerland). They were diluted in water or MRS media to desired concentration and used in same experimental setting as described above. *S. aureus* USA300 strain was a kind gift from the lab of Dr. William Kelly, University of Geneva, Switzerland. *S. aureus* cultures were grown and used in experiments in Trypticase soy broth (bioMerieux, France) at 37°C with agitation (250 rpm). For administration of *L. murinus* to mice, overnight cultures were diluted in fresh media (1:200) incubated in conditions aforementioned for 4 hr. Then, bacteria were pelleted down, washed once with PBS and diluted to ~10⁵ cfu/animal in PBS prior to administration. *S. pneumoniae* inoculation was performed as previously described (Yildiz et al., 2018).

Microscopy

Following incubation with fresh media, conditioned media or chemicals where indicated, *S. pneumoniae* cultures at optical density of 0.6 (OD600 nm) were installed on thin layer 1% pure agarose pads mounted on microscope slides. Alpha Plan-Apochromatic x 100/1.46 Ph3 (UV) VIS-IR oil objective on an Axio Imager M2 microscope (Zeiss) was used to visualize bacteria. A total number of 24–30 images of the samples were taken in triplicates; and representative images are shown. Number of individual cells per pneumococcal chain were counted to quantify the chain length.

Bacteria DNA extraction, library construction, and bioinformatics analysis

Total lung, from lower trachea downward, and BAL samples were collected as described above. DNA extraction was performed using QIAGEN Pathogen Cador Mini kit (USA) according to manufacturer's protocol with slight modifications. Briefly, whole organ samples were homogenized with ¼" stainless steel grinding balls (MPBio, USA) or a QIAGEN Pathogen Cador Mini kit (USA) according to manufacturer's protocol using matched blanks in 1 ml PBS, containing 15 µl Proteinase K supplied with the kit, using a Bead Blaster 24 (Benchmark Scientific, USA) with a speed setting of 6 m/s for 30' and 30' break, repeated 10 times. Then, together with BAL samples containing same amount of Proteinase K, all samples were incubated at 56°C for 30'. 200 µl of homogenates were used for further DNA extraction steps following the kits' guidelines with pre-treatment T3 and B1. Empty sample tubes that are underwent the whole respective extraction procedure are used to evaluate to

measure potential cross contamination during PCR. Libraries for bacterial composition analysis of total lungs and BALs were performed as previously described (Yildiz *et al.*, 2018). With exception to **Figure 8—figure supplement 1** QIIME was used for bioinformatics analysis of the sequences generated through Illumina (USA) sequencing through the pipeline previously described (Aronesty, 2013; Caporaso *et al.*, 2010a; Caporaso *et al.*, 2010b; Chao, 1984; Colwell *et al.*, 2012; DeSantis *et al.*, 2006; Lozupone and Knight, 2005; Shannon, 1984; Wang *et al.*, 2007; Yildiz *et al.*, 2018). For **Figure 8—figure supplement 1** we used QIIME2 for bioinformatics analysis of the sequences generated through Illumina (USA) sequencing through the following pipeline (Bolyen *et al.*, 2019). Samples were demultiplexed and trimmed to remove adapters, primers and primer links using *cutadapt*. Subsequently, pair ends were joined using *vsearch* with the default parameters and denoised using *deblur* with a 250nt length limit. A table was generated containing the features for each sample and was further filtered to keep samples containing features with a frequency higher than 1140 using *feature-table*.

Taxonomy attribution for each feature was performed using a Naive Bayes classifier trained on the Greengenes_13_5 database at a 97% identity level with the primer sequences of the V4 rRNA 16S region. A relative frequency table was generated and bar plots were constructed by taking the mean ceiling of each group's taxa attribution at the class level. Beta-diversity was determined with Principal of Coordinates analysis by the weighted UniFrac method using *diversity core-metrics-phylogenetic* with a level of depth set to 500 on a rooted phylogenetic tree constructed with *phylogeny align-to-tree-mafft-fasttree*. 2D plots were constructed in emperor with the two axis that could explain most of the variability.

For whole genome sequencing, DNA was extracted from colony smears of *L. murinus* and *E. coli* using MOBIO DNA extraction kit according to manufacturer's protocol. Bacterial genomic DNA was quantified with a Qubit fluorimeter (Life Technologies). The Nextera kit from Illumina (USA) was used for the library preparation with 50 ng of DNA as input. Library molarity and quality was assessed with the Qubit and TapeStation using a DNA High sensitivity chip (Agilent Technologies). Libraries were loaded on a HiSeq 4000 single-read Illumina flow cell. Single-end reads of 50 bases and barcodes strategy were obtained according to the Nextera XT kit (Illumina, USA), following the manufacturer's recommendations. Read quality was assessed with the Fastqc program (available at: <http://www.bioinformatics.babraham.ac.uk/projects/fastqc/>) and filtered using the FastqMcf program (Ea-utils; available at: <http://code.google.com/p/ea-utils/>). Genome assembly was performed using the SPAdes39. The sequencing run produced on average a total of 15.5 million reads per sample, exhibiting very high theoretical coverage values (between 150 and 250 fold). The assembly produced very similar results for each pair of strains, resulting in an average genome size of 2152198 bp and 5205614 nucleotides for *L. murinus* and *E. coli*, respectively.

Assembled genomes were annotated using the RAST program (Treangen *et al.*, 2014). Multi-locus sequence typing (MLST) analysis was performed using annotated genomes and submitted to the Center for Genomic Epidemiology database (<http://cge.cbs.dtu.dk/services/MLST>). The phylogenetic relationship of all isolates was investigated by genomic single-nucleotide polymorphism (SNP)-based analysis using as the reference genome in the Parsnp v1.0 program (Aziz *et al.*, 2008). The BlastP analysis was used to investigate the presence of specific genes involved in the phenotype, evolution, and virulence of the isolates.

The MAFFT Web Server42 was used to perform the phylogenetic analysis of 16 s rRNA gene of public sequences of *Lactobacillus* spp. Phylogenetic tree topologies of nucleotide 16S rRNA gene was constructed with the neighbor-joining method using bootstrap (the accession numbers of all species are provided in the figure). The evolutionary distances were computed using default parameters.

Determination of average nucleotide identity (ANI) and in silico DNA–DNA hybridization (DDH)

ANI- and DDH-values were assessed in silico using online tools. The assembled genome of strain Lacto_Soner was uploaded in GGDC (<http://ggdc.dsmz.de/ggdc.php#>) with the recommended local alignment tool BLAST+ and compared with the closest genomes available in public databases identified in the different phylogenetic trees, to obtain DDH-values. The accession numbers of the strains included in the phylogenetic analyses are provided in **Supplementary file 1**. The statistic

comparison (logistic regression) used a significant probability value of DDH >79%. Pairwise ANI-values were obtained using JSpeciesWS (<http://jspecies.ribohost.com/jspeciesws/#analyse>) with BLAST.

Phylogenetic analysis

The phylogeny presented is based on the alignment of approximately 1400 nucleotides of the 16S rRNA gene. The phylogenetic analyses were generated with the neighbor-joining method. The percentage of replicate trees in which the associated taxa clustered together in the bootstrap test (100 replicates) is shown next to the branches. The trees are not rooted and drawn to scale, with branch lengths in the same units as those of the evolutionary distances used to infer the phylogenetic tree. The evolutionary distances were computed using the Kimura 2-parameter method for 16S rRNA gene. The analysis included 17 sequences. Evolutionary analyses were conducted using MEGA6. All sequences are labeled according to strain name, species and accession number.

L. murinus-specific qPCR

For 16S rRNA gene DNA quantification, 200 ng of DNA extracted from organ homogenates were mixed with 10 μ l of 2X ddPCR supermix for probes (BioRad), 1.8 μ l of each Forward (10 μ M) and Reverse (10 μ M) primer, 0.4 μ l of a DNA fluorescent probe and completed the volume to 20 μ l with RNase, DNase Free Molecular Biology Grade Water (Amimed, BioConcept, Switzerland). Quantitative PCR was performed following a thermal cycling protocol of an initial denaturation step at 95°C for 5 min, followed by 80 cycles of denaturation at 95°C for 30 s and annealing/extension at 61.5°C for 60 s. *L. murinus* 16S rRNA gene-specific primers and probe were used (probe: 5'-FAM-C TCAACCGTGCCGTTCAAAGTCAACTG-MQ530-3'; 16Sfw: 5'- ACTGGCGATGTTACCTTTGG -3' and 16Srev: 5'- CAGGCCTTTGTATTGGTGGT -3'). Amplicons were loaded on a 2% agarose gel stained with ethidium bromide and visualized with a BioRad Gel DocTM XR+ (BioRad).

For the standard curve construction and colony-forming unit (CFU) correlation, serial dilutions of *L. murinus* genomic DNA extracted from a colony grown overnight as previously described were added to the mix as described above with the same thermal cycling protocol settings. Briefly, 2 ml of *L. murinus* grown in MRS broth were divided in equal volumes and: (1) washed in PBS twice to remove remaining broth, heated at 100°C for 5 min and incubated in distilled water for 2 min. (2), serial-diluted and plated on MRS agar overnight to determine CFU. Genomes/lung calculation was adjusted by correcting to the amount of total DNA extracted from each lung and the total DNA input on each qPCR.

For RNA levels where stated, 500 ng total RNA was used to synthesize cDNA using M-MLV Reverse Transcriptase kit following kit's guidelines (PROMEGA). Quantitative PCR was performed using 2X KAPA SYBR FAST qPCR Master Mix-universal according to manufacturer's instructions. The following specific primers for murine cDNAs were used: mIP-10 fw: 5'-TTCACCATGTGCCATGCC-3', mIP-10 rev: 5'-GAACTGACGAGCCTGAGCTAGG-3', mIFN- γ fw: 5'-ATGAACGCTACACACTGCATC-3', mIFN- γ rev: 5'-CCATCCTTTTCCAGTTCCTC-3', mTNF- α fw: 5'-AGAAACACAAGATGCTGGGA-CAGT-3', mTNF- α rev: 5'-CCTTTCAGAACTCAGGAATGG-3', 18S fw: 5'-GTAACCCG TTGAACCCATT-3', 18S rev: 5'-CCATCCAATCGGTAGTAGCG-3'. Gene expression was normalized to 18S and fold induction was calculated compared to the mock group using the $\Delta\Delta C_q$ formula.

Identification of metabolites in *LmCM* and *EcCM*

200 μ l of fresh media, *LmCM* or *EcCM* were de-proteinized by adding 800 μ l of ice-cold MeOH. After vortexing for 1 min, samples were centrifuged at 15000 xg and 4°C for 15 min. Supernatants were collected and evaporated under vacuum. Residues were re-dissolved in 500 μ l of MeCN:H₂O (50:50, v:v) and vortexed for 1 min. Samples were centrifuged under the same conditions prior to injection in the LC-MS system. Chromatography was performed on a Waters H-Class Acquity UPLC system composed of a quaternary pump, a column manager and an FTN autosampler (Waters Corporation, Milford, MA, USA). For RPLC analyses, samples were separated on a Kinetex C18 column (150 \times 2.1 mm, 1.7 μ m) and the corresponding SecurityGuard Ultra precolumn and holder (Phenomenex, Torrance, USA). Solvent A was H₂O and solvent B was MeCN, both containing 0.1% formic acid. The column temperature and flow rate were set at 30°C and 300 μ l min⁻¹, respectively. The gradient elution was as follows: 2 to 100% B in 14 min, hold for 3 min, then back to 2% B in 0.1 min and re-equilibration of the column for 7.9 min. aHILIC separations were conducted on a Waters Acquity

BEH Amide column (150 × 2.1 mm, 1.7 μm) bearing an adequate VanGuard pre-column. Solvent A was H₂O:MeCN (5:95, v/v) and solvent B was H₂O:MeCN (70:30, v/v) containing 10 mM ammonium formate (pH = 6.5 in the aqueous component). The following gradient was applied: 0% B for 2 min, increased to 70% B over 18 min, held for 3 min, and then returned to 0% B in 1 min and to re-equilibrate the column for 7 min (total run time was 31 min). The flow rate was 500 μl min⁻¹, and the column temperature was kept at 40°C. For the zHILIC method, separation was performed on a Merck SeQuant Zic-pHILIC column (150 × 2.1 mm, 5 μm) and the appropriate guard kit. The following gradient of mobile phase A (MeCN) and mobile phase B (2.8 mM ammonium formate adjusted to pH 9.00) was applied: 5% B for 1 min, increased to 51% B over 9 min, held for 3 min at 51% B and then returned to 5% B for 0.1 min before re-equilibrating the column for 6.9 min (total run time was 20 min) at a flow rate of 300 μl/min and a column temperature of 40°C.

In all cases, a sample volume of 0.5 μl was injected. Samples were randomized for injection, and QC pools were analyzed every six samples to monitor the performance of the analytical platform.

The UPLC system was coupled to a maXis 3G Q-TOF high-resolution mass spectrometer from Bruker (Bruker Daltonik GmbH, Bremen, Germany) through an electrospray interface (ESI). The instrument was operated in TOF mode (no fragmentation). The capillary voltage was set at -4.7 kV for ESI+, drying gas temperature was 225°C, drying gas flow rate was set at 5.50 (RPLC), 8.00 (aHILIC) or 7.00 (zHILIC) L min⁻¹ and nebulizing gas pressure was 1.8 (RPLC) or 2.0 bar (HILIC). Transfer time was set at 40 (RPLC) or 60 (HILIC) μs and pre-pulse storage duration at 7.0 (RP) or 5.0 μs (HILIC). For ESI- operation, the capillary voltage was set at 2.8 kV. All the remaining ion source and ion optics parameters remained as in ESI+. Data between 50 and 1000 m/z were acquired in profile mode at a rate of 2 Hz. ESI and MS parameters were optimised using a mix of representative standards fed by a syringe pump and mixed with the LC eluent (mid-gradient conditions) within a tee-junction. Format adducts in the 90–1247 m/z range were employed for in-run automatic calibration using the quadratic plus high-precision calibration algorithm provided by the instrument's manufacturer. MS and UPLC control and data acquisition were performed through the HyStar v3.2 SR2 software (Bruker Daltonik) running the Waters Acquity UPLC v.1.5 plug-in.

Run alignment, peak piking and sample normalization were performed on Progenesis Q1 v2.3 (Nonlinear Dynamics, Waters, Newcastle upon Tyne, UK) and peaks were identified by matching their retention times, accurate masses and isotopic patterns to those of a library of chemical standards (MSMLS, Sigma-Aldrich, Buchs, Switzerland) analyzed under the same experimental conditions, as described elsewhere (Pezzatti *et al.*, 2019).

Measurement of lactic acid levels in *LmCM*

D-/L-Lactic acid (D-/L-lactate) (Rapid) Assay Kit (Megazyme, USA) was used to quantify lactic acid levels in bacterial supernatants according to manufacturer's instructions. For GC-MS, samples were diluted 1:10 in ultra-pure water. 5 μl of diluted fresh or spent medium were transferred to GC-MS vial inserts (Machery-Nagel, 702813) and dried down in a centrifugal evaporator (Speed Vac Concentrator, Savant) together with 10 μl scyllo-inositol (1 mM, Merck, I8132) as internal standard. Samples were re-dried after addition of 20 μl methanol (Merck, 34860). Vial inserts were transferred to 1.5 ml vials suitable for mass spectrometry (Machery-Nagel, 702282) and subsequently derivatised through addition of 20 μl pyridine and 20 μl bis(trimethylsilyl)trifluoroacetamide +1% trimethylchlorosilane (BSTFA +1% TMCS, Merck, B-023).

Samples were analyzed by GC-MS after >30 min incubation at room temperature using a Trace GC Ultra (Thermo Fisher Scientific) gas chromatography system equipped with a Phenomenex ZB-5MS capillary column (30 m × 0.25 mm, 0.25 μm, with inert guard). Using a Triplus RSH autosampler (Thermo Fisher Scientific) 2 μl of sample were injected. The GC was operated in splitless mode for one minute followed by split mode (1/13). The helium carrier gas flow rate was set to 1 ml/min, the temperature of the injector and transfer line were set to 270°C and 320°C, respectively. The oven temperature was at 70°C (1 min hold), increased to 295°C (12.5 °C/min) and raised to 320°C (25 °C/min, 2 min hold). The GC was coupled to a PolarisQ ion trap mass spectrometer (Thermo Fisher Scientific), operated in electron ionization (EI) mode (70 eV). The ion source was operated at 200°C and full scan data (m/z 50–650) was acquired after a solvent delay of 5 min. Relative levels of lactate were quantified by determining the intensity of the lactate ion m/z 219 relative to an abundant ion of the internal standard (m/z 318) using XCalibur (Thermo Fisher Scientific), OpenChrom and Excel (Microsoft).

pH measure in BALF

BALF were collected as described above. For pH measurement, samples were thawed on ice and the HALO – HANNA pH probe (Hanna Instruments) was submerged in each sample with a distilled water wash in between. pH was determined with the Edgeblu – HANNA pHmeter (Hanna Instruments) calibrated on the same day of the analysis.

Virus

Reverse genetics systems were kindly provided by Dr. Peter Palese and Dr. Adolfo García-Sastre (Icahn School of Medicine at Mount Sinai, New York, NY, USA). IAV A/Viet Nam/1203/2004 (VN/1203) HALo (low pathogenic version) was rescued and stocks were prepared as previously described (Anchisi *et al.*, 2018; Einfeld *et al.*, 2014).

Statistics

In order to determine statistical significance, we applied Mann–Whitney test to OTU abundance, Shannon indices and bacterial titers from mouse organs using Graph Pad Prism 7.0. In vitro experiments were assessed with student's t-test. Where p is not indicated; ****: $p \leq 0.0001$, ***: $p \leq 0.001$, **: $p \leq 0.01$, *: $p \leq 0.05$, ns: not significant.

Ethical approval

All animal procedures were in accordance with federal regulations of the Bundesamt für Lebensmittelsicherheit und Veterenärwesen (BLV) Switzerland (Tierschutzgesetz) and approved by an institutional review board and the cantonal authorities (license number GE-159–17).

Consent for publication

All authors read the manuscript and agreed to its publication.

Acknowledgements

We are grateful for excellent technical assistance by Chengyue Niu and Filomena Silva. We thank Ingrid Wagner from the team of Dr. Doron Merkler, University of Geneva, for providing guidance in setting up the RNAScope technique. We would like to extend our gratitude to the axenic mouse facility at the University of Bern and Dr. Mercedes Gomez, to the technical support of the mouse facility at the CMU, to the excellent support by the Genomics core facility, the Histology core facility and the Bioimaging facility of the CMU.

Additional information

Funding

Funder	Grant reference number	Author
Swiss National Science Foundation	155959	Mirco Schmolke
Swiss National Science Foundation	182475	Mirco Schmolke
Fondation Ernst et Lucie Schmidheiny		Mirco Schmolke
Fondation Ernest Boninchi		Inês Boal-Carvalho
Swiss National Science Foundation	162808	Lucy J Hathaway
Swiss National Science Foundation	169791	Siegfried Hapfelmeier
Swiss National Science Foundation	182576	Patrick H Viollier
H2020 European Research Council	695596	Joachim Kloehn

The funders had no role in study design, data collection and interpretation, or the decision to submit the work for publication.

Author contributions

Soner Yildiz, Conceptualization, Data curation, Formal analysis, Investigation, Visualization, Methodology, Writing - original draft; João P Pereira Bonifacio Lopes, Inês Boal-Carvalho, Investigation; Matthieu Bergé, Joachim Kloehn, Formal analysis, Investigation, Methodology; Víctor González-Ruiz, Resources, Formal analysis, Investigation, Methodology; Damian Baud, Patrice Francois, Data curation, Formal analysis, Investigation; Olivier P Schaeren, Investigation, Methodology; Michael Schot-saert, Resources; Lucy J Hathaway, Methodology; Serge Rudaz, Supervision, Validation, Investigation, Methodology; Patrick H Viollier, Supervision, Funding acquisition, Writing - original draft; Siegfried Hapfelmeier, Supervision, Investigation, Methodology; Mirco Schmolke, Conceptualization, Supervision, Funding acquisition, Writing - original draft, Project administration

Author ORCIDs

Matthieu Bergé  <http://orcid.org/0000-0002-0910-6114>

Patrick H Viollier  <http://orcid.org/0000-0002-5249-9910>

Mirco Schmolke  <https://orcid.org/0000-0002-2491-3029>

Ethics

Animal experimentation: All animal procedures were in accordance with federal regulations of the Bundesamt für Lebensmittelsicherheit und Veterenärwesen (BLV) Switzerland (Tierschutzgesetz) and approved by an institutional review board and the cantonal authorities (license number GE-159-17).

Decision letter and Author response

Decision letter <https://doi.org/10.7554/eLife.53581.sa1>

Author response <https://doi.org/10.7554/eLife.53581.sa2>

Additional files

Supplementary files

- Supplementary file 1. Genome annotation of *L. murinus* isolate. *L. murinus* genome annotation obtained by RAST showing contig identifiers and detected features, start, stop coordinates and coding strand are indicated considering corresponding contig. Enzymatic commission number (EC), nucleotide and deduced amino acid sequences are also presented.
- Supplementary file 2. Analysis of pathogenicity islands in *E. coli* genome isolated from IAV infected mice. The tables contain the list of genes putatively present onto pathogenicity islands recovered from the annotated genomes of two individual colonies of *E. coli* (**A** and **B**) isolated from lung tissue. Gene name and short name as well as gene function are presented. Note that the two lists have almost exactly the same content.
- Supplementary file 3. Features found in metabolomics analyses of FM, LmCM or EcCM, named after their analytical technique, retention time, and mass. Sheet 1 (whole list) contains all hits sorted by the ratio of the average signal (arbitrary units) from two runs for *L. murinus* conditioned medium (LmCM) over fresh medium (FM). Sheet two lists the hits with an AVG (LmCM)/AVG (FM) >10 fold. Sheet three lists the hits with an AVG *E. coli* conditioned medium (EcCM)/AVG (LmCM) <10 fold. Sheet 4 (short list) contains only hits that are present in sheet 2 and 3. Sheet five lists identified metabolites based on their masses and retention times compared to authentic reference standards run in-house under the same analytical setup. Score (arbitrary units) indicates the goodness of the overall matching between the experimental properties of each feature and those obtained for the corresponding standard, as calculated by Progenesis Q1. Mass error express the relative mass difference (ppm) between the masses of the feature and the reference standard. Isotope similarity (%) corresponds to the matching of the isotopic profile of the feature and the reference standard.
- Transparent reporting form

Data availability

Material from this study originally generated in our team, will be made available upon request in reasonable quantities.

The following datasets were generated:

Author(s)	Year	Dataset title	Dataset URL	Database and Identifier
Schmolke M	2019	NGS MiSeq data	http://www.ncbi.nlm.nih.gov/bioproject/591377	NCBI BioProject, PRJNA591377
Schmolke M	2019	Lactobacillus murinus isolated from laboratory mice	https://www.ncbi.nlm.nih.gov/bioproject/PRJNA663937	NCBI BioProject, PRJNA663937
Schmolke M	2019	Escherichia coli isolated from laboratory mice	https://www.ncbi.nlm.nih.gov/bioproject/PRJNA591640	NCBI BioProject, PRJNA591640
Schmolke M	2020	NGS MiSeq data	http://www.ncbi.nlm.nih.gov/bioproject/663937	NCBI BioProject, PRJNA663937

References

- Abt MC**, Osborne LC, Monticelli LA, Doering TA, Alenghat T, Sonnenberg GF, Paley MA, Antenus M, Williams KL, Erikson J, Wherry EJ, Artis D. 2012. Commensal Bacteria calibrate the activation threshold of innate antiviral immunity. *Immunity* **37**:158–170. DOI: <https://doi.org/10.1016/j.immuni.2012.04.011>, PMID: 22705104
- Alakomi HL**, Skyttä E, Saarela M, Mattila-Sandholm T, Latva-Kala K, Helander IM. 2000. Lactic acid permeabilizes gram-negative Bacteria by disrupting the outer membrane. *Applied and Environmental Microbiology* **66**:2001–2005. DOI: <https://doi.org/10.1128/AEM.66.5.2001-2005.2000>, PMID: 10788373
- Almirón M**, Traglia G, Rubio A, Sanjuan N. 2013. Colonization of the mouse upper gastrointestinal tract by *Lactobacillus murinus*: a histological, immunocytochemical, and ultrastructural study. *Current Microbiology* **67**:395–398. DOI: <https://doi.org/10.1007/s00284-013-0367-9>, PMID: 23689939
- Anchisi S**, Gonçalves AR, Mazel-Sanchez B, Cordey S, Schmolke M. 2018. Influenza A virus genetic tools: from clinical sample to molecular clone. *Methods in Molecular Biology* **1836**:33–58. DOI: https://doi.org/10.1007/978-1-4939-8678-1_3, PMID: 30151568
- Aronesty E**. 2013. Comparison of sequencing utility programs. *The Open Bioinformatics Journal* **7**:1–8. DOI: <https://doi.org/10.2174/1875036201307010001>
- Aziz RK**, Bartels D, Best AA, DeJongh M, Disz T, Edwards RA, Formsma K, Gerdes S, Glass EM, Kubal M, Meyer F, Olsen GJ, Olson R, Osterman AL, Overbeek RA, McNeil LK, Paarmann D, Paczian T, Parrello B, Pusch GD, et al. 2008. The RAST server: rapid annotations using subsystems technology. *BMC Genomics* **9**:75. DOI: <https://doi.org/10.1186/1471-2164-9-75>, PMID: 18261238
- Barfod KK**, Roggenbuck M, Hansen LH, Schjørring S, Larsen ST, Sørensen SJ, Krogfelt KA. 2013. The murine lung microbiome in relation to the intestinal and vaginal bacterial communities. *BMC Microbiology* **13**:303. DOI: <https://doi.org/10.1186/1471-2180-13-303>, PMID: 24373613
- Barthel M**, Hapfelmeier S, Quintanilla-Martínez L, Kremer M, Rohde M, Hogardt M, Pfeiffer K, Rüssmann H, Hardt WD. 2003. Pretreatment of mice with streptomycin provides a *Salmonella enterica* serovar typhimurium colitis model that allows analysis of both pathogen and host. *Infection and Immunity* **71**:2839–2858. DOI: <https://doi.org/10.1128/IAI.71.5.2839-2858.2003>, PMID: 12704158
- Bensel T**, Stotz M, Borneff-Lipp M, Wollschläger B, Wienke A, Taccetti G, Campana S, Meyer KC, Jensen PØ, Lechner U, Ulrich M, Döring G, Worlitzsch D. 2011. Lactate in cystic fibrosis sputum. *Journal of Cystic Fibrosis* **10**:37–44. DOI: <https://doi.org/10.1016/j.jcf.2010.09.004>, PMID: 20947455
- Bilkova A**, Kinova Sepova H, Bukovsky M, Bezakova L. 2011. Antibacterial potential of lactobacilli isolated from a lamb. *Veterinární Medicina* **56**:319–324. DOI: <https://doi.org/10.17221/1583-VETMED>
- Blais JF**, Lavoie MC. 1990. Effect of dietary components on the indigenous oral bacterial flora of BALB/c mice. *Journal of Dental Research* **69**:868–873. DOI: <https://doi.org/10.1177/00220345900690030801>, PMID: 2324350
- Bolyen E**, Rideout JR, Dillon MR, Bokulich NA, Abnet CC, Al-Ghalith GA, Alexander H, Alm EJ, Arumugam M, Asnicar F, Bai Y, Bisanz JE, Bittinger K, Brejnrod A, Brislawn CJ, Brown CT, Callahan BJ, Caraballo-Rodríguez AM, Chase J, Cope EK, et al. 2019. Reproducible, interactive, scalable and extensible microbiome data science using QIIME 2. *Nature Biotechnology* **37**:852–857. DOI: <https://doi.org/10.1038/s41587-019-0209-9>, PMID: 31341288
- Brugiroux S**, Beutler M, Pfann C, Garzetti D, Ruscheweyh H-J, Ring D, Diehl M, Herp S, Lötscher Y, Hussain S, Bunk B, Pukall R, Huson DH, Münch PC, McHardy AC, McCoy KD, Macpherson AJ, Loy A, Clavel T, Berry D, et al. 2017. Genome-guided design of a defined mouse Microbiota that confers colonization resistance against *Salmonella enterica* serovar typhimurium. *Nature Microbiology* **2**:16215. DOI: <https://doi.org/10.1038/nmicrobiol.2016.215>

- Caporaso JG**, Bittinger K, Bushman FD, DeSantis TZ, Andersen GL, Knight R. 2010a. PyNAST: a flexible tool for aligning sequences to a template alignment. *Bioinformatics* **26**:266–267. DOI: <https://doi.org/10.1093/bioinformatics/btp636>, PMID: 19914921
- Caporaso JG**, Kuczynski J, Stombaugh J, Bittinger K, Bushman FD, Costello EK, Fierer N, Peña AG, Goodrich JK, Gordon JI, Huttley GA, Kelley ST, Knights D, Koenig JE, Ley RE, Lozupone CA, McDonald D, Muegge BD, Pirrung M, Reeder J, et al. 2010b. QIIME allows analysis of high-throughput community sequencing data. *Nature Methods* **7**:335–336. DOI: <https://doi.org/10.1038/nmeth.f.303>, PMID: 20383131
- Chao A**. 1984. Non-parametric estimation of the classes in a population. *Scandinavian Journal of Statistics* **11**: 265–270. DOI: <https://doi.org/10.2307/4615964>
- Colwell RK**, Chao A, Gotelli NJ, Lin S-Y, Mao CX, Chazdon RL, Longino JT. 2012. Models and estimators linking individual-based and sample-based rarefaction, extrapolation and comparison of assemblages. *Journal of Plant Ecology* **5**:3–21. DOI: <https://doi.org/10.1093/jpe/rtr044>
- De Keersmaecker SC**, Verhoeven TL, Desair J, Marchal K, Vanderleyden J, Nagy I. 2006. Strong antimicrobial activity of *Lactobacillus rhamnosus* GG against *Salmonella typhimurium* is due to accumulation of lactic acid. *FEMS Microbiology Letters* **259**:89–96. DOI: <https://doi.org/10.1111/j.1574-6968.2006.00250.x>, PMID: 166 84107
- Deriu E**, Boxx GM, He X, Pan C, Benavidez SD, Cen L, Rozengurt N, Shi W, Cheng G. 2016. Influenza virus affects intestinal Microbiota and secondary Salmonella infection in the gut through type I interferons. *PLOS Pathogens* **12**:e1005572. DOI: <https://doi.org/10.1371/journal.ppat.1005572>, PMID: 27149619
- DeSantis TZ**, Hugenholtz P, Larsen N, Rojas M, Brodie EL, Keller K, Huber T, Dalevi D, Hu P, Andersen GL. 2006. Greengenes, a chimera-checked 16S rRNA gene database and workbench compatible with ARB. *Applied and Environmental Microbiology* **72**:5069–5072. DOI: <https://doi.org/10.1128/AEM.03006-05>, PMID: 16820507
- Dewhirst FE**, Chien CC, Paster BJ, Ericson RL, Orcutt RP, Schauer DB, Fox JG. 1999. Phylogeny of the defined murine Microbiota: altered Schaedler flora. *Applied and Environmental Microbiology* **65**:3287–3292. DOI: <https://doi.org/10.1128/AEM.65.8.3287-3292.1999>, PMID: 10427008
- Dickson RP**, Erb-Downward JR, Prescott HC, Martinez FJ, Curtis JL, Lama VN, Huffnagle GB. 2014. Cell-associated Bacteria in the human lung microbiome. *Microbiome* **2**:28. DOI: <https://doi.org/10.1186/2049-2618-2-28>, PMID: 25206976
- Dickson RP**, Erb-Downward JR, Freeman CM, McCloskey L, Beck JM, Huffnagle GB, Curtis JL. 2015. Spatial variation in the healthy human lung microbiome and the adapted island model of lung biogeography. *Annals of the American Thoracic Society* **12**:821–830. DOI: <https://doi.org/10.1513/AnnalsATS.201501-029OC>, PMID: 25 803243
- Ding YH**, Qian LY, Pang J, Lin JY, Xu Q, Wang LH, Huang DS, Zou H. 2017. The regulation of immune cells by lactobacilli: a potential therapeutic target for anti-atherosclerosis therapy. *Oncotarget* **8**:59915–59928. DOI: <https://doi.org/10.18632/oncotarget.18346>, PMID: 28938693
- Eisfeld AJ**, Neumann G, Kawaoka Y. 2014. Influenza A virus isolation, culture and identification. *Nature Protocols* **9**:2663–2681. DOI: <https://doi.org/10.1038/nprot.2014.180>, PMID: 25321410
- Elayaraja S**, Annamalai N, Mayavu P, Balasubramanian T. 2014. Production, purification and characterization of bacteriocin from *Lactobacillus murinus* AU06 and its broad antibacterial spectrum. *Asian Pacific Journal of Tropical Biomedicine* **4**:S305–S311. DOI: <https://doi.org/10.12980/APJTB.4.2014C537>, PMID: 25183102
- Ericsson AC**, Davis JW, Spollen W, Bivens N, Givan S, Hagan CE, McIntosh M, Franklin CL. 2015. Effects of vendor and genetic background on the composition of the fecal Microbiota of inbred mice. *PLOS ONE* **10**: e0116704. DOI: <https://doi.org/10.1371/journal.pone.0116704>, PMID: 25675094
- Groves HT**, Cuthbertson L, James P, Moffatt MF, Cox MJ, Tregoning JS. 2018. Respiratory disease following viral lung infection alters the murine gut Microbiota. *Frontiers in Immunology* **9**:182. DOI: <https://doi.org/10.3389/fimmu.2018.00182>
- Guo Y**, Wang Q, Li D, Onyema OO, Mei Z, Manafi A, Banerjee A, Mahgoub B, Stoler MH, Barker TH, Wilkes DS, Gelman AE, Kreisel D, Krupnick AS. 2019. Vendor-specific microbiome controls both acute and chronic murine lung allograft rejection by altering CD4⁺ Foxp3⁺ regulatory T cell levels. *American Journal of Transplantation* **19**:ajt.15523. DOI: <https://doi.org/10.1111/ajt.15523>
- Hemme D**, Raibaud P, Ducluzeau R, Galpin JV, Sicard P, Van Heijenoort J. 1980. "Lactobacillus murinus" n. sp., a new species of the autochthonous dominant flora of the digestive tract of rat and mouse. *Annals of Microbiology* **131**:297–308.
- Hertzberger R**, Arents J, Dekker HL, Pridmore RD, Gysler C, Kleerebezem M, de Mattos MJ. 2014. H(2)O(2) production in species of the *Lactobacillus acidophilus* group: a central role for a novel NADH-dependent flavin reductase. *Applied and Environmental Microbiology* **80**:2229–2239. DOI: <https://doi.org/10.1128/AEM.04272-13>, PMID: 24487531
- Isani M**, Bell BA, Delaplain PT, Bowling JD, Golden JM, Elizee M, Illingworth L, Wang J, Gayer CP, Grishin AV, Ford HR. 2018. *Lactobacillus murinus* HF12 colonizes neonatal gut and protects rats from necrotizing enterocolitis. *PLOS ONE* **13**:e0196710. DOI: <https://doi.org/10.1371/journal.pone.0196710>, PMID: 29933378
- Ivanov II**, Frutos RL, Manel N, Yoshinaga K, Rifkin DB, Sartor RB, Finlay BB, Littman DR. 2008. Specific Microbiota direct the differentiation of IL-17-producing T-helper cells in the mucosa of the small intestine. *Cell Host & Microbe* **4**:337–349. DOI: <https://doi.org/10.1016/j.chom.2008.09.009>, PMID: 18854238
- Ivanov II**, Atarashi K, Manel N, Brodie EL, Shima T, Karaoz U, Wei D, Goldfarb KC, Santee CA, Lynch SV, Tanoue T, Imaoka A, Itoh K, Takeda K, Umesaki Y, Honda K, Littman DR. 2009. Induction of intestinal Th17 cells by segmented filamentous Bacteria. *Cell* **139**:485–498. DOI: <https://doi.org/10.1016/j.cell.2009.09.033>, PMID: 1 9836068

- Jerse AE**, Crow ET, Bordner AN, Rahman I, Cornelissen CN, Moench TR, Mehrazar K. 2002. Growth of *Neisseria gonorrhoeae* in the female mouse genital tract does not require the gonococcal transferrin or hemoglobin receptors and may be enhanced by commensal lactobacilli. *Infection and Immunity* **70**:2549–2558. DOI: <https://doi.org/10.1128/IAI.70.5.2549-2558.2002>, PMID: 11953395
- Kang TS**, Korber DR, Tanaka T. 2013. Influence of oxygen on NADH recycling and oxidative stress resistance systems in *Lactobacillus panis* PM1. *AMB Express* **3**:10. DOI: <https://doi.org/10.1186/2191-0855-3-10>, PMID: 23369580
- Kottmann RM**, Kulkarni AA, Smolnycki KA, Lyda E, Dahanayake T, Salibi R, Honnons S, Jones C, Isern NG, Hu JZ, Nathan SD, Grant G, Phipps RP, Sime PJ. 2012. Lactic acid is elevated in idiopathic pulmonary fibrosis and induces myofibroblast differentiation via pH-dependent activation of transforming growth factor- β . *American Journal of Respiratory and Critical Care Medicine* **186**:740–751. DOI: <https://doi.org/10.1164/rccm.201201-0084OC>, PMID: 22923663
- Kovacs EJ**, Boe DM, Boule LA, Curtis BJ. 2017. Inflammaging and the lung. *Clinics in Geriatric Medicine* **33**:459–471. DOI: <https://doi.org/10.1016/j.cger.2017.06.002>, PMID: 28991644
- Lozupone C**, Knight R. 2005. UniFrac: a new phylogenetic method for comparing microbial communities. *Applied and Environmental Microbiology* **71**:8228–8235. DOI: <https://doi.org/10.1128/AEM.71.12.8228-8235.2005>, PMID: 16332807
- Lu R**, Fasano S, Madayiputhiya N, Morin NP, Nataro J, Fasano A. 2009. Isolation, identification, and characterization of small bioactive peptides from *Lactobacillus* GG conditional media that exert both anti-Gram-negative and Gram-positive bactericidal activity. *Journal of Pediatric Gastroenterology and Nutrition* **49**:23–30. DOI: <https://doi.org/10.1097/MPG.0b013e3181924d1e>, PMID: 19465870
- Marty-Teysset C**, de la Torre F, Garel J. 2000. Increased production of hydrogen peroxide by *Lactobacillus delbrueckii* subsp. *bulgaricus* upon aeration: involvement of an NADH oxidase in oxidative stress. *Applied and Environmental Microbiology* **66**:262–267. DOI: <https://doi.org/10.1128/AEM.66.1.262-267.2000>, PMID: 10618234
- McCullers JA**. 2014. The co-pathogenesis of influenza viruses with Bacteria in the lung. *Nature Reviews Microbiology* **12**:252–262. DOI: <https://doi.org/10.1038/nrmicro3231>
- McCullers JA**, Rehg JE. 2002. Lethal Synergism between Influenza Virus and *Streptococcus pneumoniae*: Characterization of a Mouse Model and the Role of Platelet-Activating Factor Receptor. *The Journal of Infectious Diseases* **186**:341–350. DOI: <https://doi.org/10.1086/341462>
- Morris DE**, Cleary DW, Clarke SC. 2017. Secondary bacterial infections associated with influenza pandemics. *Frontiers in Microbiology* **8**:1041. DOI: <https://doi.org/10.3389/fmicb.2017.01041>, PMID: 28690590
- Nakatsuji T**, Chen TH, Narala S, Chun KA, Two AM, Yun T, Shafiq F, Kotol PF, Bouslimani A, Melnik AV, Latif H, Kim JN, Lockhart A, Artis K, David G, Taylor P, Streib J, Dorrestein PC, Grier A, Gill SR, et al. 2017. Antimicrobials from human skin commensal Bacteria protect against *Staphylococcus aureus* and are deficient in atopic dermatitis. *Science Translational Medicine* **9**:eah4680. DOI: <https://doi.org/10.1126/scitranslmed.aah4680>, PMID: 28228596
- Nardi RM**, Santoro MM, Oliveira JS, Pimenta AM, Ferraz VP, Benchetrit LC, Nicoli JR. 2005. Purification and molecular characterization of antibacterial compounds produced by *Lactobacillus murinus* strain L1. *Journal of Applied Microbiology* **99**:649–656. DOI: <https://doi.org/10.1111/j.1365-2672.2005.02632.x>, PMID: 16108807
- Östberg AK**, Alizadehgharib S, Dahlgren U. 2018. Sublingual administration of 2-hydroxyethyl methacrylate enhances antibody responses to co-administered ovalbumin and *Streptococcus mutans*. *Acta Odontologica Scandinavica* **76**:351–356. DOI: <https://doi.org/10.1080/00016357.2018.1460491>
- Parlet CP**, Brown MM, Horswill AR. 2019. Commensal staphylococci influence *Staphylococcus aureus* skin colonization and disease. *Trends in Microbiology* **27**:497–507. DOI: <https://doi.org/10.1016/j.tim.2019.01.008>, PMID: 30846311
- Pellaton C**, Nutten S, Thierry AC, Boudousquié C, Barbier N, Blanchard C, Corthésy B, Mercenier A, Spertini F. 2012. Intra-gastric and intranasal administration of *Lactobacillus paracasei* NCC2461 Modulates Allergic Airway Inflammation in Mice. *International Journal of Inflammation* **2012**:686739. DOI: <https://doi.org/10.1155/2012/686739>, PMID: 22762009
- Perelmutter K**, Fraga M, Zunino P. 2008. In vitro activity of potential probiotic *Lactobacillus murinus* isolated from the dog. *Journal of Applied Microbiology* **104**:1718–1725. DOI: <https://doi.org/10.1111/j.1365-2672.2007.03702.x>, PMID: 18194243
- Pezzatti J**, González-Ruiz V, Codesido S, Gagnebin Y, Joshi A, Guillarme D, Schappler J, Picard D, Boccard J, Rudaz S. 2019. A scoring approach for multi-platform acquisition in metabolomics. *Journal of Chromatography A* **1592**:47–54. DOI: <https://doi.org/10.1016/j.chroma.2019.01.023>, PMID: 30685186
- Pickard JM**, Zeng MY, Caruso R, Núñez G. 2017. Gut Microbiota: role in pathogen colonization, immune responses, and inflammatory disease. *Immunological Reviews* **279**:70–89. DOI: <https://doi.org/10.1111/imr.12567>, PMID: 28856738
- Planet PJ**, Parker D, Cohen TS, Smith H, Leon JD, Ryan C, Hammer TJ, Fierer N, Chen EI, Prince AS. 2016. Lambda interferon restructures the nasal microbiome and increases susceptibility to *Staphylococcus aureus* superinfection. *mBio* **7**:e01939. DOI: <https://doi.org/10.1128/mBio.01939-15>, PMID: 26861017
- Poroyko V**, Meng F, Meliton A, Afonyushkin T, Ulanov A, Semenyuk E, Latif O, Tesic V, Birukova AA, Birukov KG. 2015. Alterations of lung Microbiota in a mouse model of LPS-induced lung injury. *American Journal of Physiology-Lung Cellular and Molecular Physiology* **309**:L76–L83. DOI: <https://doi.org/10.1152/ajplung.00061.2014>, PMID: 25957290

- Rodrigue L**, Barras MJ, Marcotte H, Lavoie MC. 1993. Bacterial colonization of the oral cavity of the BALB/c mouse. *Microbial Ecology* **26**:267–275. DOI: <https://doi.org/10.1007/BF00176958>, PMID: 24190095
- Rodriguez JL**, Dalia AB, Weiser JN. 2012. Increased chain length promotes pneumococcal adherence and colonization. *Infection and Immunity* **80**:3454–3459. DOI: <https://doi.org/10.1128/IAI.00587-12>, PMID: 22825449
- Schaedler RW**, Dubs R, Costello R. 1965. Association of germfree mice with Bacteria isolated from normal mice. *Journal of Experimental Medicine* **122**:77–82. DOI: <https://doi.org/10.1084/jem.122.1.77>, PMID: 14325475
- Shannon C**. 1984. A mathematical theory of communication. *Bell Labs Technical Journal* **27**:tb01338. DOI: <https://doi.org/10.1002/j.1538-7305.1948.tb01338.x>
- Singh N**, Vats A, Sharma A, Arora A, Kumar A. 2017. The development of lower respiratory tract microbiome in mice. *Microbiome* **5**:61. DOI: <https://doi.org/10.1186/s40168-017-0277-3>, PMID: 28637485
- Spacova I**, Petrova MI, Fremau A, Pollaris L, Vanoirbeek J, Ceuppens JL, Seys S, Lebeer S. 2019. Intranasal administration of probiotic *Lactobacillus rhamnosus* GG prevents birch pollen-induced allergic asthma in a murine model. *Allergy* **74**:100–110. DOI: <https://doi.org/10.1111/all.13502>, PMID: 29888398
- Sun F**, Xiao G, Qu Z. 2017. Murine bronchoalveolar lavage. *Bio-Protocol* **7**:2287. DOI: <https://doi.org/10.21769/BioProtoc.2287>
- Treangen TJ**, Ondov BD, Koren S, Phillippy AM. 2014. The Harvest suite for rapid core-genome alignment and visualization of thousands of intraspecific microbial genomes. *Genome Biology* **15**:524. DOI: <https://doi.org/10.1186/s13059-014-0524-x>
- Wang Q**, Garrity GM, Tiedje JM, Cole JR. 2007. Naive bayesian classifier for rapid assignment of rRNA sequences into the new bacterial taxonomy. *Applied and Environmental Microbiology* **73**:5261–5267. DOI: <https://doi.org/10.1128/AEM.00062-07>, PMID: 17586664
- Wang C**, Chang T, Yang H, Cui M. 2015. Antibacterial mechanism of lactic acid on physiological and morphological properties of *Salmonella enteritidis*, *Escherichia coli* and *Listeria monocytogenes*. *Food Control* **47**:231–236. DOI: <https://doi.org/10.1016/j.foodcont.2014.06.034>
- Wannemuehler MJ**, Overstreet A-M, Ward DV, Phillips GJ. 2014. Draft genome sequences of the altered Schaedler Flora, a defined bacterial community from gnotobiotic mice. *Genome Announcements* **2**:14. DOI: <https://doi.org/10.1128/genomeA.00287-14>
- Wertheim HF**, Melles DC, Vos MC, van Leeuwen W, van Belkum A, Verbrugh HA, Nouwen JL. 2005. The role of nasal carriage in *Staphylococcus aureus* infections. *The Lancet Infectious Diseases* **5**:751–762. DOI: [https://doi.org/10.1016/S1473-3099\(05\)70295-4](https://doi.org/10.1016/S1473-3099(05)70295-4), PMID: 16310147
- Wymore Brand M**, Wannemuehler MJ, Phillips GJ, Proctor A, Overstreet AM, Jergens AE, Orcutt RP, Fox JG. 2015. The altered Schaedler Flora: continued applications of a defined murine microbial community. *ILAR Journal* **56**:169–178. DOI: <https://doi.org/10.1093/ilar/ilv012>, PMID: 26323627
- Yadava K**, Pattaroni C, Sichelstiel AK, Trompette A, Gollwitzer ES, Salami O, von Garnier C, Nicod LP, Marsland BJ. 2016. Microbiota promotes chronic pulmonary inflammation by enhancing IL-17A and autoantibodies. *American Journal of Respiratory and Critical Care Medicine* **193**:975–987. DOI: <https://doi.org/10.1164/rccm.201504-0779OC>, PMID: 26630356
- Yildiz S**, Mazel-Sanchez B, Kandasamy M, Manicassamy B, Schmolke M. 2018. Influenza A virus infection impacts systemic Microbiota dynamics and causes quantitative enteric dysbiosis. *Microbiome* **6**:9. DOI: <https://doi.org/10.1186/s40168-017-0386-z>, PMID: 29321057
- Yu G**, Gail MH, Consonni D, Carugno M, Humphrys M, Pesatori AC, Caporaso NE, Goedert JJ, Ravel J, Landi MT. 2016. Characterizing human lung tissue Microbiota and its relationship to epidemiological and clinical features. *Genome Biology* **17**:163. DOI: <https://doi.org/10.1186/s13059-016-1021-1>, PMID: 27468850
- Yun Y**, Srinivas G, Kuenzel S, Linnenbrink M, Alnahas S, Bruce KD, Steinhoff U, Baines JF, Schaible UE. 2014. Environmentally determined differences in the murine lung Microbiota and their relation to alveolar architecture. *PLOS ONE* **9**:e113466. DOI: <https://doi.org/10.1371/journal.pone.0113466>, PMID: 25470730
- Zhang R**, Chen L, Cao L, Li KJ, Huang Y, Luan XQ, Li G. 2018. Effects of smoking on the lower respiratory tract microbiome in mice. *Respiratory Research* **19**:253. DOI: <https://doi.org/10.1186/s12931-018-0959-9>, PMID: 30547792

Figure 2 – supplement 1

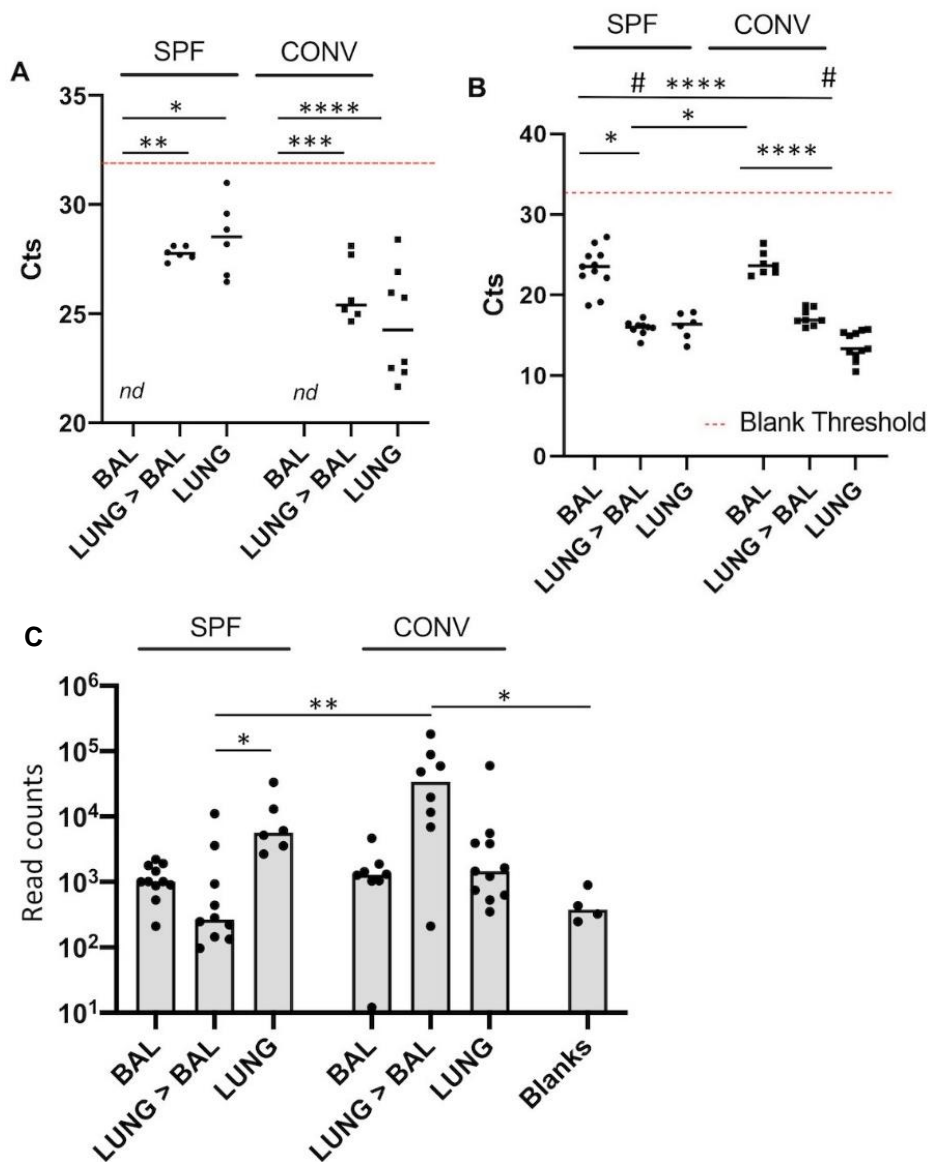
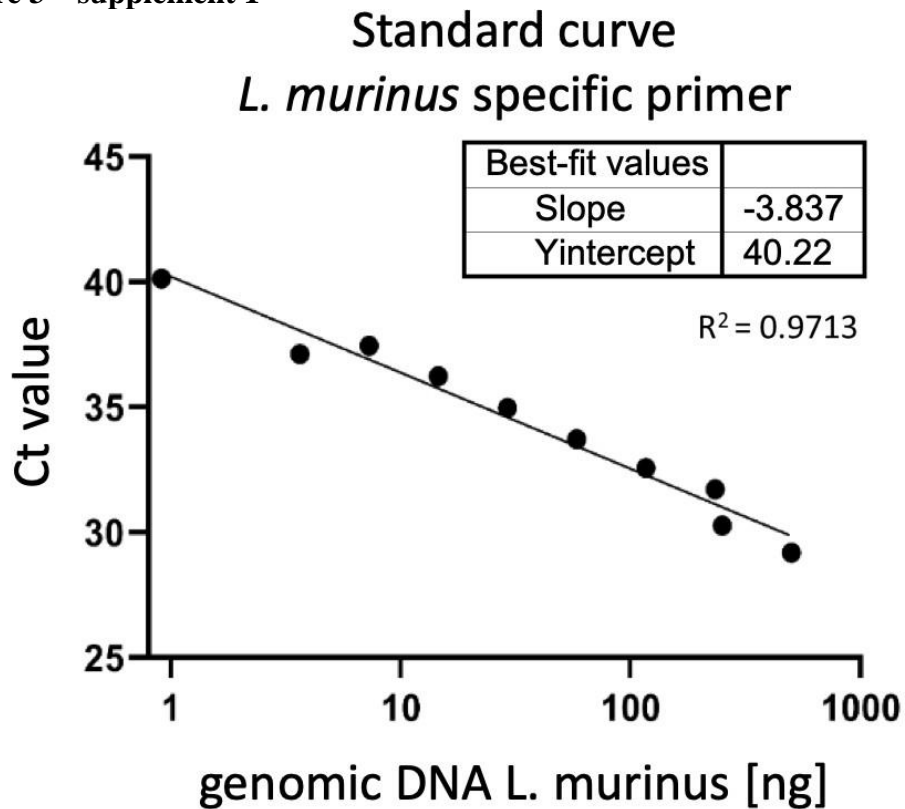


Figure 2 – supplement 1: Sensitivity controls for qPCR and 16S rRNA NGS. (A) 16S rRNA gene-specific qPCR was used to determine load of bacterial DNA in BALF, Lungs after BAL and total lung DNA extracted from SPF and conventionally housed mice (DNA samples from Figure 2A). CT values are depicted for individual animals. The dotted red line indicates the average CT value of blank samples. All BALF samples (SPF (n = 11) and CONV (n = 8)) had Ct values above the blank, 4/10 lungs after BAL (SPF) and 2/8 lungs after BAL samples had Ct values above the blank, 3/11 lungs (CONV) had Ct above the blank. Each dot indicates DNA from an individual mouse. Kruskal–Wallis test was used to determine statistical significance in multiple comparisons with Dunn’s correction, median Ct value are indicated. (B) 18S rRNA gene-specific qPCR was used to determine load of genomic mouse DNA in BALF, Lungs after BAL and total lung DNA extracted from SPF and conventionally housed mice. CT values are depicted for individual animals. Kruskal–Wallis test was used to determine statistical significance in multiple comparisons with Dunn’s correction, median Ct value are indicated and median Ct value are indicated. (C) Graphical representation of the reads counts obtained from samples presented in Figure 2A. Each dot indicates DNA from an individual mouse. Kruskal–Wallis test was used to determine statistical significance. Median read counts are indicated.

Figure 3 – supplement 1

A



B

Agarose gel electrophoresis of PCR products from
Fig. 3A

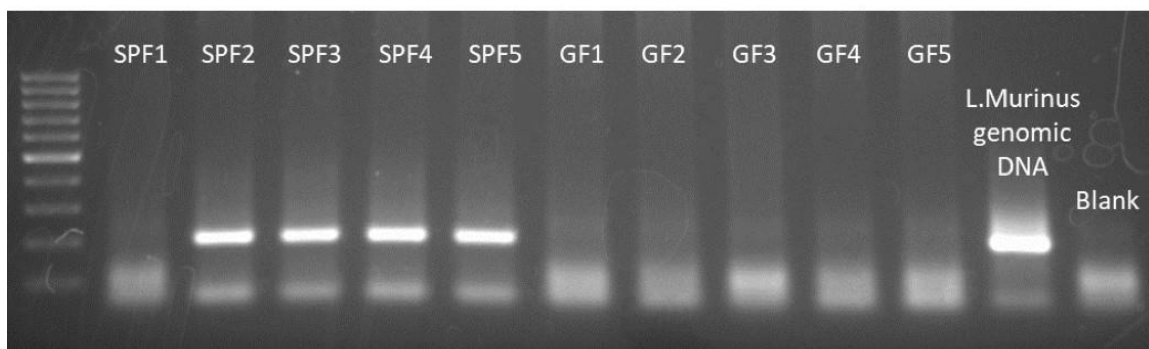


Figure 3 – supplement 1: Quality controls for *L. murinus* specific qPCR.

(A) Standard curve for *L. murinus*-specific qPCR using DNA from a defined number of CFU of a *L. murinus* culture in log phase. (B) Amplicons of qPCR were loaded on a standard agarose gel and stained with 0.1 ethidium bromide.

Figure 4 – supplement 1

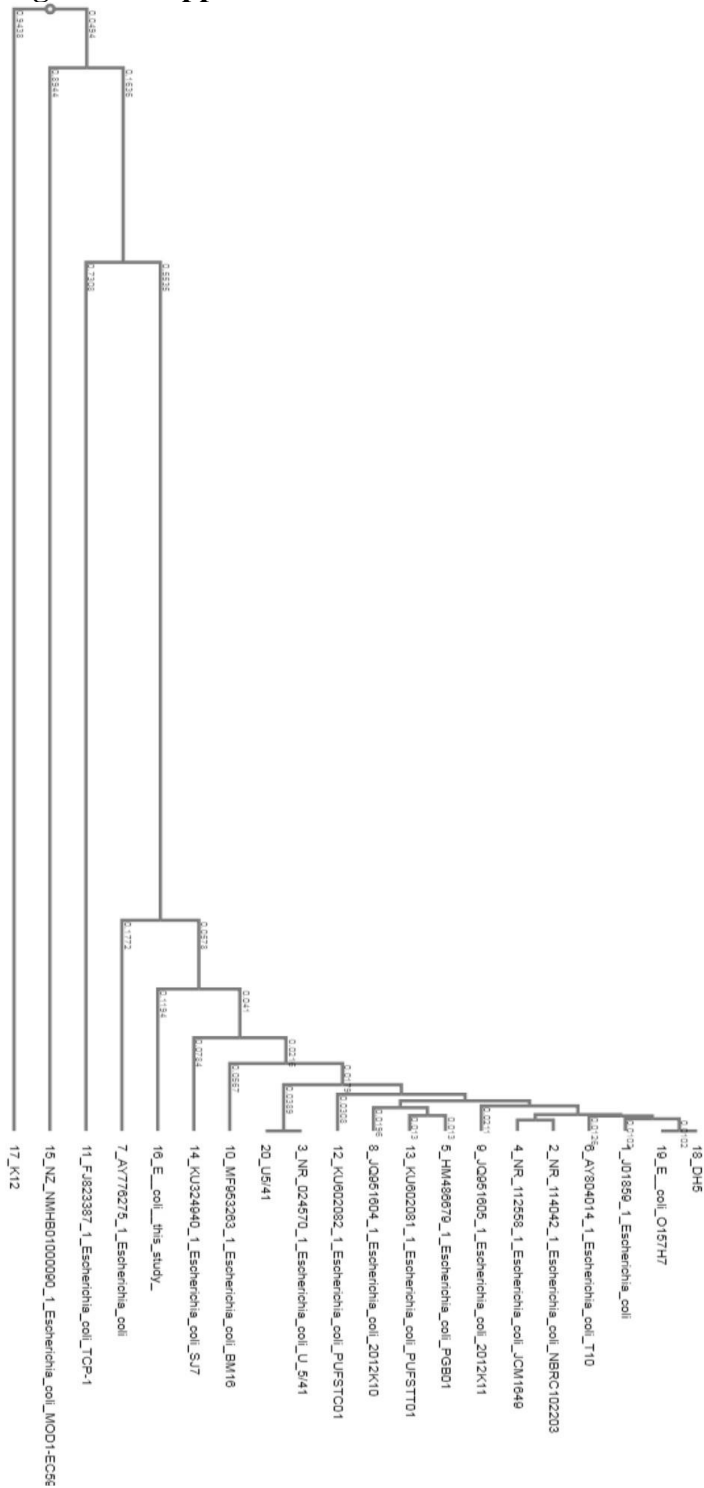


Figure 4 – supplement 1: Phylogenetic tree of *E. coli* isolate to regular lab strains and other environmental isolates. The phylogeny presented is based on the alignment of approximately 1400 nucleotides of the 16S rRNA gene. The phylogenetic analyses were generated with the neighbor-joining method. The percentage of replicate trees in which the associated taxa clustered together in the bootstrap test (100 replicates) is shown next to the branches. The trees are not rooted but drawn to scale, with branch lengths in the same units as those of the evolutionary distances used to infer the phylogenetic tree. The evolutionary distances were computed using the Kimura 2-parameter method for 16S rRNA gene. The analysis included 17 sequences. Evolutionary analyses were conducted using MEGA6. All sequences are labeled according to strain name, species and accession number.

Figure 5 – supplement 1
S. pneumoniae growth

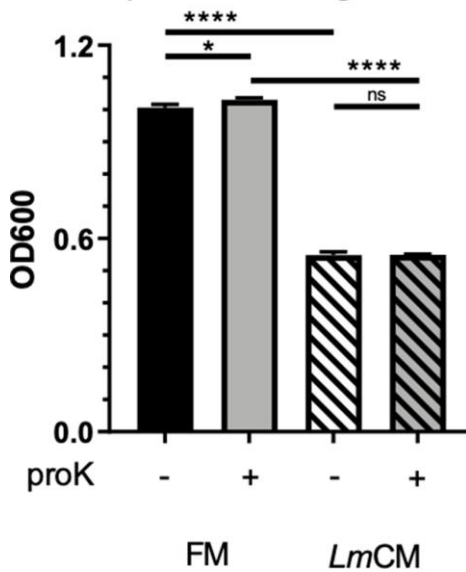


Figure 5 – supplement 1: Active substance in LmCM causing growth inhibition on *S. pneumoniae* is not protein in nature. *S. pneumoniae* cultures were grown for 6 hr in presence of mock or proteinase K (proK) treated FM and LmCM. Culture growth was measured by OD600. Representative data from two independent experiments are depicted as mean \pm SD (n = 3). Student t-test was applied for significance test.

Figure 5 – supplement 2
S. pneumoniae growth

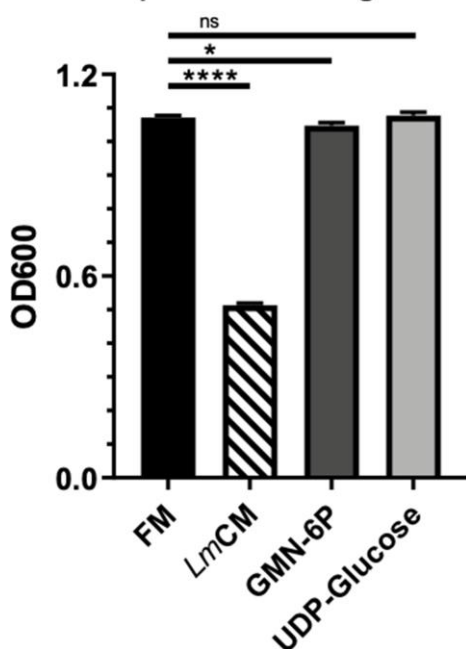


Figure 5 – supplement 2: Mass spectrometry identified hits from LmCM do not cause similar growth inhibition on *S. pneumoniae* cultures. *S. pneumoniae* cultures were grown for 6 hr in presence of FM, LmCM, Glusamine-6-phosphate (10 mM) or UDP-glucose (10 mM). Culture growth was measured by OD600. Representative data from two independent experiments are depicted as mean \pm SD (n = 3). Student t-test was applied for significance test.

Figure 5 – supplement 3

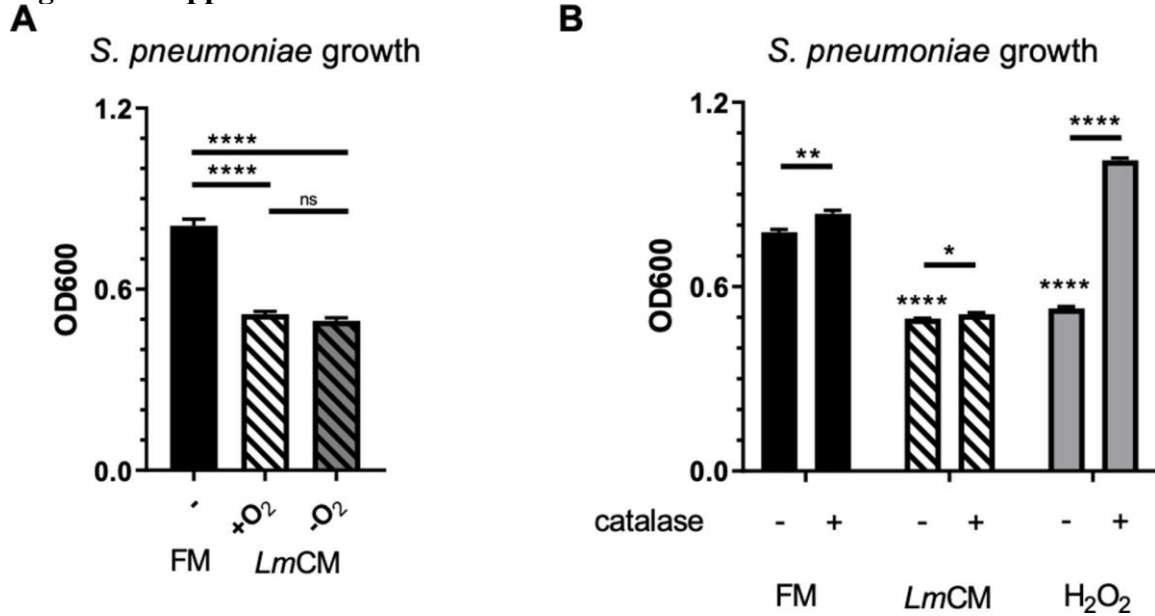


Figure 5 – supplement 3: LmCM dependent suppression of *S. pneumoniae* growth does not rely on reactive oxygen species. Hydrogen peroxide, causing similar growth inhibition on *S. pneumoniae* cultures, is not the active substance in LmCM. (A) *S. pneumoniae* cultures grown for 6 hr in presence of FM or media conditioned by *L. murinus* in aerobic (+O₂) or hypoxic environment (-O₂). Culture growth was measured by OD600. Representative data from two independent experiments are depicted as mean ± SD (n = 3). Student t-test was applied for significance test. (B) *S. pneumoniae* cultures grown for 6 hr in presence of mock or catalase treated FM, LmCM or Hydrogen peroxide solution (H₂O₂, 3.26 mM). Culture growth was measured by OD600. Mean ± SD are depicted in the graph (n = 3). Student t-test was applied for significance test in comparison to fresh media treated group unless otherwise stated by the arrows.

Figure 8 – supplement 1

A Lactic Acid in BALs - GS-MS Lactic Acid in BALs (Conc.) - Kit

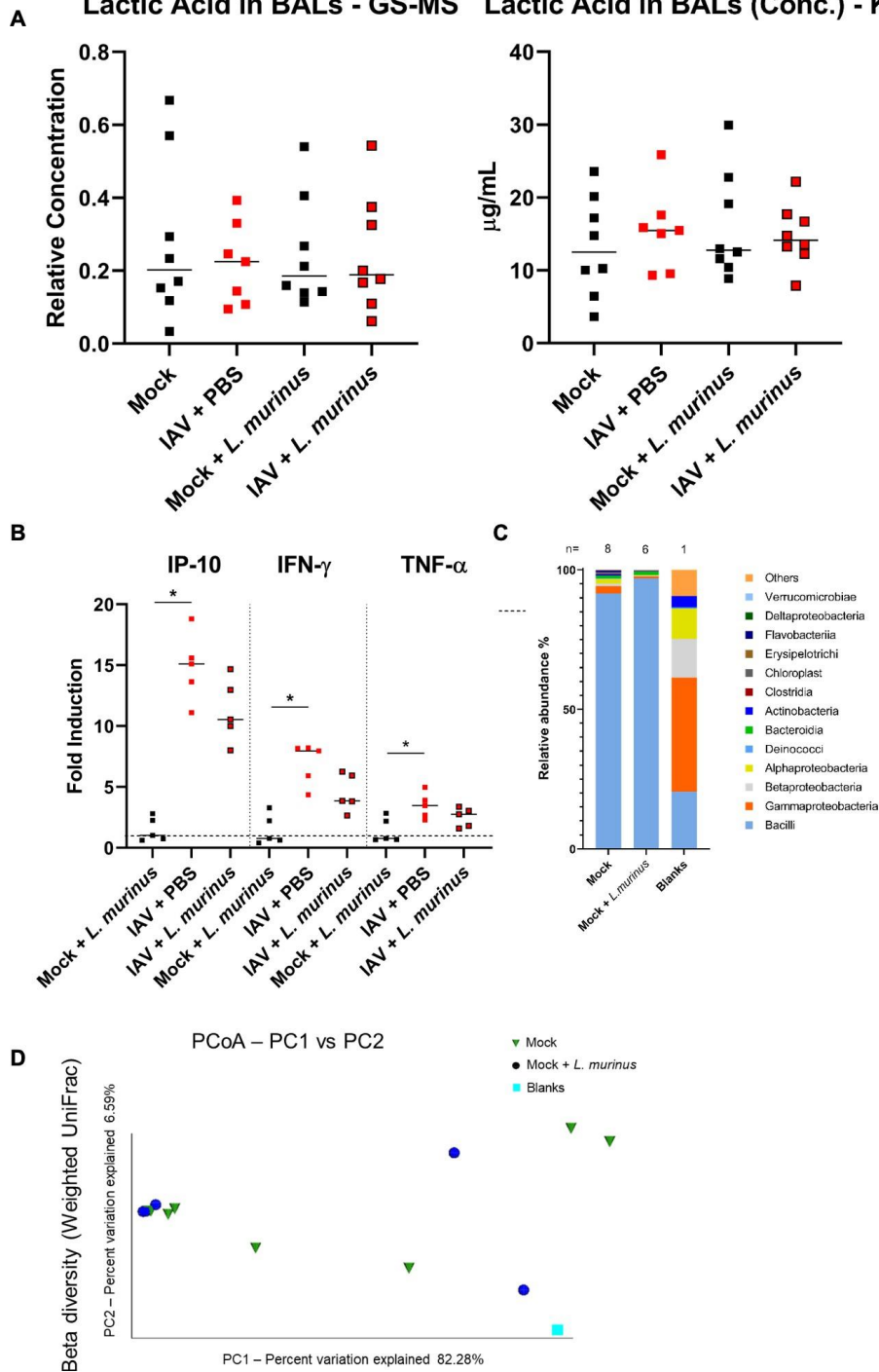


Figure 8 – supplement 1: Probiotic treatment with *L. murinus* does not alter lactic acid levels, inflammatory response or composition of commensal lung bacteria.

(A) Lactic acid in BALF was determined from $n = 7-8$ mice per group, 3 days post colonization with mock or *L. murinus* using GC/MS (left) or an LDH based assay (right) ($n = 7-8$ animals/group). Median values are indicated. Each dot represents an individual animal. (B) Specific qPCR for mRNA of indicated cytokines from total lung RNA of mice ($n = 4-5$ /group) colonized for 3 days with mock or *L. murinus*. Median values are indicated. (C) Relative composition of SPF mouse lung microbiota based on 16S-specific rRNA gene sequencing from $n = 6-8$ mice or blank. Bacterial classes are depicted. (D) Beta-diversity of mock treated or *L. murinus* challenged SPF mice 2 days post colonization. Each dot represents an individual mouse.

8.2. Influenza A viruses balance ER stress with host protein synthesis shutoff

Beryl Mazel-Sanchez¹, Justyna Iwaszkiewicz², Joao P P Bonifacio¹, Filo Silva¹, Chengyue Niu¹, Shirin Strohmeier³, Davide Eletto⁴, Florian Krammer³, Gene Tan^{5,6}, Vincent Zoete², Benjamin G Hale⁴, Mirco Schmolke⁷

¹*Department of Microbiology and Molecular Medicine, University of Geneva, 1211 Geneva, Switzerland.*

²*Molecular Modelling Group, Swiss Institute of Bioinformatics, 1015 Lausanne, Switzerland.*

³*Department of Microbiology, Icahn School of Medicine at Mount Sinai, New York, NY 10029.*

⁴*Institute of Medical Virology, University of Zürich, 8057 Zürich, Switzerland.*

⁵*Infectious Diseases, J. Craig Venter Institute, La Jolla, CA 92037.*

⁶*Division of Infectious Diseases, Department of Medicine, School of Medicine, University of California San Diego, La Jolla, CA 92093.*

⁷*Department of Microbiology and Molecular Medicine, University of Geneva, 1211 Geneva, Switzerland*

Status:

Manuscript published in Proceedings of the National Academy of Sciences of the United States of America – PMID: 34479996

Summary:

Viral infections induce tremendous stress to the endoplasmic reticulum (ER) by overloading the protein folding machinery of the host cell. To counteract this excessive protein production demand, the unfolded protein response (UPR) is launched aiming to reestablish proteostasis, e.g. by providing more ER resident chaperons and increasing ER volume. Failure of this compensatory mechanism results in cell death, an undesirable outcome both for the host and virus. On the other hand, viruses benefit from the induction of UPR by increasing the potential to fold more glycoproteins in a given time frame. In this project, we asked if influenza A virus (IAV) developed means to tune ER stress induction to a beneficial level for viral replication. We first established the determinant for ER stress and UPR induction during infection and identified neuraminidase to be the major determinant for ER stress induction. Moreover, IAV relieves ER stress by expression of its nonstructural protein 1 (NS1). We show that NS1 interferes with the host factor CPSF30 and suppresses UPR elements, such as XBP1. This effect was independent on the interferon signaling pathway and reproducible using air-liquid interface cultures from the human upper respiratory tract. In vivo, viral replication is increased when NS1 antagonizes ER stress induction. Our results reveal how IAV optimizes glycoprotein expression by balancing the folding capacity.

Personal Contribution:

For this work, I performed the infection and qPCR experiments in ALI cultures of the human respiratory tract (Figures 5C and 5D) and in the murine LA4 lung cell line (Figure S4)



Influenza A viruses balance ER stress with host protein synthesis shutoff

Beryl Mazel-Sanchez^a, Justyna Iwaszkiewicz^{b,1}, Joao P. P. Bonifacio^{a,1}, Filo Silva^a, Chengyue Niu^a, Shirin Strohmeier^c, Davide Eletto^d, Florian Krammer^c, Gene Tan^{e,f}, Vincent Zoete^b, Benjamin G. Hale^d, and Mirco Schmolke^{a,2}

^aDepartment of Microbiology and Molecular Medicine, University of Geneva, 1211 Geneva, Switzerland; ^bMolecular Modelling Group, Swiss Institute of Bioinformatics, 1015 Lausanne, Switzerland; ^cDepartment of Microbiology, Icahn School of Medicine at Mount Sinai, New York, NY 10029; ^dInstitute of Medical Virology, University of Zürich, 8057 Zürich, Switzerland; ^eInfectious Diseases, J. Craig Venter Institute, La Jolla, CA 92037; and ^fDivision of Infectious Diseases, Department of Medicine, School of Medicine, University of California San Diego, La Jolla, CA 92093

Edited by Yoshihiro Kawaoka, University of Wisconsin–Madison, Madison, WI, and approved July 15, 2021 (received for review December 9, 2020)

Excessive production of viral glycoproteins during infections poses a tremendous stress potential on the endoplasmic reticulum (ER) protein folding machinery of the host cell. The host cell balances this by providing more ER resident chaperones and reducing translation. For viruses, this unfolded protein response (UPR) offers the potential to fold more glycoproteins. We postulated that viruses could have developed means to limit the inevitable ER stress to a beneficial level for viral replication. Using a relevant human pathogen, influenza A virus (IAV), we first established the determinant for ER stress and UPR induction during infection. In contrast to a panel of previous reports, we identified neuraminidase to be the determinant for ER stress induction, and not hemagglutinin. IAV relieves ER stress by expression of its nonstructural protein 1 (NS1). NS1 interferes with the host messenger RNA processing factor CPSF30 and suppresses ER stress response factors, such as XBP1. In vivo viral replication is increased when NS1 antagonizes ER stress induction. Our results reveal how IAV optimizes glycoprotein expression by balancing folding capacity.

ER stress | influenza virus | neuraminidase | NS1 | CPSF30

Viruses are obligate intracellular parasites, which rely entirely on the host cell machinery for synthesis of viral proteins. Both host and viral surface glycoproteins are synthesized in the cytosol and are then quickly directed to the endoplasmic reticulum (ER). Here, they are folded by ER chaperones and can undergo posttranslational modification with the addition of N-linked glycosylations or disulphide bonds (1). The amount of free ER chaperones and ER resident enzymes required for posttranslational modification limit the capacity of the ER to fold newly synthesized proteins. Under physiological conditions, the ER folding capacity is adjusted to the cell's demand. However, during viral infection, the sudden need to process large amounts of viral glycoproteins can drive the ER beyond its folding capacity. In such cases, unfolded and/or misfolded proteins accumulate in the ER, causing ER stress and triggering the unfolded protein response (UPR). The ER chaperone binding immunoglobulin protein (BiP), a member of the heat shock protein family, is a master sensor of the UPR that recognizes misfolded protein accumulation (2–4). Low levels of misfolded proteins do not exceed the steady-state pool of BiP in the ER. In this steady state, a proportion of BiP is bound by the ER transmembrane sensors inositol-requiring enzyme 1 α (IRE1 α), protein kinase R-like ER kinase (PERK), and activated transcription factor 6 (ATF6) and keeps them in an inactive state. However, accumulation of misfolded proteins recruits BiP away from all three sensors, which triggers three specific signaling cascades in the cytoplasm that, in concert, aim to restore proteostasis by increasing the amount of ER chaperones (including BiP), as well as ER size (2, 5). For example, when activated, IRE1 α dimerizes, autophosphorylates, and triggers the specific cytoplasmic splicing of X-box binding protein 1 (XBP1) messenger RNA (mRNA). The spliced XBP1

(sXBP1) mRNA is translated into a functional transcription factor (6) responsible for activation of UPR-related genes (7, 8). In the case the UPR fails to return the balance between ER folding machinery and glycoprotein production, apoptosis will be induced (9). While apoptosis of the host cell may not be a key aim of the virus, one could imagine that expansion of the folding capacity in the ER would be beneficial for production of viral progeny.

Influenza A viruses (IAV) are segmented negative-sense RNA viruses that infect human airway epithelial cells. Like other viruses, they rely heavily on the ER function to produce their two envelope glycoproteins, hemagglutinin (HA) and neuraminidase (NA), as well as the transmembrane protein M2. The ER maturation steps of both IAV HA and NA were extensively studied (10–13). For both HA and NA, the folding of the monomer is guided by the ER lectin chaperones calnexin (CNX) and calreticulin (CRT), which are recruited via N-linked glycosylation (14). The monomer is then stabilized by intramolecular disulphide bonds (15). For HA, trimers are formed in the ER or at the ER–Golgi interface (16). For NA, dimers are first formed in the ER by intermolecular disulfide bonds. These dimers are then assembled to tetramers, a step requiring glycosylation of NA as well as conformational changes both in the transmembrane domain and the head domain (17, 18). During the maturation process of glycoproteins, host proteins play the role of sentinels

Significance

As intracellular parasites, viruses depend on the host cell machinery to produce and fold viral proteins. Because the capacity to fold proteins is limited, excessive viral translation of glycoproteins leads to ER stress. Unresolved ER stress drives host cells into apoptosis. We identify the expression of neuraminidase as the molecular source of influenza A virus–induced ER stress. The virus naturally balances it by the limitation of host protein production through the viral host shutoff protein NS1. The host cell mounts an unfolded protein response, creating additional protein folding reserves. Ultimately, the virus uses the stress-induced protein production capacities of the host cell to its own replication advantage.

Author contributions: B.M.-S., J.I., V.Z., and M.S. designed research; B.M.-S., J.I., J.P.P.B., F.S., C.N., V.Z., and M.S. performed research; S.S., D.E., F.K., G.T., and B.G.H. contributed new reagents/analytic tools; B.M.-S., J.I., J.P.P.B., F.S., C.N., V.Z., and M.S. analyzed data; and B.M.-S., J.I., C.N., F.K., B.G.H., and M.S. wrote the paper.

The authors declare no competing interest.

This article is a PNAS Direct Submission.

Published under the PNAS license.

¹J.I. and J.P.P.B. contributed equally to this work.

²To whom correspondence may be addressed. Email: mirco.schmolke@unige.ch.

This article contains supporting information online at <https://www.pnas.org/lookup/suppl/doi:10.1073/pnas.2024681118/-DCSupplemental>.

Published September 3, 2021.

to ensure that all proteins are folded properly before they exit the ER. It is notably the role of the ER chaperone BiP, which can recognize both influenza HA and NA when they are misfolded (19, 20).

IAV infection was previously described to modulate ER stress. According to the literature, the most prominent viral glycoprotein (HA) is responsible for triggering ER stress. Lack of HA glycosylation in pandemic or zoonotic IAV strains has been associated with more ER stress induction in human cells and more immune pathology in whole organism mouse models (21, 22). The literature agrees that IAV activates the IRE1 α pathway (23–25), but there is more controversy concerning the PERK and ATF6 pathway (23, 24). Research has focuses on activation of the UPR by IAV. However, to date, no strategies used by IAV to limit ER stress have been described.

Here, we generated IAV strains in a targeted manner that induce either a weak or strong ER stress response following infection. By genetically exchanging the glycoproteins, we show that the viral NA is the master inducer of ER stress and UPR. ER resident amounts of NA and the predicted presence of amino acid stretch recognized by BiP determine the levels of the ER stress response during viral infection. Host cells respond by expanding the ER volume and providing more ER chaperones. We further show that controlling the production of host proteins is essential for the virus to counteract ER stress. This control is achieved by the IAV nonstructural protein 1 (NS1) blocking cleavage-polyadenylation specificity factor 30 (CPSF30) function, a key factor of the cellular polyadenylation complex (26, 27). The NS1 protein of IAV prevents binding of CPSF30 to cellular pre-mRNA, thereby preventing their correct maturation and limiting host protein production (28, 29). This function was initially attributed to antagonism of type I interferon and inflammatory response (30–32). Our results reveal an additional function of NS1 in limiting the host ER stress response to the benefit of IAV replication.

Results

Induction of ER Stress Varies among Viral Isolates. Previous studies showed that IAV activates ER stress. In order to define whether this is a general feature of IAV infection, or limited to certain viral strains, we infected A549 human lung epithelial cells with a panel of representative IAV laboratory strains and clinical isolates. Then we performed a RT-PCR to compare the amount of spliced XPB1 (sXPB1) mRNA. Infection with a high multiplicity of infection (MOI) resulted in similar infection levels between the different IAV strains, as indicated by the presence of comparable amounts of viral nucleoprotein (NP) in cell lysates 8 h postinfection (pi) (Fig. 1 *A, Lower*). All viruses, except A/Switzerland/9715293/13-like (H1N1) (CH13) and A/Wyoming/03/2003 (H3N2) (Wyo03), displayed a similar number of infected cells (*SI Appendix, Fig. S1A*). Strikingly, levels of the sXPB1 amplicon at the same time point were different (Fig. 1 *A, graph and Middle*). Two strains, A/Puerto Rico/8/1934 (H1N1) (PR8) and X31 (a chimeric virus with PR8 internal genes and HA and NA from A/Aichi/2/1968 [H3N2]), induced a significant increase in the amount of sXPB1 mRNA. In contrast A/Viet Nam/1203/2004 (H5N1-HALo) (an engineered low-pathogenic variant) (VN1203), Wyo03, A/Netherlands/602/2009 (pandemic H1N1) (Neth602) and two clinical isolates (A/Hong Kong/2212/10-like (H1N1) (HK10) and CH13 did not trigger splicing of XPB1 mRNA. We furthermore observed a reduction of unspliced XPB1 mRNA, as compared with mock, for cells infected with several IAV strains (*Upper band Fig. 1 A, Upper panel*). This suggests strain-specific mechanisms regulating expression or degradation of the XPB1 mRNA. In order to rule out kinetic differences in ER stress induction between viruses, we tested XPB1 splicing 4 h and 12 h pi in cells infected with VN1203 or PR8. As for 8 h pi these early and late time points did not reveal

XPB1 splicing in VN1203-infected cells (Fig. 1*B*). Notably, transient activation of XPB1 splicing by PR8 infection may suggest a balancing of the cellular and viral responses to ER stress induction. In order to demonstrate that PR8 infection induces a broad ER stress response, while VN1203 does not, we performed qPCR for genes that are up-regulated by the different ER stress sensor (Fig. 1*C*). We picked Erdj4 (IRE1 pathway), BiP (ATF6 pathway) (33), and CHOP and GADD34 [PERK (34) and ATF6 pathway (35)]. We could observe an induction of all genes in PR8-infected cells compared with VN1203-infected cells, thus showing that PR8 infection triggers all three arms of the UPR.

As a reaction to ER stress, cells enhance the folding capacity for glycoproteins by ER volume expansion and increased expression of ER resident chaperones. In order to determine the ER volume in mock versus IAV-infected cells, we analyzed confocal Z-stack images of A549 cells, using the ER resident chaperone BiP (green) as an ER volume marker, and CD44 (red) to define the outer perimeter of each cell. After subtraction of the nuclear volume (blue, DAPI stained), we determined the relative ER volume per cytoplasm volume per cell (Fig. 1 *D and E and SI Appendix, Fig. S1 B and C and Movies S1–S6*). We used tunicamycin (Tm) treatment as a positive control to validate our microscopy approach. In the context of PR8 viral infection, the ER volume (compared with mock-treated cells) doubled after 24 h (Fig. 1*D*). No significant differences in ER volume were detectable at the time point of maximum XPB1 splicing (8 h pi) (Fig. 1*D*). The delay between appearances of sXPB1 mRNA at 8 h postinfection as a direct response to ER stress and the increase of the ER volume at 24 h could be explained by the kinetics of the UPR (36). In contrast, in the context of VN1203 viral infection, which did not induce XPB1 mRNA splicing, we did not observe a change in the ER volume compared with mock-treated cells, and this at both 8 h and 24 h postinfection (Fig. 1*E and SI Appendix, Fig. S1C*).

Our data emphasize that the magnitude of ER stress and the UPR in context of IAV infection is virus strain dependent.

IAV Activates ER Stress in an NA-Dependent Manner. IAV displays two major glycoproteins on its surface, HA and NA, with HA being approximately 10 times more abundant than NA on virions (37). The current literature on IAV-induced ER stress solely focuses on HA as a trigger for ER stress. In order to assess which glycoprotein is the main ER stress inducer, we decided to exchange HA and NA between an IAV isolate, which induces ER stress (PR8) and one, which does not induce it (VN1203). Gene segments for HA and NA were swapped (separately or together) using reverse genetics. In contrast to previous findings, indicating HA as the main protein inducing ER stress, we found that PR8 with HA of VN1203 induces equal amounts of ER stress as PR8 (Fig. 2*A*) upon infection in A549 cells. Importantly, replacement of PR8 NA by VN1203 NA abolished XPB1 splicing after PR8 VN1203 NA infection, thus identifying NA as the inducer of ER stress response. This phenotype correlated well with the expression levels of NA. Of note, we insured that our panN1 antibody displayed equal binding to H5N1 and H1N1 NAs by testing whole cell lysates of cells transfected with plasmid expressing NA tagged with a V5 epitope and compared the panN1 antibody and an anti-V5 antibody (*SI Appendix, Fig. S2A*). Notably, the inverse approach (i.e., VN1203 expressing PR8 NA) did not trigger XPB1 splicing despite high amounts of PR8 NA present in the infected cells. This could argue for an additional negative regulation of ER stress by VN1203, but not PR8. In line with these findings, the detection of sXPB1 mRNA by PCR correlates well with the presence of sXPB1 protein as seen by Western blot (WB) (Fig. 2*A*).

In order to strengthen our conclusion that HA is not the glycoprotein inducing ER stress during infection, we took advantage of a recently published recombinant PR8 virus (38). In this virus, the

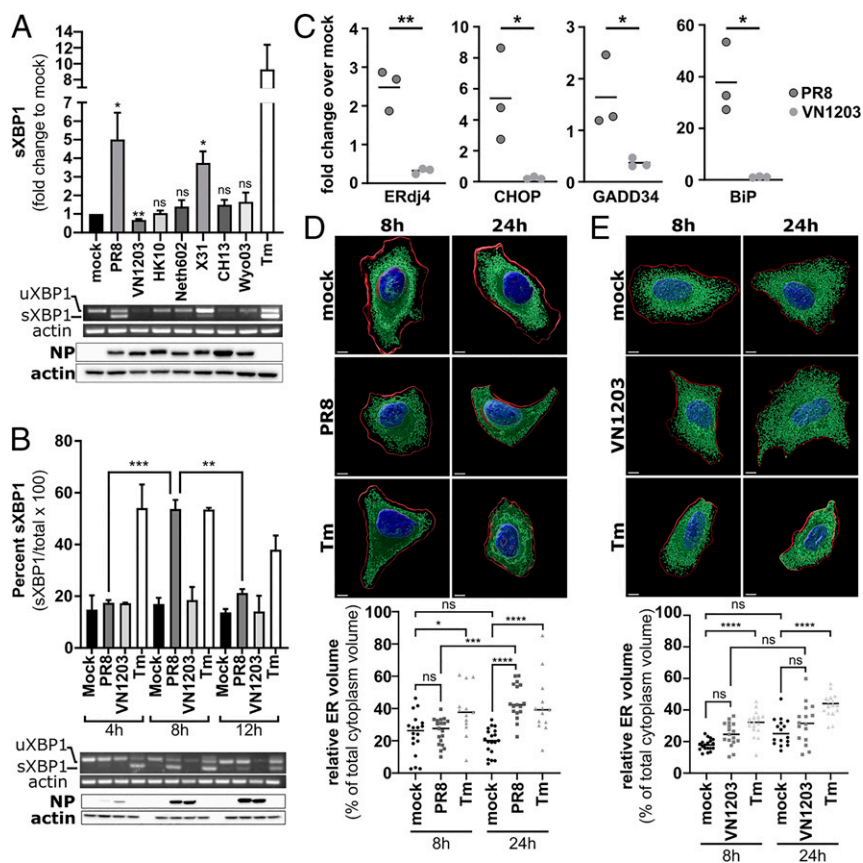


Fig. 1. Induction of ER stress varies among viral isolates. (A) A549 cells were infected at an MOI of 5 with the following strains: PR8 (A/Puerto Rico/8/1934 [H1N1]), VN1203 (A/Vietnam/1203/2004 [H5N1]), Neth602 (A/Netherlands/602/2009 [H1N1]), HK10 (A/Hong Kong/2212/10-like 2014 [H1N1]), X31 (PR8 internal genes with HA and NA from A/Aichi/2/1968 [H3N2]), CH13 (A/Switzerland/9715293/13-like 2014 [H3N2]), Wyo03 (A/Wyoming/03/2003 [H3N2]) or treated with PBS (mock) or Tm. Cells were collected 8 h postinfection and analyzed by semiquantitative RT-PCR and WB (for viral protein NP and actin), respectively. The graph represents mean with SD of the densitometry analysis of the sXBP1 mRNA ($n = 3$), and unpaired t test was used to compare each sample with mock. (B) A549 cells were infected at a MOI of 5 with PR8 and VN1203 or treated with PBS (mock) or Tm. Cells were collected 4 h, 8 h, and 12 h pi and analyzed by semiquantitative RT-PCR and WB. The graph represent means with SD of the densitometry analysis of the sXBP1 cDNA ($n = 2$). Time points were compared using one-way ANOVA with Tukey correction. (C) A549 cells were treated with PBS (mock) or infected at a MOI of 5 with PR8 or VN1203. At 8 h postinfection, cells were lysed and RNA was extracted and processed through RT-qPCR analysis for ER stress-related genes (ERdj4, CHOP, GADD34, and BiP). Each graph represents the fold change over mock for the indicated gene. Each dot represents one well and the bar represents the mean. Unpaired t test was used to compare viruses. (D and E) A549 cells were treated with PBS (mock) or Tm or infected at a MOI of 5 with either PR8 (D) or VN1203 (E). Cells were fixed 8 h and 24 h postinfection and processed for immunofluorescence. Z-stacks were analyzed. Images show 3D rendered representations of representative cells with the ER resident protein BiP in green, the plasma membrane marker CD44 in red, and the nucleus in blue. (Scale bars [Bottom Left], 5 μm). The graph below shows a quantification of the ER volume in an individual cell. Values are expressed in percentage of the cytoplasm volume. Each dot represents one cell and the median is represented by a line. The medians of each column were compared using one-way ANOVA with Tukey correction. ns $P > 0.05$, * $P \leq 0.05$, ** $P \leq 0.01$, *** $P \leq 0.001$, **** $P \leq 0.0001$.

untranslated promoter-containing regions were swapped between the HA and the NA segment (PR8 swap). In A549 cells infected with this virus, we observed a drastic reduction in the amount of HA, while the total expression of NA was only slightly increased (Fig. 2B). Importantly, the level of ER stress induced by PR8 swap was similar to the one induced by PR8. This isogenic control allowed us to rule out HA as the glycoprotein inducing ER stress.

In order to circumvent the complexity of viral replication, we individually expressed a panel of V5-tagged NAs from different viral strains using transfection. In this model system, we used a luciferase reporter activated by an IRE1 α -dependent cleavage of the XBP1 splicing motif (39). The induction of this reporter was also strain dependent, revealing that PR8 NA, but not VN1203 NA, is an inducer of ER stress when expressed in the absence of infection. Furthermore, we identified that induction can be triggered by a panel of NAs from a range of different IAVs, but this does not correlate with the amount of NA present in the cell (Fig. 2C). This result implies that specific characteristics of NA contribute to ER stress induction.

Furthermore, NA of Cal09 (whose amino acid sequence is 99.8% similar to the one of Neth602) was a strong inducer of the UPR when expressed individually (Fig. 2C and *SI Appendix, Fig. S2B*), while the full virus did not cause XBP1 splicing (Fig. 1A). These observations argue for the presence of a specific viral inhibitor of ER stress that is encoded by some viral isolates.

NA Activity and Glycosylation Pattern Are Not Determinants of ER Stress Induction. In order to better understand what defines the NA-dependent ER stress induction, we compared different properties of PR8 NA (as a strong inducer of XBP1 splicing and ATF6 activation) and VN1203 NA (as a noninducer of XBP1 splicing and a weak inducer of ATF6) (*SI Appendix, Fig. S2B*). First, we tested the impact of glycosylation, since increased glycosylation of the major surface antigen HA was associated with reduced ER stress induction (21). Based on the glycosylation motif N-X-S/T, PR8 NA is predicted to be glycosylated at five positions (N44, N58, N73, N131, and N220), while VN1203 NA is predicted to be glycosylated at three positions (N73, N131, and

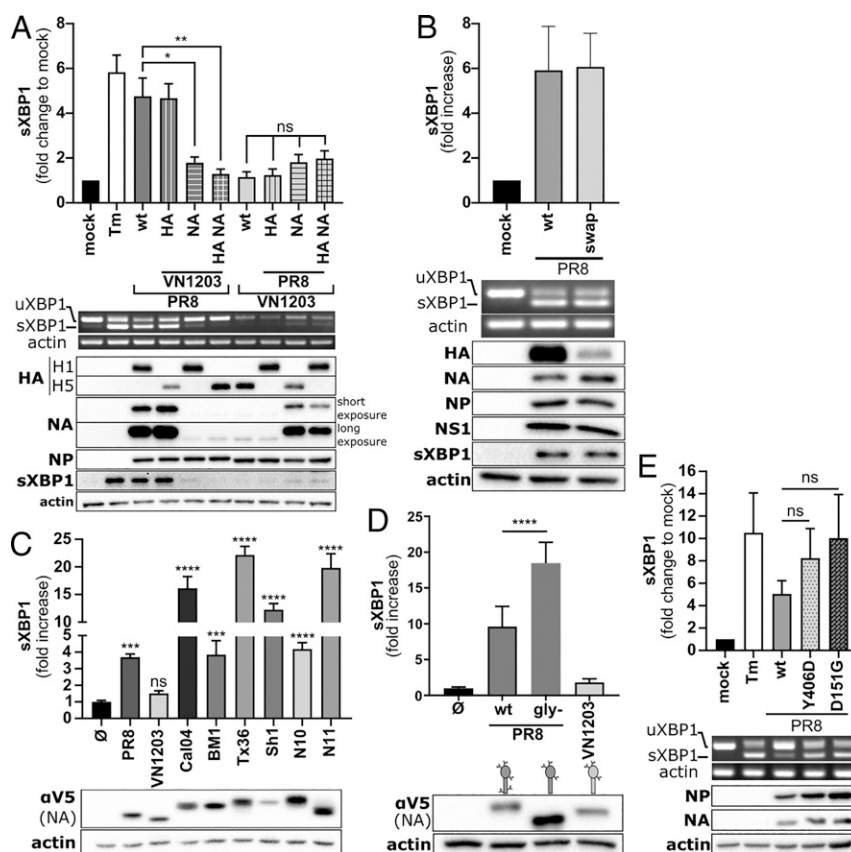


Fig. 2. IAV activates ER stress in a NA-dependent manner. (A) A549 cells were infected at a MOI of 5 with indicated WT and chimeric viruses or treated with PBS (mock) or Tm. Cells were collected 8 h postinfection and lysates were analyzed by semiquantitative RT-PCR and WB for viral proteins (HA, NA, and NP) and cellular proteins (sXBP and actin). The graph represents mean with SD of the densitometry analysis of the sXBP1 cDNA ($n = 3$) and one-way ANOVA with Dunnett correction was used to compare each mutant virus with its WT counterpart. (B) A549 cells were treated with PBS (mock) or infected at a MOI of 5 with PR8 or PR8 swap UTR viruses. Cells were collected 8 h postinfection and lysates were analyzed by semiquantitative RT-PCR and WB for viral proteins (HA, NA, NP, and NS1) and cellular proteins (sXBP1 and actin). The graph represents mean with SD of the densitometry analysis of the sXBP1 cDNA ($n = 3$). (C) The 293T cells were transfected with pFLAG-XBP1u-FLuc and pCAGGS empty vector (\emptyset) or pCAGGS encoding the V5-tagged neuraminidase from different viruses: PR8 (A/Puerto Rico/8/1934), VN1203 (A/Viet Nam/1203/2004), Cal04 (A/California/04/2009), BM1 (A/Brevig Mission/1/1918), Tx36 (A/Texas/36/1991), Stx4199 (A/Swine/Texas/4199-2/1998), Sh1 (A/Shanghai/01/2013), N10 (A/little yellow-shouldered bat/Guatemala/153/2009 [H17N10]), and N11 (A/flat-faced bat/Peru/033/2010 [H18N11]). Cells were lysed 24 h posttransfection. Lysates were subjected to luciferase activity measurement and WB analysis using anti-V5 antibody. The graph represents the mean fold increase luciferase activity normalized to mock with SD of triplicate ($n = 3$) and one-way ANOVA with Dunnett correction was used to compare each condition with mock. (D) The 293T cells were transfected with pFLAG-XBP1u-FLuc and pCAGGS empty vector (\emptyset) or pCAGGS encoding different V5-tagged neuraminidases: PR8 NA, PR8 NA glycosylation mutant (gly-) and VN1203 NA. Cells were lysed 24 h posttransfection. Lysates were subjected to luciferase activity measurement and WB analysis using anti-V5 antibody. Graphs represent the mean fold increase luciferase activity normalized to mock with SD of triplicate ($n = 5$). Unpaired t test was used to compare the two PR8 viruses. (E) A549 cells were infected at a MOI of 5 with PR8 and PR8 neuraminidase mutants as indicated or treated with PBS (mock) or Tm. Cells were collected 8 h postinfection and analyzed by semiquantitative RT-PCR and WB. The graph represents mean fold change normalized to mock with SD of the densitometry analysis of the sXBP1 cDNA ($n = 3$), and one-way ANOVA with Dunnett correction was used to compare each mutant virus with its WT counterpart. ns $P > 0.05$, $*P \leq 0.05$, $**P \leq 0.01$, $***P \leq 0.001$, $****P \leq 0.0001$.

N220) (PR8 NA numbering). By removing two predicted glycosylation sites in PR8 NA (N44A and N58A), we mimicked the predicted glycosylation pattern of VN1203 NA. This PR8 NA glycosylation mutant migrated faster in sodium dodecyl (lauryl) sulfate–polyacrylamide gel electrophoresis (SDS-PAGE) under reducing conditions, indicating that the predicted sites are indeed glycosylated. In contrast to published findings on HA glycosylation (21), removal of glycosylation sites enhanced the specific capacity of PR8 NA to induce ER stress (Fig. 2D). This could be explained by the increased amount of NA present in the cell and/or by potential misfolding of the mutant PR8 NA.

Next, we turned to possible differences in the enzymatic function of the two neuraminidases. Using an enzyme-linked assay, we compared the sialidase activities of purified, insect cell–expressed PR8 NA and VN1203 NA. In this assay, PR8 NA displayed a greater specific sialidase activity (SI Appendix, Fig. S2 C, Top). We obtained the same result using whole virions

normalized to the same plaque-forming units (pfu) (SI Appendix, Fig. S2 C, Lower). However, introduction of amino acid substitutions in the catalytic site of PR8 NA (D151G or Y406D), which lower enzymatic activity (40, 41), did not reduce ER stress induction during PR8 infection (Fig. 2E). In order to independently corroborate this result, we took advantage of the recently identified bat influenza A virus neuraminidases N10 and N11, which are devoid of intrinsic sialidase activity (42, 43). The two bat IAV NAs were strong inducers of ER stress when overexpressed (Fig. 2 C, Right). Taken together, these results argue against both glycosylation pattern and neuraminidase activity being defining features of NA responsible for ER stress induction.

NA Amount in the ER and BiP Binding Correlate with ER Stress Induction. Up to this point, we only accounted for total NA amounts. However, ER stress would presumably depend on ER-localized NA. Indeed, accumulation of misfolded or unfolded

viral glycoproteins is proposed to lead to ER stress (25, 44). In general, misfolded glycoproteins in the ER are actively transported from the ER to the cytoplasm by the ERAD machinery, where they undergo proteasomal degradation (45). To test the possibility that NA overload in the ER is responsible for ER stress, we blocked the retrograde ER-cytoplasmic transport of misfolded proteins with kifunensine and measured ER stress induction using the XBP1 luciferase reporter assay (Fig. 3A) (46). Cells transfected with an empty plasmid and treated with kifunensine did not show any increase in XBP1 splicing. This shows that the ER of cells in a physiological state is not under stress, even if the ERAD pathway is blocked. However, following overexpression of PR8 NA, we observed a dose-dependent increase of XBP1 splicing. This effect was clearly increased by kifunensine. In contrast, overexpression of VN1203 NA did not cause ER stress in the presence of kifunensine. However, the baseline expression of this NA was substantially lower than that of PR8. This result confirms that for NAs with the intrinsic capacity to induce ER stress, the ER resident portion of the protein constitutes the main trigger.

BiP is a key sensor for unfolded proteins in the ER lumen. We used the method developed by Schneider et al. to predict the potential BiP binding site in different NA proteins (47). BiPPred evaluates the BiP binding probability and gives a forward and

reverse score for each consecutive 7 amino acid stretch of a given protein sequence. The probability of a given peptide being a BiP binding site is attributed a score between 0 (minimal) and 1 (maximal). In our analysis, we counted the total number of peptides scoring 0.8 or higher. We hypothesized two potential scenarios, in which 1) NA is fully unfolded and accessible to BiP or 2) only unstructured regions are bound by BiP. Obviously, both scenarios could take place in parallel during infection. When looking at the whole protein sequence of NA (scenario 1), we established that there is a significant correlation between the total number of peptides scoring equal or higher than 0.8 and the capacity of the protein to induce ER stress (Fig. 3B). However, glycoproteins are rapidly folded upon synthesis at the ER membrane; thus we also evaluate the number of peptides recognized by BiP within the intrinsically disordered or exposed part of NA, which are the N-terminal 75 to 95 amino acids and the internal exposed loop whose sequences are described in *SI Appendix, Tables S1 and S2*, respectively (scenario 2). We chose to focus on those two features of the NA because, according to the model, they should be exposed even when the NA monomer is fully folded. As for the full NA sequence, we could observe a good correlation between the number of peptides with a high probability of BiP binding and the induction of ER stress (Fig. 3C). Accumulation of NA in the ER could at a certain point

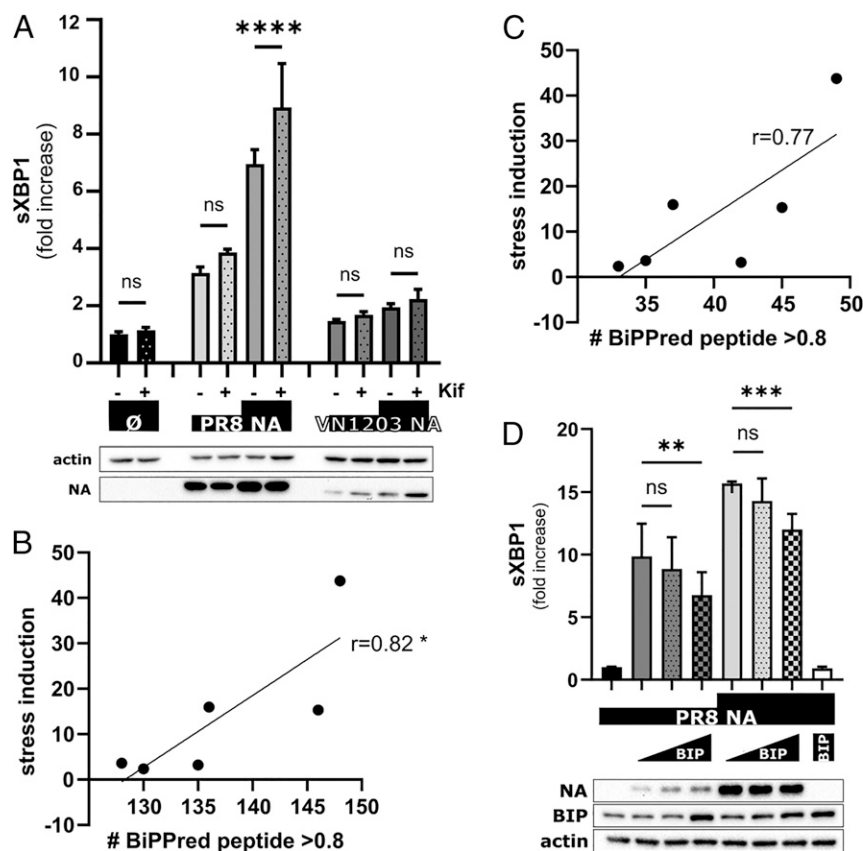


Fig. 3. NA amount in the ER and NA/BiP interaction play a role in ER stress induction. (A) The 293T cells were transfected with pFLAG-XBP1u-FLuc and pCAGGS empty vector (\emptyset) or pCAGGS encoding V5-tagged PR8 NA at different amounts. At 6 h posttransfection, cells were treated with kifunensine for 24 h and lysed. Lysates were subjected to luciferase activity measurement and WB analysis using an anti-V5 antibody. Graphs represent the mean fold increase over mock with SD of technical triplicates ($n = 2$). One-way ANOVA with Turkey correction was used for statistical analysis. (B and C) Correlation between predict differences in the number of peptide with a BiPPred score higher than 0.8 for the whole NA (B) or the internal loop and the N terminus of NA (C) and specific induction of ER stress (normalized to NA amount). (D) The 293T cells were transfected with pFLAG-XBP1u-FLuc, pCAGGS empty vector (\emptyset), or pCAGGS encoding V5-tagged PR8 NA and pCAGGS3.1(+)-GRP78/BiP. Cells were lysed 24 h posttransfection and lysates were subjected to luciferase activity measurement and WB analysis using an anti-V5 and anti-BiP antibody. Graphs represent the mean Firefly luciferase activity normalized to mock with SD of technical triplicates ($n = 2$). One-way ANOVA with Turkey correction was used for statistical analysis. ns $P > 0.05$, * $P \leq 0.05$, ** $P \leq 0.01$, *** $P \leq 0.001$, **** $P \leq 0.0001$.

exceed the pool of free BiP. We thus supplemented BiP to compensate NA overload in the ER (Fig. 3D). Overexpression of BiP alone did not modify the basal level of XBP1 reporter activity. However, in combination with PR8 NA overexpression, XBP1 splicing was decreased in a dose-dependent manner. These experiments show that NA accumulation in the ER triggers a stress response, with BiP being the limiting host factor. Taken together, these data suggest an important role for NA accumulation and BiP recognition in the induction of ER stress.

NS1-Induced Shutoff Inhibits ER Stress Induction. Up to this point, two findings suggested the presence of a virus-encoded inhibitor of ER stress responses: first, chimeric VN1203 displaying PR8 NA did not induce XBP1 splicing; and second, while exogenously expressed Cal04 NA was a potent ER stress inducer, infection with a closely related virus (A/Netherlands/602/2009) did not cause XBP1 splicing in A549. Notably, we found that both PR8 and X31 viruses induced XBP1 splicing in infected A549. X31 is a chimeric virus that harbors HA and NA from A/Aichi/2/1968 (H3N2), while having the internal genes of PR8. In contrast, the clinical H3N2 isolate did not trigger ER stress. This points toward the existence of a viral inhibitor encoded by one or more of the remaining IAV segments 1, 2, 3, 5, 7, or 8, and which is potentially nonfunctional in PR8.

We hypothesized that one way of reducing the combined burden of host and viral protein folding on the ER is to reduce overall host protein synthesis. Two viral proteins, PA-X and NS1, have been particularly implicated in regulating general host protein expression, the so-called host protein shutoff. PA-X is an alternative translation product from segment 3 mRNA, sharing the endonuclease domain with PA, which resides in the cytoplasm and stress granules. PA-X was proposed to cleave host mRNAs (48, 49). The nonstructural protein 1 (NS1) targets CPSF30 and prevents polyadenylation of host mRNAs in the nucleus, which ultimately leads to mRNA degradation (28). When testing a PA frameshift mutant of PR8 and VN1203, we did not observe an increase in ER stress induction in infected A549s, as indicated by sXBP1 both at the mRNA level and protein level (Fig. 4A). These data suggest that PA-X is not a major antagonist of the IAV-induced ER stress response.

We next focused on the NS1 protein and its ability to bind CPSF30. Strikingly, NS1 of PR8 is known to lack the capacity to bind CPSF30 and block mRNA maturation, while the NS1 from VN1203 is a strong inhibitor of CPSF30, and the NS1 from Cal04 is partially functional, but largely inefficient (31, 32). In order to test specifically whether exogenous expression of NS1 relieves ER stress, we used a luciferase reporter assay for XBP1 splicing in cells treated or not with tunicamycin, and transfected a panel of NS1 constructs as indicated, to represent the different NS1/CPSF30 binding phenotypes (Fig. 4B). First, we observed that NS1 overexpression itself does not lead to induction of ER stress and we observed that, as previously described, NS1 inhibits its own expression when binding to CPSF30 (32). In addition, we found that the ability of NS1 to bind CPSF30 correlated well with its capacity to inhibit tunicamycin-induced ER stress: PR8 NS1 was unable to limit tunicamycin-induced ER stress despite expressing very well, while VN1203 NS1 was a potent inhibitor and Neth602 NS1 had a small effect (Fig. 4B). We observed the same correlation when testing a panel of NS1 proteins (Fig. 4C and *SI Appendix, Table S3*).

In order to confirm this correlation in functional tests, we introduced the NS1 binding mutations into the respective viruses using reverse genetics. We introduced nucleotide changes (*SI Appendix, Table S3*) into the NS segment in order to either induce binding of NS1 to CPSF30 or disrupt this ability. We generated two mutants that gained the ability to bind to CPSF30, i.e., PR8 NS1⁺ and Neth602 NS1⁺ and two mutants that lost the ability to bind CPSF30, i.e., VN1203 NS1⁻ and Neth602 NS1⁻. We used these viruses to confirm the gain or loss of binding of

NS1 to CPSF30. The 293T cells expressing a Flag-tagged human CPSF30 protein were infected with the different viruses, i.e., PR8, PR8 NS1⁺, VN1203, VN1302 NS1⁻, Neth602, Neth602 NS1⁻ and Neth602 NS1⁺. Cell lysates were subjected to immunoprecipitation (IP) using anti-Flag affinity beads. The Flag-CPSF30/NS1 complexes were analyzed by WB (Fig. 4D) and the relative amount of NS1 bound to CPSF30 was quantified (Fig. 4E). We observed that the NS1⁺ mutants, which have the amino acid sequence associated with CPSF30 binding phenotype, indeed bind more to CPSF30 than their cognate NS1 wild type (WT). On the other hand, NS1⁻ mutants bind less to CPSF30 than NS1 WT. Of note the presence of viral PA and NP during infection stabilizes the NS1/CPSF30 complex (50), which could explain the residual binding observed for PR8. We corroborated the binding data functionally with a surrogate assay for NS1-mediated host protein synthesis shutoff. Previous data have shown the link between efficient control of reporter gene expression and efficient binding of NS1 to CPSF30 (32). A constitutively active Gaussia luciferase reporter was coexpressed with each of the different NS1, and luciferase activity was measured 24 h posttransfection. We observed an enhanced expression of Gaussia luciferase with NS1⁻ mutants and a suppressed expression with NS1⁺ mutants (Fig. 4F). These data confirm that the mutations we introduced are involved in NS1/CPSF30 binding and more generally in host cell mRNA polyadenylation.

Next, we tested the ability of the NS1 mutants to inhibit tunicamycin-induced ER stress compared with their cognate NS1. In accordance with our pulldown experiment, the NS1 CPSF30 binding “gain-of-function” mutant of PR8 (NS1⁺) blocked XBP1 reporter activation (Fig. 4G). Inversely, loss of CPSF30 binding in VN1203 NS1 (NS1⁻) abolished its inhibitory function on XBP1 splicing (Fig. 4H). Lastly, Neth602 NS1 displays an intermediate CPSF30 binding phenotype, and introduction of a strong CPSF30 binding interface increases its XBP1 antagonistic function, while introduction of a weak interface removes this capacity (Fig. 4I).

Then, we tested the ability of NS1 to inhibit or not the induction of ER stress in the context of infection. We could recapitulate the effect in A549 infected with PR8: when PR8 NS1 can functionally bind CPSF30, ER stress induction in infected cells is inhibited when measuring levels of sXBP1 by RT-PCR (Fig. 4J), despite similar expression of the ER stress inducing PR8 NA (Fig. 4K). We also found matching host responses (BiP induction and sXBP1 levels) at the protein level (Fig. 4K, protein quantification of sXBP1 below). For cells infected with VN1203 NS1⁻, we did not observe induction of ER stress, presumably because the VN1203 NA fails to induce this stress response irrespective of the function of NS1. Unexpectedly, engineered NS1 mutants of the Neth602 strains also behaved like the parental virus with regards to ER stress induction, possibly indicating that this strain has evolved additional uncharacterized inhibitors of this pathway (*SI Appendix, Fig. S3 A and B*). However, Neth602 NS1⁺ also displayed more NA upon infection, which might shield the results (*SI Appendix, Fig. S3 A and B*).

In order to delineate whether NS1-dependent antagonism of ER stress by CPSF30 binding depends on the antagonism of type I interferon or is an independent function, we took advantage of A549 cell lines lacking the expression of either the retinoic acid-inducible gene I (RIG-I) or the signal transducer and activator of transcription 1 (STAT1) (*SI Appendix, Fig. S3C*). RIG-I is the bona fide cytosolic sensor responsible for the induction of type I interferon expression in IAV-infected epithelial cells. STAT-1 is a key signaling molecule downstream of the IFN type I receptor and directly responsible for the transcription of interferon-stimulated genes (ISGs). Importantly, inhibition of ER stress induction during infection occurs independently of a functional host type I interferon system. Indeed, we observe that both A549 RIG-I^{-/-} and STAT1^{-/-} cells respond with comparable levels of XBP1 splicing as A549 WT to infection with PR8, VN1203, or Neth602 (Fig. 4L).

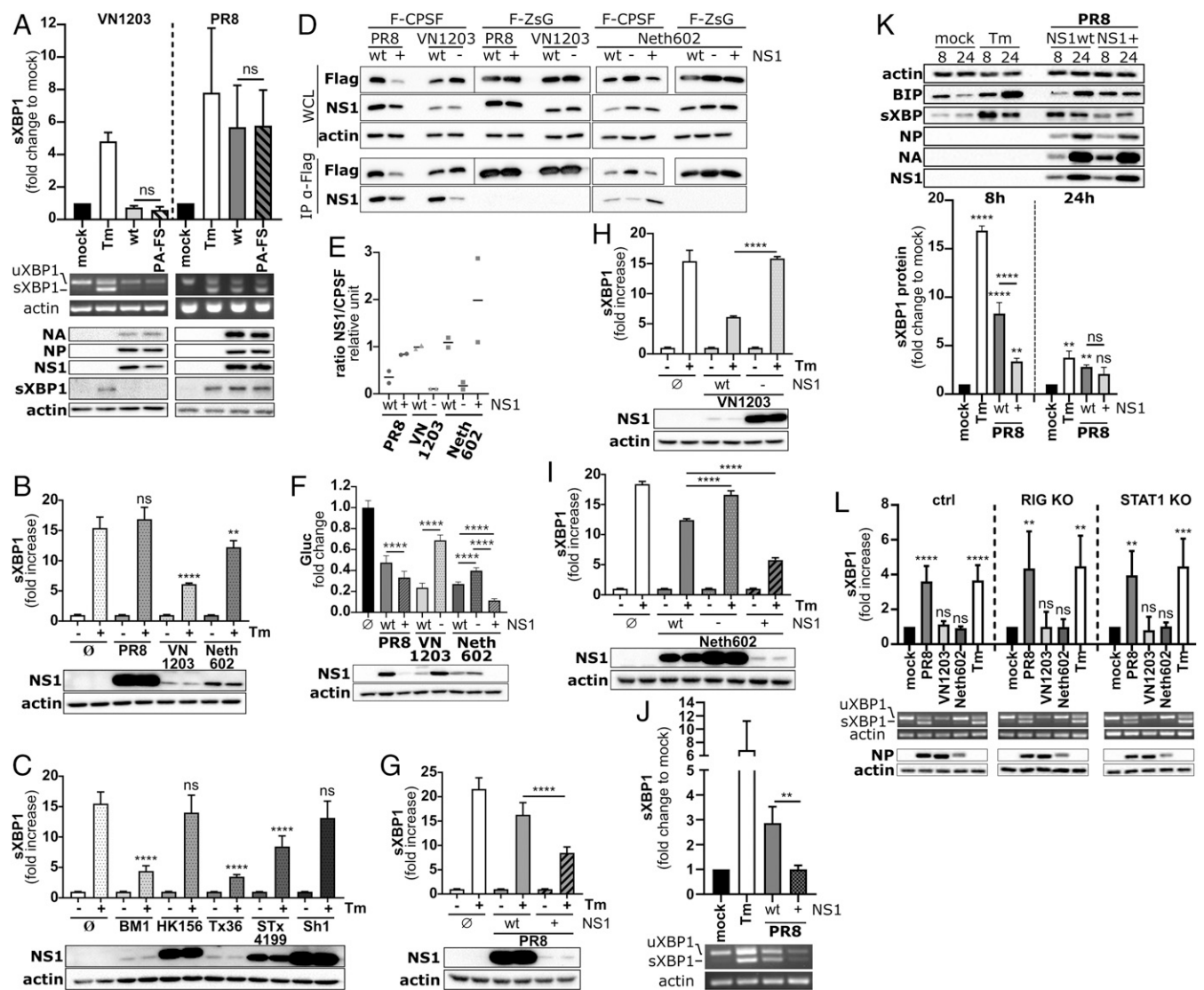


Fig. 4. NS1 prevents UPR, independently of IFN signaling, through its CPSE30 binding ability. (A) A549 cells were treated with PBS (mock) or Tm or infected at a MOI of 5 for 8 h with VN1203 or PR8 or the isogenic PA frameshift (PA-FS) mutants ($n = 3$). At 8 h postinfection, cells were lysed and analyzed by semi-quantitative RT-PCR and WB for viral proteins (NA, NP, and NS1) and the cellular proteins (XBP1 and actin). The graph represent mean with SD of the densitometry analysis of the sXBP1 cDNA ($n = 3$) and unpaired t test was used to compare WT and mutant viruses. (B and C) The 293T cells were transfected with pFLAG-XBP1u-FLuc and pCAGGS empty vector (\emptyset) or pCAGGS encoding NS1 proteins from different viruses: PR8, VN1203, Neth602, BM1, HK156 (A/Hong Kong/156/1997), Tx36, Stx4199 (A/Swine/Texas/4199-2/1998), and Sh1. At 16 h posttransfection, cells were treated with solvent or tunicamycin and lysed 8 h posttreatment. Lysates were subjected to luciferase activity measurement and WB analysis using anti-NS1 antibody. For each condition the luciferase activity of the treated sample was normalized to the untreated. Graphs represent the mean fold increase with SD of triplicate ($n = 2$). One-way ANOVA with Dunnett correction was used to compare treated samples with mock. (D and E) The 293T cells were transfected with pCAGGS.Flag-CPSE30 (F-CPSF) or pCAGGS.Flag-ZsGreen (F-ZsG) for 24 h prior to infection with either PR8, PR8 NS1⁺, VN1203, VN1203 NS1⁻, Neth602, Neth602 NS1⁻, or Neth602 NS1⁺. Anti-Flag M2 affinity beads were used to IP the Flag-tagged proteins and their interactors. (D) Results were analyzed by WB using anti-Flag antibody and anti-NS1 antibody. (E) The amount of NS1 protein bound to Flag-CPSE30 was quantified using densitometric analysis ($n = 2$). (F) The 293T cells were transfected with pCMV.Gluc (M601) and pCAGGS empty vector (\emptyset) or pCAGGS expressing different NS1 as indicated. Supernatants were analyzed to luciferase activity measurement and cell lysates to WB analysis using anti-NS1 antibody. The luciferase activity was normalized to one transfected with the Gluc-expressing plasmid and the empty vector. Graphs represent the mean fold increase with SD of triplicate ($n = 3$). (G–I) The 293T cells were transfected with pFLAG-XBP1u-FLuc and pCAGGS empty vector (\emptyset) or pCAGGS encoding NS1 proteins from different viruses as indicated. At 16 h posttransfection, cells were treated with solvent or tunicamycin and lysed 8 h posttreatment. Lysates were subjected to luciferase activity measurement and WB analysis using anti-NS1 antibody. For each condition the luciferase activity of the treated sample was normalized to the untreated. Graphs represent the mean fold increase with SD of triplicate. Tm-treated conditions were compared using unpaired t test in G and H while we used one-way ANOVA in I. (J and K) A549 cells were treated with PBS (mock) or Tm or infected at a MOI of 2 with PR8 and PR8 NS1⁺ as indicated ($n = 3$). (J) Cells were lysed 8 h postinfection and subjected to semiquantitative RT-PCR. The graph represents mean with SD of the densitometry analysis of the sXBP1 cDNA, and unpaired t test was used. (K) Cells were lysed at the indicated time point and analyzed by WB for host proteins (actin, BiP, and XBP1) and viral proteins (NP, NS1, and NA). Exposures shown are the same for all samples. The WB shown is representative of three experiments. The amount of sXBP1 protein was quantified using densitometric analysis and the graph represents the mean fold increase in XBP1 protein amount over mock with SD. Samples within the same time point were compared using multiple comparison one-way ANOVA with Turkey correction. (L) A549 ctrl, RIG1 knockout (KO), and STAT1 KO cells were infected with PR8, VN1203, or Neth602 at a MOI of 5. Cells were lysed 8 h pi and subjected to semi-quantitative RT-PCR and WB analysis. The graph represents mean with SD of the densitometry analysis of the sXBP1 cDNA (for each cell type the results for two clones were pooled, $n = 2$), and one-way ANOVA with Dunnett correction was used to compared each virus with mock within each cell line. ns $P > 0.05$, * $P \leq 0.05$, ** $P \leq 0.01$, *** $P \leq 0.001$, **** $P \leq 0.0001$.

These results define an additional role for NS1 in modulating antiviral host responses.

NS1 CPSF30 Binding Ability Confers a Replication Advantage In Vivo and Prevents UPR in Three-Dimensional (3D) Human Epithelial Airways.

In order to assess whether the binding of NS1 to CPSF30 confers an overall advantage to the virus in vivo, we inoculated groups of six mice with phosphate buffer saline (PBS) or 40 pfu of PR8 or PR8 NS1⁺. Mouse weights were monitored daily (Fig. 5A) and viral titer was determined on days D2, D4, and D6 pi (Fig. 5B). PR8 NS1⁺ shows a growth advantage from 2 d postinfection (dpi) with this advantage beginning to be statistically significant at 4 and 6 dpi. This replication phenotype was reflected in mice weight. Indeed, mice infected with PR8 NS1⁺ lost weight faster than the ones infected with PR8 (most prominent at 6 dpi) Our results indicate that the capacity of NS1 to bind and antagonize CPSF30 confers a replicative advantage to the virus in vivo. Mechanistically, data from infected murine lung epithelial cells (LA4) suggest that as in human cells, NS1 binding to CPSF30 reduces the UPR as indicated by specific qPCR for DNAJb9 (mouse homolog to ERdj4) (SI Appendix, Fig. S4).

Finally, we tested the NS1 mutant viruses in a stratified primary human airway epithelial cell model, cultured in an air-liquid interface. We infected these cells apically with PR8, PR8 NS1⁺, VN1203, and VN1203 NS1⁻. RNA was extracted 24 h pi and processed for RT-qPCR analysis. First, we determined viral replication using M1 cDNA copies as a surrogate marker. Within each virus pair, WT and mutant viruses replicated to the same level (Fig. 5C). Then, we performed qPCR for the ER stress-related genes ERdj4, CHOP, and BiP (Fig. 5D). In the case of PR8, we observed a differential expression, with those genes

being down-regulated during PR8 NS1⁺ infection compared with PR8. For VN1203, the expression of ERdj4 and BiP are the same for the two viruses, while CHOP expression is slightly increased in VN1203 NS1⁻ compared with VN1203. Taken together, these data confirm IAV NS1-dependent antagonism of host cell ER stress in a relevant primary human cell model in context of infection.

Discussion

Multiple papers have identified that modification in the glycosylation pattern of the HA have an impact on the host inflammatory response and overall virus virulence in vivo (51, 52). This increased virulence was later linked to ER stress induction. More specifically removing glycosylation sites on HA was associated with higher ER stress levels and higher virulence, while addition of glycosylation sites was associated with reduced ER stress and reduced virulence (21, 22). These results are probably in line with the observation that N-linked glycans are important for glycoprotein stability and folding and that mutants might enter a misfolded state easier (14).

To date, the role of NA in ER stress induction was not investigated. We demonstrate here by combining genetic, biochemical, and cell biological approaches that in fact expression of the minor glycoprotein NA is the major determinant for ER stress induction during IAV infection. In order to assess ER stress response induced by IAV, we largely relied on measurement of XBP1 splicing as a surrogate marker for the overload of the ER protein folding machinery. Indeed, splicing of XBP1 mRNA is a direct readout for IRE1 α activation. While we do not believe this diminishes our findings in general, we believe a detailed assessment of the remaining PERK and ATF6 pathways would be of interest.

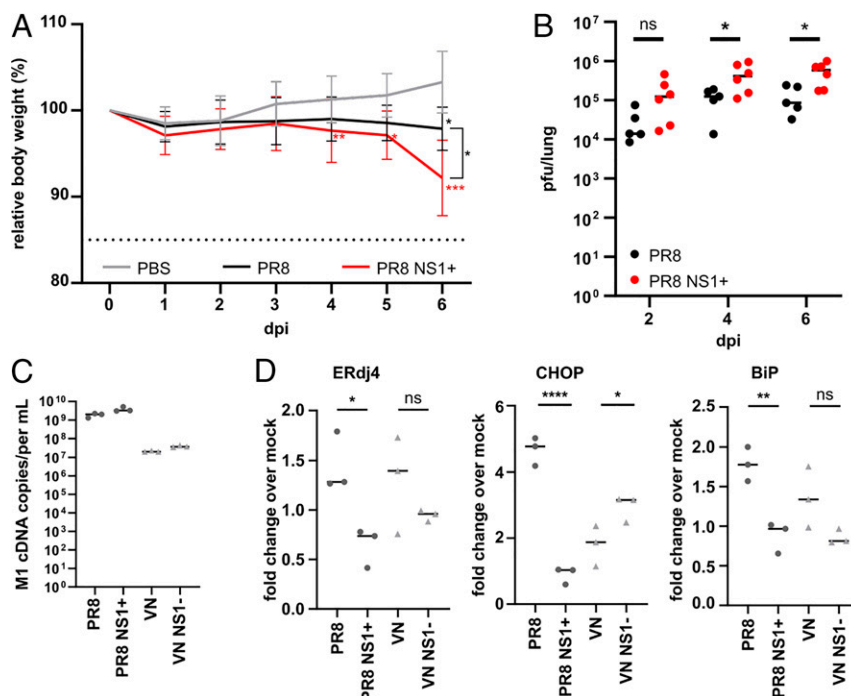


Fig. 5. NS1 CPSF30-binding ability confers an advantage in vivo and prevents UPR in 3D human epithelial airways. (A and B) Eight-week-old female C57B/6 mice were inoculated with PBS or 40 pfu of PR8 or PR8 NS1⁺ ($n = 6$ per group). (A) Weight was monitored daily and the relative body weight was plotted. Two-way ANOVA (or mixed-effects model) with Turkey's correction was used to compare each group within the same time pi. The dotted line represents the 15% body weight loss defined as the humane endpoint. (B) Whole lungs were collected at 2, 4, and 6 dpi and processed for analysis by plaque assay. Viral lung titers are shown in pfu/lung. Each dot represents an individual mouse and the bar represents the mean. Two-way ANOVA (multiple comparisons) with Sidak correction was used to compare each group each day. (C and D) Three-dimensional epithelial airways were infected apically at a MOI of 5 with PBS, PR8, PR8 NS1⁺, VN1203, and VN1203 NS1⁻ ($n = 3$). At 24 h pi, cells were lysed, total cellular RNA was extracted, and samples were processed by RT-qPCR for viral M1 (C), and ER stress-related genes (D) ERdj4, CHOP, and BiP. Each dot represents a Transwell and the bar represents the median. One-way ANOVA with Sidak correction was used to compare the values. ns $P > 0.05$, * $P \leq 0.05$, ** $P \leq 0.01$, **** $P \leq 0.0001$.

Our results implicate that both the quantity of NA and the sequence of the NA protein are essential determinants for NA's specific capacity to induce ER stress. However, from our sample set of viruses we conclude that ER stress leading to a substantial activation of the UPR is rather the exception than the rule in IAV biology. Most IAV strains appear to welcome a low level of ER stress, potentially for increased glycoprotein folding capacity, while avoiding a full activation of the otherwise potentially deleterious UPR. Additionally, ER stress was recently proposed to increase the tolerance for mutations in the major glycoproteins HA and NA (53). For the virus this is an important escape route to avoid the adaptive immune response of the host. A fine-tuned level of ER stress response might thus be overall beneficial for the virus. In order to achieve this low level of ER stress response, IAV would have in theory three options: 1) reducing the trigger load by reducing overall expression of NA, 2) express an easily foldable NA less recognized by BiP, or 3) antagonizing host glycoprotein production or even host protein production in general. Intriguingly, all strategies seem to be used by IAVs. They even seem to be used in combination as seen for A/Vietnam/1203/2004. Indeed, during infection with the VN1203 strain, little NA is produced despite the fact that the NS1 protein of VN1203 is able to antagonize CPSF30, thus preventing the polyadenylation of newly synthesized host mRNA. However, a true correlation between NA amounts and the capacity of NS1 to antagonize CPSF30 is bioinformatically difficult, since the prediction of ER stress induction potential requires nonavailable data.

Shutdown of host translation by NS1 was so far only associated with antagonism of innate immune responses. Here, we demonstrate in two knockout cell lines of major signaling hubs for anti-IAV responses, that the capacity to temper the ER stress response functions independently of a functional innate immune system. This means that the selection pressure to maintain this function is not only dictated by the innate host response, especially in view of the numerous, apparently redundant strategies the virus developed to counteract innate immunity. Additionally, NS1 is described to target protein kinase activated by dsRNA (PKR) a second signaling hub downstream of ER stress responses, which might also contribute to control host protein synthesis (54, 55).

Many viruses, both RNA and DNA, have been described to subvert the ER stress response to the best of their advantage (56). Viruses have evolved mechanisms to antagonize, induce, or even keep the ER stress response under tight control. A good example of this fine-tuned balance was recently described for Kaposi's sarcoma-associated herpesvirus (KSHV). Indeed, KSHV activates the UPR sensors but inhibits accumulations of downstream transcription factors (57). Murine cytomegalovirus (MCMV) was also recently shown to activated ER stress, since it requires the transcription factor sXBP1 and AT6 for the expression of its viral immediate early genes (58). Interestingly, herpes simplex virus 1 (HSV-1) has evolved a way to suppress IRE α signaling. Indeed, Zhang et al. showed that the tegument host shutoff protein UL41 degrades XBP1 mRNA via its endoribonuclease activity (59). This strategy, reducing the total amount of XBP1 mRNA, is fairly similar to the one we described in this paper for IAV. For influenza B, C, and D viruses, no shutoff activity was described for their NS1 proteins (60). It would be of interest to investigate whether these cousins of IAV developed alternative strategies to inhibit ER stress and/or keep it at a tolerable level.

In summary, we demonstrated here that IAV NA is the major determinant of ER stress induction during viral infection and that inhibition of cellular mRNA polyadenylation by NS1 is an important control mechanism to fine tune this proapoptotic host response to the virus advantage.

Materials and Methods

Materials Availability. All unique/stable reagents generated in this study are available from the lead contact with a completed Materials Transfer Agreement.

Cells. A549 (adenocarcinomic human alveolar basal epithelial cells, ATCC) and A549-derived cell lines were grown in DMEM/F12 (Dulbecco's Modified Eagle Medium: Nutrient Mixture F-12, Gibco). HEK 293T (human embryonic kidney, ATCC) and MDCK (Madin-Darby canine kidney, ATCC) cells were grown in DMEM. LA4 (murine epithelial lung adenoma, ATCC) cells were grown in DMEM/F12 supplemented with 15% foetal bovine serum (FBS). Cell culture media were supplemented with 10% (vol/vol) heat-inactivated FBS (Gibco) and 100 U/mL penicillin/streptomycin (Pen/Strep). Cells were maintained at 37 °C with 5% CO₂ and 90% humidity. RIG-1 and STAT1 knockout A549 clones were generated by the means of CRISPR-Cas9-mediated genome editing using ribonucleoproteins (RNPs) consisting of Alt-R SpCas9 nuclease in complex with Alt-R CRISPR-Cas9 CRISPR RNA (crRNA) (RIG-1 protospacer domain targeted in RIG-1 KO-1 clone, CCACCGAGCAGCGACGAGCTG, RIG-1 protospacer domain targeted in RIG-1 KO-2 clone: AAACAACAAGGGCCC-AATGGAGG; STAT1 protospacer domain targeted in both STAT1 KO-1 and -2, TCAGACAGTACCTGGCACAGTGG, underlined the NGG \cdot). TracerRNA, crRNA oligos, and recombinant Cas9 endonuclease were obtained from Integrated DNA Technology. In brief, preassembled RNP complexes were delivered into A549 cells by reverse transfection, using RNAiMax (Thermo Fisher Scientific). At 48 h posttransfection, cells were subjected to T7 endonuclease I (New England Biolabs) assay to estimate the frequency of genome-editing events. Screening of individual clones, generated by limiting dilution, was performed by immunoblotting to determine the protein expression of the target genes, followed by genotyping by next-generation sequencing (NGS) or Sanger sequencing. Of note, matching control lines were subjected to the same protocol, but carried no InDel mutations.

Plasmids. Plasmids are listed in *SI Appendix, Table S4*.

Antibodies. Antibodies for immunoblotting and immunofluorescence are listed in *SI Appendix, Table S5*.

Oligonucleotides. All oligonucleotides were purchased from Microsynth (France) represented in *SI Appendix, Table S6*.

Viruses. Virus stocks were grown in MDCK II cells or embryonated chicken eggs (*SI Appendix, Table S7*). For virus infections, cells were washed once in PBS, viruses were diluted in PBS-0.2% bovine serum albumin (BSA) and added to cell monolayer. At 45 min pi, cells were washed once with PBS and 1 mL of infection media was added (DMEM/F12 with 0.2% BSA and 1% Pen/Strep). Recombinant viruses were produced using the eight-plasmid rescue system (61). Unique viral clones were isolated after plaque assay on MDCK, grown in eggs or cells, and their genome fully sequenced.

Immunofluorescence, Z-Stack Imaging, and Analysis. A549 cells were infected with PR8 at a MOI of 5 for 8 h or 24 h, treated with PBS or tunicamycin at 5 μ g/mL. Cells were fixed in 4% formaldehyde for 20 min and blocked in PBS 1% BSA for 1 h. Then cells were stained with primary/secondary antibody pairs depending on the experiment: Anti-BIP and secondary anti-rabbit Alexa Fluor 488, anti-CD44 and secondary anti-rat Alexa Fluor 555, mouse anti-NP, and secondary anti-mouse Alexa Fluor 633 or rabbit anti-NP and secondary anti-rabbit Alexa Fluor 488.

Widefield images were acquired using a Nikon Eclipse ts2R microscope and Nis-Elements BR v4.60 software. Confocal images were acquired using a Zeiss LSM 800 Airyscan confocal laser scanning microscope with ZEN 2.3 software and a Plan Apochromat 63 \times 1.4 NA objective with oil immersion. The fluorophores DAPI, AF-488, AF-555, and AF-633 were excited by 405-, 488-, 561-, and 640-nm laser lines, respectively. Pinhole diameters, detector gains, and laser intensities were optimized thanks to the bioimaging staff and kept constant throughout the same experiment. Cells with few neighboring cells were selected for image acquisition in order to facilitate the delimitation of a single cell in the following image analysis step. For the infected conditions, cells were screened for infection with the 640-nm track prior to imaging. Z-stacks were acquired using three tracks, 405, 488, and 561 nm.

XBP1 mRNA Splicing Assay Using Semiquantitative RT-PCR. Following infection, total cellular RNA was isolated using the E.Z.N.A. Total RNA kit (Omega Bio-Tek #R6834-01) according to the manufacturer's instructions. cDNA was synthesized using M-MLV reverse transcriptase (Promega #M170A) according to the manufacturer's instructions but using 100 ng of RNA as starting material and oligo dT as primers. PCR was performed using GoTaq G2 DNA polymerase (Promega #M784B) with 5 \times Green GoTaq reaction buffer (Promega #M791A). The primers were designed to flank the splicing site of the XBP1 mRNA in order to amplify both the unspliced and the spliced form. A PCR for β -actin was used as a control. PCR products were separated on a 3% agarose

gel containing EtBr for visualization. Images were acquired using the GelDoc XR⁺ System (Bio-Rad) and analyzed with Image Lab software (v4.1 from Bio-Rad).

XBP1 mRNA Splicing Using Luciferase Reporter. Subconfluent 293T cells were transfected (using TransIT-LT1, Mirus #Mir2304) with pFLAG-XBP1u-Fluc (39). Cells were also transfected with other expression plasmids (pCAGGS constructs expressing either influenza NA or NS1, or pcDNA3.1(+)-GRP78/BiP expressing the chaperone BiP) and treated or not with tunicamycin (Merck #T7765) at 1 μg/mL or kifunensine (Merck #K1140) at 10 μg/mL. At the indicated time, cells were lysed and the luciferase assay was performed using a dual-luciferase reporter assay system (Promega #E1910).

Enzyme-Like Lectin Assay. The neuraminidase activity was quantified using a lectin (peanut agglutinin, PNA) linked to a peroxidase (Po-PNA), described by Lambré et al. (62). Fetuin 50 μg/mL (Merck #F3385) in 0.1 M carbonate/bicarbonate buffer pH 9.6 was coated on a high-protein binding plate (Nunc MaxiSorp # 44-2404-21) overnight at 4 °C. Plates were washed three times with PBS, blocked with PBS 5% BSA for 1 h and then washed three times in PBS 0.5% Tween-20. For NA activity, 100 μL of serial dilution of viruses or purified proteins were added to the fetuin-coated plate and incubated for 2 h at 37 °C. For viruses, the starting concentration was 10⁷ pfu/mL in PBS-CaCl₂-MgCl₂ (Gibco #14040091) with 1% BSA followed by a threefold dilution. For purified proteins (63), the starting concentration was 100 ng/mL in PBS-CaCl₂-MgCl₂ with 1% BSA followed by a twofold dilution. Plates were washed six times in PBS 0.5% Tween-20 and then 100 μL of Po-PNA (Merck #L7759) at 5 μg/mL diluted in PBS was added for 2 h at room temperature and in the dark. Plates were washed six times in PBS 0.5% Tween-20, and 100 μL of TMB (3,3',5,5'-tetramethylbenzidine, Merck #860336) was added. After a 1- to 5-min incubation, the reaction was stopped using 50 μL of 2 M sulfuric acid. Plates were read at 450 nm using a BioTek Synergy H1 plate reader.

Immunoprecipitation Assay. The 293T cells were transfected with 1 μg of pCAGGS.Flag-CPSF30 or with 0.5 μg of pCAGGS.Flag-ZsGreen using 2 μL/μg DNA of TransIT-LT1 (Mirus #Mir2304). At 24 h posttransfection, cells were infected at a MOI of either 5 (for PR8 and VN1203) or 0.5 (for Neth602). For PR8 and VN1203, cells were lysed on ice after 8 h in 300 μL IP lysis buffer (50 mM Tris HCl pH 7.5, 150 mM NaCl, 0.5% vol/vol Nonidet P-40, 5 mM EDTA with protease inhibitors) (Pierce #88266). For Neth602 infection, cells were lysed after 24 h. Fifty microliters of the cleared lysate was mixed 1:1 with protein lysis buffer (50 mM Tris HCl pH 6.8, 10% glycerol, 2% SDS, 0.1 M DTT and 0.1% bromophenol blue in H₂O) to serve as whole cell lysate control, while the remaining 200 μL was processed for immunoprecipitation at 4 °C using anti-Flag M2 affinity gel (Sigma #A2220). Samples were then used in a Western blot.

Gaussia Luciferase Assay. Subconfluent 293T cells were transfected (using TransIT-LT1, Mirus #Mir2304) with pCMV.Gluc (M60). This construct expresses Gaussia luciferase under the control of a CMV promoter. Cells were also transfected with other expression plasmids for NS1 (pCAGGS constructs expressing different NS1 proteins). At 24 h posttransfection, culture media were collected and frozen at -20 °C. At the same time, cells were lysed for subsequent WB analysis.

RT-qPCR. cDNA was synthesized using M-MLV reverse transcriptase (Promega #M170A) according to the manufacturer's instructions, using 100 ng of RNA as starting material and oligo dT as primers. For quantitative PCR, 1 μL of cDNA was mixed with 10 μL of 2X KAPA SYBR FAST Universal (#KK4602), 0.4 μL of each forward (10 μM) and reverse (10 μM) primer, and 8.2 μL of UltraPure DNase/RNase free distilled water (Invitrogen #10977). qPCR was performed on a BioRad CFX96 Real-Time System with the following protocol: initial denaturation step at 95 °C for 5 min, followed by 40 cycles of denaturation at 95 °C for 30 s, and annealing/extension at 60 °C for 30 s.

Structural Modeling. The models of neuraminidases of different influenza strains were calculated with Modeler 9.18 (64). The used templates and the sequence similarity are presented in *SI Appendix, Table S8*. For each protein

the 500 models were calculated that were subsequently assessed by the discrete optimized protein energy (DOPE) method (65). The visual inspection and assessment of secondary structural elements were done on models with the best DOPE score using Chimera software (66). The BiPPred server was used to evaluate the probability of BiP protein binding to the different peptides on the sequences of NA (47). The sequences of the N-terminal fragments and of the loop are included in the analysis are shown in *SI Appendix, Tables S1 and S2*, respectively.

Infection of 3D Human Upper Airway Epithelium. The 3D human upper airway epithelium (MucilAir) from a pool of healthy donors was purchased from Epithelix and cultured in an air-liquid interface. Cells were infected after six washes with PBS Ca²⁺ Mg²⁺ with 100 μL of virus suspension (MOI 5) from the apical side. Virus was removed after 3 h and Transwells were incubated for an additional 21 h at 37 °C. RNA was isolated 24 h pi, using E.Z.N.A. Total RNA kit (Omega Bio-Tek #R6834-01) according to the manufacturer's instructions.

Mice and Viral Lung Titer. C57BL/6J mice (female, 8 wk of age) were purchased from Charles River Laboratories and housed under SPF/BSL2 conditions. All animals were housed for 7 d to adjust to housing conditions under a strict 12 h light/dark cycle and fed ad libitum. For IAV infection, mice were injected intraperitoneally with a mix of ketamin/xylazine (100 and 5 mg/kg, respectively) in 100 μL of sterile PBS. Upon reaching deep anesthesia, mice were inoculated intranasally with 40 μL of PBS or with 40 μL of PBS containing 40 pfu of virus. Animal weights were measured daily. Animals were killed using controlled CO₂ exposure at 2, 4, and 6 dpi. Whole lungs were sampled immediately after killing using sterile tools. Tools were changed in between experimental groups to avoid cross-contamination. Whole lungs were homogenized with 1/4 inch stainless steel grinding balls (MPBio) in 1 mL PBS, using a Bead Blaster 24 (Benchmark Scientific) with a speed setting of 6 m/s for 30 s and 30-s intervals, repeated two times. Samples were centrifuged at 2,000 × g for 5 min and supernatant was used for plaque assay in MDCK cells.

Plaque Assay. A confluent monolayer of MDCK cells was infected with 200 μL of serially diluted virus. Viruses were diluted in PBS 0.2% (wt/vol) bovine serum albumin (BSA) (Millipore; 126579). Forty-five minutes pi, the inoculum was removed and an agarose overlay (final concentrations: 1× minimal essential medium [MEM], 1% agarose, 100 mM l-glutamine, 2.5% sodium bicarbonate, 0.5 M Hepes, 5 mg/mL of Pen/Strep, 0.2% BSA, and 0.01% diethylaminoethyl-dextran) was added. Cells were incubated at 37 °C for 48 h. Then cells were fixed in formaldehyde, the overlay was removed, and the cell monolayer was stained with a solution of crystal violet.

Statistics. Statistical analysis was performed using GraphPad Prism 8. Statistical tests applied are indicated in each respective figure legend. ns $P > 0.05$, * $P \leq 0.05$, ** $P \leq 0.01$, *** $P \leq 0.001$, **** $P \leq 0.0001$.

Ethical Approval. All animal procedures were in accordance with federal regulations of the Bundesamt für Lebensmittelsicherheit und Veterenärwesen (BLV), Switzerland (Tierschutzgesetz) and approved by direction de l'expérimentation animale and the cantonal authorities of the Canton Geneva (license number GE/92/15). Embryonated chicken eggs were obtained from the University of Geneva Animalerie d'Arare and infected on day 10 of embryonic development.

Data Availability. All study data are included in the article and/or supporting information.

ACKNOWLEDGMENTS. This work was supported by the Swiss National Science Foundation through Grants 182475 to M.S. and 182464 to B.G.H. and by the Gertrude von Meissner Foundation. Molecular graphics and analyses were performed with University of California San Francisco (UCSF) Chimera, developed by the Resource for Biocomputing, Visualization, and Informatics at UCSF, with support from NIH Grant P41-GM103311. We thank the Protein Modelling Unit of the University of Lausanne for structural bioinformatics support.

1. K. W. Moremen, M. Tiemeyer, A. V. Nairn, Vertebrate protein glycosylation: Diversity, synthesis and function. *Nat. Rev. Mol. Cell Biol.* **13**, 448–462 (2012).
2. A. Bakunts et al., Ratiometric sensing of BiP-client versus BiP levels by the unfolded protein response determines its signaling amplitude. *eLife* **6**, e27518 (2017).
3. M. Vitale et al., Inadequate BiP availability defines endoplasmic reticulum stress. *eLife* **8**, e41168 (2019).
4. K. F. R. Pobre, G. J. Poet, L. M. Hendershot, The endoplasmic reticulum (ER) chaperone BiP is a master regulator of ER functions: Getting by with a little help from ERdj friends. *J. Biol. Chem.* **294**, 2098–2108 (2019).

5. P. Walter, D. Ron, The unfolded protein response: From stress pathway to homeostatic regulation. *Science* **334**, 1081–1086 (2011).
6. H. Yoshida, T. Matsui, A. Yamamoto, T. Okada, K. Mori, XBP1 mRNA is induced by ATF6 and spliced by IRE1 in response to ER stress to produce a highly active transcription factor. *Cell* **107**, 881–891 (2001).
7. K. Yamamoto, H. Yoshida, K. Kokame, R. J. Kaufman, K. Mori, Differential contributions of ATF6 and XBP1 to the activation of endoplasmic reticulum stress-responsive cis-acting elements ERSE, UPRE and ERSE-II. *J. Biochem.* **136**, 343–350 (2004).

8. A. H. Lee, N. N. Iwakoshi, L. H. Glimcher, XBP-1 regulates a subset of endoplasmic reticulum resident chaperone genes in the unfolded protein response. *Mol. Cell. Biol.* **23**, 7448–7459 (2003).
9. R. Iurlaro, C. Muñoz-Pinedo, Cell death induced by endoplasmic reticulum stress. *FEBS J.* **283**, 2640–2652 (2016).
10. W. Chen, J. Helenius, I. Braakman, A. Helenius, Cotranslational folding and calnexin binding during glycoprotein synthesis. *Proc. Natl. Acad. Sci. U.S.A.* **92**, 6229–6233 (1995).
11. D. N. Hebert, B. Foellmer, A. Helenius, Calnexin and calreticulin promote folding, delay oligomerization and suppress degradation of influenza hemagglutinin in microsomes. *EMBO J.* **15**, 2961–2968 (1996).
12. N. Wang, E. J. Glidden, S. R. Murphy, B. R. Pearce, D. N. Hebert, The cotranslational maturation program for the type II membrane glycoprotein influenza neuraminidase. *J. Biol. Chem.* **283**, 33826–33837 (2008).
13. C. F. Basler, A. Garcia-Sastre, P. Palese, Mutation of neuraminidase cysteine residues yields temperature-sensitive influenza viruses. *J. Virol.* **73**, 8095–8103 (1999).
14. R. Daniels, B. Kurowski, A. E. Johnson, D. N. Hebert, N-linked glycans direct the cotranslational folding pathway of influenza hemagglutinin. *Mol. Cell* **11**, 79–90 (2003).
15. M. S. Segal, J. M. Bye, J. F. Sambrook, M.-J. H. Gething, Disulfide bond formation during the folding of influenza virus hemagglutinin. *J. Cell Biol.* **118**, 227–244 (1992).
16. U. Tatu, C. Hammond, A. Helenius, Folding and oligomerization of influenza hemagglutinin in the ER and the intermediate compartment. *EMBO J.* **14**, 1340–1348 (1995).
17. T. Saito, G. Taylor, R. G. Webster, Steps in maturation of influenza A virus neuraminidase. *J. Virol.* **69**, 5011–5017 (1995).
18. D. V. da Silva, J. Nordholm, U. Madjo, A. Pfeiffer, R. Daniels, Assembly of subtype 1 influenza neuraminidase is driven by both the transmembrane and head domains. *J. Biol. Chem.* **288**, 644–653 (2013).
19. B. Hogue, D. Nayak, Synthesis and processing of the influenza virus neuraminidase, a type II transmembrane glycoprotein. *Virology* **188**, 510–517 (1992).
20. S. M. Hurtle, D. G. Bole, H. Hoover-Litty, A. Helenius, C. S. Copeland, Interactions of misfolded influenza virus hemagglutinin with binding protein (BiP). *J. Cell Biol.* **108**, 2117–2126 (1989).
21. E. R. Hrinicus *et al.*, Acute lung injury results from innate sensing of viruses by an ER stress pathway. *Cell Rep.* **11**, 1591–1603 (2015).
22. Y. Yin *et al.*, Glycosylation deletion of hemagglutinin head in the H5 subtype avian influenza virus enhances its virulence in mammals by inducing endoplasmic reticulum stress. *Transbound. Emerg. Dis.* **67**, 1492–1506 (2020).
23. I. H. Hassan *et al.*, Influenza A viral replication is blocked by inhibition of the inositol-requiring enzyme 1 (IRE1) stress pathway. *J. Biol. Chem.* **287**, 4679–4689 (2012).
24. E. C. Roberson *et al.*, Influenza induces endoplasmic reticulum stress, caspase-12-dependent apoptosis, and c-Jun N-terminal kinase-mediated transforming growth factor- β release in lung epithelial cells. *Am. J. Respir. Cell Mol. Biol.* **46**, 573–581 (2012).
25. D. A. Frabutt, B. Wang, S. Riaz, R. C. Schwartz, Y.-H. Zheng, Innate sensing of influenza A virus hemagglutinin glycoproteins by the host endoplasmic reticulum (ER) stress pathway triggers a potent antiviral response via ER-associated protein degradation. *J. Virol.* **92**, e01690–17 (2018).
26. Y. Sun *et al.*, Molecular basis for the recognition of the human AAUAAA polyadenylation signal. *Proc. Natl. Acad. Sci. U.S.A.* **115**, E1419–E1428 (2018).
27. L. Schönemann *et al.*, Reconstitution of CPSF active in polyadenylation: Recognition of the polyadenylation signal by WDR33. *Genes Dev.* **28**, 2381–2393 (2014).
28. M. E. Nemeroff, S. M. Barabino, Y. Li, W. Keller, R. M. Krug, Influenza virus NS1 protein interacts with the cellular 30 kDa subunit of CPSF and inhibits 3' end formation of cellular pre-mRNAs. *Mol. Cell* **1**, 991–1000 (1998).
29. K. Y. Twu, D. L. Noah, P. Rao, R. L. Kuo, R. M. Krug, The CPSF30 binding site on the NS1A protein of influenza A virus is a potential antiviral target. *J. Virol.* **80**, 3957–3965 (2006).
30. I. Ramos *et al.*, Contribution of double-stranded RNA and CPSF30 binding domains of influenza virus NS1 to the inhibition of type I interferon production and activation of human dendritic cells. *J. Virol.* **87**, 2430–2440 (2013).
31. G. Kochs, A. Garcia-Sastre, L. Martinez-Sobrido, Multiple anti-interferon actions of the influenza A virus NS1 protein. *J. Virol.* **81**, 7011–7021 (2007).
32. B. G. Hale *et al.*, Inefficient control of host gene expression by the 2009 pandemic H1N1 influenza A virus NS1 protein. *J. Virol.* **84**, 6909–6922 (2010).
33. M. D. Shoulders *et al.*, Stress-independent activation of XBPs1 and/or ATF6 reveals three functionally diverse ER proteostasis environments. *Cell Rep.* **3**, 1279–1292 (2013).
34. L. Plate *et al.*, Small molecule proteostasis regulators that reprogram the ER to reduce extracellular protein aggregation. *eLife* **5**, e15550 (2016).
35. H. Yang, M. Niemeijer, B. van de Water, J. B. Beltman, ATF6 is a critical determinant of CHOP dynamics during the unfolded protein response. *iScience* **23**, 100860 (2020).
36. H. Quan, Q. Fan, C. Li, Y. Y. Wang, L. Wang, The transcriptional profiles and functional implications of long non-coding RNAs in the unfolded protein response. *Sci. Rep.* **8**, 4981 (2018).
37. E. C. Hutchinson *et al.*, Conserved and host-specific features of influenza virion architecture. *Nat. Commun.* **5**, 4816 (2014).
38. A. Zheng *et al.*, Enhancing neuraminidase immunogenicity of influenza A viruses by rewiring RNA packaging signals. *J. Virol.* **94**, e00742-20 (2020).
39. J. R. Jheng, K. S. Lau, W. F. Tang, M. S. Wu, J. T. Horng, Endoplasmic reticulum stress is induced and modulated by enterovirus 71. *Cell. Microbiol.* **12**, 796–813 (2010).
40. H. L. Yen *et al.*, Importance of neuraminidase active-site residues to the neuraminidase inhibitor resistance of influenza viruses. *J. Virol.* **80**, 8787–8795 (2006).
41. X. Zhu *et al.*, Influenza virus neuraminidases with reduced enzymatic activity that avidly bind sialic acid receptors. *J. Virol.* **86**, 13371–13383 (2012).
42. Q. Li *et al.*, Structural and functional characterization of neuraminidase-like molecule N10 derived from bat influenza A virus. *Proc. Natl. Acad. Sci. U.S.A.* **109**, 18897–18902 (2012).
43. X. Zhu *et al.*, Crystal structures of two subtype N10 neuraminidase-like proteins from bat influenza A viruses reveal a diverged putative active site. *Proc. Natl. Acad. Sci. U.S.A.* **109**, 18903–18908 (2012).
44. J. M. Brunner *et al.*, Morbillivirus glycoprotein expression induces ER stress, alters Ca²⁺ homeostasis and results in the release of vasostatin. *PLoS One* **7**, e32803 (2012).
45. J. Hwang, L. Qi, Quality control in the endoplasmic reticulum: Crosstalk between ERAD and UPR pathways. *Trends Biochem. Sci.* **43**, 593–605 (2018).
46. A. D. Elbein, J. E. Tropea, M. Mitchell, G. P. Kaushal, Kifunensine, a potent inhibitor of the glycoprotein processing mannosidase I. *J. Biol. Chem.* **265**, 15599–15605 (1990).
47. M. Schneider *et al.*, BiPPred: Combined sequence- and structure-based prediction of peptide binding to the Hsp70 chaperone BiP. *Proteins* **84**, 1390–1407 (2016).
48. A. E. Firth *et al.*, Ribosomal frameshifting used in influenza A virus expression occurs within the sequence UCC_UUU_CGU and is in the +1 direction. *Open Biol.* **2**, 120109 (2012).
49. B. W. Jagger *et al.*, An overlapping protein-coding region in influenza A virus segment 3 modulates the host response. *Science* **337**, 199–204 (2012).
50. R. L. Kuo, R. M. Krug, Influenza A virus polymerase is an integral component of the CPSF30-NS1A protein complex in infected cells. *J. Virol.* **83**, 1611–1616 (2009).
51. Y. Zhang *et al.*, Glycosylation on hemagglutinin affects the virulence and pathogenicity of pandemic H1N1/2009 influenza A virus in mice. *PLoS One* **8**, e61397 (2013).
52. X. Sun *et al.*, N-linked glycosylation of the hemagglutinin protein influences virulence and antigenicity of the 1918 pandemic and seasonal H1N1 influenza A viruses. *J. Virol.* **87**, 8756–8766 (2013).
53. A. M. Phillips *et al.*, Enhanced ER proteostasis and temperature differentially impact the mutational tolerance of influenza hemagglutinin. *eLife* **7**, e38795 (2018).
54. Y. Lu, M. Wambach, M. G. Katze, R. M. Krug, Binding of the influenza virus NS1 protein to double-stranded RNA inhibits the activation of the protein kinase that phosphorylates the eIF-2 translation initiation factor. *Virology* **214**, 222–228 (1995).
55. J. Y. Min, S. Li, G. C. Sen, R. M. Krug, A site on the influenza A virus NS1 protein mediates both inhibition of PKR activation and temporal regulation of viral RNA synthesis. *Virology* **363**, 236–243 (2007).
56. J. R. Jheng, J. Y. Ho, J. T. Horng, ER stress, autophagy, and RNA viruses. *Front. Microbiol.* **5**, 388 (2014).
57. B. P. Johnston, E. S. Pringle, C. McCormick, KSHV activates unfolded protein response sensors but suppresses downstream transcriptional responses to support lytic replication. *PLoS Pathog.* **15**, e1008185 (2019).
58. F. Hinte, E. van Anken, B. Tirosh, W. Brune, Repression of viral gene expression and replication by the unfolded protein response effector XBP1u. *eLife* **9**, e51804 (2020).
59. P. Zhang, C. Su, Z. Jiang, C. Zheng, Herpes simplex virus 1 UL41 protein suppresses the IRE1/XBP1 signal pathway of the unfolded protein response via its RNase activity. *J. Virol.* **91**, e02056-16 (2017).
60. A. Nogales *et al.*, Functional characterization and direct comparison of influenza A, B, C, and D NS1 proteins in vitro and in vivo. *Front. Microbiol.* **10**, 2862 (2019).
61. M. Quinlivan *et al.*, Attenuation of equine influenza viruses through truncations of the NS1 protein. *J. Virol.* **79**, 8431–8439 (2005).
62. C. R. Lambre, H. Terzidis, A. Greffard, R. G. Webster, Measurement of anti-influenza neuraminidase antibody using a peroxidase-linked lectin and microtitre plates coated with natural substrates. *J. Immunol. Methods* **135**, 49–57 (1990).
63. I. Margine, P. Palese, F. Kramer, Expression of functional recombinant hemagglutinin and neuraminidase proteins from the novel H7N9 influenza virus using the baculovirus expression system. *J. Vis. Exp.*, e51112 10.3791/51112 (2013).
64. B. Webb, A. Sali, Comparative protein structure modeling using Modeller. *Curr. Protoc. Bioinform.* **54**, 5.6.1–5.6.37 (2016).
65. M. Y. Shen, A. Sali, Statistical potential for assessment and prediction of protein structures. *Protein Sci.* **15**, 2507–2524 (2006).
66. E. F. Pettersen *et al.*, UCSF Chimera—A visualization system for exploratory research and analysis. *J. Comput. Chem.* **25**, 1605–1612 (2004).